ABSTRACT

Title of Dissertation:	NON-DESTRUCTIVE TESTING FOR QUALITY ASSURANCE OF CONCRETE & PERFORMANCE PREDICTION OF BRIDGE DECKS WITH MACHINE LEARNING
	Setare Ghahri Saremi, Doctor of Philosophy, 2022
Dissertation directed by:	Associate Professor, Dimitrios Goulias, Department of Civil and Environmental Engineering

Non-destructive testing (NDT) methods are particularly valuable in the quality assurance (QA) process since they do not interfere with production of concrete and reduce testing time and cost. NDTs can provide early warnings in meeting strength requirements at early ages of concrete as well as long term strength. NDTs are also valuable in providing evaluation of health of in-service infrastructures such as bridge and pavement.

The results of this study can be used for potential adoption of an NDT-based QA plan. Their adoption in QA will provide the opportunity to test a larger portion of concrete during assessment without a significant increase in QA cost and testing time. To achieve that purpose, the selected NDTs should be fast, accurate, reliable and simple

to run. The NDT methods explored in this study included infrared thermography, ultrasonic pulse velocity (UPV), fundamental resonance frequency, rebound hammer, ground penetrating radar (GPR), and ultrasonic pulse echo (UPE).

Different sets of NDTs were selected in each experimental study undertaken in this dissertation appropriate to the research objectives and goals in each case. For strength gain monitoring, (i.e., maturity modeling during early ages of hydration), the suggested NDTs need to provide an assessment of the mechanical properties of concrete. To assess the concrete quality during production and/or construction the selected NDTs should rapidly identify potential issues concerning uniformity and/or the presence of production and placement defects. For evaluating the condition of concrete bridge decks with asphalt overlays, GPR response was used to detect layer thickness and concrete quality and to evaluate reinforcement condition. For addressing the transition from lab to field results, machine learning modeling was used to predict the structure condition. Therefore, two artificial neural network (ANN) models were proposed and assessed in this study to predict the condition of bridge decks in Maryland and Massachusetts.

Thus, the objectives of this research were to identify and assess alternative NDT methods that can be used in: i) monitoring and/or estimating strength gain (i.e., maturity modeling) in concrete; ii) evaluating concrete uniformity and production quality; iii) detecting and measuring the extent of delamination in concrete slab representing small scale field conditions; iv) evaluating GPR in assessing the condition of pavement layers, concrete quality and reinforcement in bridge decks; and v) employing machine learning modeling to predict the condition of bridge decks.

NON-DESTRUCTIVE TESTING FOR QUALITY ASSURANCE OF CONCRETE & PERFORMANCE PREDICTION OF BRIDGE DECKS WITH MACHINE LEARNING

by

Setare Ghahri Saremi

Dissertation submitted to the Faculty of the Graduate School of the
University of Maryland, College Park, in partial fulfillment
of the requirements for the degree of
Doctor of Philosophy
2022

Advisory Committee:
  Professor Dimitrios G. Goulias, Chair
  Professor M. Sherif Aggour
  Professor Ahmet Aydilek
  Professor Miroslaw J. Skibniewski
  Professor Sung Lee

© Copyright by
Setare Ghahri Saremi
2022

Dedication

To Abbas, my love and my best friend.

Acknowledgements

This dissertation would have been far from reach without the guidance, support, knowledge and help of many individuals and institutes to whom I owe the greatest of gratitude.

First and foremost, I would like to express my sincere gratitude to my advisor, Professor Dimitrios Goulias, for his continuous support and guidance, for his patience, motivation, enthusiasm, and immense knowledge. His guidance helped me in the time of the research and writing of this dissertation.

I would like to express my deepest thanks to my dissertation committee, Professor M. Sherif Aggour, Professor Ahmet Aydilek, Professor Miroslaw J. Skibniewski, Professor Sung Lee for their valuable comments, advice, and discussions.

I would like to express my special gratitude to Mr. Alfredo Bituin, laboratory manager of the Whiting-Turner Infrastructure Engineering Laboratories in University of Maryland, Anjuman Akhter, and Yunpeng Zhao, my lab mates, for their help and assistance in performing the extensive laboratory experiments. I would also like to thank Mr. Stuart Sherman, lab manager at national ready mixed concrete association (NRMCA) and his team for their kind assistance. I am also thankful for learning a great deal from my ENCE 300 students.

Finally, completing this important step of my academic life could have not been possible without support and love from my family and friends. I would like to thank my parents and my sisters for their support through my life. I would like to pay my special regards to all of my friends, especially Aref Darzi, Shahrzad Saffari, Arash Karimipour, Sara Ghafarsamar, Shakiba Nikfarjam, Mani Karimzadeh, and Somayeh Mohammadi for their support and inspiration during my life as a Maryland terrapin.

I am extremely grateful for receiving the greatest support and inspiration from my better half, Abbasali Taghavi. Words are powerless to express my gratitude and appreciation. Abbas, consider yourself heartily thanked.

Table of Contents

DEDICATION .... **II**

ACKNOWLEDGEMENTS .... **III**

TABLE OF CONTENTS .... **IV**

LIST OF FIGURES .... **VII**

LIST OF ABBREVIATIONS .... **XIII**

CHAPTER 1. INTRODUCTION **1**

1.1 SUMMARY 1
1.2 ORGANIZATION OF THE DISSERTATION 3

CHAPTER 2. MONITORING THE STRENGTH GAIN OF CONCRETE BY MEANS OF NDT FOR POTENTIAL ADOPTION IN QUALITY ASSURANCE (QA) **5**

2.1. INTRODUCTION 5
2.2. BACKGROUND & LITERATURE REVIEW ON NDTS 6
  2.1.1 Infrared Thermography (IRT) *6*
  2.1.2. Ultrasonic Pulse Velocity (UPV) *8*
  2.1.3. Resonant Frequency *9*
  2.1.4. Rebound Hammer *11*
2.3 INITIAL ASSESSMENT OF CONCRETE STRENGTH GAIN MONITORING WITH NDTS 12
  2.3.1 Experimental Testing *12*
  2.3.2 Results *13*
2.4 VALIDATION OF CONCRETE STRENGTH GAIN MONITORING WITH ADDITIONAL CONCRETE MIXTURES 20
  2.4.1. Experimental Testing and Results *20*
  2.4.2 Developing Master Curves for UPV and Dynamic Modulus *22*
  2.4.3. Rebound Hammer on Selected Mixes *27*
  2.4.4. Compressive Strength Modeling *29*
2.5. TESTING REPEATABILITY 31
2.6. SUMMARY & CONCLUSIONS 32

CHAPTER 3. ASSESSING CONCRETE UNIFORMITY WITH NDTS IN QUALITY ASSURANCE. **34**

3.1 INTRODUCTION 34
3.2. EXPERIMENTAL PROGRAM 35
  3.2.1. UPV Testing *37*
  3.2.2. Resonant Test Gauge *38*
  3.2.3. Rebound Hammer Testing *38*
  3.2.4. Chloride Permeability *38*
3.3. ANALYSES & RESULTS 40
  3.3.1. Effect of Honeycombing on Ultrasonic Pulse Velocity and Dynamic Modulus *40*
  3.3.2. Effect of Segregation on Ultrasonic Pulse Velocity and Dynamic Modulus *41*
  3.3.3. Chloride Permeability and Rebound Number of Segregated Samples *45*
3.4. TESTING REPEATABILITY 49
3.5. SUMMARY & CONCLUSIONS 51

CHAPTER 4. DELAMINATION AND VOID DETECTION IN CONCRETE WITH NDTS 53

4.1. INTRODUCTION 53
4.2. BACKGROUND & LITERATURE REVIEW ON THE NDTS 54
  4.2.1. Ground Penetrating Radar (GPR) *54*
  4.2.2. Ultrasonic Pulse Echo (UPE) *55*
4.3. MATERIALS & METHODS 58
  4.3.1. Materials *58*
  4.3.2. Dimensions of Samples & Materials *59*
  4.3.3. Monitoring the Strength Gain *61*
  4.3.4. NDT on Concrete Slab *62*
  4.3.5. Theory of Lamb Waves and Finite Element Method (FEM) *63*
4.4 RESULTS & DISCUSSION 67
  4.4.1. Detecting Delamination with Ultrasonic Pulse Velocity *67*
  4.4.2. Monitoring Maturity and Strength Gain of Concrete *69*
  4.4.3. UPE *72*
  4.4.4. GPR *78*
  4.4.5. Rebound Hammer *79*
  4.4.6. Finite Element *80*
4.5 SUMMARY & CONCLUSIONS 90

CHAPTER 5. CONDITION ASSESSMENT OF BRIDGE DECKS WITH GROUND PENETRATING RADAR 91

5.1. BRIDGE DECK INSPECTION & GPR 91
5.3. GPR WAVE PROPAGATION PRINCIPLES 93
  5.3.1. Overlay Thickness *93*
  5.3.2. Concrete Cover & Rebar Location *94*
  5.3.3. Corrosion of Rebar *94*
  5.3.4. Effect of Moisture *95*
5.4. CHARACTERISTIC OF SURVEYED BRIDGE DECK & GPR DATA COLLECTION 96
5.5. SIGNAL PROCESSING 98
  5.5.1. Time-zero Correction *98*
  5.5.2. Band-pass Filtering *99*
  5.5.3. Background Removal *99*
5.6. ANALYSIS & RESULTS 100
  5.6.1. Asphalt Overlay Thickness *100*
  5.6.2. Cover Depth and Reinforcement Condition *101*
  5.6.3. Rebar Conditions *104*
5.7. SUMMARY & CONCLUSION 105

CHAPTER 6. DEVELOPMENT OF ALTERNATIVE SEQUENCE CLASSIFICATION NETWORKS FOR PREDICTING CONDITION RATING OF BRIDGE DECKS 108

6.1. INTRODUCTION 108
6.2. NATIONAL BRIDGE INVENTORY (NBI) DATABASE 109
6.3. NEURAL NETWORK FOR SEQUENCE DATA 110
  6.3.1. Long Short-Term Memory (LSTM) *112*
  6.3.1.1. Network Architecture *113*
  6.3.1.2. Optimization Algorithm (Solver) *114*
  6.3.1.3. Sequence-to-one and Sequence-to-Sequence classification using LSTM *115*
  6.3.2. Convolutional Neural Network (CNN) *115*
  6.3.2.1. Sequence-to-Sequence Classification Using 1-D Convolutions (Temporal Convolutional Network, TCN) *116*
6.4. DATA PRE-PROCESSING 119

6.4.1. Dimensionality Reduction *121*
6.5. RESULTS OF ML MODELING 123
6.5.1. Long-Short Term Memory (LSTM): Sequence-to-one Classification *123*
6.5.2. Long-Short Term Memory (LSTM): Sequence-to-Sequence Classification *125*
6.5.3. Convolutional Neural Network: Sequence-to-One Classification *126*
6.5.4. Temporal Convolutional Network (Sequence-to-Sequence CNN) *128*
6.6. ASSESSING ML MODELS RESPONSE WITH ADDITIONAL DATA 129
6.7. SUMMARY & CONCLUSIONS 130
CHAPTER 7. CONCLUSIONS AND RECOMMENDATIONS 132
BIBLIOGRAPHY 136

List of Figures

Figure 1.1. Components of a QA program for concrete products incorporating NDT (Goulias, 2019). 3
Figure 2.1 Infrared thermography camera measuring the temperature of a concrete sample. 8
Figure 2.2. Ultrasonic pulse velocity (UPV) testing setup 10
Figure 2.3. Resonant frequency test gauge used to measure laboratory-made samples 11
Figure 2.4. Transverse and longitudinal mode configuration in resonant frequency testing (ASTM C215) 11
Figure 2.5. Schmidt rebound hammer 12
Figure 2.6. (a) iButtons for temperature monitoring, (b) location within the cylinder 14
Figure 2.7. Temperature - time history of concrete during (a) 28 days curing period, and, (b) first 24 hours. 16
Figure 2.8. Compressive strength versus temperature-time factor during 28 days of curing 16
Figure 2.9. a) Temperature through IRT, b) Maturity Index calculated from iButtons and IRT data. 17
Figure 2.10. Relationship between UPV and temperature-time product. 18
Figure 2.11. Compressive strength versus average dynamic modulus. 19
Figure 2.12. Dynamic modulus versus temperature-time product. 20
Figure 2.13. Relationship between a) UPV, and b) dynamic modulus and Temp-Time factor with the constant “a”. 24
Figure 2.14. Master curves for a) UPV, b) dynamic modulus. 25
Figure 2.15. Comparison of observed a) UPV, b) dynamic modulus shift factor and predicted shift factors. 27
Figure 2.16. Correlation between compressive strength and rebound number of each mix. 28
Figure 2.17. Relationship between compressive strength and rebound number of Mix 5 to Mix 8. 29
Figure 2.18. Model developing for compressive strength prediction, a) relationship between predicted and actual compressive strength, b) residuals of the model versus fitted values. 31
Figure 3.1. Honeycombing in concrete (a) Presence of honeycombing in a sample, (b) Location of honeycombing in different samples 37
Figure 3.2. Dimension and preparation of segregated samples, a) location of the cores, b) cores from top and bottom of the sample. 37
Figure 3.3. Testing (a) UPV in indirect mode on the control sample and (b) RTG in direct mode on the control sample 39
Figure 3.4. Rebound hammer a) testing on a segregated sample, b) testing grids. 39
Figure 3.5. Pulse velocities for honeycombing and control concrete, a) Mix 1, b) Mix 2, c) Mix 3. 42

Figure 3.6. Dynamic modulus of honeycombed and control samples, a) Mix 1, b) Mix 2, c) Mix 3. 43
Figure 3.7. UPV results at top, middle, and bottom of the segregated samples, a) Sample 4S-H, b) Sample 5S-M, c) Sample 6S-L. 44
Figure 3.8. Chloride permeability testing, a) setup for cores taken from segregated samples, b) thresholds. 46
Figure 3.9. Change in current and temperature of the a) Sample 4S, b) Sample 5S, c) Sample 6S. 47
Figure 3.10. Rebound number at top, middle, and bottom of the sample at age 3, 7, and 28 days (n=15). 48
Figure 3.11. Variation of different test results at top, middle, and bottom of the samples. 49
Figure 4.1. Ground penetrating radar and electromagnetic wave transmission and reflection in a GPR survey (Worksmart, Inc.). 55
Figure 4.2. Ultrasonic pulse echo (UPE), a) measurement unit, b) detecting a void at depth D (Misak et al., 2019), c) pulse inversion at a boundary (Pundit 2 operation instruction, 2017). 57
Figure 4.3. The behavior of a P-wave incident on an interface between two dissimilar media: a) reflection and refraction, b) mode conversion (Malhotra & Carino, 2003). 57
Figure 4.4. Delamination in concrete beam, a) formwork and artificial delamination, b) dimension of beam and location of delamination. 59
Figure 4.5. UPV measurements on delaminated beam, a) direct method, b) semi-direct method. 59
Figure 4.6. Concrete slab with embedded plexiglasses, a) top view, b) side view. 60
Figure 4.7. Concrete slab, a) formwork, b) finished product. 61
Figure 4.8. NDT on concrete slab, a) ultrasonic pulse echo (UPE), b) ground penetrating radar (GPR). 63
Figure 4.9. Different views of discretized (meshed) slab with embedded plexiglasses in ABAQUS 66
Figure 4.10. Schematic of position of the sensors and the load during finite element analysis. 67
Figure 4.11. Input unit pulse 67
Figure 4.12. Determining the location of delamination with UPV, a) direct measurement, b) semi-direct measurement. 69
Figure 4.13. Temperature history of concrete cylinder by iButton during hydration 70
Figure 4.14. Maturity index of concrete from iButton sensors and infrared thermography (IRT) on the cylinder 70
Figure 4.15. Relationship between UPV and temp-time factor 71
Figure 4.16. A-scan (two-way travel times) measured by UPE at early ages. 73
Figure 4.17. A-scan (two-way travel times) measured at later ages, a) at age 28 days with 2-cm increments, b) at age 28 days with 10-cm increments, c) at age 60 days with 2-cm increments, d) at age 60 days with 10-cm increments. 74

Figure 4.18. Signals of edge and middle locations at age a) 7 days, b) 28 days, and c) 60 days. The backwalls are shown by the vertical lines. 76
Figure 4.19. Mode conversion of the signals at the interface, a) delaminated area with depth at 95 µs, b) sound area with backwall at 131 µs. 77
Figure 4.20. B-scan (radargram) of the slab at age 60 days through a) line 1, b) line 2, c) line 3, and d) line 4 of Figure 4.4b. 79
Figure 4.21. Wave propagation snapshots resulting from FEM simulation after excitation of the transducers at the location of the larger delamination Point 1. 81
Figure 4.22. Wave reflection and refraction around the delamination, after a) 10 µs, b) 100 µs. 82
Figure 4.23. UPE repetition at a specific location (x=20 cm, y=40 cm). 83
Figure 4.24. Comparison of signals at a delaminated location at Point 1 (x=28 cm, y=20 cm). 83
Figure 4.25. Wave propagation simulation by finite element, a) plan view of the slab, b) side view of the slab. 85
Figure 4.26. Vertical wave propagation over the slab's thickness at different sections in x-direction (along the length of the slab). 85
Figure 4.27. Radial wave propagation in y and x directions 86
Figure 4.28. Stress change at the contact surface of the plexiglass and slab at Point 1. 87
Figure 4.29. Comparison of signals at a sound concrete location (Point 2). 88
Figure 4.30. Vertical and radial wave propagation in the slab 89
Figure 5.1. GPR travel time and distance for a rebar in concrete (Al-Qadi et al., 2005). 94
Figure 5.2. Schematic example of waveform of time domain bridge deck GPR, comparison of wet vs. dry. (Goulias and Scott, 2015) 96
Figure 5.3. GPR Surveys and bridge deck joints, a) Survey alignments, b) Overall view of survey paths (image source: Google©2020). 97
Figure 5.4. Open joint measurements and drilled holes, a) Open joint 1, b) Drilled holes. 98
Figure 5.5. GPR B-Scan with depth of asphalt overlay at location close to a) joint 1, and b) joint 2. 101
Figure 5.6. A-scan of GPR for locations close to a) joint 1, and b) joint 2. 101
Figure 5.7. GPR signal at the proximity of joint 1. a) B-scan, b) A-scan. 103
Figure 5.8. GPR signal at mileposts 72 (green) and 86 (red). a) B-scan, b) A-scan. 104
Figure 5.9. GPR signal at mileposts 28.7 and 29.2m, a) B-Scan, b) Enlarged B-scan. 106
Figure 5.10. GPR signal at mileposts 28.7 m (red) and 29.2 m (blue), A-Scan. 107
Figure 6.1. Summary of neural network models used for bridge sequence classification. 112
Figure 6.2. Long short_term memory cell (Wang et al., 2018). 113
Figure 6.3. Bidirectional long short_term memory layer (Wang et al., 2018). .. 114
Figure 6.4. Architecture of LSTM networks. 115
Figure 6.5. Architecture of temporal convolutional network (TCN). 118
Figure 6.6. Variation in deck condition rating of a bridge during 27 years. 120

Figure 6.7. Distribution of sequence length of Maryland's bridges. 121
Figure 6.8. Distribution of sequence length of Maryland's bridges after data cleaning. 121
Figure 6.9. Score of categorical features, with (a) Pearson's chi-squared & (b) Mutual information. 122
Figure 6.10. Input data for LSTM for a bridge with length of sequence of 4 and 6... 124
Figure 6.11. Confusion matrix for sequence-to-one LSTM for Maryland NBI_2 with variable sequence lengths. 125
Figure 6.12. Labeling the sequence of condition rating sequence-to-sequence classification... 125
Figure 6.13. Comparison of predicted and actual condition rating of a bridge deck by sequence-to-sequence LSTM. 126
Figure 6.14. Input data preparation for sequence-to-one CNN (Liu and Zhang, 2020). 127
Figure 6.15. Architecture of sequence-to-one classification built in Trial 6....... 128
Figure 6.16. Confusion matrix of sequence-to-one LSTM for MD and MA bridges (variable lengths)... 130

List of Tables

Table 2-1. Concrete proportioning and properties. 12
Table 2-2. Testing plan & replicates/repetition of each test. 13
Table 2-3. Slope of temperature change during curing period intervals 14
Table 2-4. Average of UPV and compressive strength of cylinders 17
Table 2-5. Dynamic moduli during the curing period from NDT devices 19
Table 2-6. Concrete mix proportion and properties 21
Table 2-7. Mix-specific relationships between UPV or dynamic modulus and Temp-Time factor. 21
Table 2-8. Modified equations of best fit for each mix. 23
Table 2-9. Shift factors and curing and hardening properties of each mixture. . 26
Table 2-10. Pearson's correlation coefficient among shift factors and mix properties. 26
Table 2-11. Models for predicting UPV shift factor. 26
Table 2-12. Models for predicting dynamic modulus shift factor. 26
Table 2-13. Rebound Number and Compressive Strength of four mixes at age 28 days. 27
Table 2-14. RMSE of compressive strength from literature and this study's data. 29
Table 2-15. Models for predicting compressive strength. 30
Table 2-16. Testing Repeatability of Mix 3 and Mix 4. 32
Table 3-1. Mix properties of samples. 36
Table 3-2. UPV and resonant frequency results on segregated samples. 45
Table 3-3. Results of chloride permeability test on cores taken from segregated samples. 47
Table 3-4. Coefficient of variation of a) UPV, b) dynamic modulus of Mixture 1, 2, and 3 50
Table 3-5. Coefficient of variation of a) UPV, b) dynamic modulus of Mixture 3 and Mixture 4. 51
Table 4-1. Mix proportions and mix properties. 58
Table 4-2. Concrete and plexiglass mechanical properties 66
Table 4-3. Temperature of the slab, cylinder, cylinder submerging water measured by IRT. 71
Table 4-4. Compressive and shear wave velocity of concrete 72
Table 4-5. Rebound hammer and compressive strength on the cylinder. 72
Table 4-6. Average shear velocity and depth of delamination from UPE. 78
Table 4-7. Rebound number on the slab from Proceq rebound hammer. 80
Table 4-8. Rebound number on the slab from Humbolt rebound hammer. 80
Table 6-1. Description of NBI features selected for analysis. 111
Table 6-2. P-values of numerical features. 122
Table 6-3. Datasets from the data reduction analysis. 123
Table 6-4. Trial of sequence-to-sequence LSTM with different parameters 125

Table 6-5. Summary of the trials and results of the CNN sequence-to-one classification. 127
Table 6-6. Alternative Model Performance 129
Table 6-7. Alternative Model Performance with MD and MA data. 130

List of Abbreviations

ADAM: adaptive moment estimation

ADT: average daily traffic

AEA: air-entrainer agent

AIC: Akaike's information criteria

ANOVA: analysis of variance

ASTM: American society of testing and materials

BIC: Bayesian information criteria

BiLSTM: bidirectional LSTM

CNN: convolutional neural network

CS: compressive strength

CV: coefficient of variation

DM: dynamic modulus of elasticity

DSNW: number of days with snowfall greater than 1 inch (25 mm)

FEM: finite element method

GPR: ground penetrating radar

HRWR: high-range water reducer

IRT: infrared thermography

LSTM: long-short term memory

MI: maturity index

ML: machine learning

NBI: national bridge inventory

NDT: non-destructive test

NOAA: National Centers for Environmental Information

QA: quality assurance

QC: quality control

RELU: rectifier linear unit

RNN: recurrent neural network

RTG: resonant test gauge

SGD: stochastic gradient descent

SNOW: total annual snowfall

TCN: temporal convolutional network

UPE: ultrasonic pulse echo

UPV: ultrasonic pulse velocity

Chapter 1. Introduction

1.1 Summary

Quality assurance (QA) and quality control (QC) are key elements in highway construction in order to ensure that the target level of quality of materials and structures is achieved. Identifying lack of compliance in regard to (i) either the desired level of quality during construction early on, or (ii) at a later time when the structure is in service for premature deterioration and damage, may provide effective response and fast remedies, potentially limiting loss of life and/or litigation.

The oldest and simplest method used by transportation agencies to detect flaws and damages in a concrete structure is the visual surveys. But visual observations (which are still used in practice by several DOTs for bridge decks, precast concrete and sound walls) are time consuming and subjective, and their accuracy depends on the investigator's expertise and training. This approach can only detect deteriorations that can be seen on the surface of a concrete member (e.g., bridge deck, bridge abutments, sound walls, concrete traffic barriers, and other precast concrete elements). Due to the aging of the U.S. infrastructure, identifying other methods that can provide quick, unbiased, and timely assessment in terms of condition and analysis is essential.

Non-destructive techniques (NDTs) in QA involve non-invasive methods to evaluate the condition of materials and structural members. Non-destructive techniques are able to evaluate the cover depth, concrete properties, internal flaws, and reinforcement location and properties. Among the advantages of NDT over the destructive testing, in many cases, are shorter testing time, lower inspection costs and higher inspection rates versus destructive testing. Additional benefits include the availability of real-time results as production goes on, and reduction in bias that can occur in subjective visual inspections.

Previous studies have explored to some extent specific NDTs in terms of accuracy and precision. However, in order to define NDT-based acceptance for QA/QC purposes, further assessment is often needed in order to identify quality acceptance thresholds for concrete properties. Figure 1.1 presents the components of a QA program where NDTs may be adopted (i.e., highlighted sections).

One of the objectives of this study was to investigate and assess how specific non-destructive testing methods (NDTs) can be incorporated in the QA process of concrete construction. Particularly, it aimed to test the NDTs' ability to provide accuracy and repeatability in laboratory samples in small scale highway structures such as concrete slabs and bridge decks. The study plan considered a variety of different experiments designed to assess the response of the selected NDTs. Multiple NDTs were employed to test concrete at different stages (i.e., during the hydration process for adoption in maturity modeling) and/or compare the response on flawed concrete elements as opposed to sound concrete. The results of different NDTs were compared for (i) evaluating the repeatability and performance of each method in identifying specific defects (such as cracking, delamination, honeycombing, segregation, voids), and (ii) assessing the possibility of integrating "blended" NDTs in QA. Specifically, the experimental studies focused on a) strength gain monitoring of concrete and maturity modeling; b) identifying segregation and honeycombing in concrete production; c) detecting delamination in small scale reinforced concrete members; and d) assessing pavement layer and reinforcement condition of bridge decks. In each of these experimental studies a combination of destructive and non-destructive tests was employed to assess the mechanical properties and/or response of NDTs to defective versus sound concrete. Furthermore, the development of "master curves" for strength gain (i.e., maturity modeling) was achieved by developing the transfer functions in relation to proportioning, composition and mixture properties. The NDTs included in this study included infrared thermography (IRT), ultrasonic pulse velocity (UPV), resonant frequency, rebound hammer, ground penetrating radar (GPR), and ultrasonic pulse echo (UPE). These NDTs were selected based on past studies assessment, and the ranking of these methods in a recent FHWA national study for developing NDT based QA plans (Goulias, 2017c). The criteria for their selection included accuracy and repeatability, level of operator training, ease of use, and cost.

The second objective was to assess the conditions of bridge decks in the field and predict their performance condition. For the assessment aspect, Ground Penetration Radar (GPR) was used in an in-service bridge, for the prediction aspect the national bridge inventory (NBI) database of FHWA was used. By predicting the condition of bridge decks, frequency of timely inspections and optimized allocation of resources can be achieved to improve the maintenance and rehabilitation strategies of the highway network.

Finally, for predicting the future condition of bridge decks, two different machine learning (ML) methods, long-short term memory (LSTM) and convolutional neural network (CNN) were employed to classify the sequences of bridge condition ratings. The objective was to develop sequential models by employing these methods to consider Maryland bridge deck condition data, identify the best predictive models and test their transferability with data from another state (i.e., Massachusetts). The accuracy of the developed models for predicting bridge deck conditions was high, ranging from more than 80% all the way to 97% depending on the model and the various hyperparameters used in each case. The sequence-to-sequence convolutional neural network classification model outperformed the remaining ML models and the models developed in previous studies. The transferability of the ML models to other regions of similar bridge and climatic conditions was confirmed with the successful model response for the Massachusetts data providing high predictive accuracy and thus validating model response.

In the first part of each chapter, the literature review on these non-destructive methods is provided. It includes background and a summary of the importance of these NDTs in quality assurance based on previous studies findings and recommendations (Goulias, 2019). Then the design of the experiments for assessing such NDTs in concrete and concrete members are presented along with the results and modeling from the laboratory experimentation. The analysis based on the GPR field data on an existing bridge structure is included, followed by the machine learning modeling for predicting bridge deck conditions. Finally, the conclusions and recommendation for future studies are presented.

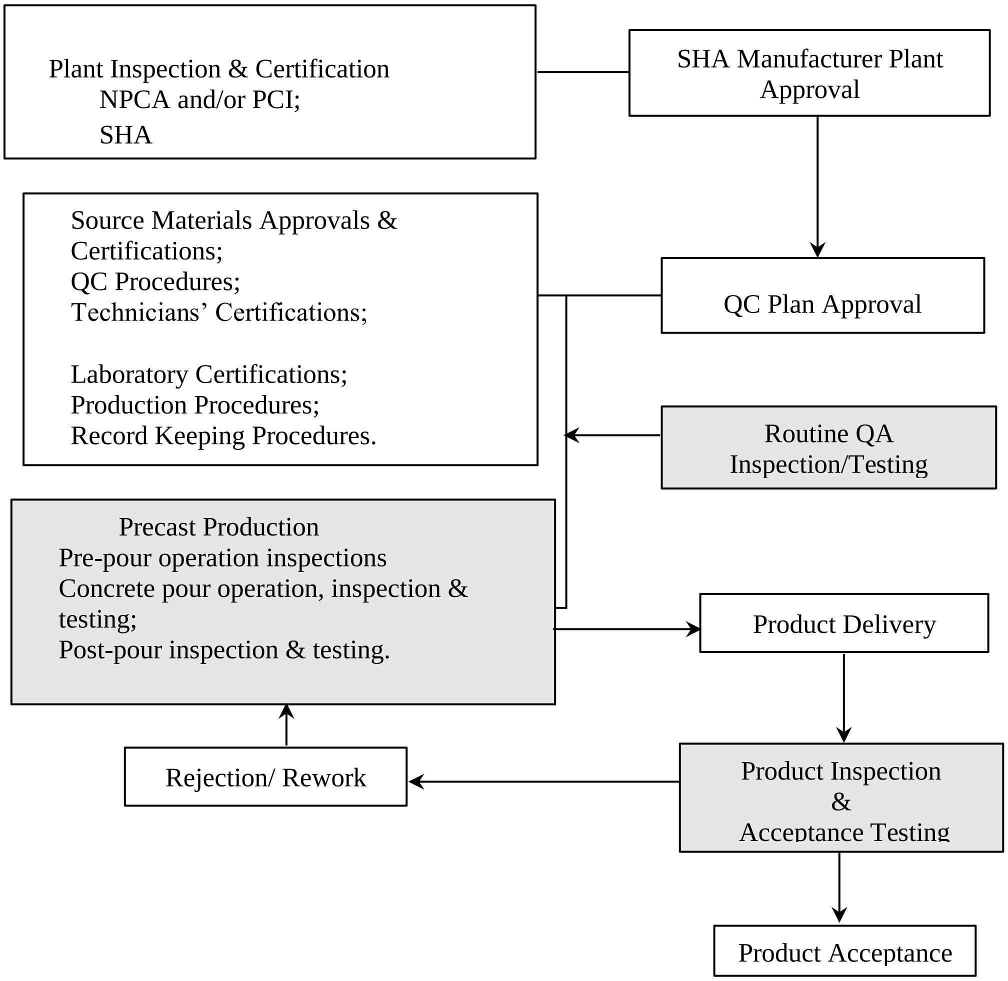
Plant Inspection & Certification
NPCA and/or PCI;
SHA
SHA Manufacturer Plant Approval
Source Materials Approvals & Certifications;
QC Procedures;
Technicians' Certifications;
Laboratory Certifications;
Production Procedures;
Record Keeping Procedures.
QC Plan Approval
Routine QA Inspection/Testing
Precast Production
Pre-pour operation inspections
Concrete pour operation, inspection & testing;
Post-pour inspection & testing.
Product Delivery
Rejection/ Rework
Product Inspection & Acceptance Testing
Product Acceptance

Figure 1.1. Components of a QA program for concrete products incorporating NDT (Goulias, 2019).

1.2 Organization of the dissertation

Chapter 1 includes the summary and key objectives of the research.

Chapter 2 provides a brief introduction of the NDTs used in this study and describes the non-destructive evaluation during strength gain of concrete. This chapter includes the following sections: (1) detailed evaluation of strength gain for a specific mixture, (2) model development for predicting concrete properties based on multiple mixtures, and (3) development of the "master curve" modeling approach for concrete maturity. The primary results of this section were presented in 99th and 100th Transportation Research Board meeting (Saremi et al., 2020; Saremi & Goulias, 2021) and published in a major referred journal (Saremi and Goulias, 2020), while the remaining results of this chapter are submitted to refereed journals.

Chapter 3 presents the experimental testing for assessing concrete production quality with NDTs. In this chapter, honeycombing and segregation, which are two common failings deficiencies during mixing and placing of concrete, are evaluated by NDTs such as UPV, resonant frequency, and rebound hammer. To assess the repeatability of the selected NDTs, statistics between data on defected concrete samples and sound samples are compared. This chapter was also presented in 101st Transportation Research Board meeting (Saremi et al., 2022a) and published in a major refereed journal (Saremi et al., 2022b)

Chapter 4 presents the experimental results and analysis on a concrete slab with internal defects (delamination) to evaluate NDT response, such as ultrasonic pulse echo, ground penetrating radar (GPR) and rebound hammer, in terms of accuracy in identifying the location and dimensions of defects. Simulation with finite element method was also carried out to simulate UPE wave propagation in a defected concrete slab.

Chapter 5 provides the results and analysis from a real case study of an existing in-service bridge deck with GPR. In this research asphalt overlay thickness, concrete cover depth and reinforcement condition were assessed. This chapter is also published in a major refereed journal (Goulias et al., 2020).

Chapter 6 presents the machine learning models to predict the performance of bridge decks based on the national bridge inventory (NBI) database which includes data collected during the past three decades through the long-term bridge performance (LTBP) program. The ML modeling is submitted to a major referred journal as well.

Chapter 7 summarizes the finding and conclusions of the study and provides recommendations for future research.

Chapter 2. Monitoring the Strength Gain of Concrete by Means of NDT for Potential Adoption in Quality Assurance (QA)

2.1. Introduction

Estimating the compressive strength of concrete at each stage of construction is one of the most critical aspects in providing safety and revenue. Failure in determining the suitable time for removing formwork and applying load on concrete structures leads to catastrophic failures and in some cases loss of life. Collapse of the Skyline Plaza in Fairfax County, Virginia, due to premature shoring removal, or the Willow Island cooling tower collapse in West Virginia due to premature loading and inadequately cured concrete are only some examples of unsuccessful estimation of concrete strength gain (Carper, 1987).

Chemical interaction among concrete ingredients (i.e., cement hydration) is causing strength gain. The hydration of the cement in the presence of water, and thus strength gain, has been modeled through the maturity concept as a function of temperature and time. The interaction between cement and water, as well as other ingredients in concrete, such as admixtures, is governed through chemistry kinetics and represents an exothermic reaction. Thus, during the early ages of concrete hydration strength gain can be monitored through concrete temperature. For typical concrete mixtures about 85% of the hydration process is complete within the first 28 days (Uddin et al., 2013). Measuring the temperature of concrete during the curing process is typically achieved using embedded wired or wireless thermal sensors (Azenha et al., 2011; Upadhyaya et al., 2014). Hansen and Surlaker (2006) also used Radio Frequency Identification maturity tags (RFID) in monitoring concrete maturity, while Ghods et al. (2017) developed an application for smartphones.

Although maturity has been successful in monitoring the concrete hydration process, it does not always guarantee successful results. For example, in situations where concrete mixtures are not well mixed or properly placed, honeycombing, segregation, or excessive bleeding may occur (Graveen et al., 2003). While the cement and water interaction may proceed, such effects may produce variable strength within the concrete structure that might not be detectable from the maturity monitoring. Therefore, for QA/QC purposes, monitoring the strength gain by another method is necessary. Even though destructive tests such as compressive tests of cylinders (ASTM C39) can be used, NDT methods provide the benefits of (i) sampling a large portion of concrete within the structure capturing thus in-place strength variability, and/or, (ii) assessing the quality of a higher number of samples (i.e., testing frequency), which is particularly important in the production of manufactured concrete such as precast and pre-stressed members (Goulias, 2017c).

Following the recommendations of a FHWA study, the need to develop an NDT based QA process for highway materials was identified (Goulias, 2017c). Therefore, it was the objective of this study to identify and assess alternative NDT methods that can be used in monitoring and/or estimating strength gain in concrete, and thus could be adopted in an NDT based QA process. For these NDTs to be used in QA/QC and/or in acceptance testing specifications, they should be fast, accurate, reliable, and simple to run for both owners and concrete producers. The alternative NDTs explored in this study included: infrared thermography (IRT); ultrasonic pulse velocity (UPV); and fundamental resonance frequency. The use of infrared thermography (IRT) for monitoring surface temperature of concrete for structures such as pavements, buildings and tunnels has been explored in past studies (Solla et al., 2014). Its use in monitoring the hydration process and strength gain has been studied to a limited degree (Azenha et al. 2011). For mass concrete structural elements, a significant temperature gradient is expected from the interior to the surface of concrete, while for thin concrete members such a difference is negligible (Upadhyaya et al., 2014). Some studied the use of ultrasonic pulse velocity (UPV) to assess the ability of maturity to properly predict in-place strength (Graveen et al. 2003; Krauß et al., 2006; Gebretsadik, 2013). In early concrete ages the wave propagation velocity is dependent on the concrete density and thus strength. Therefore, UPV can be employed to validate the maturity strength predictions.

In addition to wave propagation velocity, the fundamental resonance frequency of concrete can be used to calculate the dynamic modulus of elasticity and related to compressive strength. Such approach is more appropriate for lab and field samples casted and cured on site next to the concrete structure. Past studies explored the ability of resonance frequency testing as well to measure the dynamic modulus of concrete during the early curing time (Jin and Li, 2001; Azenha et al., 2010). A summary of the principles behind each NDT method is presented in Chapter 1, while a more detailed description is available in standard NDT handbooks (Malhotra et al., 2003) and pertinent ASTM standards.

The initial assessment whether NDTs can be successfully used in maturity modeling was investigated using a typical concrete mix used in infrastructure projects in the northeast region of US. The results are presented in the following section and published (Saremi and Goulias, 2020). Follow-up experimentation on additional mixtures validated such findings and the analysis, and the results are presented as well herein.

2.2. Background & Literature Review on NDTs

A summary of the principles and operation of each NDT used in these experiments is provided in the following subsections.

2.1.1 Infrared Thermography (IRT)

Any material that has a temperature above absolute zero (-273°C or 0°K) emits IR radiation (Solla et al., 2014, Omar et al., 2017). The emitted infrared radiation from most materials is within the wavelength spectrum of 2 to 15 microns (µm). The intensity of radiation is correlated with the material's absolute temperature. Therefore, the temperature can be indirectly determined by measuring the emitted IR radiation (Clemena et al., 1978).

Infrared thermography is a thermal imaging method that includes a camera to capture the emission from the material, converts the energy into an electric signal, and produces an image that provides the distribution of temperature on the surface of the material. The emitted radiation per unit area is calculated through the Stefan–Boltzmann equation (Ede, 1967):

$$E = \varepsilon \sigma T^4 \tag{2-1}$$

where E is the energy flux (Wm^{-2}), σ is Stefan-Boltzmann constant ($5.67 \times 10^{-8}\ \ Wm^{-2}K^{-4}$), ε is the emissivity (defined as the ratio between the thermal energy radiated from the material and a black body), and T is the surface temperature (K). In civil engineering, IRT has been used for finding source of energy loss in heating, ventilation, and air conditioning (HVAC) systems, finding the location of plumbing clogs, or providing quality control and detecting the structural defects such as delamination (Maierhofer et al., 2006), overlay debonding (Tsubokawa et al., 2007), voids in concrete structures and tunnels, voids in shallow tendon ducts (Maierhofer et al., 2006), near surface cracks in asphalt and concrete pavements (Solla et al., 2014), and detection of segregation/honeycombing in concrete. The objective is finding the areas with temperature differential due to external temperature effects (i.e., air temperature and heat transfer at the interface of materials). However, when IRT is used to determine the temperature of concrete during curing, the source of the heat is the hydration itself. Since the reaction of cement with water is exothermic, the inner temperature of concrete continuously changes, even with constant curing temperature in the lab. Using IRT in determining the temperature of concrete during hydration can be a faster approach relative to other methods since (1) every pixel is equivalent to a temperature sensor; (2) no direct contact is needed; and (3) a large area can be examined in real-time. The IRT camera used in this study, Figure 2.1, has a resolution of 80×60 equivalent to 4800 measuring sensors and an accuracy of about ±2℃ ($\pm$3.6°F).

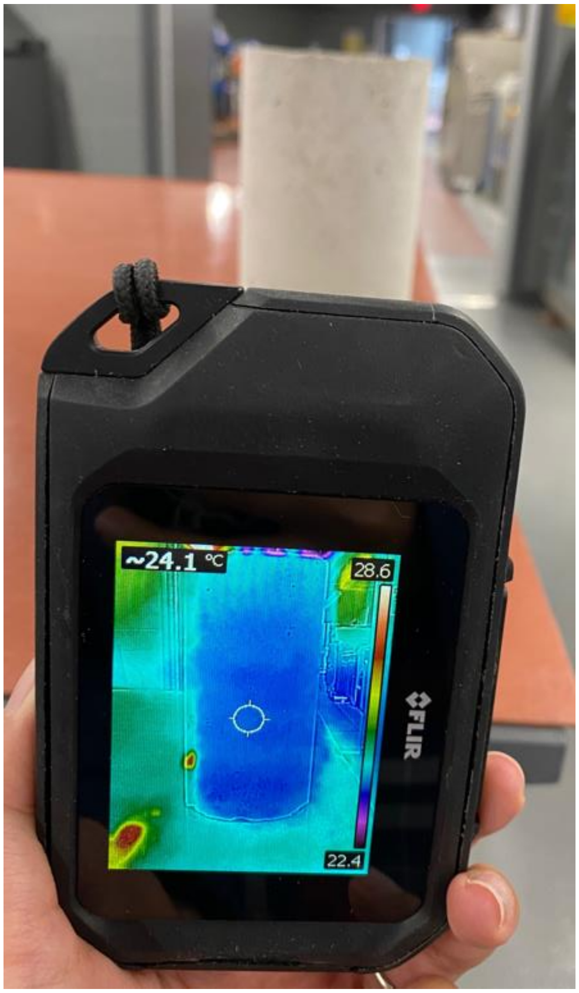

Figure 2.1 Infrared thermography camera measuring the temperature of a concrete sample.

2.1.2. Ultrasonic Pulse Velocity (UPV)

In ultrasonic wave propagation method, three types of mechanical waves are generated: compression waves (also known as longitudinal or P-waves); shear waves (transverse or S-waves); and surface waves (Rayleigh waves). The propagation of compression waves is similar to the propagation of sound waves in air. Compression waves have the highest propagation velocity while surface waves have the lowest (Malhotra and Carino, 2003). The ultrasonic pulse velocity (UPV) transducers emit all these waves at the same time. An UPV is illustrated in Figure 2.2. The UPV transducers are placed in the following configurations on the concrete samples: direct mode, when the transducers are placed at the opposite sides of the sample; semi-direct, when the transducers are placed at surfaces with a right angle; and indirect, when both transducers are on the same surface of the sample. In a structure, depending on the feature of interest and accessibility, one can choose the desired configuration of testing.

For sound concrete and direct method of testing (i.e., compression waves) the speed of propagation is provided by Equation 2-2:

$$V_p = \frac{L}{\Delta t} \tag{2-2}$$

where Vp is the propagation velocity in concrete, L is the shortest distance between transducers (in case of direct mode, L is equal to the length of the concrete sample), Δt is the travel time of the wave. The pulse velocity of compression waves in concrete is correlated to concrete's elastic properties and density. Equation 2-3 demonstrate the relationship among concrete properties and compression wave velocity (ASTM C597). Equation 2-3 can be rewritten to calculate dynamic modulus, E_d, from pulse velocity and concrete properties.

$$V_p = \sqrt{\frac{E(1-\nu)}{p(1+\nu)(1-2\nu)}} \text{ or } E_d = \frac{(1+\nu)(1-2\nu)}{(1-\nu)}\rho {V_p}^2 \tag{2-3}$$

where E_d is dynamic modulus, ν is dynamic Poisson's ratio, ρ is density, Kg/m3, and Vp is ultrasonic pulse velocity, m/s.

The wave velocity in concrete is a function of its elastic properties (dynamic modulus and Poisson's ratio) and density, and typically ranges between 3700 to 4200 m/s (Malhotra and Carino, 2003). Concrete properties such as aggregate size and gradation, cement and water-cement ratio, admixtures, uniformity, and age of concrete can affect the pulse velocity. In addition, transducer contact, temperature of concrete, moisture and curing condition, and the presence of reinforcement will affect pulse velocity as well. Several researchers have attempted to develop models relating concrete strength to ultrasonic pulse velocity (Turgut, 2004; Tanyidizi et al., 2008; Uysal et al., 2011; Santhanam et al., 2012; Rao, 2016), providing good relationships.

2.1.3. Resonant Frequency

In fundamental resonance frequency testing the concrete sample is impacted with a small hammer and the response frequency is monitored with an accelerometer. A frequency analyzer is used to monitor the wave propagation in the frequency domain. A resonance frequency testing gauge is shown in Figure 2.3. When the sample is not constrained and free to vibrate, the resonance frequency is detected and related to the dynamic modulus of elasticity and density of the concrete. Different locations of the impactor (hammer) and accelerometers are used to determine concrete properties (i.e., dynamic modulus). In a longitudinal mode, the hammer strikes the sample at the opposite side of the sample (Figure 2.4). The longitudinal dynamic modulus can be calculated from Equation 2-4 (ASTM C215).

$$E = DM(n')^2 \tag{2-4}$$

where E is the dynamic modulus, Pa, n' is the fundamental longitudinal frequency, in Hz, and D is 5.093 ($\frac{L}{d^2}$), in m^{-1}, for a cylinder, or 4 ($\frac{L}{bt}$), in m^{-1}, for a prism. In transverse mode of testing, the hammer strikes the sample at the middle of it (Figure 2.4). The dynamic modulus of elasticity from transverse frequency can be calculated from Equation 2-5.

$$E_d = CMn^2 \tag{2-5}$$

where, E_d is dynamic modulus of elasticity (*MPa*), $C = 0.9464(L^3T/bt^3)$, *M* is the mass of the beam (*Kg*), and *n* is the fundamental transverse frequency (*Hz*). The term, *C*, is dependent on the length, *L*, of the specimen, the width, *b*, the height, *t*, and a correction factor, *T*. *T* depends on the radius of gyration, *K*, length of the specimen, *L*, and the Poisson's ratio, ν. The dynamic modulus of elasticity typically varies from 14 *GPa* for low quality concrete at early ages to 48 *GPa* for sound and fully cured concrete (Malhotra and Carino, 2003).

Historically, the resonance frequency method was used to assess durability effects and concrete deterioration. However, this method can be used to monitor changes in dynamic modulus with increasing age of concrete (i.e., hardening and thus strength). Factors such as age, moisture content and curing conditions will affect the dynamic modulus (Malhotra and Carino, 2003). Kesler and Higuchi (1953) concluded that in a similar curing condition the dynamic modulus of elasticity increases with increasing strength. The resonant frequency testing devices used in this study were resonant test gauge (RTG) or Emodumeter (E-meter).

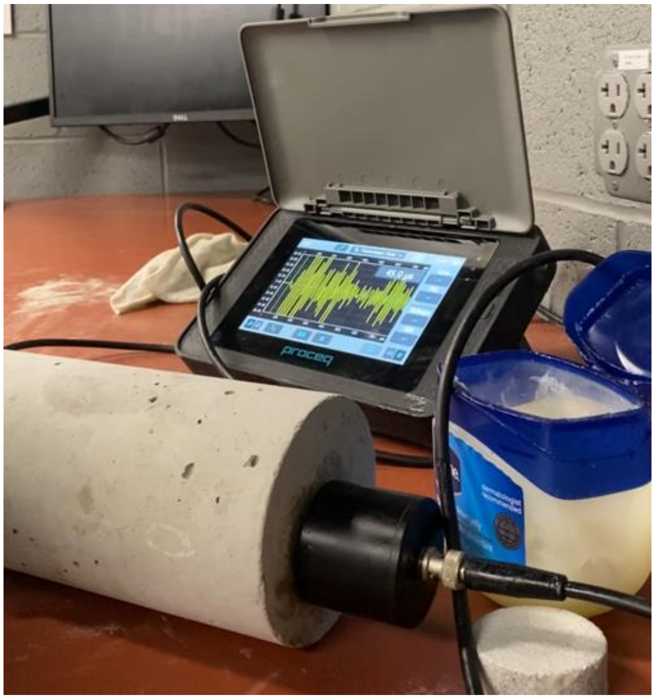

Figure 2.2. Ultrasonic pulse velocity (UPV) testing setup

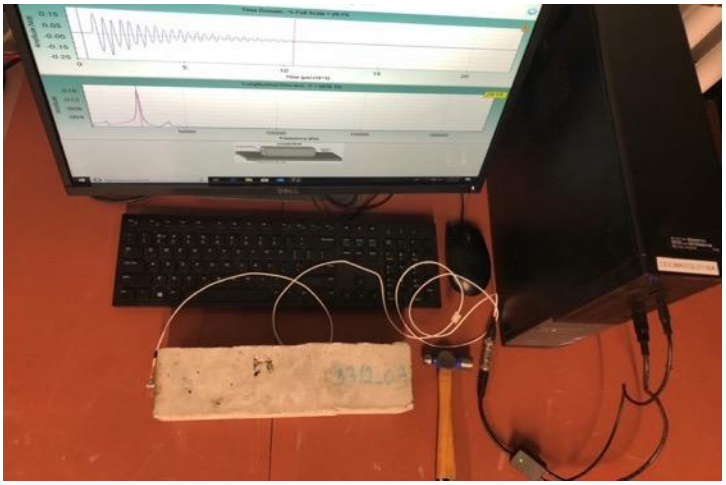

Figure 2.3. Resonant frequency test gauge used to measure laboratory-made samples

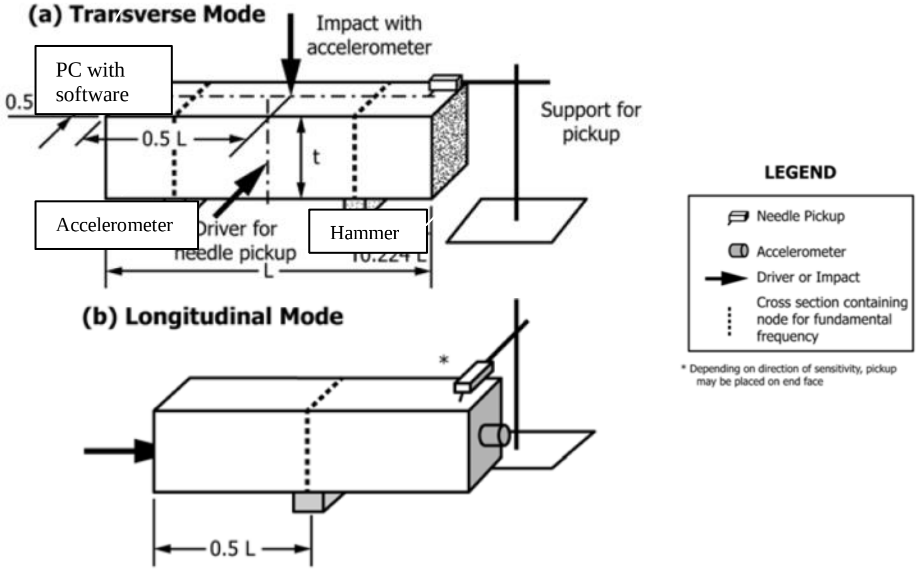
(a) Transverse Mode
Impact with accelerometer
PC with software
0.5
0.5 L
t
Support for pickup
Accelerometer
Driver for needle pickup
Hammer
0.224 L
L
(b) Longitudinal Mode
*
0.5 L
LEGEND
Needle Pickup
Accelerometer
Driver or Impact
Cross section containing node for fundamental frequency
* Depending on direction of sensitivity, pickup may be placed on end face

Figure 2.4. Transverse and longitudinal mode configuration in resonant frequency testing (ASTM C215)

2.1.4. Rebound Hammer

The rebound hammer test is used to evaluate the uniformity of concrete across a concrete member or to estimate the in-place strength of concrete. For a given concrete mixture, the rebound number is a function of factors such as concrete stiffness, moisture content at the surface, quality of surface finishing, and other parameters (ASTM C805). The rebound hammer consists of a spring-loaded steel hammer that, when released, impacts a metal plunger in contact with the concrete surface. The spring-loaded hammer must travel with a consistent and reproducible speed. The rebound number depends on the rebound distance of the hammer after it strikes the plunger, or it is based on the ratio of the hammer speed before and after impact.

Various studies examined the effects of testing conditions on the results (Demirdag et al., 2009; Mahmoudipour, 2009). Mahmoudipour (2009) indicated that the rebound hammer test results on cylinders can be combined with UPV testing to successfully estimate compressive strength of concrete. Amini et al. (2019) combined results of UPV and rebound hammer to successfully estimate concrete strength properties (i.e., $R^2= 0.94$) for various mixtures. The rebound hammer used in this study was the Silver Schmidt Hammer (Figure 2.5) with impact energy of 0.735 Nm, suitable for concrete with compressive strength between 5 to 30 MPa (Proceq, 2017).

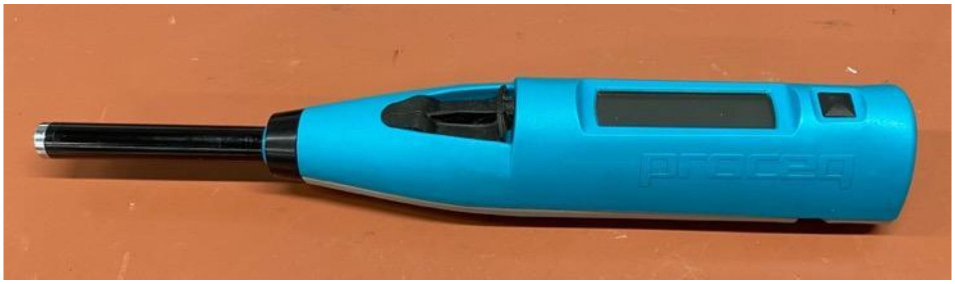

Figure 2.5. Schmidt rebound hammer

2.3 Initial Assessment of Concrete Strength Gain Monitoring with NDTs

2.3.1 Experimental Testing

For assessing hydration and strength gain of concrete during early ages (i.e., within 28 days), a combination of destructive and non-destructive tests was conducted on 100 x 200 mm (4×8 in) concrete cylinders. The properties of the initial concrete mixture are presented in Table 2-1. The selected concrete represents a typical mixture used in building construction and highway applications in Maryland and the surrounding regions. The cylinders were cured in standard lab conditions (temperature and moisture) for 28 days. Table 2-2 shows the testing plan. The time-temperature history of concrete during curing was recorded every half an hour with two iButton sensors embedded into cylinders. All cylinders were kept in a water bath during the 28 days of curing. The iButton sensors and their locations are illustrated in Figure 2.6. After 28 days, the iButtons were removed and placed in a data reader and the data were retrieved. The recorded temperatures from the iButton sensors were identical in almost all cases, while any differences observed were not more than half of a degree Celsius. Thus, in the analyses the average values were used.

Table 2-1. Concrete proportioning and properties.

Cement Type	Water Cement Ratio	Admixtures[1]		Unit Weight (kg/m^3)		28 days Compressive Strength (MPa)		Air Content		Slump (mm)	
		AEA[2]	HRWR[3]	μ[4]	CV	μ	CV	μ	CV	μ	CV
Portland cement, type II	0.44	0.8 %	0.5%	2415	3%	31	3.5%	3.5 %	7.9 %	13	24 %

[1] Percentage relative to water
[2] Air entrainer
[3] High-range water reducer
[4] Mean

Table 2-2. Testing plan & replicates/repetition of each test.

	Age (days)					
Tests	**1**	**2**	**3**	**7**	**14**	**28**
Compression	3	3	3	3	3	3
Infrared Thermography	10	16	10	3	3	3
Resonance Test Gauge	5	5	5	5	5	5
E-meter	5	5	5	5	5	5
Ultrasonic Pulse Velocity	10	10	10	10	10	10

2.3.2 Results

The recorded temperature from the iButtons during the curing period is shown in Figure 2.7. In this figure the sudden drop in temperature after about 24 hours corresponds to unmolding and transferring the dried samples to the water for curing. The average of absolute slope of the temperature change is shown in Table 2-3. As expected, the temperature variation during the first 24 hours is higher, and thus the monitoring frequency of temperature during the initial period should be higher.

As concrete matures, compressive strength increases. One of the methods to estimate the in-place strength of concrete is calculating the maturity index (MI). The most common method of calculating the maturity index in construction and commercial maturity meters is the temperature-time product, described in Equation 2-6. This is also known as the Nurse-Saul maturity function (ASTM C1074, 2017; Upadhyaya et al., 2014).

$$M(t)=\sum(T_a-T_o)\Delta t \tag{2-6}$$

where:

M(t) = the temperature-time factor at age t, degree-days or degree-hours
Δt = time interval, days or hours
T_a = average concrete temperature during time interval Δt, $°C$, and,
T_o = datum temperature, $°C$, temperature below which the chemical reaction ceases.

Table 2-3. Slope of temperature change during curing period intervals

Age	1 day	2 days	3 days	7 days	14 days	28 days
Average of temperature slope ($°C/hr$)	0.6	0.1	0.1	0.1	0.1	0.1

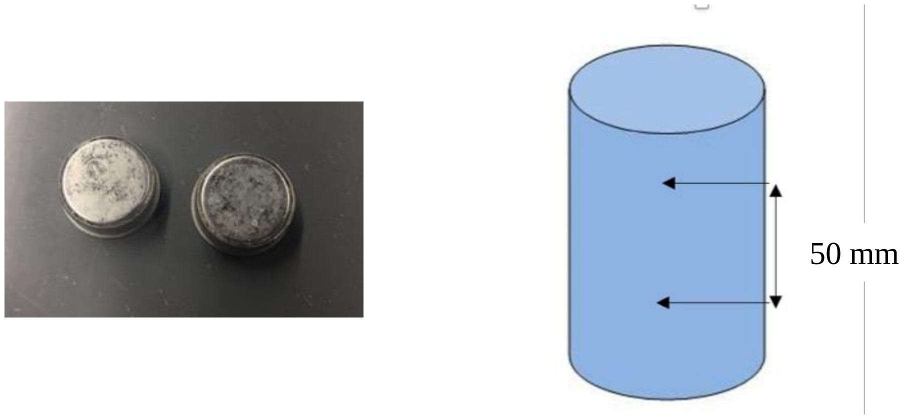

(a) **(b)**

Figure 2.6. (a) iButtons for temperature monitoring, (b) location within the cylinder

In measuring concrete temperature and calculating the temperature-time factor, time intervals of half an hour were considered for the first seven days. After that, intervals of one hour were used since a lower change in temperature is observed. During the 28 days, 100×200 mm (4×8 in) cylinders were tested in compression according to ASTM C39 and the testing schedule of Table 2-2. The strength-maturity relationship was developed based on the average compressive strength of three cylinders and the temperature-time factor of the cylinders with the iButtons. The results are shown in Figure 2.8. As expected, the compressive strength increased with curing age.

To assess whether infrared thermography can provide strength predictions through the maturity approach, the relationship between the temperature-time factors calculated from the iButtons data and that from the infrared thermography was examined. To this aim, the temperature-time product was calculated from temperatures recorded with an infrared camera and using the Nurse-Saul maturity function. Figure 2.9 shows the infrared image of a cylinder after the mold removal. The temperature of the cylinder is relatively uniform through the cylinder surface, and equal to 20.2℃ as shown in the infrared camera "target" circle location. When comparing the temperature data recorded from the embedded iButtons and the infrared thermography, it should be noticed that the iButtons measure the internal concrete temperature, while the infrared camera measures the surface concrete temperature. However, since these are small samples (cylinders) and at controlled curing conditions (room temperature and water bath) no significant temperature gradient is expected from the surface to the inner portion of the samples (as opposed to large mass concrete samples exposed to field conditions). The IRT and iButton measurements were cross checked at 40 points and the results showed the differences between two temperatures can be as small as 0.2°C or as large as 2.8°C. The maturity indices calculated from both temperature sensing methods are shown in Figure 2.9. As can be observed the two approaches provided identical results (i.e., no difference on MI calculated from the two sensing methods) at early ages of 1 to 7 days, which is the primary reason for using maturity for predicting early strength. Comparing the temp-time factor at 6 ages shows the temp-time factor calculated from iButton can be 8% larger than that calculated from IRT. Therefore, even though internal temperature is more desirable for evaluating the hydration of concrete, especially in mass concrete structural elements, for thin concrete members using an infrared camera to record the temperature-time history is possible and beneficial due to the speed of data collection and its non-destructive characteristics.

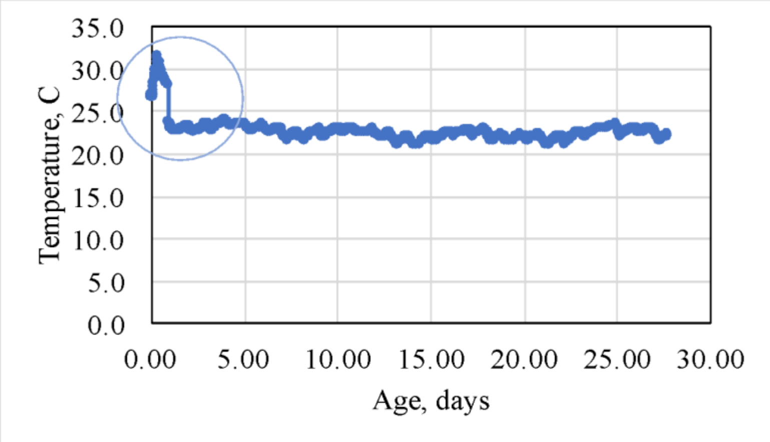

(a)

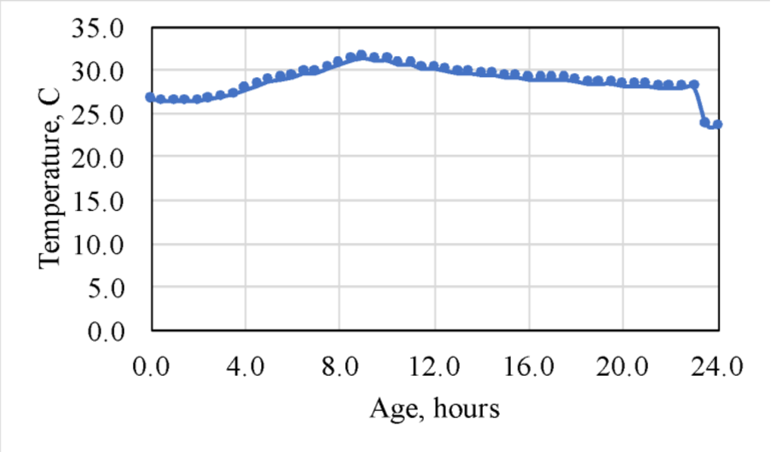

(b)

Figure 2.7. Temperature - time history of concrete during (a) 28 days curing period, and (b) first 24 hours.

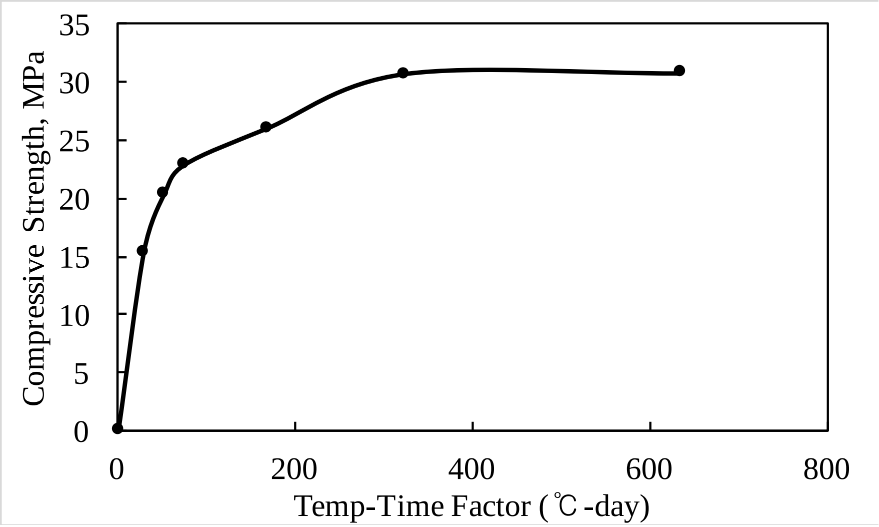

Figure 2.8. Compressive strength versus temperature-time factor during 28 days of curing

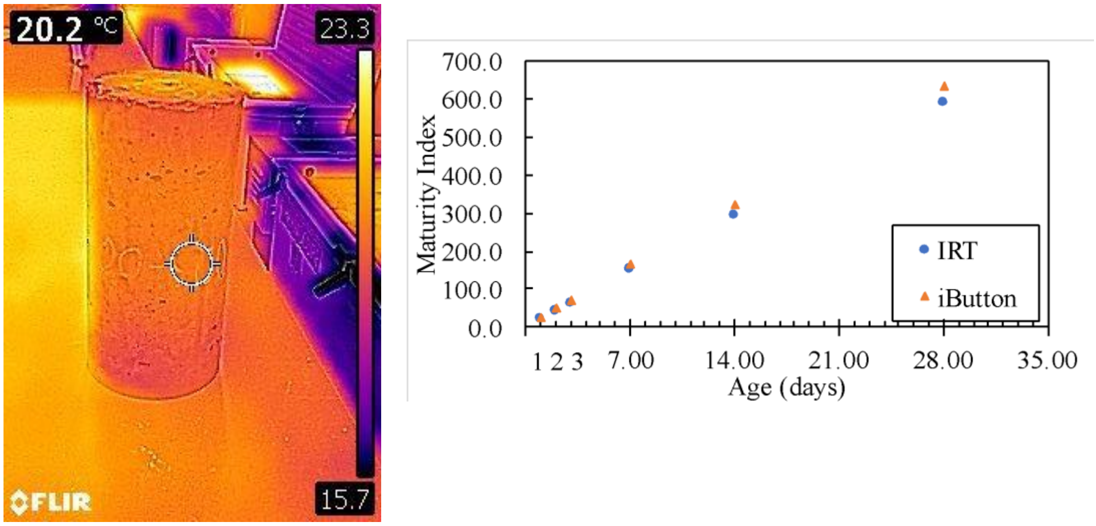

(a) (b)

Figure 2.9. a) Temperature through IRT, b) Maturity Index calculated from iButtons and IRT data.

Thus, the use of IRT during production is particularly valuable in QA/QC since concrete strength development is based on lab and field cured cylinders (i.e., small samples with minimal temperature gradient between the surface and interior temperature). Furthermore, in mass concrete structural elements the interior concrete temperature will be higher than the surface temperature, and thus maturity prediction using IRT will be on the conservative side (i.e., lower MI and strength prediction values than the actual field values in the structure).

As indicated in past studies, it is highly recommended in the QA/QC process to couple and verify concrete strength predictions from the maturity approach with non-destructive testing (Goulias, 2019). Similarly, ASTM C1074 indicates that the temperature monitoring and maturity index modeling should be accompanied by at least one other test for estimating the in-place strength of concrete. Therefore, the UPV and resonance frequency methods were employed in this study to monitor the strength gain of concrete.

Table 2-4 shows the compressive strength results versus ultrasonic pulse velocity, while Figure 2.10 presents the relationship of UPV with the temperature-time product. Once the Maturity Index (i.e., relationship of temperature-time product and concrete strength) has been established from laboratory samples for a specific concrete mixture, UPV can be used for assessing and correlating the results to compressive strength without: (i) having to install and monitor temperature sensors during concrete production; and, (ii) test companion samples for compressive strength representing the field conditions for verification purposes.

Table 2-4. Average of UPV and compressive strength of cylinders

Age	Average of Compressive Strength (MPa)	UPV				
		Minimum (m/s)	Maximum (m/s)	Average (m/s)	Standard Deviation (m/s)	Coefficient of Variation%
1	15.44	3785.8	4130.0	4005.9	126.20	3.15
2	20.42	4151.2	4291.0	4211.6	41.76	0.99
3	22.94	4261.8	4343.4	4306.9	28.06	0.65
7	26.07	4193.9	4458.8	4364.4	87.04	1.99
14	30.78	4406.4	4553.9	4476.7	56.91	1.27
28	30.82	4540.0	4632.9	4589.2	30.71	0.67

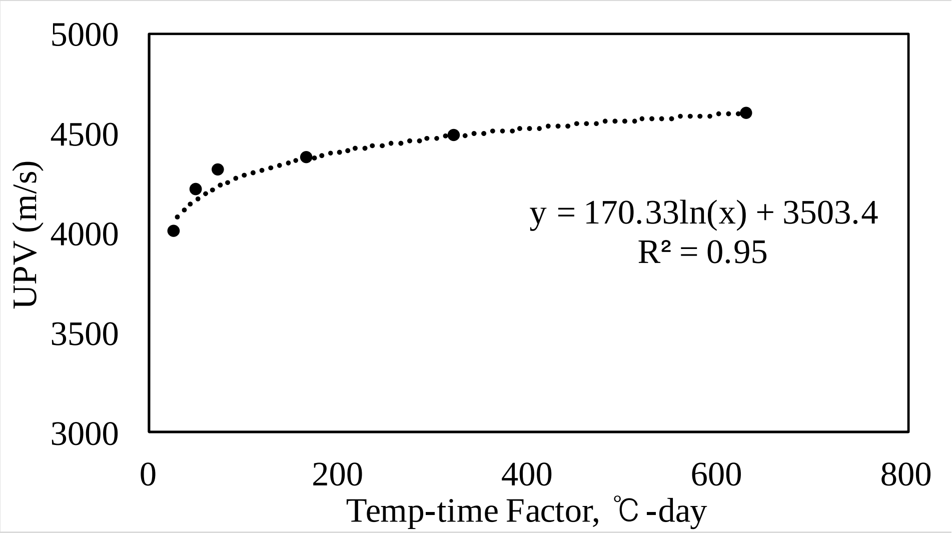

Figure 2.10. Relationship between UPV and temperature-time product.

The hardening process of concrete is also reflected in the dynamic modulus determined from the resonance frequency testing. Similar to compressive strength, dynamic modulus obtained from this NDT method is also expected to increase during the hardening and strength gain process. For comparative purposes two different testing units were used in this study: the Resonance Test Gauge (RTG) and the Emodumeter (E-Meter). The resonance frequency tests were performed according to ASTM C215 and the results are shown in Table 2-5. The average dynamic moduli from each device were related to both compressive strength and the temperature-time product, shown in Figures 2.11 and 2.12, respectively. As expected, an increase in dynamic modulus with hardening of concrete was observed. Even though the dynamic moduli from the two devices are very close at early ages (i.e., day 2 and 3), after 7 days of curing the E-meter provides systematically higher dynamic moduli values, Table 2-5.

As in the case of UPV, once the relationship between temperature-time factor (MI) and concrete strength has been established from laboratory samples, dynamic modulus testing can be used for assessing in-place field conditions. Therefore, the results can be correlated to compressive strength without (i) having to install and monitor temperature sensors in concrete, and (ii) test companion samples for compressive strength representing the field conditions. The results show that the use of UPV and resonant frequency method provide: (i) the ability to test a larger portion of cast-in-place concrete without significant increase in QA/QC cost and testing time; and (ii) real time monitoring of construction quality (in this case strength).

Table 2-5. Dynamic moduli during the curing period from NDT devices

Age	Dynamic Moduli from E-Meter				Dynamic Moduli from RTG			
	Min (GPa)	Max (GPa)	Average (GPa)	Coefficient of Variation %	Min (GPa)	Max (GPa)	Average	Coefficient of Variation %
1	30.39	30.66	30.47	0.39	29.94	29.94	29.94	0.00
2	31.97	32.10	32.07	0.19	31.64	31.64	31.64	0.00
3	33.32	33.60	33.49	0.35	33.13	33.13	33.13	0.00
7	35.86	36.30	36.03	0.44	35.51	35.85	35.64	0.52
14	37.60	37.76	37.67	0.22	37.11	37.45	37.18	0.41
28	38.67	38.97	38.76	0.35	37.64	37.98	37.91	0.40

Note: number of repetitions (n) =5

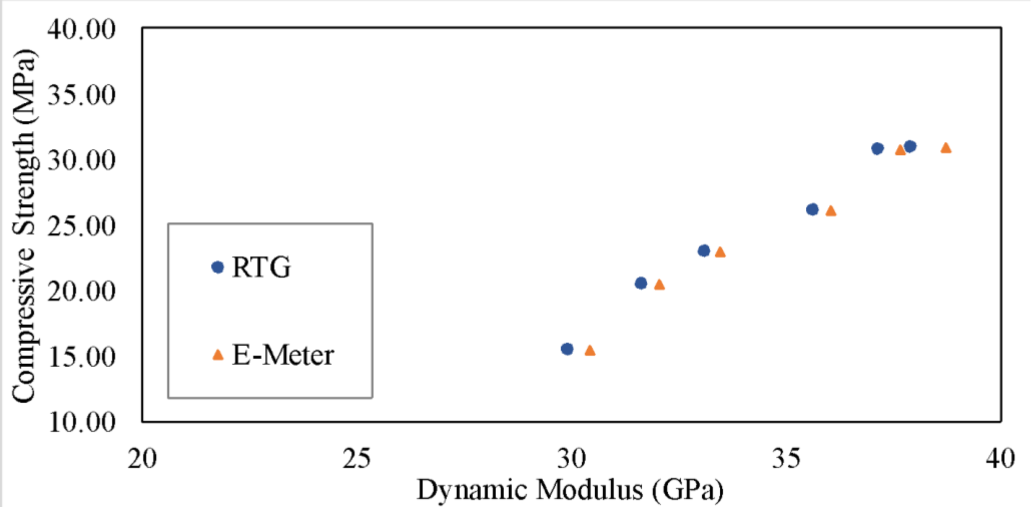

Figure 2.11. Compressive strength versus average dynamic modulus.

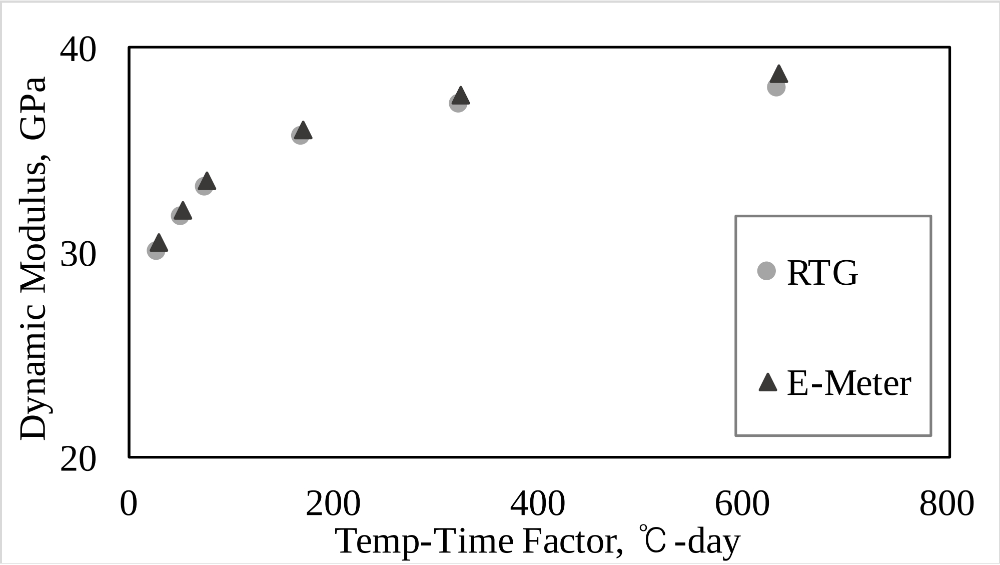

Figure 2.12. Dynamic modulus versus temperature-time product.

2.4 Validation of Concrete Strength Gain Monitoring with Additional Concrete Mixtures

2.4.1. Experimental Testing and Results

In order to validate the proposed approach of relating maturity to alternative NDTs for strength predictions in QA, different mixtures were prepared. Some mixtures included in the experimental testing representing typical concrete used in the construction of infrastructure projects in the region (Mix 1 to 8), others could deviate from a typical mix (Mix 9 to11). The typical mixtures must meet proportioning and acceptance requirements similar to the typical MD7 (Maryland designation 7). The deviation from MD7 was intentionally in order to observe the effect of different parameters on NDT response. Thus, such alternative mixtures, Table 2-6, were generated by fine tuning adjustments in proportioning of typical MD7 (MDSHA). These mixtures could as well represent potential mixture proportioning variability during production in regard to water to cement ratio, ranging from 0.43 to 0.50. The concrete ingredients include coarse aggregate (#57), fine aggregate, cement, water, and admixtures, such as air entraining admixture (AEA) and high-range water reducer (HRWR). Air entraining admixtures provide resistance to freeze-thaw, while decreasing strength. High-range water reducers provide concrete strength at lower water content with acceptable workability (Arras et al., 2019).

Cylinders of 100×200 mm were prepared from each mixture and tested with UPV, RTG and for compressive strength at different hardening ages. The same process explained in the last section for hardening and temperature monitoring was followed during curing of these 11 mixtures. The samples were tested with UPV and RTG, and monitored with IRT, on 1, 3, 7, 14, and 28 days after production. Some of these mixtures were also tested by a rebound hammer. Since maturity index, MI, is mixture specific, the results for each mixture are presented separately in Table 2-7. Table 2-7 includes the best fit equations (in logarithmic form of $y = a\ ln(x) + b$) and their R^2s among ultrasonic pulse velocity, dynamic modulus, or compressive strength and maturity index (temperature-time factor). Since calculating the dynamic modulus form UPV needs information on Poisson's ratio, the dynamic modulus was obtained from RTG, and UPV data was used independently. The pulse velocity itself is a significant characteristic that can hold useful information about concrete independent from its shape or dimension (Philleo ,1955).

For all three mixtures a very good relationship between UPV and the temperature-time factor or dynamic modulus and temperature-time factor is observed with an R^2 ranging between 0.86 to 0.99. Since these mixtures were specifically designed to present small variations in proportioning, such relationships are similar in form and shape. This implies that potentially a "master curve" concept may be defined and used for UPV and/or dynamic modulus versus MI representing a family of similar concrete mixtures. A shift factor of the individual concrete mixture's UPV and/or dynamic modulus versus MI relationships may be then developed in function of mixture specific concrete ingredients and proportioning.

Table 2-6. Concrete mix proportion and properties

Mixtures	W_{AEA}/W_{cement}	W_{HRWR}/W_{cement}	Fresh Unit Weight (kg/m^3)	w/c	Air content	Slump (mm)	Average of 28-day Compressive Strength (MPa)
Mix 1	0.16%	0.11%	2352	0.44	4.0%	25	38
Mix 2	0.40%	0.24%	2418	0.44	3.6%	15	31
Mix 3	0.40%	0.24%	2274	0.45	6.5%	98	31
Mix 4	0.40%	0.24%	2336	0.43	4.6%	111	31
Mix 5	0.40%	0.24%	2287	0.45	5.4%	76	25
Mix 6	0.40%	0.24%	2271	0.45	6.0%	146	22
Mix 7	0.40%	0.24%	2278	0.45	5.8%	105	23
Mix 8	0.40%	0.24%	2271	0.45	6.1%	76	25
Mix 9	0.40%	0.24%	2253	0.48	6.2%	130	19
Mix 10	0.40%	0.32%	2258	0.48	5.4%	175	25
Mix 11	0.40%	0.40%	2232	0.50	5.6%	226	26

Table 2-7. Mix-specific relationships between UPV or dynamic modulus and Temp-Time factor.

Mix No.	UPV vs. Temp-Time (*y = a Ln (x) + b*)			DM (RTG) vs. Temp-Time (*y = a’ Ln (x) + b’*)			Compressive Strength vs. Temp-Time (*y = a” Ln (x) + b”)*		
	a	b	R^2	a'	b'	R^2	a"	b"	R^2
1	68.25	4003.10	0.99	4.46	14.89	0.95	6.91	-4.34	0.97
2	170.33	3503.42	0.95	2.69	21.27	0.97	5.04	0.07	0.95
3	166.08	3405.43	0.86	2.91	16.5	0.97	NA*	NA*	NA*
4	230.33	3242.31	0.96	3.36	17.39	0.96	NA*	NA*	NA*
5	228.10	3070.10	0.92	2.12	19.30	0.97	3.99	-0.29	0.98
6	210.71	3174.50	0.96	1.92	19.70	0.96	3.14	1.80	0.99
7	230.63	3165.97	0.97	2.18	20.01	0.95	1.76	3.51	0.92
8	274.6	2876.5	0.92	2.73	15.93	0.97	3.69	2.53	0.90
9	197.24	3140.23	0.94	2.17	15.04	0.95	3.01	-0.17	0.98
10	240.38	3153.38	0.99	2.51	17.67	0.99	3.21	4.60	0.99
11	255.64	3138.14	0.95	2.64	16.79	0.96	1.42	17.61	0.99

* Not enough data points.

2.4.2 Developing Master Curves for UPV and Dynamic Modulus

The following steps were taken in order to develop the master curve for UPV and/or dynamic modulus:

1. The coefficient of Ln(x), “a” and/or “a`”, is set to constant value, i.e., a = average of coefficient “a” and/or “a`” of all equations. Then, new coefficients “b” and/or “b`” for each mix are calculated and corresponding R^2s are shown in Table 2-8. After this step, all the mixes will have the same shape (Figure 2.13).

2. One mixture is selected as the reference mix. As can be seen in Figure 2.13, Mix 5 is representing a typical MD 7 mix with test results very close to the center of the all-mixes’ results. Therefore, Mix 5 is selected as the reference mix.

3. The vertical shift factors, which are the difference between the intercepts of governing equations of any mix and reference mix (Mix 5), are calculated. Examples are shown in Figure 2.13. The resulting master curves from shifting the results (dynamic modulus and/or UPV) are shown in Figure 2.14.

4. The characteristics of the mix most related to the shift factor are found by Pearson’s correlation analysis. Table 2-9 includes the shift factors of each mix next to their curing and hardening properties. The Pearson’s correlation coefficients are summarized in Table 2-10. The parameters with higher absolute value of Pearson’s correlation coefficient are selected to be the predictors of shift factors. To find the relationships, linear regression method is employed (Equation 2-7).

$$y = \beta_0 + X_1\beta_1 + X_2\beta_2 + X_3\beta_3 + \varepsilon \qquad (2\text{-}7)$$

where y is response variable, x is independent variable (predictor), β is unknown variable, and ε is residuals. In a linear model, the parameters enter linearly, however, the predictors themselves do not have to be linear. Here, the objective is finding $\vec{\beta}$ (i.e., β_0, β_1, β_2, and β_3) to minimize the residual error (ε), further details can be found in Faraway (2004). Primary bivariate analysis on shift factors and each of these selected variables are showing that the best relationships among most of them has a polynomial format. To describe the shift factors, polynomial relationships (second degree) for each shift factor (UPV or dynamic modulus) are found (Table 2-11 and Table 2-12). In selecting the best models, R-squared, P-value, residual standard error, and simplicity of the model are considered (i.e., highest R-squared and P-value less than 0.05). Residual standard error (RSE), also known as the model sigma, is a variant of the RMSE (root mean squared error) attuned for the number of predictors in the model. The lower the RSE, the better the model. In practice, the difference between RMSE and RSE is very minor, especially for large multivariate data. These models are highlighted in table 2-11 and 2-12 and described as following:

$$\delta_{UPV} = 357.91(CS)^2 + 229.99CS - 14.4A^2 + 176.97A - 54.71T^2 + 154.53T - 59.81 \tag{2-8}$$

$$\delta_{DM} = 4.6(CS)^2 + 0.28CS + 0.51(UW)^2 - 4.51UW - 1.45WC^2 + 0.48WC - 0.55 \tag{2-4}$$

where δ_{DM} and δ_{UPV} are the shift factors of dynamic modulus and UPV, respectively, *CS* is compressive strength, MPa, *UW* is unit weight (Kg/m^3), *A* is air content, *T* is average temperature (^oC) of curing period, and *WC* is water-cement ratio.

In Figure 2.15, the predicted shift factors of UPV and dynamic modulus are compared with the actual values. Since the number of data is limited in relation to the number of variables, deviation from the line of equality (y=x) is expected.

Table 2-8. Modified equations of best fit for each mix.

Mix No.	UPV vs. Temp-Time	DM (RTG) vs. Temp-Time

	($y = a^{*} Ln(x) + b$)		($y = a^{`**} Ln(x) + b^{`}$)	
	b	R^2	b	R^2
1	2915.7	0.82	16.86	0.95
2	3243.0	0.95	22.17	0.97
3	3131.8	0.91	18.42	0.96
4	3299.8	0.96	21.44	0.95
5	3089.6	0.92	17.38	0.97
6	3107.0	0.96	16.82	0.96
7	3197.9	0.97	18.42	0.95
8	3128.1	0.92	17.09	0.97
9	3009.0	0.94	13.45	0.95
10	3233.5	0.99	17.73	0.99
11	3288.1	0.95	17.44	0.96

*a = 224.26, **a` = 2.5

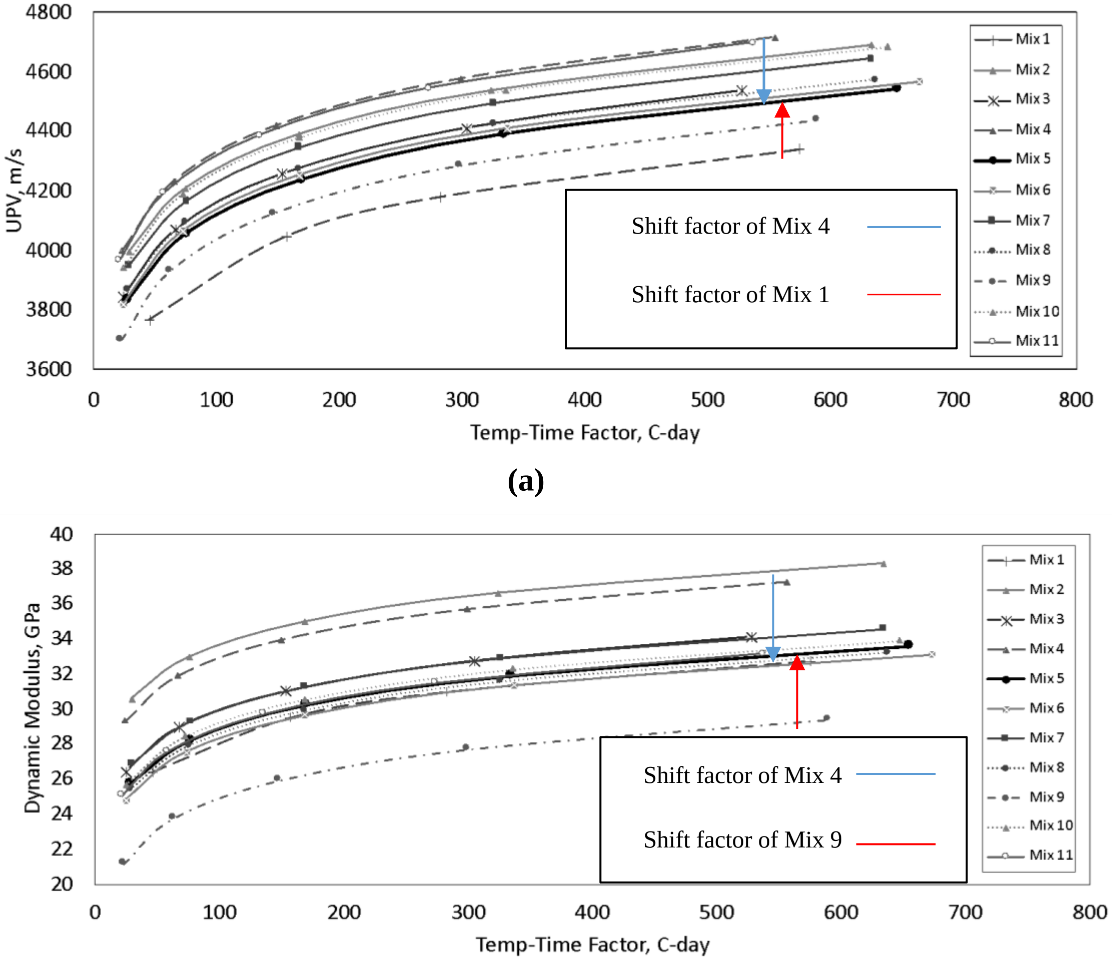

(a)

(b)

Figure 2.13. Relationship between a) UPV, and b) dynamic modulus and Temp-Time factor with the constant “a”.

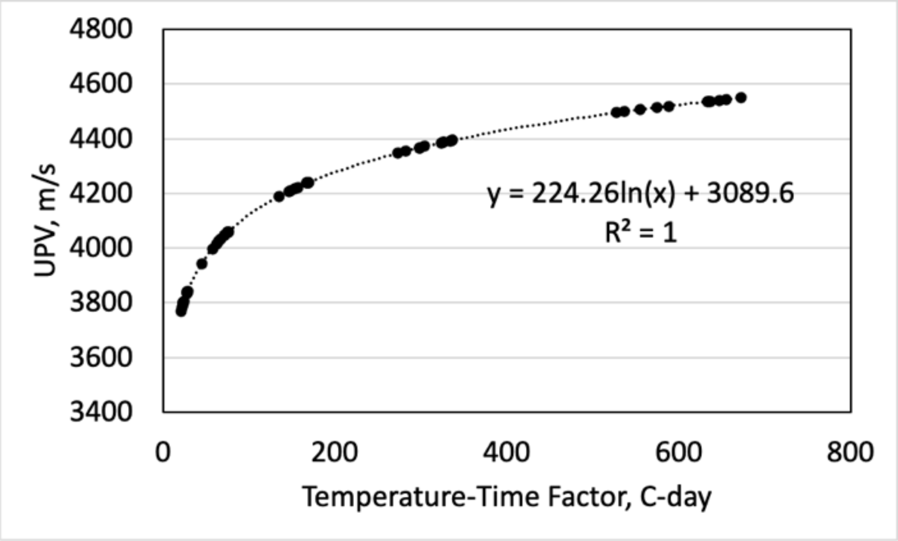

(a)

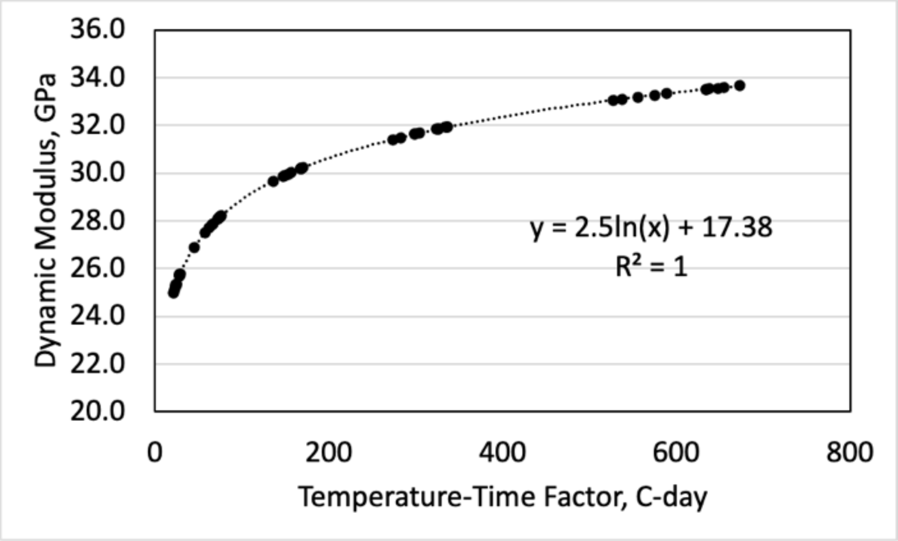

(b)

Figure 2.14. Master curves for a) UPV, b) dynamic modulus.

Table 2-9. Shift factors and curing and hardening properties of each mixture.

Mix	Shift Factor (DM)	Shift Factor (UPV)	Initial Temperature	Slump	Average Temperature	Air Content	Unit Weight	W-C Ratio	Compressive Strength
1	0.52	173.9	25.3	25	20.5	0.04	2352	0.44	38
2	-4.70	-156.90	26.80	15	22.90	0.036	2418	0.44	30.83
3	-0.98	-38.57	17.00	98	21.99	0.065	2274	0.45	30.96
4	-4.02	-181.88	16.00	111	21.70	0.046	2336	0.43	30.48
5	0.00	0.00	24.00	76	23.38	0.054	2287	0.45	25.26
6	0.56	-21.19	23.30	146	23.43	0.060	2271	0.45	22.42
7	-1.00	-107.98	23.00	105	22.62	0.058	2278	0.45	23
8	0.45	-28.90	23.50	76	22.75	0.061	2271	0.45	25.3
9	3.98	77.53	16.50	130	21.80	0.062	2253	0.48	19.24
10	-0.24	-142.04	16.00	175	21.47	0.054	2258	0.48	25.36
11	0.02	-199.82	15.00	226	19.94	0.056	2232	0.5	26.51

Table 2-10. Pearson's correlation coefficient among shift factors and mix properties.

Mix Properties	Shift factor (UPV)	Shift Factor (DM)
Initial Temperature	0.38	-0.19
Slump	-0.42	0.33
Average Temperature	0.03	-0.14
Air Content	0.08	0.60
Unit Weight	0.00	-0.69
W-C Ratio	-0.15	0.54
Compressive Strength	0.12	-0.49

Table 2-11. Models for predicting UPV shift factor.

Model Number	Coefficients									Performance		
	Intercept	Compressive Strength		Unit Weight		Air Content		Average Temperature		R^2	RSE	P-value
		a*	b*	a	b	a	b	a	b			
1	-59.81	426.79	464.11	134.62	-392.67	-36.75	-42.21	-35.93	395.65	0.95	60.8	0.19
2	-59.81	357.91	229.99	0	0	-14.40	176.97	54.71	154.53	0.91	57.06	0.05
3	-59.81	137.77	-169.0	-349.81	-714.24	479.38	-738.61	0	0	0.81	80.88	0.16

*The equations are in the form of ax^2+bx.

Table 2-12. Models for predicting dynamic modulus shift factor.

Model Number	Coefficients									Performance		
	Intercept	Compressive Strength		Unit Weight		Air Content		W-C Ratio		R^2	RSE	P-value
		a*	b*	a	b	a	b	a	b			
1	-0.55	3.72	-1.36	-0.80	-10.80	2.91	-6.30	-1.34	-0.56	0.94	1.32	0.23
2	-0.55	1.73	-5.33	-5.32	-19.85	9.14	-16.97	0	0	0.93	1.01	0.03
3	-0.55	4.6	0.28	0.51	-4.51	0	0	-1.45	0.48	0.94	0.94	0.02
4	-0.55	4.95	-0.41	0.47	-4.82	0	0	0	0	0.91	0.90	0.003

*The equations are in the form of ax^2+bx.

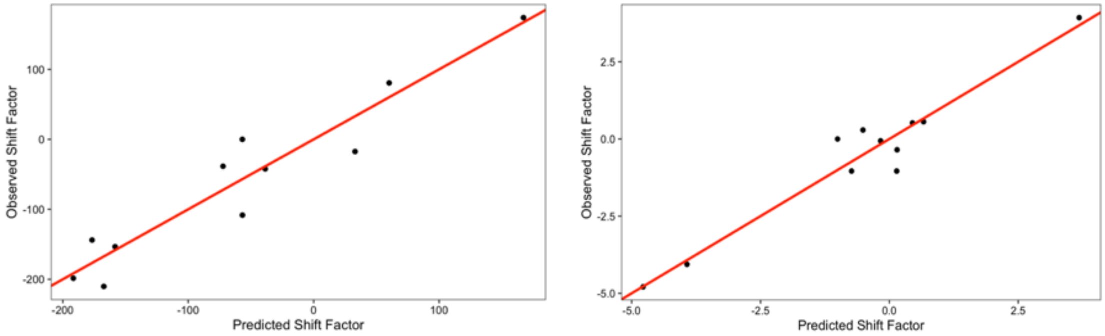

(a) (b)

Figure 2.15. Comparison of observed a) UPV, b) dynamic modulus shift factor and predicted shift factors.

2.4.3. Rebound Hammer on Selected Mixes

In order to assess rebound number response, rebound hammer was tested on Mix 5 to 8, which have the same mix component but slightly different fresh and hardened properties. Testing was performed at age of 3, 7, 14, and 28 days of curing along with destructive compressive strength. More than 5 repetitions on each sample were performed following ASTM C805. The relationship between the rebound number for each mix are displayed in Figure 2.16, and for all mixes together in Figure 2.17. These two figures show that even though the type and amount of coarse aggregate, and other components are the same, compaction and quality of production as well as curing condition of samples play a significant role in concrete strength. The difference between the average compressive strength at age 28 days of Mix 5 and 8 with Mix 6 and 7 also confirm this result. Therefore, deriving mix-specific relationships between rebound number and compressive strength for each mix is essential. Table 2-13 includes the averaged rebound number of three samples and their corresponding averaged compressive strength. Comparison of the results from Table 2-13 shows that the standard deviation of rebound hammer and compressive strength can be equal to 2.5 versus 1.5 for the mixes with similar composition.

Table 2-13. Rebound Number and Compressive Strength of four mixes at age 28 days.

Test	Mix 5	Mix 6	Mix 7	Mix 8
28-days Averaged Rebound Number	33.57	28.03	32.86	30.20
28-days Averaged Compressive Strength (MPa)	25.26	22.42	23.00	25.30

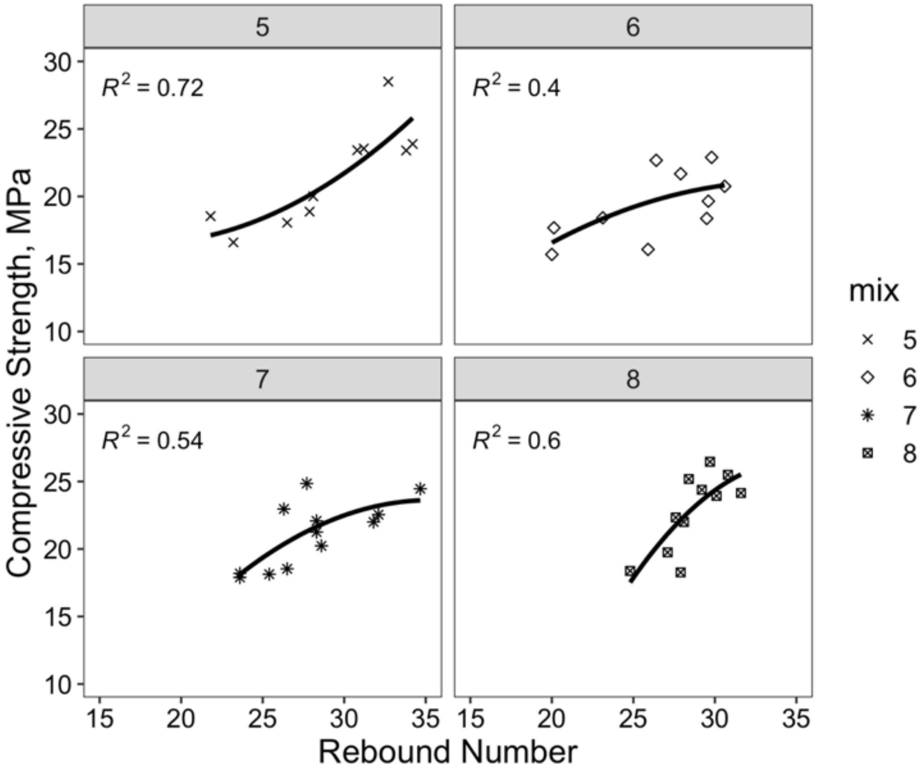

Figure 2.16. Correlation between compressive strength and rebound number of each mix.

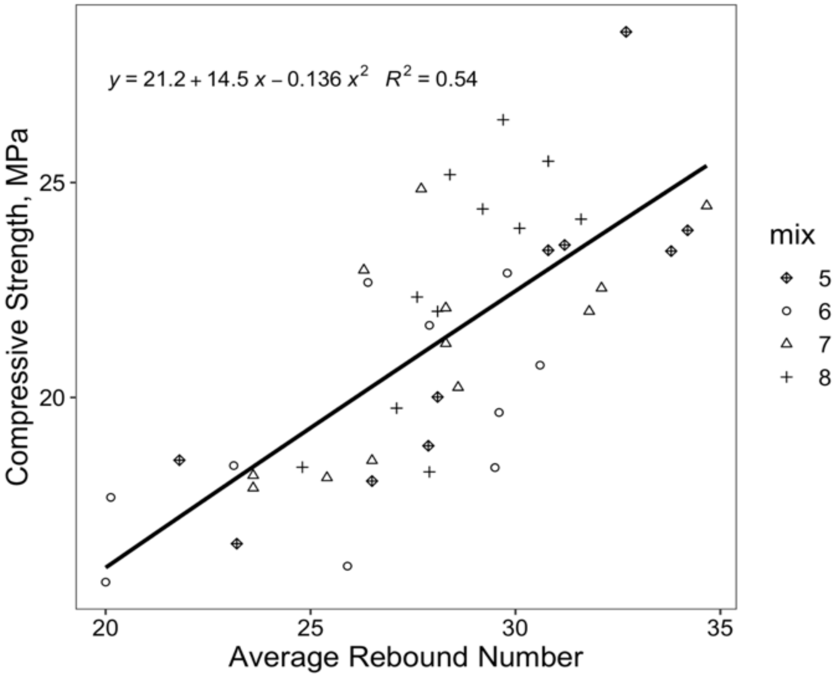

Figure 2.17. Relationship between compressive strength and rebound number of Mix 5 to Mix 8.

2.4.4. Compressive Strength Modeling

Experimental relationships among compressive strength and other properties, such as temperature-time factor, UPV, and dynamic modulus have been developed through studies (Qasrawi, 2000; Turgut, 2004; Tanyidizi et.al., 2008; Uysal et.al., 2011; Santhanam et. al., 2012; Amini et al., 2019;). Some of these models are presented in Table 2-14 and the root mean squared error (RMSE) is calculated based on this study's data (N=41). It should be noted that some of these models are developed based on specific mixes. For example, Tanyidizi et al. (2008) developed the relationship for self-consolidating concrete (SCC). Lower RMSE of Amini et al. (2019) and Turgut (2004) models are validating that the relationship between compressive strength and UPV is non-linear (Tharmaratnam & Tan, 1990).

Table 2-14. RMSE of compressive strength from literature and this study's data.

Research	Amini et al. (2019)	Turgut (2004)	Tanyidizi et al. (2008)	Qasrawi (2000)	Malhotra & Carino (2003)
Model	$CS = 0.7237e^{0.8V}$	$CS = 0.0872e^{1.29V}$	$CS = 0.2291V^2 + 5.939V + 0.258$	$CS = 36.72V - 129.077$	$CS = 33V - 109.6$
RMSE	5.16	6.21	9.52	10.52	12.16

* CS= Compressive strength (MPa), V= UPV (km/s)

Similar to UPV, experimental relationships have been developed to relate compressive strength to dynamic modulus of elasticity (Kesler & Higuchi, 1953; Sharma & Gupta, 1960; Hansen, 1986; Arras et al., 2019).

In this study testing results of 11 mixes at different ages were used to develop a relationship between compressive strength and UPV, dynamic modulus, and the temperature-time factor. Linear regression method, as explained earlier, was employed to find the best fit based on higher R^2, lower p-value, residual standard error, AIC (Akaike's information criteria), and BIC (Bayesian information criteria). AIC and BIC are indices representing the complexity of a model, higher AIC and BIC represent higher levels of complexity. Generally, simple models may be more practical. Some of the models with higher performances are presented in Table 2-15. Considering all aforementioned factors, Model 4 seems to be a better representation of the data (Equation 2-9).

$$CS = 1.36\, ln(MI) - 6.76 ln\,(V) + 1.29\, DM + 30.92 \qquad (2\text{-}9)$$

where *CS* is compressive strength (MPa), *MI* is maturity index (temperature-time factor), °C-day, V is UPV, m/s, and DM is dynamic modulus of elasticity, GPa. Figure 2.18 compares the observed and predicted compressive strength from Equation 2-9. In this figure, the residuals for each value are shown to verify the randomness of residuals hypothesis.

Table 2-15. Models for predicting compressive strength.

	Term	Model 1	Model 2	Model 3	Model 4
Coefficient	Intercept	-23.01	-49.79	-18.65	30.92
	Temp-Time	0.00298	-	-	-
	Ln (Temp-Time)	-	1.38	1.35	1.36
	UPV	0.00047	-	-0.0016	-
	Ln (UPV)	-	-8.76	-	-6.76
	Dynamic Modulus	1.34	-	1.29	1.29
	Ln (Dynamic Modulus)	-	40.11	-	-
Performance	R^2	0.92	0.91	0.92	0.93
	Standard Residual Error	1.99	2.13	1.91	1.91
	P-value	3.73e-20	4.37e-19	7.56e-21	7.21e-21
	AIC	178.63	184.10	175.08	174.98
	BIC	187.20	192.67	183.65	183.55

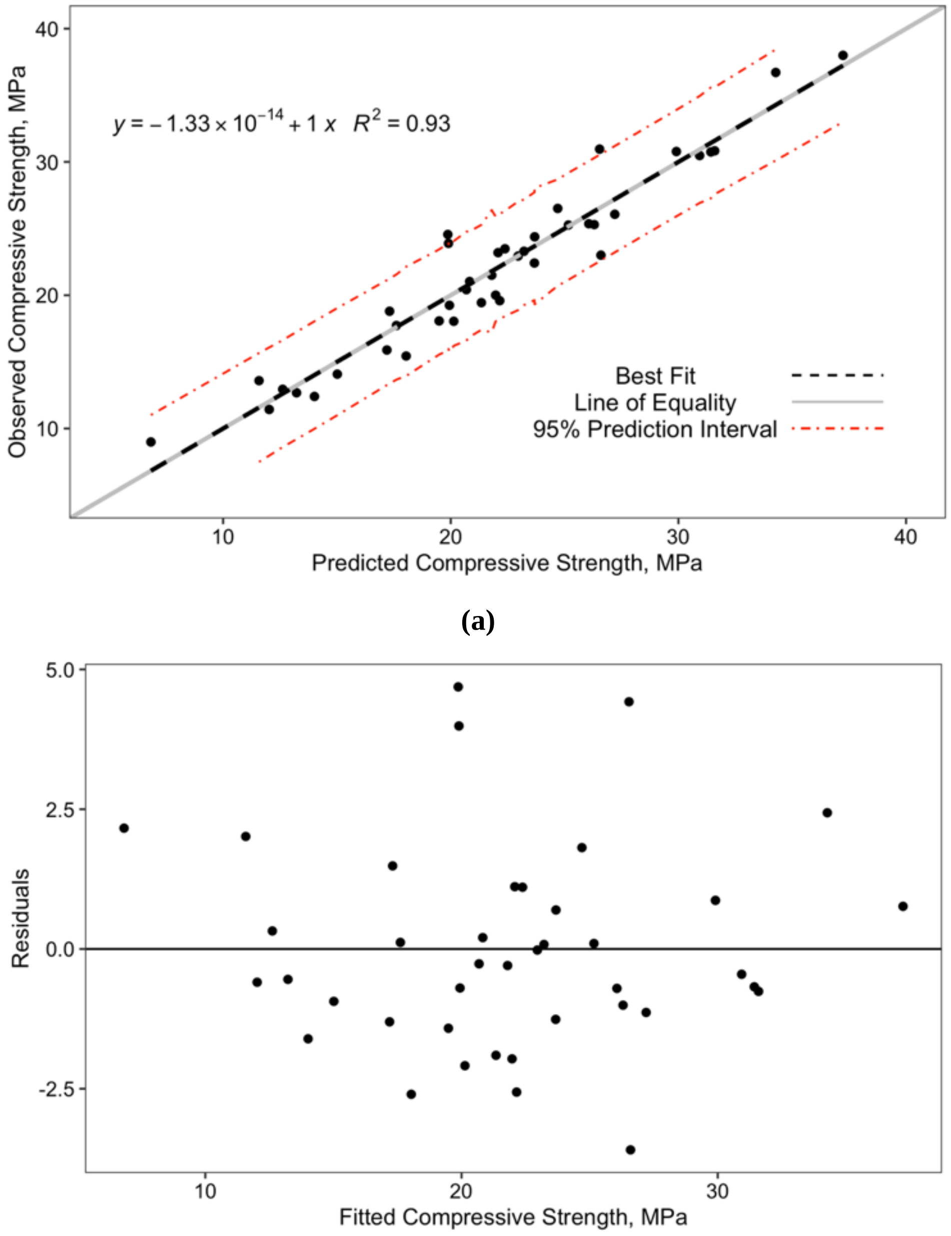

(a)

(b)

Figure 2.18. Model developing for compressive strength prediction, a) relationship between predicted and actual compressive strength, b) residuals of the model versus fitted values.

2.5. Testing Repeatability

Testing repeatability was assessed within operator and between operators for each NDT and compressive strength testing. For this purpose, Mix 3 and Mix 4 results are presented as example in Table 2-16. The samples from each mixture were prepared and tested with significant monitoring and training to minimize variation in both sample preparation and testing. Each NDT was performed by at least 3 operators at each curing age. Thus, the coefficient of variation within operator represents the variation in testing by a specific operator averaged over various ages. The coefficient of variation between operators was calculated based on the pooled data of all operators and averaged over all concrete ages. Similarly, for compressive strength when one operator tested the samples, the coefficient of variation corresponds to within operator variability, while when three operators performed the tests, the coefficient of variation represents the between operator variability. Thus, in this case the pooled data were used as well for calculating the coefficient of variation. As can be observed from Table 2-16, both within and between operators' variability for UPV and RTG were low, and either below or close to the recommended target repeatability. These target coefficient of variations are reported in past studies for potential adoption of NDT in QA. Within operator repeatability in compressive strength testing was at low levels, however between operators was a little higher than within operator. In regard to rebound hammer, both within and between operators' variability was lower than what was reported in many studies. However as shown earlier, the rebound number between the four mixtures with the same components and similar compressive strength presented a significant difference. This turns out to be within the target repeatability reported in past studies, however not necessarily acceptable for adoption in a QA plan.

Table 2-16. Testing Repeatability of Mix 3 and Mix 4.

Test	Within Operator CV (%)		Between Operator CV (%)		Target Repeatability
	Mix 3	Mix 4	Mix 3	Mix 4	
IRT	1.3	1.4	3.5	3.5	1 to 2%**
UPV	0.9	0.7	1.3	1.2	3%**
RTG	0.4	0.2	2.6	2.0	1 to 3%**
Compressive Strength	0.4	0.8	1.8	3.32	1 to 4%***
Rebound Hammer	4.2	3.8	4.3	6.4	10 to 15%**

*****CV = coefficient of variation

** Malhotra and Carino (2003), Goulias (2016).

*** ACI 214.3R-88 Rating System

2.6. Summary & Conclusions

The adoption of quick, easy to run and reliable NDT methods in the QA/QC process provides several benefits. This study explored the use of alternative NDTs for monitoring and estimating concrete strength gain at early ages. Historically, maturity modeling has been successfully used in monitoring the hydration process in concrete, yet it does not always guarantee successful results. For this reason, it has been recommended that maturity monitoring is coupled with additional lab and in-place testing for verifying strength predictions.

This study examined alternative NDT methods that can be used in monitoring and/or estimating strength gain in concrete, and thus can be adopted in an NDT based QA process. These NDTs included: infrared thermography (IRT), ultrasonic pulse velocity (UPV), fundamental resonance frequency, and rebound hammer. The measured parameters from these NDT methods were successfully related to the temperature-time history of concrete during hydration, and thus related to strength.

Results of UPV and resonant frequency method showed that concrete properties can be measured with minimum variation and high reliability. The second part of the study included more mixes to evaluate the repeatability and reproducibility of the results. All the mixtures had the same format of relationships among UPV and RTG responses and maturity index. This led to developing a generalized model or “master curve” to predict concrete properties at different ages based on maturity index and most relevant parameters (such as compressive strength, unit weight, etc.). The NDT data and maturity index of these mixtures was also used to develop a model for predicting compressive strength with high R^2 (i.e., 0.93).

While all NDTs considered in this approach related well to strength predictions and modulus, the rebound hammer presented higher variability levels associated potentially with concrete surface irregularity, presence of coarse and/or fine particles in the vicinity of concrete surfaces, as well as operator training and expertise. The findings of this study can be further validated with concrete mixtures from other infrastructure applications. Infrastructure agencies can use the methodology to assess the potential adoption of these and other NDTs in a QA plan elsewhere.

Chapter 3. Assessing Concrete Uniformity with NDTs in Quality Assurance.

3.1 Introduction

The objective of this experimentation was to provide an assessment of the response of the selected NDTs in regard to the presence of honeycombing and segregation for laboratory prepared concrete samples. Such concrete defects are encountered in situations where concrete mixtures are not well proportioned and/or properly mixed and consolidated (Graveen et al., 2003). Various NDT methods have been explored over the years for assessing concrete quality. Some of them include ground penetrating radar (GPR), ultrasonic wave propagation methods, resonant frequency methods, rebound hammer, infrared thermography, image analysis and other (Davis et al., 1998; Malhotra & Carino, 2004; Breul et al., 2008; Johnson et al., 2010). However, limited studies focused on using NDTs in detecting honeycombing and segregation during production and/or in the quality assurance process. Image analysis of hardened concrete has been explored in a couple of studies for detecting inhomogeneity in concrete (Breul et al., 2008; Johnson et al., 2010). This method focuses on the spatial distribution of aggregates to detect segregation. However, the presence of fine particles and/or the presence of hardened cement paste on the concrete surface may shadow such effects. Furthermore, the suggested approach does not provide a quantifiable measure of the degree of segregation within the concrete member.

The use of ultrasonic pulse velocity (UPV) in assessing the mechanical properties and quality of concrete has been examined by various studies (Goulias & Ali,1998; Chang et al., 2006; Petro & Kim, 2012; Bogas et al., 2013). UPV is related to the dynamic elastic modulus and correlated to concrete strength and static modulus. It has been also used to accurately detect cracking and other defects in concrete materials and structures by examining the effects on the transmission time (Komlos et al., 1996; Zhu et al., 2011; Azari et al., 2014). While UPV has been used for forensic assessment of concrete structures, it has never been incorporated into the QA process of concrete during production. The resonant frequency of concrete has also been related to the dynamic elastic modulus and correlated to concrete strength and static modulus (Hassan & Jones, 2012; Sajid & Chouinard, 2017; Saremi & Goulias, 2020). The presence of defects (i.e., cracking, poor bonding between aggregates and cement paste) leads to a lower resonant frequency associated with lower stiffness (Leśnicki, 2011; El-Newihy, 2017; Yang & Gupta, 2018). So far, this method has been used for assessing laboratory produced concrete samples while in construction its use is limited. As in the case of UPV, this NDT has never been incorporated into the QA process of concrete as well. Nevertheless, during concrete production such methods could be adopted in QA/QC as a laboratory assessment of concrete strength, stiffness and uniformity at early stages of production (i.e., 1, 7, 14 days, without having to wait for the 28 days strength results).

Segregation has been identified as a significant concern in past studies for a variety of mixtures due to the potential variability in strength within a concrete structure (Safawi et al., 2004; Gao et al., 2019; Yim et al., 2020). Gao et al. (2019) used rebound hammer and chloride permeability tests on segregated samples to assess the severity of the segregation on self-consolidating concrete. Early detection of these defects will assure better quality control during concrete production and casting.

The objective of this experimentation was to document the response of UPV, RTG, and rebound hammer in terms of their ability in identifying and comparing defective concrete (e.g., segregated and honeycombed) with sound concrete based on laboratory produced samples. The specific objectives included:

(i) comparing the response of UPV and RTG between the control "sound" concrete and beam samples with honeycombing for providing an initial set of recommendations on whether such methods can be used in QA.

(ii) comparing the response of NDT and chloride permeability among concrete samples with different level of segregation.

(iii) assessing whether the reported levels of accuracy and repeatability in the literature were reproducible and within acceptable levels for potential inclusion of these methods in an NDT-based QA plan.

(iv) providing an initial set of feedback on the applicability of these NDTs when alternative levels of segregation and honeycombing are observed.

3.2. Experimental Program

Honeycombing and segregation in concrete can be the result of deviation from mix design or improper mixing and placement of concrete. In this study, in order to evaluate the effect of sample preparation, different samples with different methods were prepared and their properties were evaluated. Table 3-1 includes the samples description. As shown, six different mixtures were used for this investigation, three for honeycombed samples and their controls [76×76×305 mm (3×3×12 in.) or 150×150×500 mm (6×6×21 in.)], and three for segregated samples [150×150×500 mm (6×6×21 in.)]. To evaluate the effect of honeycombing, samples were prepared from each concrete batch, by (i) following the standard practice of ASTM C192 (control), and (ii) deviating from the standard for producing poorly mixed concrete (honeycombed). The control mix represents a typical concrete used in building construction and highway applications in Maryland and the surrounding regions. In sample 1H-H, the honeycombed part is almost half of the beam, while in samples 2H-M and 3H-L, the honeycombed part is located in the middle third of the beams (Figure 3.1). The honeycombed concrete was mixed in the mixer for only one minute. A partition was held at the boundary of honeycombed and sound concrete while pouring the concrete into the mold, then removed before consolidation, so they bond. In more fluid concrete (i.e., higher slum) the paste fills the voids during hardening and reduces the level of honeycombing. Therefore, the honeycombed samples can be divided to three levels of low, medium, and high depending on the mix fluidity (slump).

According to ASTM C192, vibrating is one of the consolidation methods, strongly recommended for concrete with a slump less than 25 mm (1 in.). In the laboratory scale samples, internal vibration is not recommended. ASTM C192 suggests filling molds layer by layer while vibrating. The upper layer should be added when the surface of concrete becomes smooth and large air bubbles cease to break through the top surface. Determining the appropriate time for adding the upper layer and finishing the consolidation is a crucial step in that over-consolidation leads to segregation. Either higher amplitude or longer duration of vibration causes the severe segregation of fresh concrete. In order to assess the segregation, samples were prepared from concrete with high fluidity with prolonged consolidation time, about 4 minutes. High fluidity in concrete can be achieved by incorporating a high amount of high-range water reducer (HRWR) and higher water-cement ratio. Excess HRWR and water reduces the friction among particles and increases the level of segregation. Therefore, regarding the amount of HRWR and water in mixes, segregation levels can be categorized as low, medium and high. In a segregated sample, heavier components of concrete such as coarse aggregate gather in the bottom of the element, while lighter components such as fine aggregate and paste stay at top of the element. Therefore, properties of concrete were expected to vary at different locations of samples. Thus, the tests such as UPV and rebound hammer were repeated at top, middle, and bottom of each sample (Figure 3.2).

Table 3-1. Mix properties of samples.

Mix	Sample(s)	W_{AEA}[5]/ W_{cement}	W_{HRWR}[6]/ W_{cement}	Water-Cement Ratio	Coarse Aggregate/ Fine Aggregate	Air Content	Slump (mm)	Fresh Unit Weight (Kg/m^3)
1	1H[1]-H[2], 1C[3]	0.18%	0.12%	0.44	1.38	5%	100	2410
2	2H-M[2], 2C	0.39%	0.24%	0.44	1.38	7%	120	2300
3	3H-L[2], 3C	0.39%	0.24%	0.45	1.38	6%	165	2260
4	4S[4]-H	0.39%	0.39%	0.50	1.39	5.5%	226	2230
5	5S-M	0.39%	0.31%	0.48	1.39	5.5%	175	2250
6	6S-L	0.39%	0.24%	0.45	1.39	7%	108	2260

[1]H=Honeycombed, ^{2}H, M, L= High, Medium, Low, [3]C=Control, [4]S=Segregated
[5]Air entrainer agent, [6]High-range water reducer

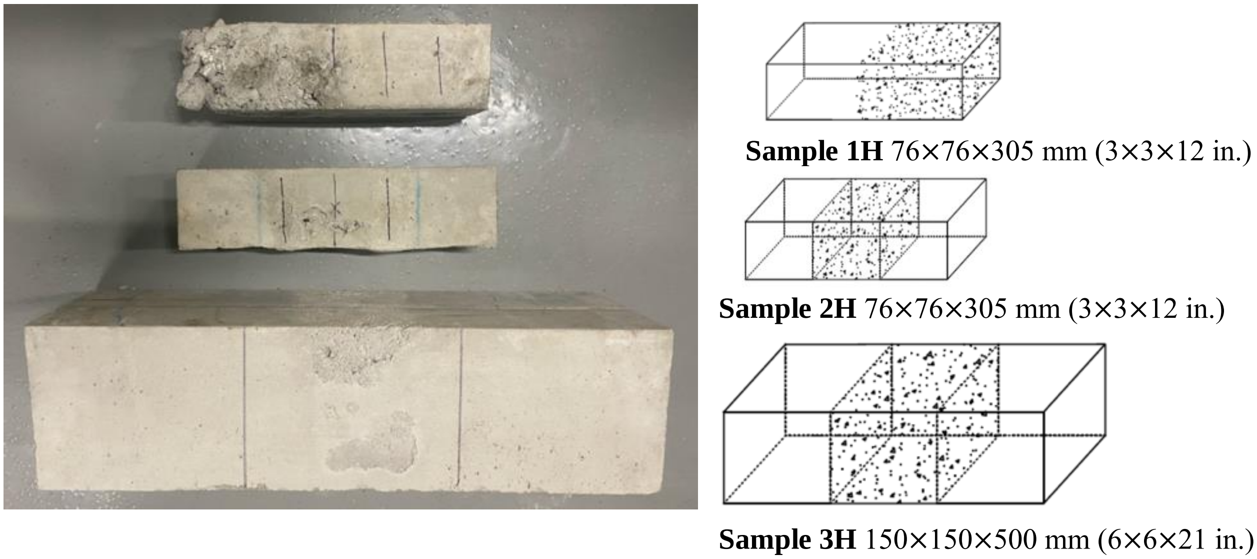
Sample 1H 76×76×305 mm (3×3×12 in.)
Sample 2H 76×76×305 mm (3×3×12 in.)
Sample 3H 150×150×500 mm (6×6×21 in.)

(a) (b)

Figure 3.1. Honeycombing in concrete (a) Presence of honeycombing in a sample, (b) Location of honeycombing in different samples

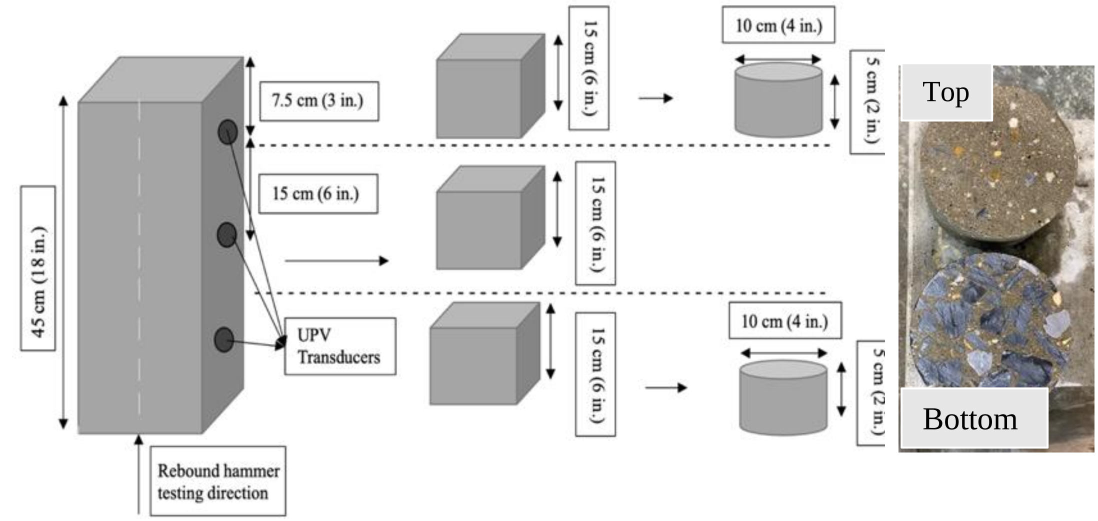
45 cm (18 in.)
7.5 cm (3 in.)
15 cm (6 in.)
15 cm (6 in.)
10 cm (4 in.)
5 cm (2 in.)
15 cm (6 in.)
UPV Transducers
15 cm (6 in.)
10 cm (4 in.)
5 cm (2 in.)
Rebound hammer testing direction
Top
Bottom

(a) (b)

Figure 3.2. Dimension and preparation of segregated samples, a) location of the cores, b) cores from top and bottom of the sample.

3.2.1. UPV Testing

For honeycombed samples, the indirect or direct testing mode of UPV was used, depending on the surface shape of the sample. Control concrete samples were tested following the same testing modes. For indirect mode, the distance between the transducers is recommended to be from 100 mm to 200 mm (Malhotra & Carino, 2004).

The transmitter was placed in the sound portion of the concrete beam and the receiver was in the honeycombed portion while maintaining the spacing between the transducers at 150 mm (6”). For segregation, the direct mode of UPV testing was used on the beams. Location of transducers at top, middle, and bottom of the segregated samples are shown in Figure 3.2. The transmission times of pulse traveling between two transducers were collected for the honeycombed, the segregated and the control samples at curing ages. During curing age, i.e., the first 28 days, samples were kept submerged in water at room temperature. The UPV test was repeated at least three times at each location for all ages to assess the repeatability of the test.

3.2.2. Resonant Test Gauge

The resonant frequency data were collected according to ASTM C215. For this, a Resonance Test Gauge (RTG) was used, Figure 3.3(b). Resonant frequencies were collected on the samples in the longitudinal and transverse modes. The dynamic moduli from resonant frequency of the samples are compared to assess the effect of honeycombing or segregation on mechanical properties of the samples.

3.2.3. Rebound Hammer Testing

In order to assess the concrete uniformity, the rebound hammer test was performed at every 1 in. of the segregated samples. The testing grid was selected in a way to avoid the edges at least by 1 in. and avoid repeating the test at the same location since the rebound hammer may leave chips where it hit (Figure 3.4). The rebound hammer testing was repeated three times at each age of age 3, 7, and 28 days (Figure 3.4), and rebound number was averaged over each one-third of the sample. The rebound number can be different at top, middle, and bottom of the samples since it is very sensitive to the type and distribution of coarse aggregate. Due to the rough surface of honeycombed samples, the rebound hammer was not performed on those samples.

3.2.4. Chloride Permeability

Since presence of air voids affects the permeability of concrete, the resistance to chloride ion penetration was obtained in accordance with ASTM C1202. Chloride permeability of cores taken from top and bottom of the samples (Figure 3. 2), at age 28 days, were also compared to evaluate the severity of the segregation for the samples. In this method, the cored samples with dimensions shown in Figure 3.2, have been in vacuum condition overnight. Then, subjected to 60 V dc, while one end of the specimen is immersed in a sodium chloride solution (3.0% NaCl), and the other end is immersed in a sodium hydroxide solution (0.3 mol/L NaOH). The total charge is calculated from the integration of area under current (in amperes) versus time (in seconds) or Equation 3-1:

$$Q = 900(I_0 + 2I_{30} + 2I_{60} + \cdots + 2I_{300} + 2I_{330} + I_{360}) \tag{3-1}$$

where Q is the charge passed (coulombs), I_0 is the current (amperes) immediately after voltage is applied, and I_t is the current (amperes) *t* minutes after voltage is applied.

Even though there is some criticism of the chloride permeability test in regard to measurements affected by high voltage leading to an increase in temperature, and thus affects physical and chemical properties including permeability (Bryant, 2014), it is still used in many studies since it is relatively quick and easy to perform.

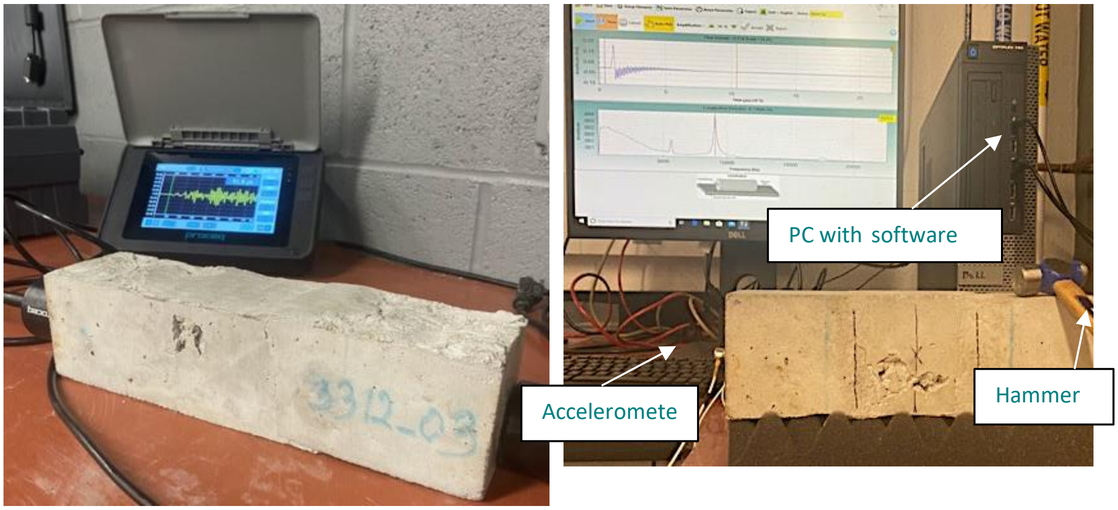

(a) (b)

Figure 3.3. Testing (a) UPV in indirect mode on the control sample and (b) RTG in direct mode on the control sample

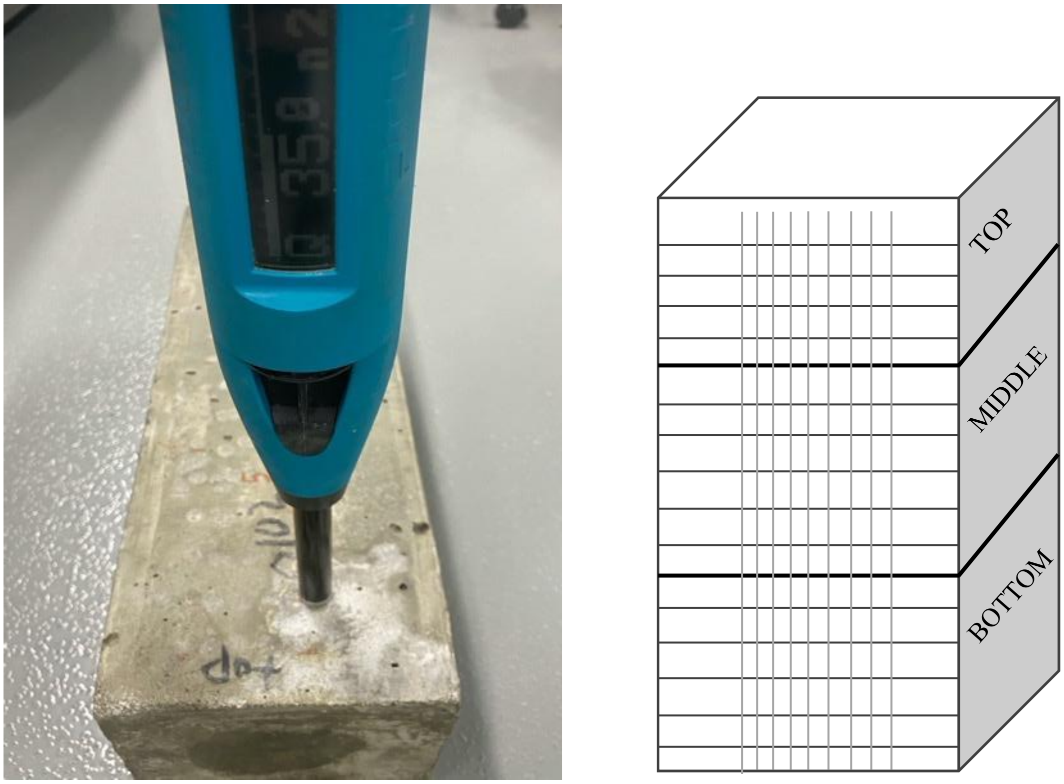

(a) (b)

Figure 3.4. Rebound hammer a) testing on a segregated sample, b) testing grids.

3.3. Analyses & Results

3.3.1. Effect of Honeycombing on Ultrasonic Pulse Velocity and Dynamic Modulus

The average velocities of the replicate measurements on the control and honeycombed samples are shown in Figure 3.5. The differences in UPV results were significant for mixtures 1 and 2, and more pronounced at early ages (7 to 14 days of curing), while for mixture 3 the difference was in the range of 100-150 m/s. This represents the combined effects of larger sample size and the lower degree of honeycombing for mixture 3H-L (due to higher slump). Larger beam specimens provide the opportunity for the transmission waves to propagate to a larger region of the cross section of the beam where the presence of large air voids might be minimal (Hobbs, 1991). As indicated above, the degree of honeycombing in mixture 3 was lower than those in mixtures 1 and 2 (i.e., representing better concrete mixing conditions and thus producing lower voids due to honeycombing). Considering that just the effects of moisture in UPV may be of the order of 50 m/s, the presence of low levels of honeycombing in concrete provide little impact on pulse velocity, like those for mixture 3. In terms of QA, lower levels of honeycombing might not be of concern since the effects on concrete quality might be minimal. The impact of 50 to 100 m/s between sound and honeycombed concrete for mixture 3 is insignificant. Honeycombing effects on UPV were more prominent for the beams of mixture 1 since the defective area was at the edge of the beam, affecting the contact quality as well between the transducers and the concrete surface.

Resonant frequency testing provides an assessment of the variation in concrete stiffness through the dynamic modulus of elasticity. Thus, the presence of honeycombing will affect the dynamic modulus (Ed). The dynamic modulus of elasticity (Ed) was calculated from the transverse resonant frequency, Equation 1-5, for the beams prepared with mixture 1, (i.e., 1H-H and 1C) since in these beams the honeycombed area was at one end of the sample, Figure 3.1. This provided the opportunity to compare Ed measured primarily in the honeycombed area and compare it to the control mix. For the beams where the honeycombed area was in the middle third (designated with 2H-M and 3H-L, Figure 3.1) the longitudinal resonant frequency was used for calculating Ed, Equation 1-4. The change in dynamic modulus with age for the honeycombed and control concrete are shown in Figure 3.6. As expected, the dynamic modulus increases with curing time due to the hardening of concrete, increasing thus the stiffness. Also, for the honeycombed concrete a lower stiffness is observed in relation to the control concrete mixture. The differences in dynamic modulus of the controlled and honeycombed concrete beams were significant for mixtures 1 and 2, while for mixture 3 such a difference was smaller. As discussed in the UPV testing results, this represents the lower degree of honeycombing for mixture 3.

3.3.2. Effect of Segregation on Ultrasonic Pulse Velocity and Dynamic Modulus

Segregation produces non-uniform distribution of particles within a mixture and thus variable properties within a concrete member. Due to this effect, the pulse velocity from mixture to mixture will fluctuate in relation to the degree of segregation in each one, and throughout the concrete specimen with depth (Komlos et al., 1996). The pulse velocities were calculated from the transmission time measured in the direct testing mode. The results of UPV on segregated samples, measured at top, middle, and bottom of the samples are shown in Figure 3.7. As expected, the ultrasonic pulse velocity increases with curing age due to the hydration. The results show that pulse velocity is higher at bottom of the sample than the middle and top. The UPV differences are shown in Table 3-2. The difference between UPV at top and bottom is higher for the highly segregated sample (Sample 4S-H) than the other samples (5S-M and 6S-L).

Longitudinal and transverse frequencies and dynamic moduli of each sample are shown in Table 3-2 as well. As can be seen, the samples have very similar transverse frequency, since the wave propagation in samples this large is less affected by distribution of the air voids. However, differences in weight and dimension led to minor differences in dynamic modulus of elasticity of samples.

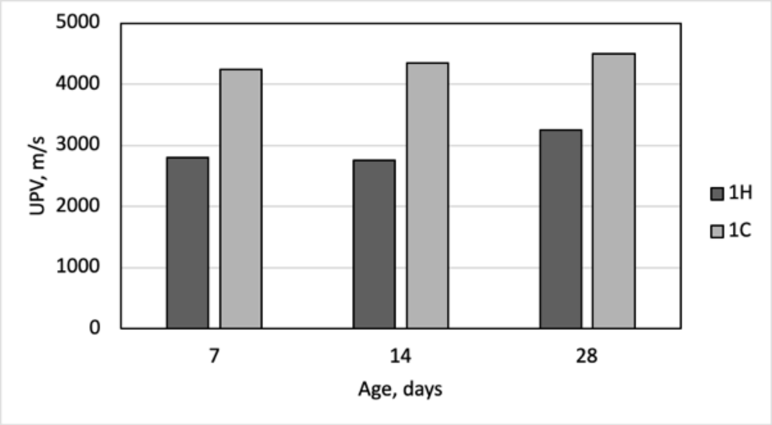

(a)

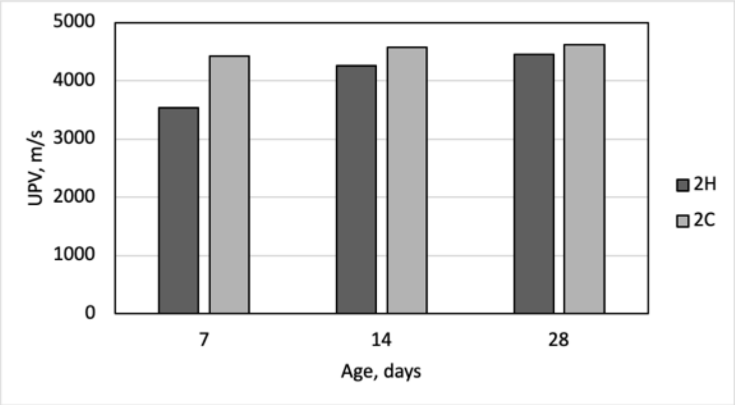

(b)

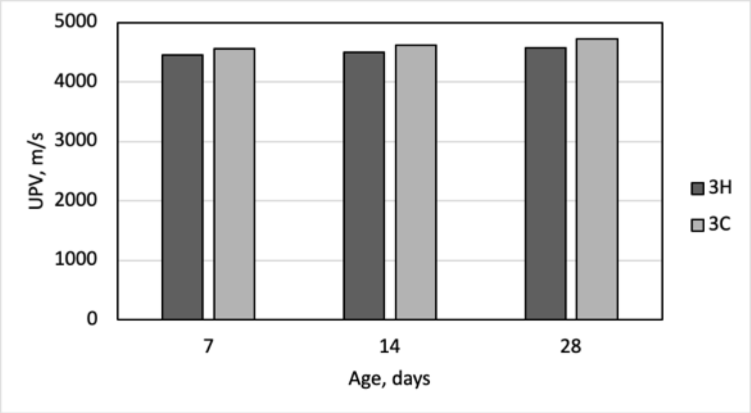

(c)

Figure 3.5. Pulse velocities for honeycombing and control concrete, a) Mix 1, b) Mix 2, c) Mix 3.

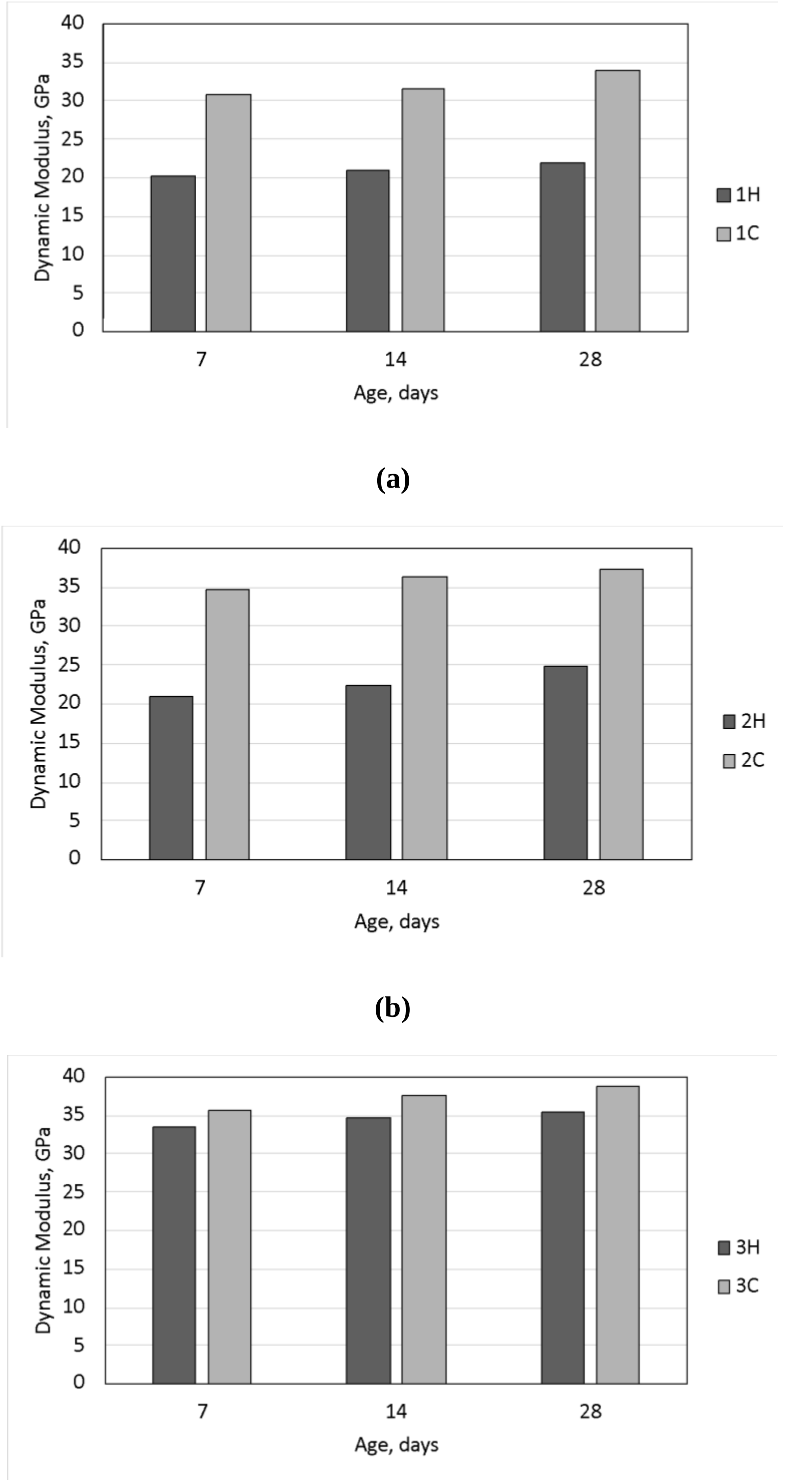

(a)

(b)

(c)

Figure 3.6. Dynamic modulus of honeycombed and control samples, a) Mix 1, b) Mix 2, c) Mix 3.

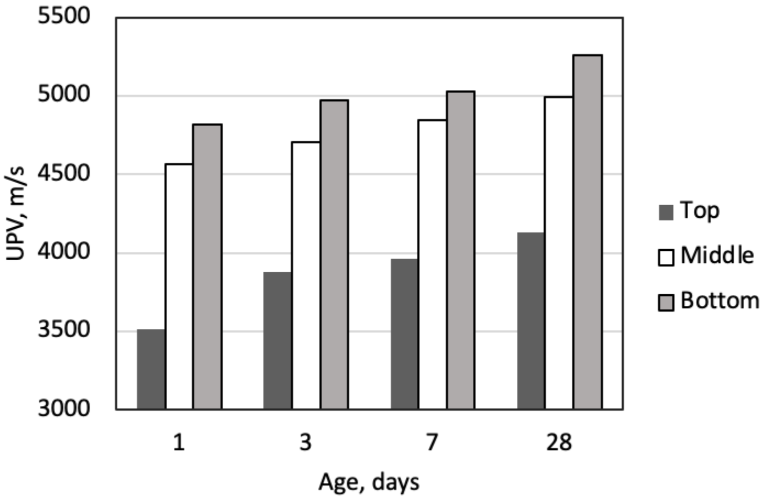

(a) Sample 4S-H

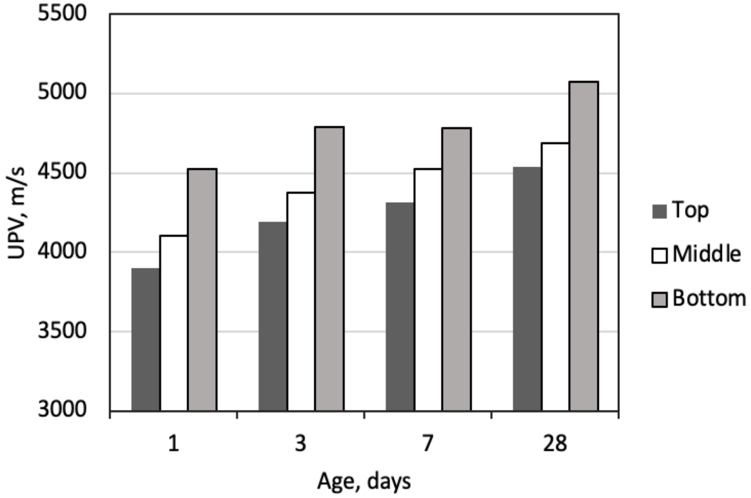

(b) Sample 5S-M

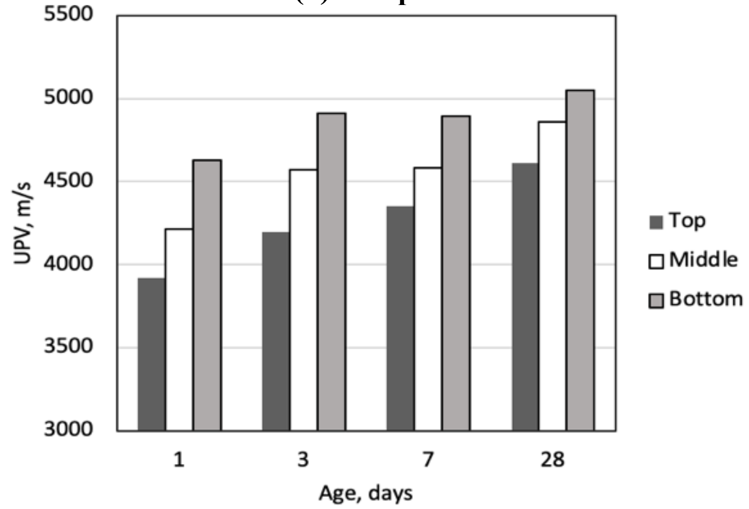

(c) Sample 6S-L

Figure 3.7. UPV results at top, middle, and bottom of the segregated samples, a) Sample 4S-H, b) Sample 5S-M, c) Sample 6S-L.

Table 3-2. UPV and resonant frequency results on segregated samples.

Sample	Age (days)	V_{top} (m/s)	V_{mid} (m/s)	V_{bot} (m/s)	UPV Difference ($V_{bot} - V_{top}$) (m/s)	Long. Freq. (Hz)	Trvs. Freq. (Hz)	Long. Modulus (GPa)	Trvs. Modulus (GPa)
4S-H	1	3509.9	4562.3	4814.8	1305.0	2109	-	26.25	-
	3	3874.7	4706.0	4969.7	1095.0	2266	4219	30.37	30.93
	7	3964.4	4848.9	5029.0	1064.6	2263	4261	30.35	31.62
	28	4130.9	4995.4	5257.0	1126.1	2308	4394	31.66	33.72
5S-M	1	3902.6	4107.7	4528.1	625.6	2109	-	29.60	-
	3	4193.6	4375.8	4787.3	593.7	2266	4141	34.25	31.33
	7	4312.8	4523.4	4782.3	469.5	2263	4172	34.25	31.88
	28	4536.2	4686.1	5072.3	536.2	2352	4305	37.30	34.09
6S-L	1	3922.8	4215.9	4631.0	708.1	2109	-	27.99	-
	3	4200.2	4570.0	4913.2	713.0	2266	4063	32.44	28.76
	7	4354.1	4584.0	4897.2	543.1	2263	4172	32.42	30.39
	28	4612.1	4858.6	5047.8	435.7	2352	4305	35.14	32.46

3.3.3. Chloride Permeability and Rebound Number of Segregated Samples

Chloride permeability is a measure of density/porosity and durability of concrete, which is highly affected by the quality of the mixing, compaction, curing condition and presence of air voids. In this study, chloride permeability testing was performed to find the degree of segregation. Figure 3.8 shows the setup of chloride permeability testing (ASTM C1202) and the threshold of permeability. The current and temperature during permeability testing on core samples taken from top and bottom of the segregated samples is shown in Figure 3.9. For the top cores the current and temperature increase with time, whereas in bottom cores, the current reduces with time. The total charge of each sample was calculated and summarized in Table 3.3. The charge difference percentage ($\Delta C\%$) is calculated from:

$$\Delta C = \frac{C_{top} - C_{bot}}{C_{top}} \times 100 \qquad (3\text{-}2)$$

where C_{bot} and C_{top} are the total charges (coulomb) at bottom and top of the samples, respectively. Comparing the results to the threshold of the charges (Figure 3.8) the two samples with higher water-cement ratio (i.e., Sample 4S-H and 5S-M) have high permeability. As expected, higher water-cement ratio produces a more porous cementitious paste in concrete.

Segregated samples were tested by rebound hammer at different ages according to the pattern shown in Figure 3.4. The average values of the rebound number on each section (i.e., top, middle, or bottom) after eliminating the outliers (ASTM C805) is shown in Figure 3.10. The difference between the average rebound number at top and bottom of the samples is very significant. Also, in most cases the rebound number is able to assess the hardening and strengthening of concrete. It should be noted that 1 unit of rebound number is about 1 MPa of compressive strength. The rebound number difference percentage ($\Delta R\%$) is calculated from:

$$\Delta R = \frac{R_{bot}-R_{top}}{R_{bot}} \times 100 \tag{3-2}$$

where R_{bot} and R_{top} are the average rebound number at bottom and top of the samples, respectively. Figure 3.11 compares the difference in measurements by UPV, rebound hammer, and chloride permeability at top and bottom of the segregated samples. The higher the difference between measurements at top and bottom, the higher is the segregation level. As can be seen, for Sample 4S-H and 5S-M, the results are in agreement, where Sample 4S-H has higher $\Delta C\%$, $\Delta V\%$, and $\Delta R\%$ than Sample 5S-M (i.e., 77%, 21%, and 22% versus 70%, 11%, and 8%). However, for Sample 6S-L, even though both $\Delta V\%$ and $\Delta C\%$ (9% and 56%, respectively) are smaller than for those values of Sample 4S-H (21% and 77%) and Sample 5S-M (11% and 70%), $\Delta R\%$ has an opposite relationship (i.e., 29% versus 22% and 8%). Even though less variability in data for Sample 6S-L was expected, rebound hammer showed high variability (29%) between top and bottom of the sample. This variability can be due to the level of uncertainty related to the method, and effect of moisture and surface finish on the rebound number.

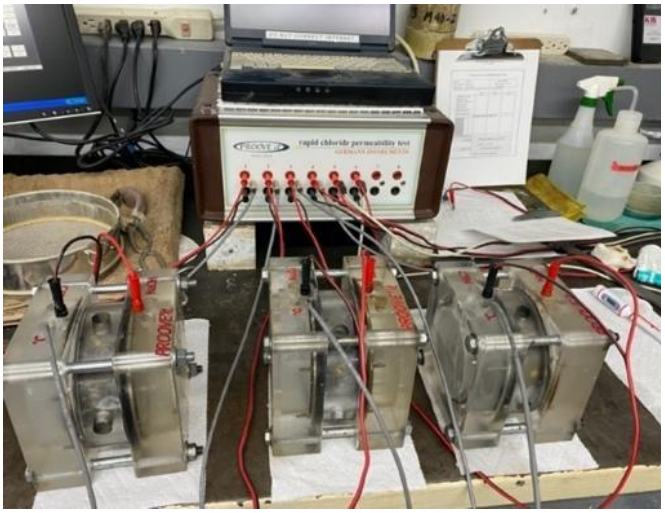

Charge (Coulomb)	Permeability
> 4000	High
2000 – 4000	Moderate
1000 - 2000	Low
100 - 1000	Very Low
< 100	Negligible

(a) **(b)**

Figure 3.8. Chloride permeability testing, a) setup for cores taken from segregated samples, b) thresholds.

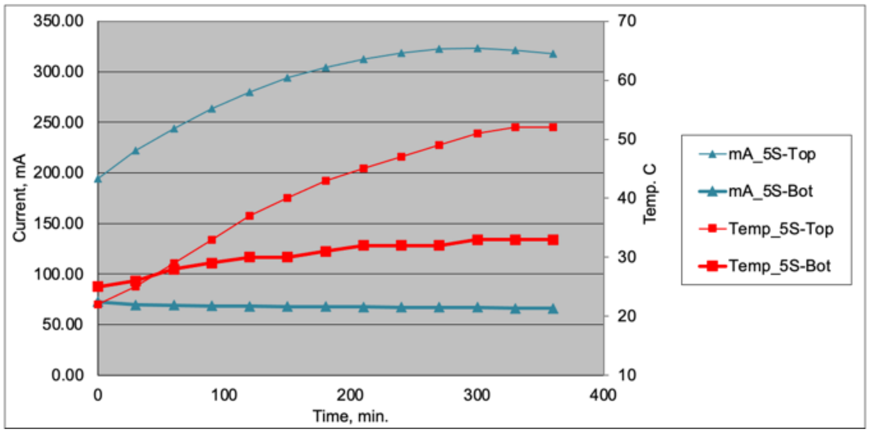

(a) Sample 4S-H

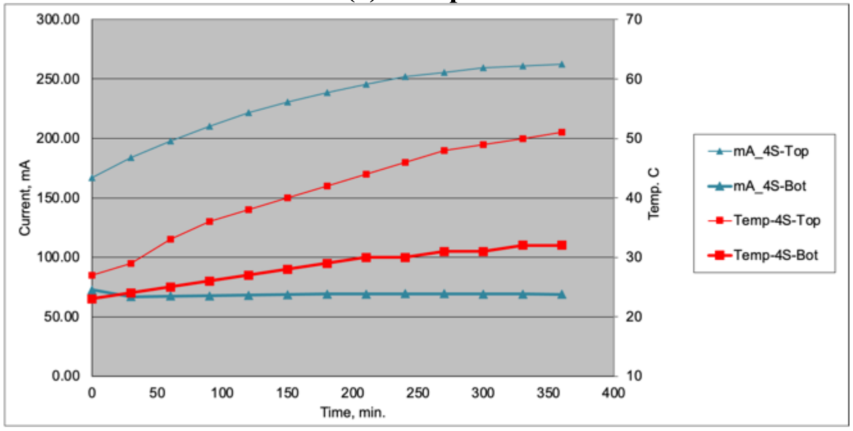

(b) Sample 5S-M

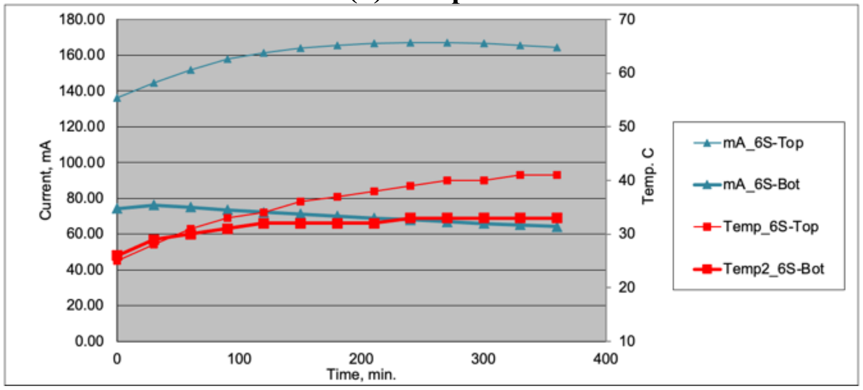

(c) Sample 6S-L

Figure 3.9. Change in current and temperature of the a) Sample 4S, b) Sample 5S, c) Sample 6S.

Table 3-3. Results of chloride permeability test on cores taken from segregated samples.

Sample	Chloride permeability Charge (Coulomb)		
	Top	Bottom	Difference
4S-H	6448	1515	76.50%
5S-M	5159	1535	70.25%
6S-L	3583	1568	56.24%

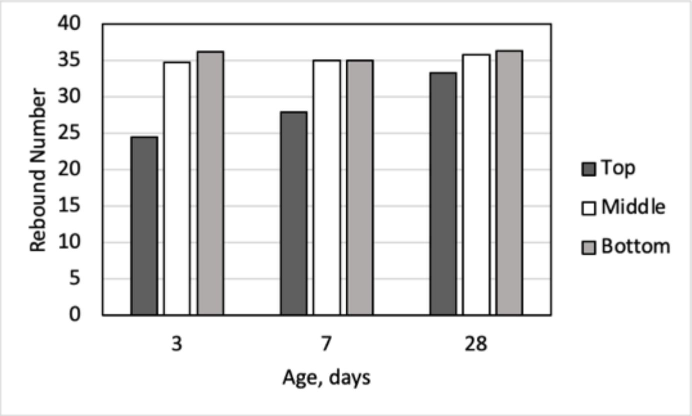

(a) Sample 4S-H

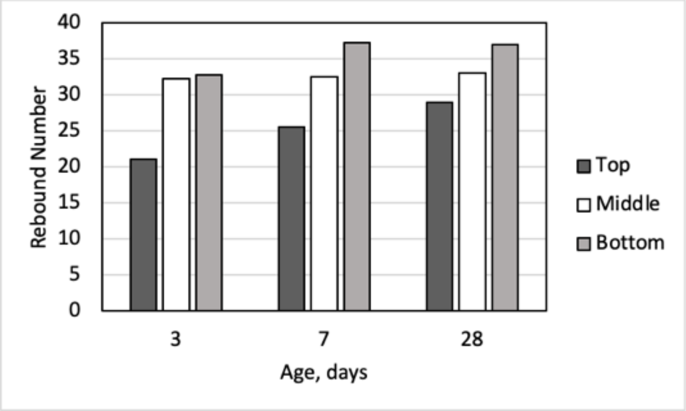

(b) Sample 5S-M

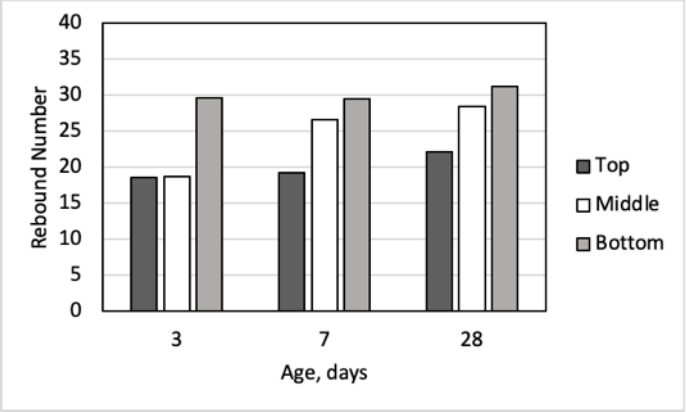

(c) Sample 6S-L

Figure 3.10. Rebound number at top, middle, and bottom of the sample at age 3, 7, and 28 days (n=15).

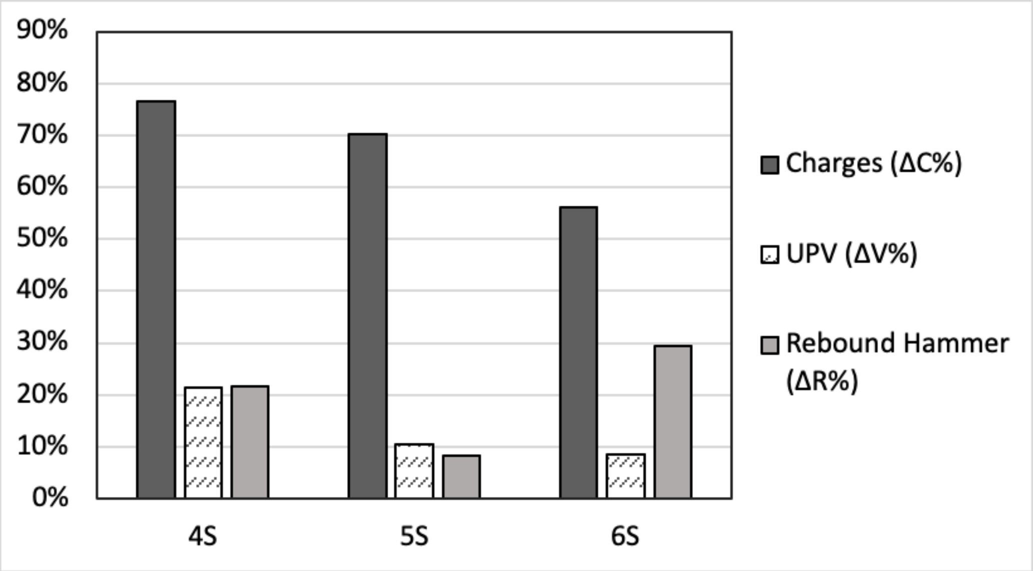

Figure 3.11. Variation of different test results at top, middle, and bottom of the samples.

3.4. Testing Repeatability

In addition to the ability of an NDT method to be able to provide measurable output regarding concrete uniformity and presence of defects, testing repeatability should be assessed (MacLeod, 1971; Wu et al., 2008; Breysse, 2012). The common sources producing variability in NDT testing may be attributed to a variety of factors and including mix proportions and batch to batch variability; variability in casting conditions; homogeneity of the concrete within the member and/or specimen; arrangement of instrumentation and training of the operator; as well as external factors like air temperature and humidity. While quantifying the contribution of all these parameters on testing variability requires an extensive and systematic study under controlled conditions (i.e., a factorial experiment considering the effects of various levels of such factors), in this study the repeatability of UPV and RTG on the honeycombed, segregated, and sound concrete was assessed based on replicate measurements on the same samples.

Table 3-4(a) presents the coefficient of variation, CV%, of UPV from repeated measurements on concrete samples from mixtures 1, 2, and 3, while Table 3-4(b) presents the CV% results for the dynamic modulus determined with RTG. These measurements were obtained from a single operator and/or three operators. UPV repeatability on sound concrete has been reported at 2% to 3% level from past studies, while repeatability on defective concrete can be up to 20% (Goulias, 2017c; Malhotra & Carino, 2004). For the tests conducted in this study, the control concrete samples provided a testing variability on replicates of around 2% or lower. However, for honeycombed concrete the location of the honeycombed area with the concrete beams had a significant impact on reflecting the ability of the operator to identify proper contact between the defective area and the transducers. For the concrete beams designated with 1H-H the honeycombed area was at one end of the sample, and thus such variability was higher reflecting the variable and irregular surface characteristics in the defective area. For the honeycombed beams designated with 2H-M where the defective area was in the middle third of the beams good transducer contact with the concrete surfaces provided much lower variability in repeated measurements. Overall, the honeycombed specimens have higher testing variability compared to the sound concrete. The poor bonding between concrete ingredients and the presence of higher and random voids results in higher inhomogeneity of concrete, and thus affects UPV and resonant frequency repeatability. However, due to the larger effect of smoothness of contact area between the UPV transducers and the concrete, the surface roughness has a higher impact on UPV measurements than RTG ones. Thus, the coefficient of variation is higher for UPV than RTG.

Table 3-4. Coefficient of variation of a) UPV, b) dynamic modulus of Mixture 1, 2, and 3

(a)

	Sample					
Age (days)	1H-H	1C	2H-M	2C	3H-L	3C
7	19.93%	0.67%	0.37%	0.23%	0.69%	0.76%
14	9.75%	2.11%	0.86%	1.26%	0.47%	0.67%
28	9.97%	1.55%	0.22%	0.61%	0.2%	0.05%

(b)

	Sample					
Age (days)	1H-H	1C	2H-M	2C	3H-L	3C
7	4.26%	0.00%	0.00%	0.00%	0.98%	0.39%
14	2.32%	0.32%	0.93%	0.00%	1.24%	0.69%
28	2.40%	0.00%	1.13%	0.00%	0.00%	0.00%

To quantify the “within” and “between” operator’s variability in testing results, repeated measurements were conducted on the concrete beams of mixtures 4, 5, and 6 at age 7 days. The coefficient of variation for the measurements pertinent to UPV and RTG dynamic modulus are presented in Tables 3-5. These results indicate that in almost all cases, the between operator variability in repeated testing is higher than when a single operator has performed the tests. The within operator testing repeatability is of the order of 1.0% for UPV and 0% for RTG dynamic modulus. The corresponding testing repeatability between operators is of the order of less than 2.2% for UPV and 1.0% for RTG dynamic modulus. Similar to the conclusions from the previous mixtures, the segregated samples with higher fluidity (4S-H and 5S-M) show higher variability in results than Sample 6S-L does. Honeycombed specimens have inherently higher non-homogeneity than segregated specimens, and this is reflected as well in the repeatability of the NDT measurements.

Table 3-5. Coefficient of variation of a) UPV, b) dynamic modulus of Mixture 3 and Mixture 4.

(a)

Age (days)	Coefficient of variation in UPV-within operator			Coefficient of variation in UPV-between operators		
	4S	5S	6S	4S	5S	6S
3	0.3%	1.19%	0.46%			
7	1.08%	1.22%	0.54%	2.19%	1.27%	1.12%
28	0.32%	0.99%	0.65%			

(b)

Age (days)	Coefficient of variation in UPV-within operator			Coefficient of variation in UPV-between operators		
	4S	5S	6S	4S	5S	6S
3	0.00%	0.00%	0.00%			
7	0.00%	0.00%	0.00%	0.28%	0.94%	0.10%
28	0.00%	0.00%	0.00%			

3.5. Summary & Conclusions

As mentioned earlier, following the recommendations of a recent national study in developing NDT based QA process for concrete materials, this research investigated whether the proposed NDTs are responsive in detecting the presence of honeycombing and segregation at early ages. These NDTs included UPV, resonant frequency testing, and rebound hammer. In addition to NDTs, chloride permeability test was used to assess the degree of deficiency in the segregated concrete. The overall study findings include:

- Ultrasonic pulse velocity (UPV) is an effective method to detect honeycombing. Overall, pulse velocity was lower in concrete with honeycombing in relation to the control sound concrete. This reflects the presence of large voids in concrete and partially hydrated paste due to improper mixing producing lower density and stiffness. Similarly, RTG is able to detect honeycombing in concrete.
- UPV and rebound hammer are able to detect segregation. UPV and rebound number are highly sensitive to the distribution of coarse aggregate and air voids. Variability in testing results at various locations of a concrete element can be representative of segregation. The variation of UPV within a segregated sample (top vs. bottom) can be as low as 9% in a more mature and less segregated sample, or as high as 27% in a greener and/or higher fluidity concrete mix. Similarly, the difference in rebound number can be in the range of 10% to 38% and reduces through time.

- Comparison of transverse and longitudinal dynamic modulus suggests that the dynamic modulus from the transverse and longitudinal testing mode are almost equal for all three segregated samples, with lower values for sample (6S-L) having the lowest dynamic modulus of elasticity in most cases. Since RFA is evaluating the sample response as a whole, and in converting resonant frequency to dynamic modulus of elasticity (Equation 2 and/or 3), non-uniformity in mass is not considered. Thus, the effect of segregation cannot be very well reflected by this method.
- The increase in UPV, dynamic modulus, and/or rebound number through time reflects the hardening process of concrete, which depending on the mix, presents different rates. This is also associated with the effects of mixing and placement on the strength of the concrete.
- Chloride permeability testing was used to identify level of segregation by means of porosity which is correlated to the level of fluidity (slump). The order of observed segregation is: Sample 4S-H > Sample 5S-M > Sample 6S-L. The difference in chloride permeability and UPV at top and bottom of the samples was in agreement, and to some degree the difference in the observed rebound number results.
- Repeatability of UPV and RTG were within the acceptable levels for almost all cases. The variability of testing results for both “within” and “between” operators were at comparable levels. Overall, the honeycombed specimens have shown higher testing variability compared to sound concrete. In regard to QA, such methods provide acceptable levels of repeatability and in agreement to those levels reported in past studies.

This study provides encouraging results in regard to the potential adoption of UPV, resonant frequency, and rebound hammer in QA and QC of concrete at early ages. While the overall study findings are transferable elsewhere where similar concrete mixtures and testing procedures are used, further steps for adopting such NDTs in QA/QC will require to validate the study findings with: additional concrete mixtures; higher control on production variability, alternative levels of segregation and honeycombing; assess sampling size effects; identify required testing frequencies.

While the focus of this study was on the QA of concrete production rather than in assessing field conditions, the transition from laboratory assessment of the concrete mixtures to field testing in structures will require further investigation since many factors (such as site-specific conditions, presence of moisture, presence of reinforcing steel bars, geometry of the concrete element), will affect the response of such NDT methods. An intermediate transition between laboratory to field conditions could be the use of cores collected from structural elements.

Chapter 4. Delamination and Void detection in Concrete with NDTs

4.1. Introduction

During years of service, the reinforcement in bridge decks or reinforced concrete pavements will corrode if they are not protected from moisture and chlorides (i.e., salt/deicing agents). Corroded steel will expand such that a separation within the depth of the slab is produced. This separation or gap is called delamination. Delamination is a serious form of deterioration in concrete slabs. It can be localized or may extend over a large area. Delaminated areas should be identified and assessed in time to preserve structural capacity. Delamination in concrete slabs is not visible at the surface. Historically, methods such as chain drag and hammer sounding are used to find locations of delamination. Chain drag includes dragging several lengths of heavy chain over the concrete surface. Hammer sounding is tapping on the surface. In both methods, the inspector must identify hollow locations based on the reflected sound. These methods must be performed in a quiet environment, and the results can be biased and dependent on the inspector's hearing ability and training. Therefore, the use of NDT in assessing delamination is strongly recommended to overcome these shortcomings (Malhotra and Carino, 2003; Gucunski et al., 2013).

Clemena and McKeel (1987) used infrared thermography along with chain dragging and hammer sounding on several bridge decks to identify the delaminated areas and found the results very promising. Sansalone and Carino (1989) used impact echo (IE) to detect defects such as delamination in concrete. Impact echo includes striking the surface of the tested object and measuring the response at a nearby location. Gucunski et al. (2013), as part of the State Highway Research Program (SHRP 2), employed a combination of NDTs to detect delamination. Among those NDTs, impact echo, chain dragging and hammer sounding, ultrasonic pulse echo (UPE), infrared thermography (IRT), and ground-penetrating radar showed promising results for detecting delamination.

Delamination in bridge decks can be projected by change in the dielectric constant of the concrete surface (Maser & Rawson, 1992) and/or an increase in the attenuation levels of the signal through depth of the deck (Romero et al., 2000; Goulias et al., 2020). These two phenomena can happen due to presence of excessive moisture and chloride ions in active corrosion in concrete reinforcement (Barnes & Trottier, 2002). Martino et al. (2015) showed that GPR and half-cell potential (HCP) indicated the same areas of deterioration for over 90% of the surface area, while GPR and impact echo agreed in about 80% of cases. That is because GPR is better correlated with half-cell potentials or active corrosion.

In order to evaluate the performance of NDT methods, Maierhofer et al. (2008) employed GPR and UPE tomography on samples with different concrete properties for data fusion. Janku et al. (2019) employed IRT, GPR and UPE to detect delamination in slabs with artificial embedded delamination. Further, Lin et al. (1990) employed finite element analysis to check the responses of thin layers (e.g., concrete structures with steel liners and post-tensioned concrete structures containing thin metal or plastic tendon ducts) containing voids. Lin et al. (2018) employed finite element simulation to evaluate ultrasonic imaging for multi-layer concrete structures. Their result was also confirmed by experimental data from a three-layer structure. Datta and Kishoret (1996) simulated the wave propagation of UPV in isotropic and orthotropic media with or without flaw. They analyzed the sensitivity of harmonics to different types of flaws, wave propagation, and scattering around flaws.

Due to a limited number of studies and evaluations of UPE in detecting delamination, in this study, a concrete slab with two artificial embedded delamination areas was produced and evaluated by rebound hammer, UPE, and GPR. At early ages, rebound hammer testing was coupled with infrared thermography for: (i) monitoring concrete maturity and (ii) developing a blended NDT during curing. A companion cylinder was added to the experimental testing with 2 iButtons for time temperature history monitoring. The results of the study showed that UPE can detect the delaminated area accurately. However, the rebound hammer and GPR methods were less successful in detecting delamination. The main reason was the high quality of the concrete around the delaminated area, while in a delaminated bridge deck, corrosion would degrade the quality of the concrete in that area.

Simulation is a significant design tool that can be used to improve engineering practices. The simulation can empower engineers to evaluate and assess the reliability of the design or quality. The advantages of employing finite element simulation in engineering practices include: (1) producing a much more detailed set of results than experimental investigations in a faster manner, (2) saving time and energy associated with making prototypes before construction, (3) reducing the costs associated with experimental investigation and human error. However, to rely on simulation results can be misleading. Therefore, in this study, a combination of experimental and numerical analyses was performed to assess the reliability of UPE in detecting delamination.

4.2. Background & Literature Review on the NDTs

A summary of the principles and operation of each NDT used in this study is provided in the following subsections.

4.2.1. Ground Penetrating Radar (GPR)

Ground penetrating radar (GPR) employs electromagnetic waves to detect layer thickness, material quality, presence of rebar, and any abnormality beneath the surface (Figure 4.1). The GPR transmitter antenna emits electromagnetic waves in the microwave band through materials and layers. The reflection signal is received by the same antenna in a monostatic system, or by a receiver antenna in a bi-static system. A change in dielectric constant of material during propagation and reflection is a sign of variation in the homogeneity of the material (Lahouar et al., 2002), materials with different dielectric properties (e.g., asphalt, concrete, rebars), and/or the presence of defects (e.g., voids, cracking, delamination in concrete). The antennas are transducers that convert electrical current into electromagnetic waves that propagate in the medium and vice versa: converting the electromagnetic wave into electrical impulses. Further details on data pre-processing and processing are presented in Chapter 5.

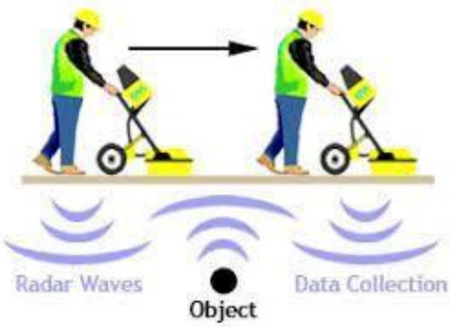

Figure 4.1. Ground penetrating radar and electromagnetic wave transmission and reflection in a GPR survey (Worksmart, Inc.).

4.2.2. Ultrasonic Pulse Echo (UPE)

In a manner similar to UPV, ultrasonic pulse echo (UPE) employs ultrasonic (acoustic) stress waves to detect objects, interfaces, and anomalies (Figure 4.2b & c). In a conventional pulse-echo method, a stress pulse is introduced by a transmitter into an object from an accessible surface. The transmitted pulse into the test object is reflected by flaws or interfaces. The surface response caused by the arrival of reflected waves, or echoes, is received by either the transmitter acting as a receiver (in a true pulse-echo method) or by a second transducer located near the pulse source (in a pitch–catch method). The receiver output is displayed on a time-domain waveform display device.

The behavior of stress waves such as P-Wave or S-Wave is very similar to that of light waves. When a light wave is incident on a boundary between dissimilar media, reflection and refraction happens. An example of reflection and refraction of a P-wave is shown in Figure 4.3. In this case, the angle of refraction, β, is a function of the incident angle, θ, and the ratio of wave speed in different materials, C_2/C_1, (see Equation 4-1 known as Snell's law).

$$\sin\beta = \frac{C_2}{C_1}\sin\theta \tag{4-1}$$

However, in case of the stress waves, the mode of propagation can be changed as well when striking a boundary at an oblique angle (see Figure 4.3b). The relative amplitudes of reflected waves depend on the discrepancy in specific acoustic impedances at the interface, the angle of incidence, the distance of an interface from the pulse source, and attenuation along the wave path. Further details can be found in Malhotra and Carino (2003).

UPE employs a synthetic aperture focusing technique (SAFT). The SAFT is often used in active imaging systems (e.g., radar) with measurements taken in several positions and then combined to obtain a synthetic aperture. Nine sensors on one side act as transmitters, while the other nine sensors act as receivers. Advantages of UPE over UPV include a) UPE can be used when the structural element (concrete element) is accessible only from one side, b) low-frequency transducers (50 – 200 kHz) can be employed to overcome high scattering of the transmitted pulses, c) no coupling agent is needed between the transducer and the surface of the element. UPE can be used for thickness measurement, flaw detection, and integrity testing of piles (Malhotra and Carino, 2003). In a system where the transmitter and transducer are one unit, round-trip travel time can be used to measure the velocity of wave propagation (Equation 4-2).

$$L = \frac{1}{2} \Delta t \, V_p \qquad (4\text{-}2)$$

where V_p is the P-wave velocity in concrete, L is the depth, and Δt is the round-trip travel time. However, the UPE used in this study (Figure 4.2), emits shear waves (S-waves), whose velocity is proportional to P-wave velocity by α, shown in Equation 4-3.

$$\alpha = \frac{V_s}{V_p} = \sqrt{\frac{(1-2\upsilon)}{2(1-\upsilon)}} \qquad (4\text{-}3)$$

where V_s and V_p are S-wave and P-wave velocity (m/s), respectively, and υ is Poisson's ratio. For Poisson's ratio of 0.2, α is 0.61.

Kozlov et al. (1997) used ultrasonic echo for thickness measurement and flaw detection in concrete with one-side access. They showed the possibility of receiving a concrete cross section at depths of up to one meter and to detect hollow defects with diameters of more than 50 mm. Janku et al. (2019) employed UPE, IRT, and GPR to detect delamination in laboratory-made slabs. IRT was only used for identifying the location of the delaminated parts, while 2 GPRs, and pulse echo were employed to measure the depth of the delamination. UPE was not very successful in detecting small delamination with shallow depths. While the accuracy of GPRs was about 1 mm to 5 mm, the measured depth by UPE could be twice the real depth.

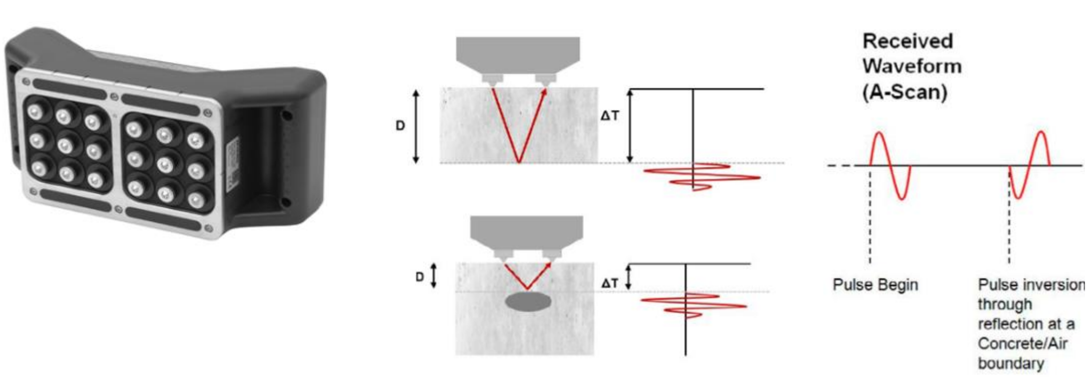
D
ΔT
D
ΔT
Received
Waveform
(A-Scan)
Pulse Begin
Pulse inversion
through
reflection at a
Concrete/Air
boundary

(a) (b) (c)

Figure 4.2. Ultrasonic pulse echo (UPE), a) measurement unit, b) detecting a void at depth D (Misak et al., 2019), c) pulse inversion at a boundary (Pundit 2 operation instruction, 2017).

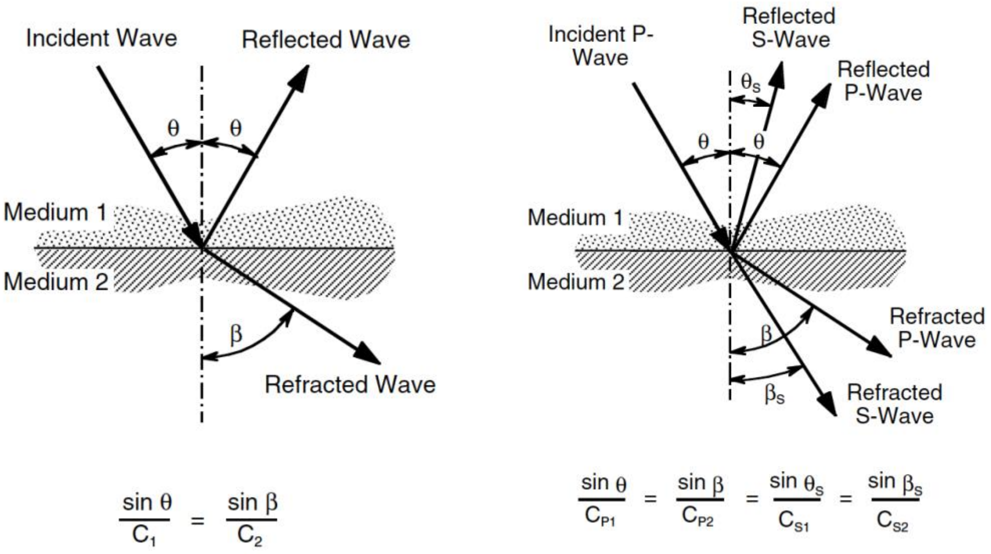
Incident Wave
Reflected Wave
θ
θ
Medium 1
Medium 2
β
Refracted Wave
sin θ / C1 = sin β / C2
Incident P-Wave
Reflected S-Wave
θS
Reflected P-Wave
θ
θ
Medium 1
Medium 2
Refracted P-Wave
β
βS
Refracted S-Wave
sin θ / CP1 = sin β / CP2 = sin θS / CS1 = sin βS / CS2

(a) Reflection and refraction **(b) Mode conversion**

Figure 4.3. The behavior of a P-wave incident on an interface between two dissimilar media: a) reflection and refraction, b) mode conversion (Malhotra & Carino, 2003).

4.3. Materials & Methods

4.3.1. Materials

The selected concrete represents a typical mixture used in building construction and highway applications in Maryland and the surrounding regions. The mix proportions and properties are presented in Table 4-1.

Table 4-1. Mix proportions and mix properties.

Material	Cement (Kg/m^3)	Coarse Aggregate (#57) (SSD in Kg/m^3)	Fine Aggregate (SSD in Kg/m^3)	Water-Cement Ratio (Kg/m^3)	W_{AEA}/W_{cement}	W_{HRWR}/W_{cement}	28-day Compressive Strength (MPa)
	378	1013	730	0.45	0.4%	0.24%	24

[1] SSD=Saturated surface dry
[2] AEA=Air entraining admixture
[3] HRWR=High range water reducer

In selecting the material for making sheets and embedding them as artificial delamination in the concrete slab, two main factors should be considered: (1) the material should have a dielectric constant lower than concrete's dielectric constant ($\varepsilon_r = 5\ to\ 10$), and closer to the dielectric constant of air (i.e., $\varepsilon_r = 1$); (2) the material should not absorb water and be sturdy enough to resist the load of poured concrete. Considering these two factors, plexiglass was selected to be used as the material (dielectric constant = 3.4). In an initial study, a small piece of plexiglass was embedded in a concrete beam with dimensions of $150\,mm \times 150\,mm \times 530\,mm$ ($6\,in \times 6\,in \times 21\,in$), shown in Figure 4.4. This beam was tested with UPV in direct and semi-direct configuration of transducers as explained in Chapter 2. In the direct mode, UPV transducers were placed at two sides of the beam with the delaminated area in the middle. In this method, transmission velocity is expected to be lower when delamination is present. Therefore, the transmission time and distance (width of the beam) were measured every 5 cm (2 in.) to find the location of the delaminated area. The location of each measurement is shown with the arrows in Figure 4.5a. Each measurement was repeated three times. In the semi-direct method, one transducer is placed at one side and the other one is on the adjacent side and moved away at 5cm intervals. In this case, the distance between the transducers is the direct distance which is calculated from the Pythagorean theorem. Each measurement was repeated from the other side, as well. Figure 4.2b shows the location of the transducers. The velocity of wave propagation is expected to be constant for all locations unless there is an obstruction in the material (e.g., delamination). The ability of UPV in detecting delamination based on the results and analysis of this study are presented in section 4.3 "Results & Discussion".

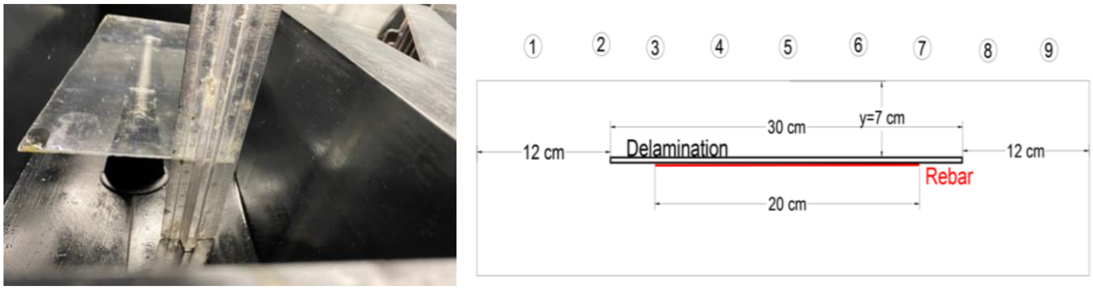

(a) **(b)**

Figure 4.4. Delamination in concrete beam, a) formwork and artificial delamination, b) dimension of beam and location of delamination.

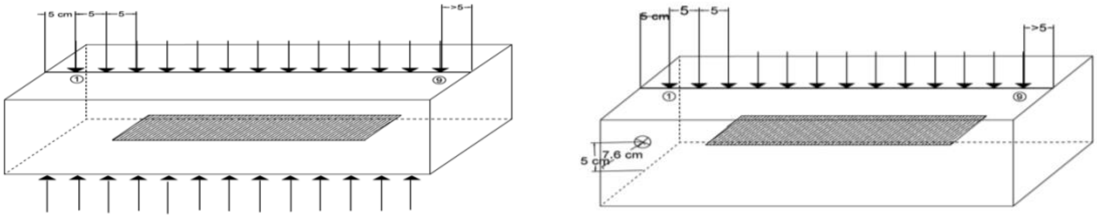

(a) **(b)**

Figure 4.5. UPV measurements on delaminated beam, a) direct method, b) semi-direct method.

4.3.2. Dimensions of Samples & Materials

To assess the accuracy and precision of NDT in detecting delamination, a 1020 mm (length) × 610 mm (width) × 130 mm (depth) concrete slab was cast in the laboratory. Figure 4.6 shows the plan view of the slab with metal mesh and delaminated areas and dimensions. To simulate delamination, two plexiglass sheets with 2.3 mm thickness at depth of 9 cm were used (Figure 4.6). The objectives of using two sheets were assessing the sensitivity of the NDTs to the delamination dimension and assessing whether NDTs will be able to differentiate well between the two delaminated areas. Two wood strips were used to support the wire mesh and plexiglass in place. Figure 4.7 shows the formwork and finished slab. For collecting the NDT measurements and assessing repeatability, 2 cm grids in “X” direction and 10 cm grids in “Y” direction were identified.

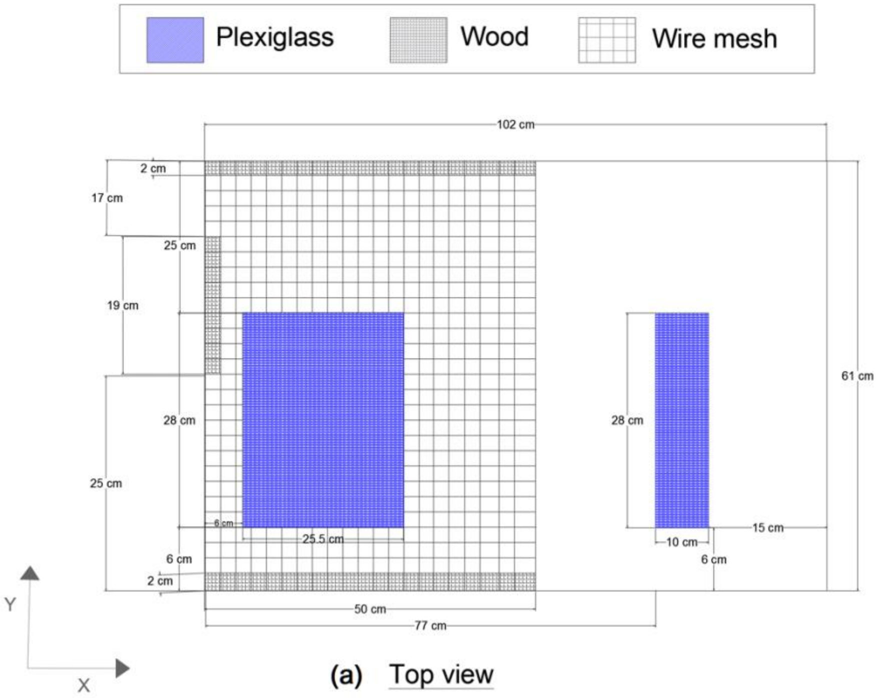
Plexiglass
Wood
Wire mesh
102 cm
2 cm
17 cm
25 cm
19 cm
28 cm
25 cm
6 cm
25.5 cm
6 cm
2 cm
28 cm
10 cm
15 cm
6 cm
61 cm
50 cm
77 cm
Y
X

(a) Top view

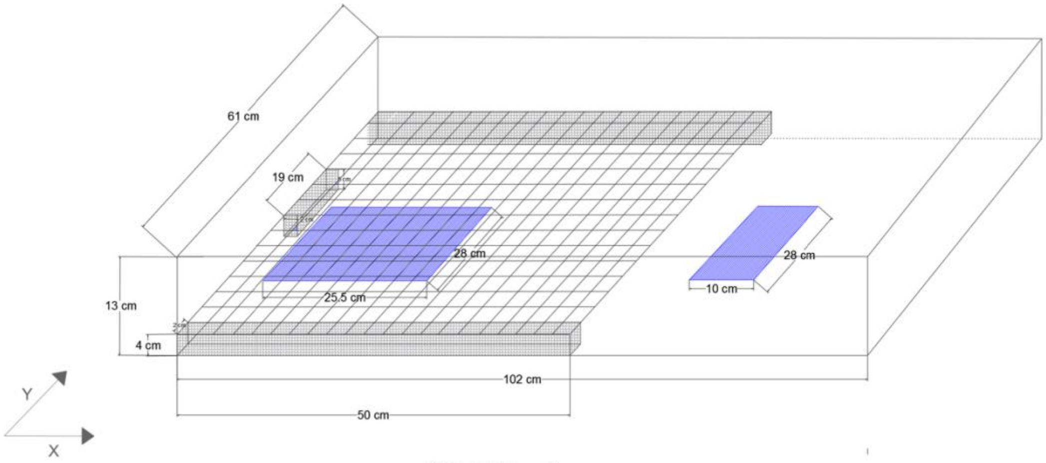
61 cm
19 cm
28 cm
25.5 cm
28 cm
10 cm
13 cm
4 cm
102 cm
50 cm
Y
X

(b) Side view

Figure 4.6. Concrete slab with embedded plexiglasses, a) top view, b) side view.

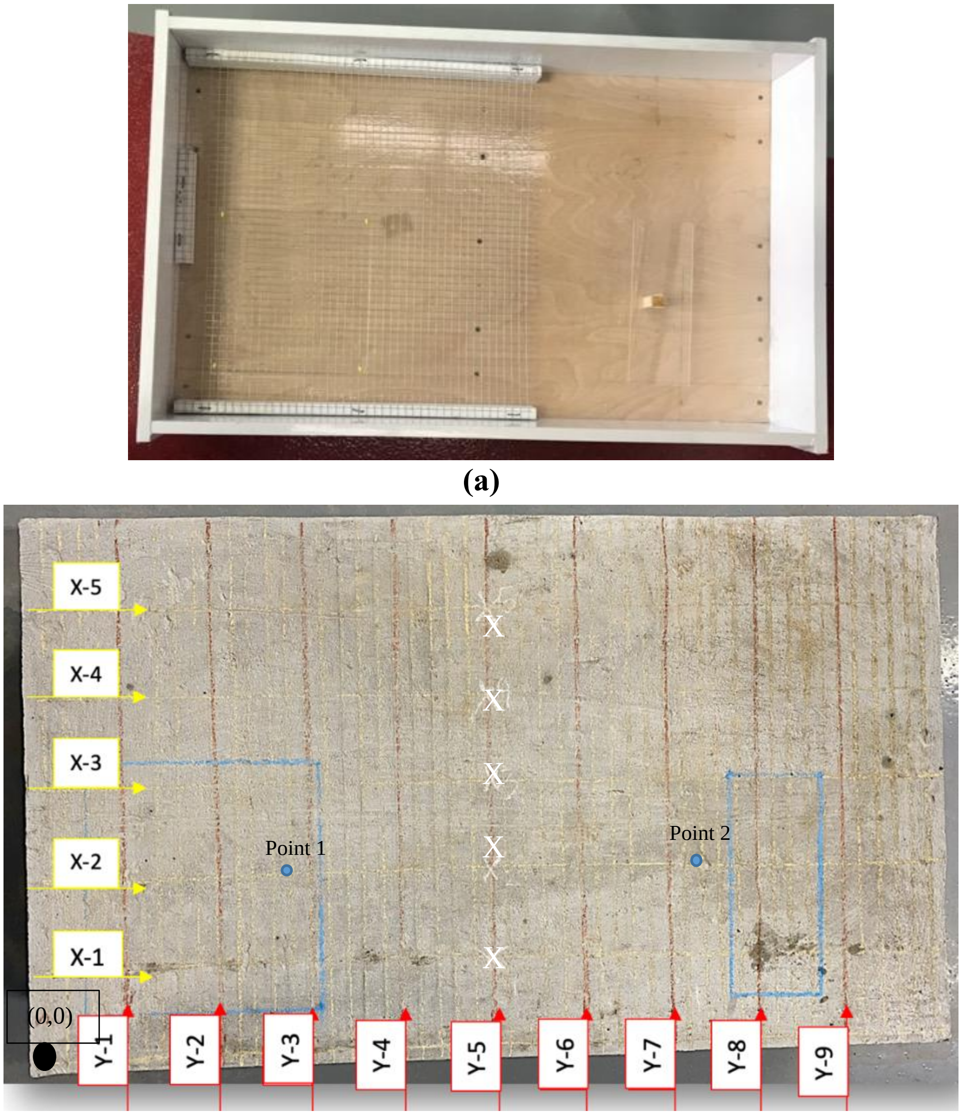

(a)

(b)

Figure 4.7. Concrete slab, a) formwork, b) finished product.

Note: the origin (0,0) is shown as a black dot.

4.3.3. Monitoring the Strength Gain

In order to monitor the curing process and 28-day compressive strength of the concrete, a companion cylinder was cast. The slab was cured in field conditions. To simulate the curing in field conditions, the cylinder was kept in water for 7 days, and then removed from water and cured at room temperature for another 21 days. Two thermocouples (iButtons) were embedded in the cylinder and the temperatures of the cylinder and the slab were checked regularly with an infrared camera to ensure adequate curing. At ages of 1, 2, 3, 7, and 28 days, the cylinder was tested with ultrasonic pulse velocity (UPV). The cylinder was tested with the rebound hammer at ages of 3, 7, and 28 days and then tested for destructive compressive strength.

4.3.4. NDT on Concrete Slab

For testing the concrete slab with UPE, a horizontal grid with a distance of 2 cm (X direction), and another grid (Y direction) with a distance of 10 cm were specified. The UPE manufacturer recommendations and past studies suggested measurements at every 10 cm for detecting delamination, and at 2 cm intervals for thickness detection (Proceq Manual). Considering the dimension of the specimen, both 10 cm and 2 cm increments through the x-axis direction were considered for comparative analysis. UPE measurements were collected during curing (i.e., 1, 2, 3, 7 days), at 28 days and at 60 days to account for hardening and the effects of moisture.

At every measurement location, UPE reports the two-way travel time of the shear wave through concrete. Shear wave velocity is calculated based on the relationship between compressive wave and shear wave velocity. Their relationship is described in Equation 4-3.

The Quantum mini-dual frequency GPR unit was used in this study in detecting concrete slab delamination. This GPR unit features a 1000 MHz antenna for analyzing structures as deep as 1800 mm (72 in), as well as a 2000 MHz antenna for high resolution with fine analysis of shallow targets. For this study, the 2000 MHz antenna was used due to the scale of the slab. The GPR was moved through lines 1 to 4 in the direction of the X-axis (Figure 4.4b). UPE and GPR testing on the concrete slab are shown in Figure 4.8. In conducting non-destructive testing, care should be taken in avoiding edges, since the reflections from side walls would interfere with reflections from the back wall. Therefore, a margin of at least 2 cm (0.8 in.) was considered from the slab edges.

Two different rebound hammers were used to test the hardness of the slab, i.e., Proceq and Humbolt. These two rebound hammers were applied at the intersection of each grid, spaced at 10 cm through the X and Y-axes. This procedure was repeated three times at each location at the age of 28 days.

(a) **(b)**

Figure 4.8. NDT on concrete slab, a) ultrasonic pulse echo (UPE), b) ground penetrating radar (GPR).

4.3.5. Theory of Lamb Waves and Finite Element Method (FEM)

Because of the implementation of UPE wave propagation in simulation and analysis, the theory of the Lamb waves is reviewed in this section.

Lamb waves propagate in solid surfaces. Lamb waves, also known as plate waves, can exist in a thin plate-like medium, directed by free upper and lower surfaces. The entry angle, frequency, and structural geometry can affect their propagation characteristics. Lamb waves, in thin, isotropic, and homogeneous plates, regardless of the mode, can generally be described in a form of Cartesian tensor notation as (Su & Ye, 2009; Marković et al., 2018):

$$\mu . u_{i,jj} + (\lambda + \mu) . u_{j,ji} + \rho . f_i = \rho . \ddot{u}_i \qquad i,j = 1,2,3 \qquad \text{(4-4)}$$

where u_i is the displacement, f_i is the and body force, ρ is density, μ is the shear modulus of the plate, and λ is Lamb constant. Equation 4-4 can be decomposed into two equations uncoupled parts by applying Helmholtz decomposition under plane strain condition (see Equation 4-5a and Equation 4-5b).

$$\frac{\partial^2 \Phi}{\partial x_1^2} + \frac{\partial^2 \Phi}{\partial x_3^2} = \frac{1}{s_L^2} \frac{\partial^2 \Phi}{\partial t^2} \qquad \text{(Governing longitudinal wave modes)} \qquad \text{(4-5a)}$$

$$\frac{\partial^2 \Psi}{\partial x_1^2} + \frac{\partial^2 \Psi}{\partial x_3^2} = \frac{1}{s_S^2} \frac{\partial^2 \Psi}{\partial t^2} \qquad \text{(Governing longitudinal wave modes)} \qquad \text{(4-5b)}$$

where:

$$\Phi = [A_1 \sin(px_3) + A_2 \cos(px_3)] . \exp[i(kx_1 - \omega t)] \qquad \text{(4-6a)}$$

$$\Psi = [B_1 \sin(qx_3) + B_2 \cos(qx_3)] . \exp[i(kx_1 - \omega t)] \qquad \text{(4-6b)}$$

$$p^2 = \frac{\omega^2}{c_L^2} - k^2, \; q^2 = \frac{\omega^2}{c_T^2} - k^2, \; k = \frac{2\pi}{\lambda_{wave}} \qquad \text{(4-6c)}$$

with the following designation: A_1, A_2, B_1, B_2 are four constants determined by the boundary condition, k is the wave number, ω is circular frequency and λ_{wave} is the wavelength of the wave. Longitudinal velocity c_L and transverse (shear) velocity c_S are defined by:

$$c_L = \sqrt{\frac{E(1-\upsilon)}{\rho(1+\upsilon)(1+2\upsilon)}} = \sqrt{\frac{2\mu(1-\upsilon)}{\rho(1-2\upsilon)}} \qquad \text{(4-7)}$$

$$c_S = \sqrt{\frac{E}{2\rho(1+\upsilon)}} = \sqrt{\frac{\mu}{\rho}} \qquad \text{(4-8)}$$

In plane strain condition, the displacement in the wave propagation direction (x_1) and normal direction (x_2) can be described as:

$$u_1 = \frac{\partial \Phi}{\partial x_1} + \frac{\partial \Psi}{\partial x_3} \qquad \text{(4-9a)}$$

$$u_2 = 0 \qquad \text{(4-9b)}$$

$$u_3 = \frac{\partial \Phi}{\partial x_3} - \frac{\partial \Psi}{\partial x_1} \quad \text{(4-9c)}$$

However, the conditions which correspond to the propagation of lamb waves are:

$$u(x,t) = u_0(x,t), \quad t_i = \sigma_{ji} n_j\,, \quad \sigma_{31} = \sigma_{33} = 0 \text{ at } x_3 = \pm\frac{d}{2} = \pm h \quad \text{(4-10)}$$

where d is the plate thickness, and h is the half plate thickness. After applying the boundary condition (i.e., Equation 4-8) to Equation 4-9, the general description of Lamb waves in an isotropic and homogeneous plate are obtained as:

$$\frac{tantan\,(qh)}{tantan\,(ph)} = \frac{4k^2 qp\mu}{(\lambda k^2 + \lambda p^2 + 2\mu p^2)(k^2 - q^2)} \quad \text{(4-11)}$$

Applying Equation 4-6c, 4-7, and 4-8 into the Equation 4-11, and considering that trigonometric function tangent is defined with “sine” and “cosine” which have symmetric and anti-symmetric properties, respectively. Equation 4-11 can be split into two parts with uniquely symmetric and anti-symmetric characteristics, respectively. The symmetric and antisymmetric modes of the Lamb wave in a plate are:

$$\frac{tantan\,(qh)}{tantan\,(ph)} = -\frac{4k^2 qp}{(k^2 - q^2)^2} \quad \text{for symmetric modes} \quad \text{(4-12a)}$$

$$\frac{tantan\,(qh)}{tantan\,(ph)} = -\frac{(k^2 - q^2)^2}{4k^2 qp} \quad \text{for antisymmetric modes} \quad \text{(4-12b)}$$

Equations 4-12a and 4-12b are known as the Reyleigh-Lamb equations.

The finite element method includes discretization of the area into finite elements. The element’s displacement values are defined based on their nodal values from the shape functions of the selected element (Datta & Kishore, 1996). Depending on the problem, i.e., whether it is time-dependent or time-independent, two forms of finite element methods are defined. For the former state, the explicit type of finite element method is used, while for the latter, the implicit finite element is employed. In this study, the dynamic explicit form of finite element was used since the effect of acceleration of Lamb wave propagation is pronounced and cannot be neglected. The relationship between body force (*F*) and acceleration (*A*) is defined by Newton’s second law in matrix form:

$$F = M.A \quad \text{(4-13)}$$

where, *M* is the mass matrix. The parameters in Equation 4-10 can be expressed as following:

$$F_i^m = -\int_\Omega \left(\sigma_{ij} \Phi_{M,j}\right) d\Omega + \int_\Omega f_i \Phi_M d\Omega + \int_{\Gamma_S} g_i \Phi_M d\Gamma_S \quad \text{(4-14a)}$$

$$M_{MN} = \int_{\Omega} (\rho \Phi_M \Phi_N) d\Omega \tag{4-14b}$$

$$A_i^N = \ddot{u}_i^N(t) \tag{4-14c}$$

where F_i^m is body force, σ_{ij} is the stress, Φ_M and Φ_N are base functions, f_i represents the component of the body force, g_i represents the components of the tractions on part of the boundary Γ_S, M_{MN} is the mass matrix, ρ is the mass density, $\ddot{u}_i^N$ is the second derivative of displacement, u, A_i^N is the acceleration, t is the time, Ω is the space domain, Γ_S is the boundary domain (Wu & Gu, 2012). The equations defined in Equation 4-14 (a, b, c) are a system of second-order ordinary differential equations in time, whether linear or nonlinear. For solving this system in explicit form, a central difference method is used to approximate the acceleration, velocity, and displacement. These, as time derivatives, are approximated by the finite difference method, expressed in vector form as:

$$\begin{cases} \partial_t u_{n+1/2}^h = (u_{n+1}^h - u_n^h)/\Delta t \approx \dot{u}_{n+1/2}^h \\ \partial_{t^2} u_n^h = (\partial_t u_{n+\frac{1}{2}}^h - \partial_t u_{n-\frac{1}{2}}^h)/\Delta t = (u_{n+1}^h - 2u_n^h + u_{n-1}^h)/\Delta t^2 \\ \ddot{u}_n^h \approx (\dot{u}_{n+1/2}^h - \dot{u}_{n-1/2}^h)/\Delta t \end{cases} \tag{4-15}$$

$$\begin{cases} \partial_t u_{n+1/2}^h = \partial_t u_{n-1/2}^h + \partial_{t^2} u_n^h \Delta t \\ u_{n+1}^h = u_n^h + \partial_t u_{n+1/2}^h \Delta t \end{cases} \tag{4-16}$$

where u is displacement, $\dot{u}$ and $\ddot{u}$ are velocity and acceleration, respectively, Δt is time intervals from total time (T) equally divided to N subintervals (i.e., T/N or $t_{n+1} - t_n$).

Dynamic finite element modeling in 3D ABAQUS was developed for the slab with the geometry described in Section 4.2.2 and Figure 4.6 to simulate the UPE testing with lamb wave propagation in the delaminated area. It should be noted that the plexiglass was considered as embedded in concrete (Figure 4.9). To apply load, there are two methods: load control and displacement control conditions. The disadvantage of the load control condition is stress concentration which leads to response divergence. Therefore, in this study, the displacement control condition was used, and a harmonic unit load was applied based on the location of the sensor, as presented in Figure 4.10. The responses at two points, the first one at x=28 cm and y= 20 cm (i.e., Point 1), and the second one at x=72, and y=20 cm (Point 2). In addition, the applied load history is also shown in Figure 4.11. In these analyses, the wave propagation when the center of the UPE is placed on top of a delaminated area (Point 1) and when the smaller delamination is partially covered under the UPE (Point 2) are compared with the experimental results.

In this simulation concrete is assumed to be a linear-elastic material with characteristics described in Table 4-2. This table also includes the material characteristics of the plexiglass used as delamination.

Table 4-2. Concrete and plexiglass mechanical properties

Concrete			
Compressive strength	Modulus of elasticity	Poisson's ratio	Density
2400 N/cm^2 (3480 psi)	2302500 N/cm^2 (3340 ksi)	0.15	0.0024 kg/cm^3 (0.09 lb/in^3)
Plexiglass			
Tensile strength	Modulus of elasticity	Poisson's ratio	Density
7142.37 N/cm^2 (10360 psi)	310344.72 N/cm^2 450 ksi	0.35	0.0012 kg/cm^3 (0.04 lb/in^3)

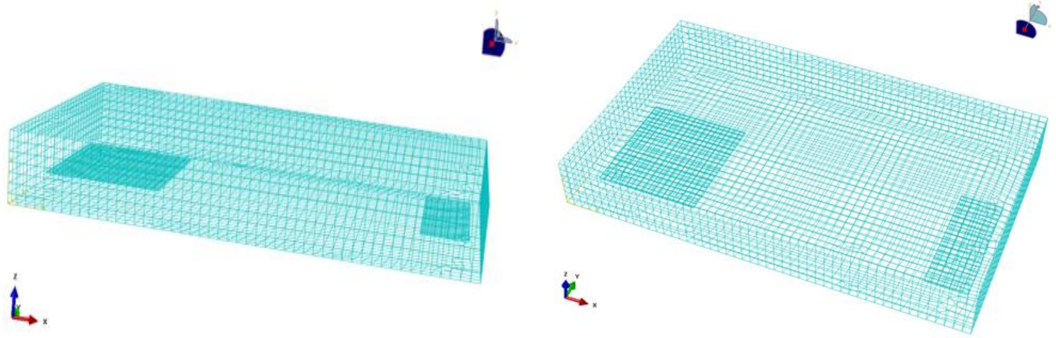

Figure 4.9. Different views of discretized (meshed) slab with embedded plexiglasses in ABAQUS

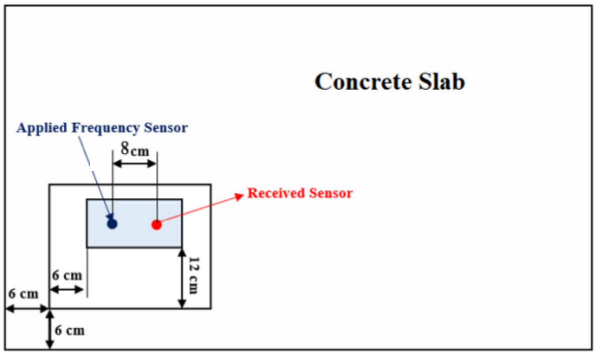
Concrete Slab
Applied Frequency Sensor
8cm
Received Sensor
12 cm
6 cm
6 cm
6 cm

(a) Top view

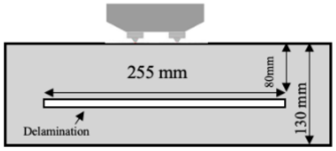
255 mm
80mm
130 mm
Delamination

(b) Side view

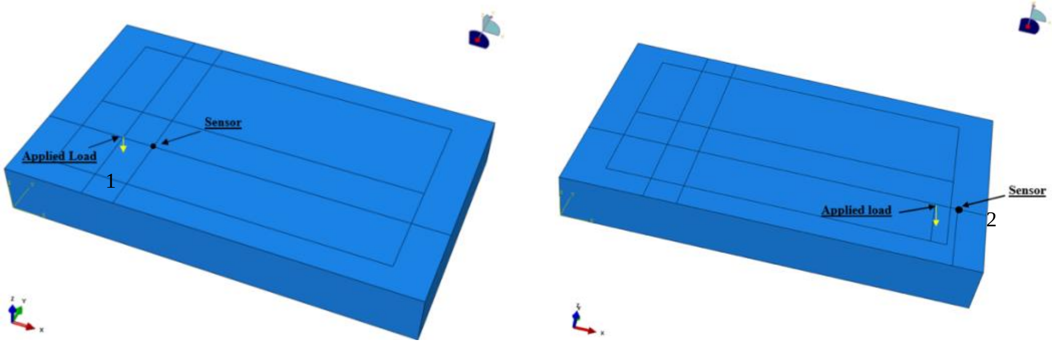

(c) Location of applied load (Point 1 and Point 2)

Figure 4.10. Schematic of position of the sensors and the load during finite element analysis.

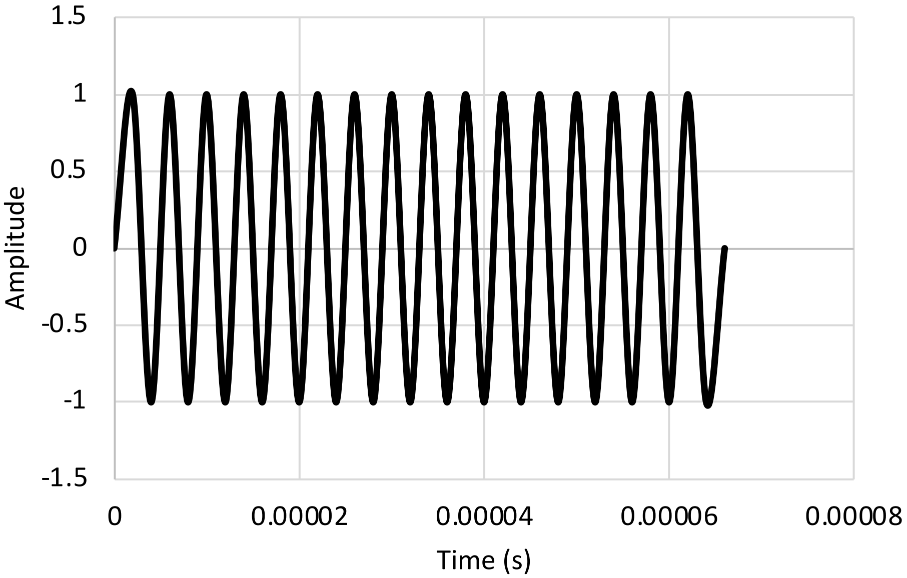

Figure 4.11. Input unit pulse

4.4 Results & Discussion

4.4.1. Detecting Delamination with Ultrasonic Pulse Velocity

The direct UPV testing was repeated three times on the beam sample $(150\,mm \times 150\,mm \times 530\,mm)$ at 5 cm intervals and average velocity at each location shown in Figure 4.12a. In this figure, the true location of the delamination and the estimated ones are shown by solid and dashed lines, respectively. Based on UPV measurements, the velocity starts to decrease at 10 cm from the edge of the beam and starts to increase again at about the 45 cm mark, while in reality, as shown in Figure 4.4b, the delamination starts at 12 cm from the edge and continues for 30 cm. In the semi-direct measurements, the results of measuring pulse velocity from right-to-left is plotted in along with left-to-right direction in Figure 4.12b. The measurements are dependent on position of the transducers, so the variation in these measurements is expected since the delamination changes the wave propagation in a non-uniform way. In calculating the extent of the delamination in this method, the velocity is constant while there is no delamination or anomaly in the concrete. In Figure 4-12b, the UPVs measured at sound areas (point 1 to 2, and 9 to 10) start to decline after point 2, and before point 9. Thus, these locations can be considered as the start and end of the delamination. With this method the estimated length of the delaminated area is 35 cm in length, starting at 10 cm distance from the edge. This is only a rough estimate; for more accurate estimation the measurements should be repeated between these points and their preceding or next point, depending on their location. For example, the measurements can be repeated between x=10 cm and x=15 cm at 1 cm increments, and between x=40 cm and x=45 cm at 1 cm increments.

Comparing the extent and the location of the delamination in Figures 4.12a, and 4.12b shows only a few centimeters difference in estimation. These values show that UPV can give a good estimate of the location and extent of the delamination.

In addition to direct and semi-direct measurements, the indirect method, where both transducers are located on the same surface, was also employed to find the depth of the delamination. Even though the minimum distance of 10 cm (4 in) between transducers was compiled, only the surface wave was detected, and the surface wave's (Rayleigh waves) velocity was measured. Therefore, for cases where the concrete element is only accessible from one side, such as concrete slabs in pavements or bridge decks, use of ultrasonic pulse echo is suggested.

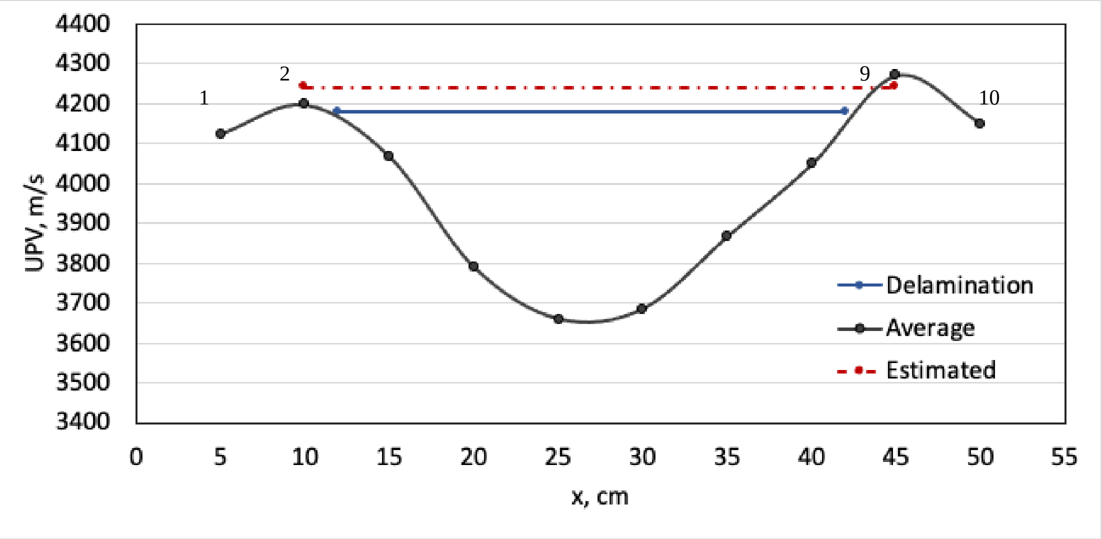

(a)

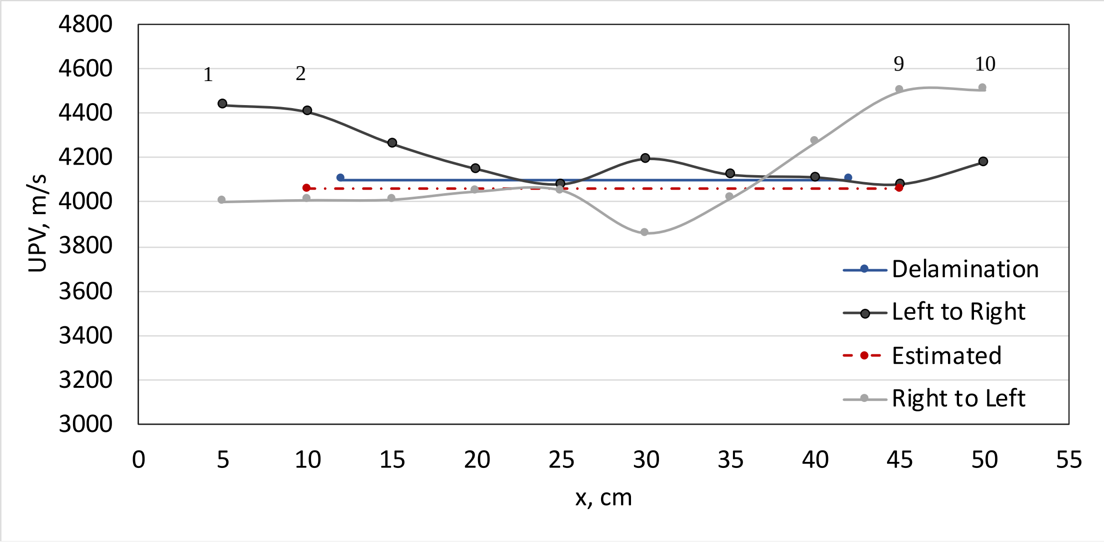

(b)

Figure 4.12. Determining the location of delamination with UPV, a) direct measurement, b) semi-direct measurement.

4.4.2. Monitoring Maturity and Strength Gain of Concrete

Figure 4.13 presents the average temperature-time history of concrete measured by the embedded iButtons in the accompanying cylinder. Table 4-3 shows the temperature of the water bath in which the cylinder was cured, the temperature of the cylinder at top, middle, and bottom, and the temperature at 5 points in the surface of the slab, all measured with IRT. These 5 points are the intersections of line number 5 on the x-axis with 5 lines parallel to y-axis (Figure 4.7). The last column of Table 4-3 shows the difference between the surface temperature of the cylinder and the slab, with the slab having a higher average temperature. It seems that the difference between temperatures is minimal when the concrete surface is dry (at age 28 days). The objective of curing slabs and companion cylinders in the same or similar conditions is so that the data collected from the cylinder are transferable to those from the slab. It is perceived that any two samples made from the same mix, and compacted and cured in a similar way, should have similar properties such as wave propagation velocity and strength. The Maturity index (temperature-time factor) was calculated with Equation 2-6 and the results are shown in Figure 4.14. The maturity index from the iButton and the infrared thermography camera are in good agreement for the cylinder, which confirms the accuracy of IRT in assessing concrete temperature.

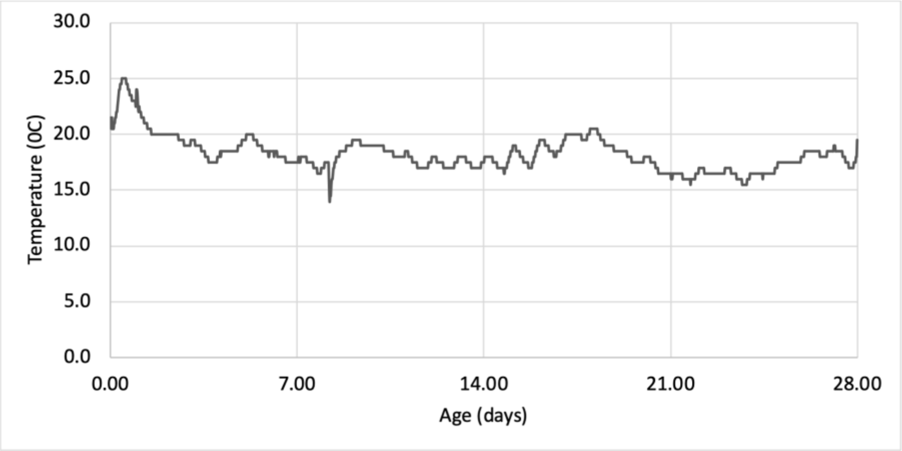

Figure 4.13. Temperature history of concrete cylinder by iButton during hydration

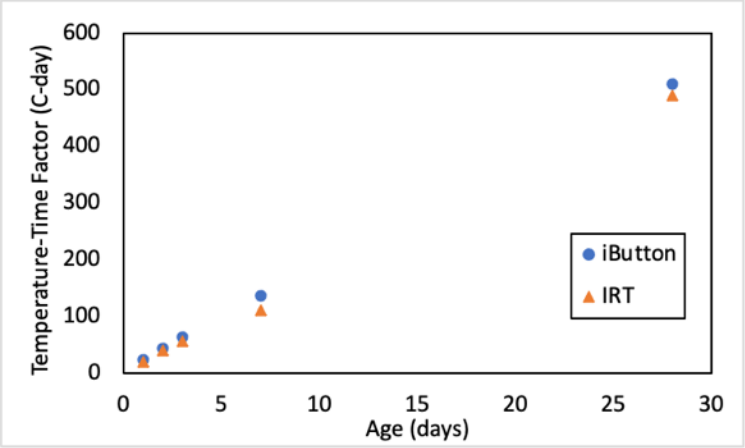

Figure 4.14. Maturity index of concrete from iButton sensors and infrared thermography (IRT) on the cylinder

Table 4-3. Temperature of the slab, cylinder, cylinder submerging water measured by IRT.

	Temperature (^{0}C)											
Age	Water	Cylinder			Average	Slab					Average	Difference
		Top	Mid	Bot		1	2	3	4	5		
1	21.1	22.5	22.8	22.9	22.7	22.5	23.9	24.4	25	24.5	24.06	1.3
2	19.6	18.9	18.8	19	18.9	22	22	21.1	21.5	21.5	21.62	2.7
3	17.6	18.3	18.6	18.5	18.5	19	19.8	20.5	20.8	20.8	20.18	1.7
4	16.9	17.6	17.9	17.6	17.7	19.5	19.2	19.2	19.1	19.3	19.26	1.6
5	18.3	19.1	19.1	19.5	19.2	20.4	20.8	20.4	20.5	20.7	20.56	1.3
6	16.5	17.3	17.4	17.6	17.4	19.6	19.5	19.6	19.5	19.5	19.54	2.1
7	16.5	16.9	16.6	17	16.8	18.8	18.8	18.7	18.6	18.8	18.74	1.9
28	-	17.7	17.7	17.6	17.7	17.3	17.4	17.7	18.4	18.2	17.8	0.1

The UPV testing results for the cylinder at ages of 1, 2, 3, 7, and 28 days are presented in Table 4-4, while Figure 4.15 presents the relationship between UPV and the temperature-time factor. At ages 3, 7, and 28 days the concrete cylinder was also tested with the rebound hammer and the results are shown in Table 4-5. As expected, for the first week of curing, the UPV and rebound number are increasing with increase in age of the concrete. At 28 days the concrete was dry, which led to a slight decrease in UPV at the age of 28 days. The results of maturity and UPV and rebound number are in agreement with the findings of Chapter 2.

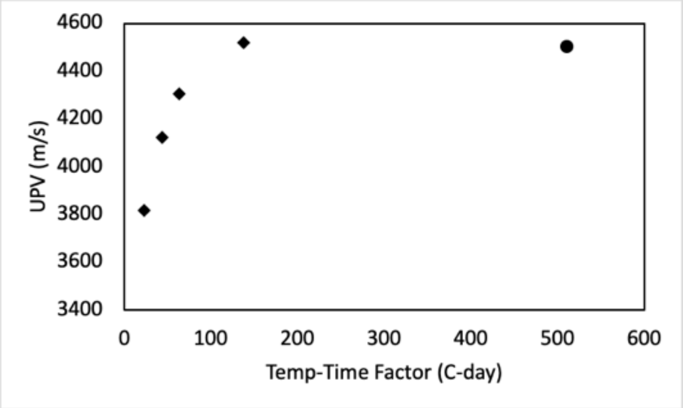

Figure 4.15. Relationship between UPV and temp-time factor

Table 4-4. Compressive and shear wave velocity of concrete

Age (days)	Compressive wave velocity from UPV-on the cylinder (m/s)
1	3815.8
2	4124.3
3	4306.3
7	4521.2
28	4505.1

Table 4-5. Rebound hammer and compressive strength on the cylinder.

Age	Rebound number (avg.)	Coefficient of variation	Compressive Strength (MPa)
3	20.5	7.1%	NA
7	26.2	7.9%	NA
28	41.3	11.9%	23.81

4.4.3. UPE

By plotting the two-way travel time of shear wave (in μs) for each location, an area-scan of the slab can be obtained. Figure 4.16 shows the area-scan of the slab, after removing outliers at edges, at ages 1, 2, 3 and 7 days. At these ages, the data (two-way travel times) were collected at every 10 cm. As mentioned earlier, this increment is suggested by the manufacturer for detecting delamination. The black rectangles in the figure are added to show the location of the actual delamination and the orange rectangles show the location of the wood strips. As can be seen, by comparing the results at different ages, the presence of surface moisture affects the response of UPE. However, the regions of sound concrete locations (i.e., no delamination) corresponding to higher travel times (see Figure 4.2) can be identified, with some scatter.

Figure 4.17 shows the area-scan at ages 28 and 60 days with 2 cm and 10 cm intervals of the UPE measurements. It should be noted that, due to the dimension of the UPE apparatus, the first value (0,0) in the A-scan is measured at 6 cm from the edge of the slab. Even though the slab is not completely dry after 28 and/or 60 days, the surface-dry condition has provided improved results relative to the earlier ages. Figure 4.17 also shows how the resolution of the area-scan is affected by reducing the measurement increments. However, in all cases the dimensions of the wood strips shown in the results are higher than their actual dimensions. The reason is that the dimension of the wood strips (2 cm) is less than the UPE measurement increments. This implies that the measurement intervals should vary from case to case and the suggested interval of 10 cm does not apply to all cases. To assess the behavior of the waves at the boundary conditions (i.e., around slab edges), signals of two locations with coordinates of (0, 0.5 m) and (0.2 m, 0.4 m) were compared at ages 7, 28 and 60 days, Figure 4.18. In this figure, “Edge” refers to location at (0, 0.5 m) and “Middle” to location (0.2 m, 0.4 m). The two-way travel times are also reported in μs. In this figure the two-way travel time from the backwall corresponds to the strongest signal. The effect of surface moisture can be identified in Figure 4.18 where day 7 has a higher range of amplitude. As concrete dries, the strongest reflection signals are more distinctive move towards higher depths.

Mode conversion (change in amplitude sign) in signals happens upon encountering a new layer or change in material type. In order to identify the mode conversion in UPE signals, signals at two locations, top of the delaminated area (i.e., X, Y = 18 cm, 22cm), and top of sound concrete (i.e., X, Y = 76 cm, 46 cm) were selected and compared. For the delaminated concrete, change in the mode is expected to happen upon entering the delamination, and for the sound concrete, at the bottom of the slab. The signals, shown in Figure 4.19, are marked at their interfaces, i.e., 95 μs for the delaminated area (Figure 4.19a) and 131 μs for the sound area (Figure 4.19b). In the former case, this is the two-way travel time from the delaminated area, and in the latter case, this time corresponds to two-way travel time to the backwall. The mode conversions at these points, where the interfaces are located, are very clear and show change in layer properties vibrantly. These points are shown in Figure 4.19 for better clarification. The depth of delamination can be calculated based on these time differences; more explanation in this regard is provided in the next section.

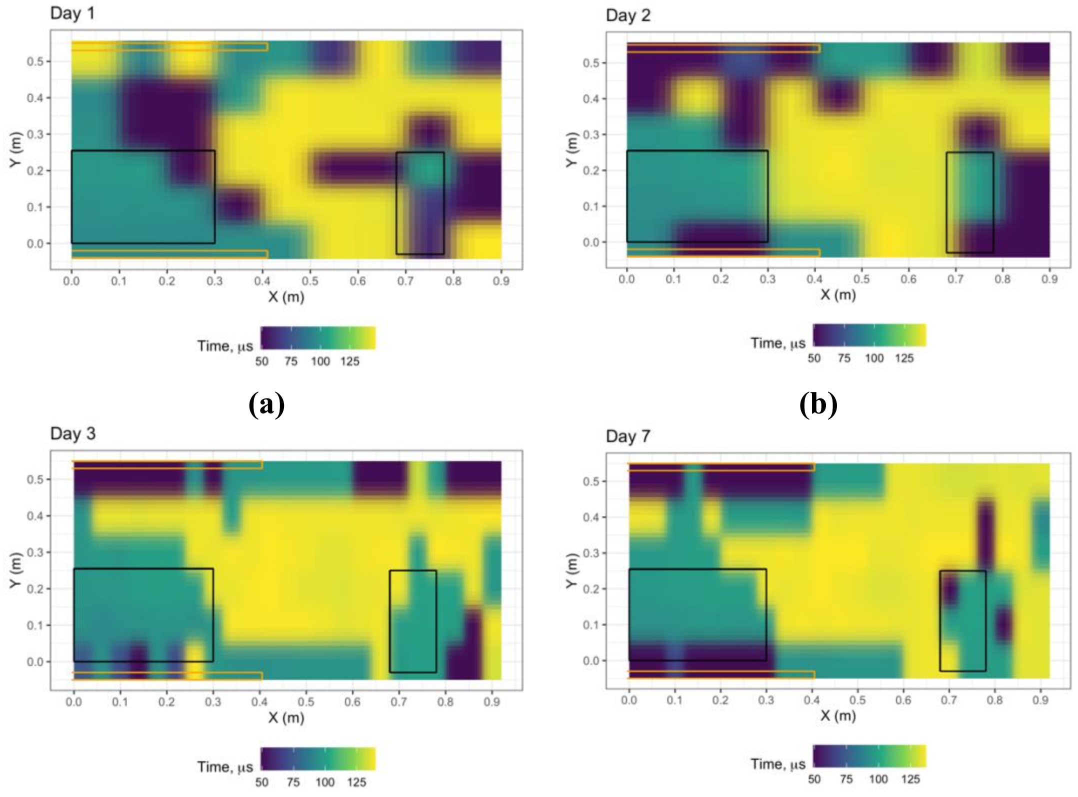

(a) (b)

(c) (d)

Figure 4.16. A-scan (two-way travel times) measured by UPE at early ages.

Note: black and orange rectangles represent delamination locations formwork wood strips, respectively.

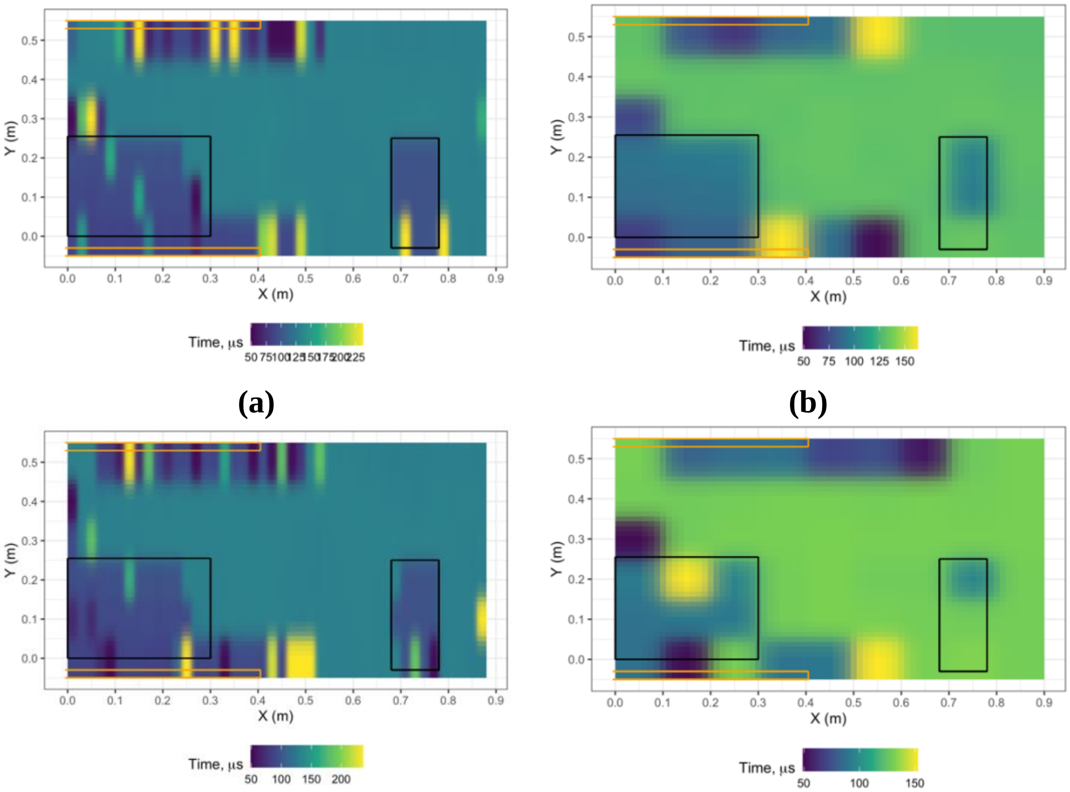

(a)

(b)

(c)

(d)

Figure 4.17. A-scan (two-way travel times) measured at later ages, a) at age 28 days with 2-cm increments, b) at age 28 days with 10-cm increments, c) at age 60 days with 2-cm increments, d) at age 60 days with 10-cm increments.

Note: black and orange rectangles represent delamination locations formwork wood strips, respectively.

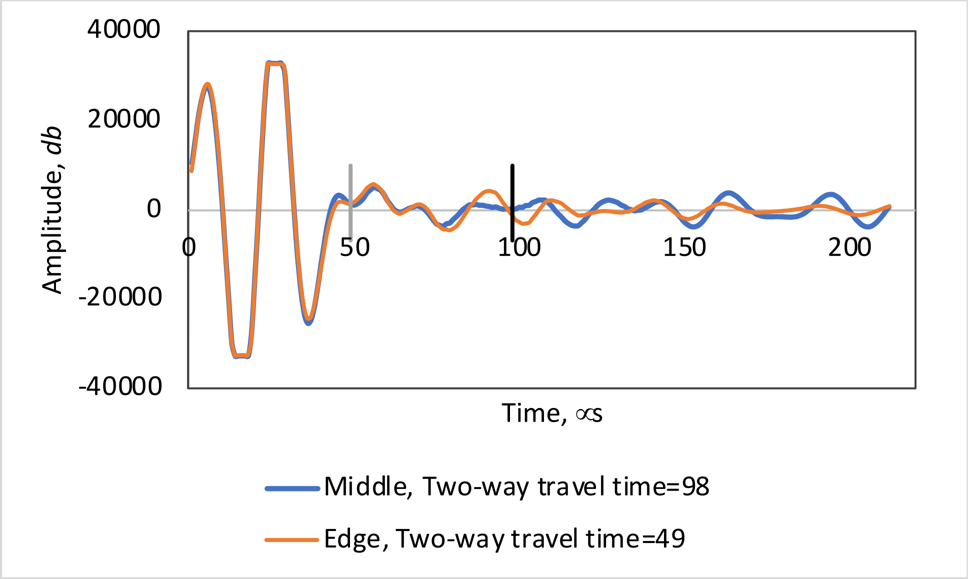

(a) 7 days

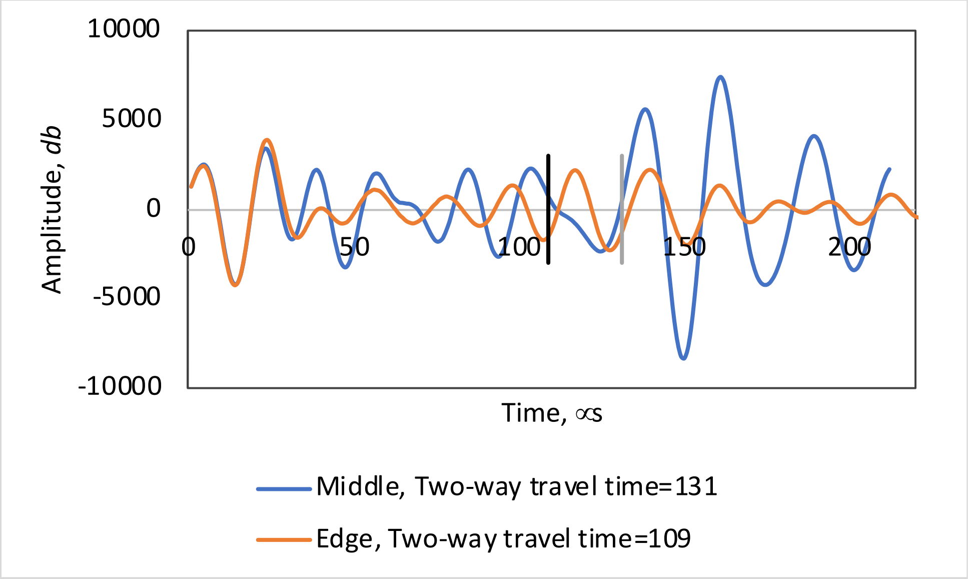

(b) 28 days

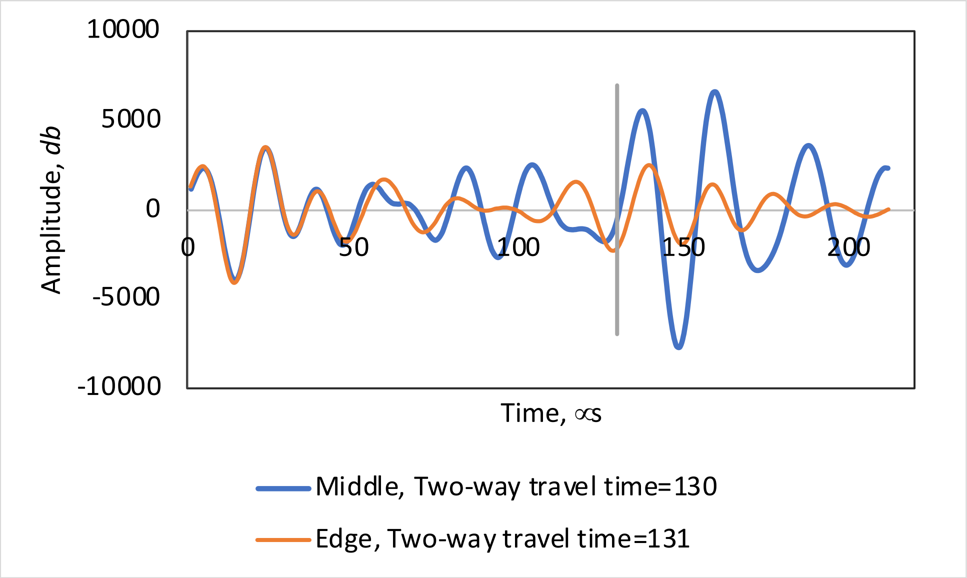

(c) 60 days

Figure 4.18. Signals of edge and middle locations at age a) 7 days, b) 28 days, and c) 60 days. The backwalls are shown by the vertical lines.

Note: edge at (0, 0.5 m) and middle location at (0.2 m, 0.4 m)

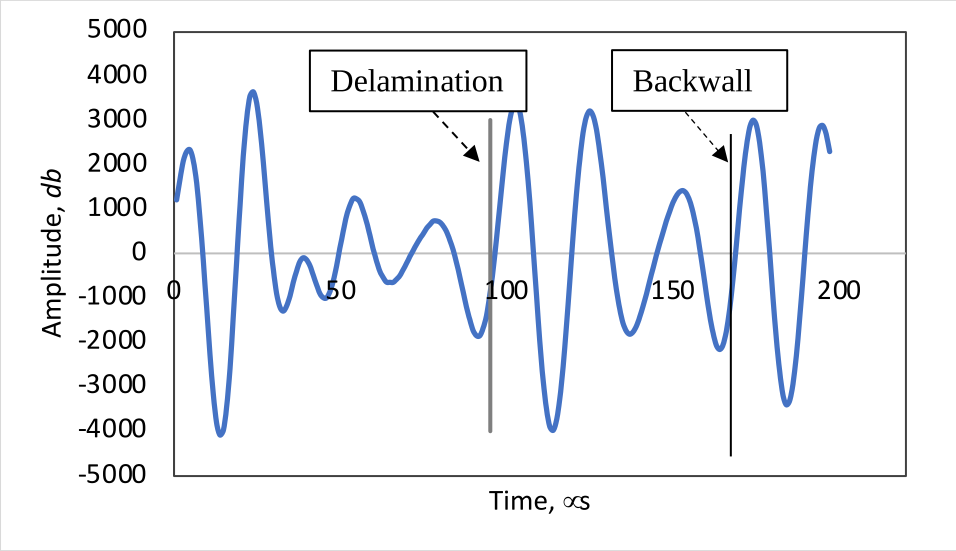

(a)

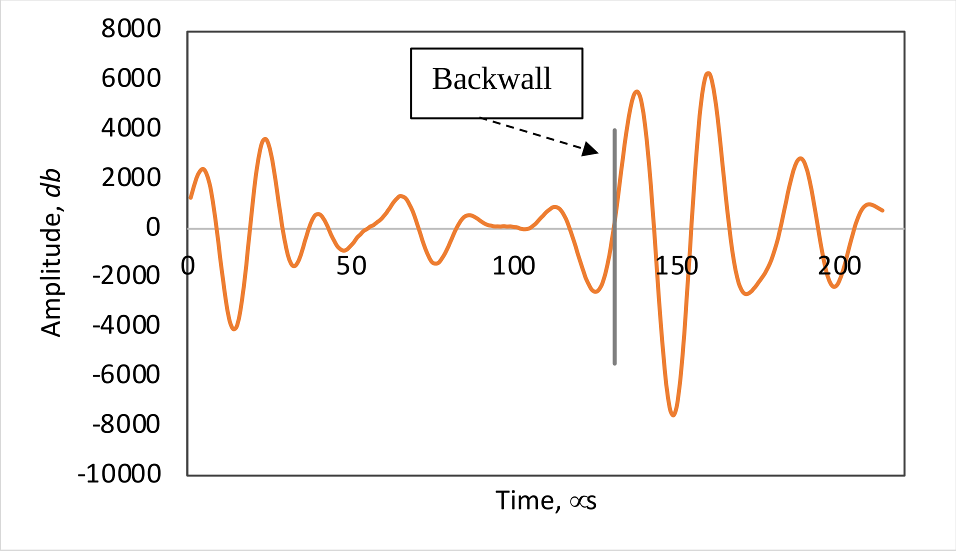

(b)

Figure 4.19. Mode conversion of the signals at the interface, a) delaminated area with depth at 95 µs, b) sound area with backwall at 131 µs.

The average shear wave velocity at the sound area of the slab is calculated from two-way travel time and the known thickness of the slab (i.e., 13 cm). For each age, the average values of shear wave velocity are reported in Table 4-6. The depth of the delamination at any location is calculated based on the velocity. The accuracy of the measurements is calculated based on the difference of calculated depth and actual depth relative to the actual depth (9 cm). The results are presented in Table 4-6. From Table 4-6 it can be seen that the accuracy tends to increase with concrete drying and maturing.

The ratio of the average shear wave velocity to the UPV at ages of 1 to 28 days changes from 0.52 to 0.46, which is equivalent to Poisson's ratio of 0.31 to 0.36 (see Equation 4-3). From Table 4-6, the effect of delamination extension is evident: while the estimated depth is very close to the actual depth (i.e., up to 1 cm difference) for the larger delamination (255 mm × 280 mm), the estimated depth of the smaller delamination fluctuates more (up to 2.4 cm). Nevertheless, estimating the depth with accuracy of 1 to 2 cm can be reflected as "good" accuracy, considering the possible movement of the delamination sheet during concrete pouring and placement.

Table 4-6. Average shear velocity and depth of delamination from UPE.

Age	Average shear wave velocity in concrete (m/s)	Average depth for the larger delamination (cm)	Relative Difference %	Average depth for the smaller delamination (cm)	Relative Difference %
1	1965.5	8.0	11%	6.6	27%
2	1972.7	8.3	8%	6.9	16%
3	1995.8	9.1	2%	8.7	3%
7	2117.0	8.6	5%	8.8	4%
28	2064.0	9.2	2%	9.1	2%
60	2068.7	9.2	2%	9.7	5%

4.4.4. GPR

The larger delaminated area (at depth 9 cm) appeared more clearly in GPR results after 60 days of concrete placement. Presence of moisture makes the results challenging to interpret unless STFT (short-time Fourier transform) signal processing and migration analysis are conducted (Goulias et al., 2015). Figure 4.20 shows the B-scans through four measuring paths, in the X- direction, in which line X-1 and X-2 are above the delaminated area, line X-4 is above the sound concrete, and line X-3 is partially above both areas (Figure 4.7). As can be seen, in survey line X-1 high reflections appear at a depth of 9 cm at the location of the larger delaminated area, whereas in both survey lines X-1 and X-2, high reflections appear at a depth of 9 cm where the larger and smaller delaminated areas exist. Metal mesh and the smaller delaminated area did not appear as strong reflections in the B-scan.

According to Spagnolini (1997) the minimum thickness for a layer to be detectable is calculated from:

$$D_{min} = \frac{\lambda_0}{2\sqrt{\varepsilon_r}} \tag{4-16}$$

where λ_0 is the wavelength of the EM in the air and the ε_r is permittivity of the target. In case of a GPR with a central frequency of 2000 MHz the wavelength of the EM in the air ($\lambda_0 = C/f$), is 15 cm. Therefore, the minimum thickness of the plexiglass (ε_r =3.2) must be 1.47 cm. However, since detecting delamination at early stages was the focus of this study, a thinner layer of 0.23 cm representing delamination was selected. In addition, according to the literature (Barnes & Trottier, 2002) the attenuation in electromagnetic waves is more pronounced in the presence of corrosion, which was not present in this case.

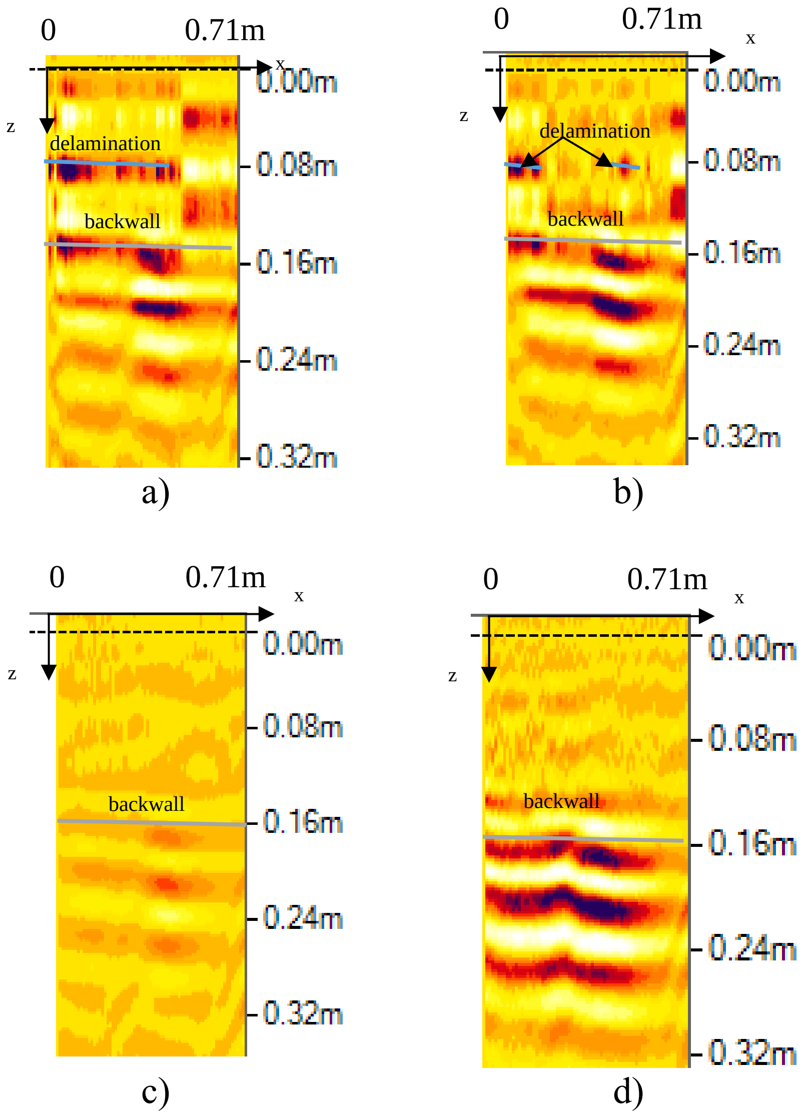

Figure 4.20. B-scan (radargram) of the slab at age 60 days through a) line 1, b) line 2, c) line 3, and d) line 4 of Figure 4.4b.

4.4.5. Rebound Hammer

The results of repeated measurement by two rebound hammers, Proceq and Humbolt, on the slab are presented in Table 4-7 and Table 4-8. Each cell of the table is the average of three rebound numbers at the corresponding X and Y. Therefore, the highlighted gray cells are rebound numbers at the delaminated areas. For example, the rebound number from Proceq at a point with x=10 cm and y=20 cm is 43.3 (see Figure 4-3 and Figure 4-4 for more details).

Only Proceq showed a slight difference in average rebound number above the delaminated area and the sound area (41.3 versus 42.6). The difference between average rebound numbers, (i.e., equal to 1.3), is equivalent to about 1 MPa in compressive strength. It should be noted that, in the field, the delaminated area is not filled with solid materials as in this study and this difference is expected to be higher.

Table 4-7. Rebound number on the slab from Proceq rebound hammer.

	Y distance (cm) from the origin (0,0)								
X distance (cm)	10	20	30	40	50	60	70	80	90
50	45.0	43.5	42.3	42.7	40.3	42.3	41.7	41.0	43.8
40	43.7	47.2	46.0	41.2	43.2	43.0	40.8	41.3	43.3
30	41.5	42.8	44.3	42.3	40.3	44.5	39.0	42.0	42.7
20	44.7	40.5	39.3	42.2	43.0	39.5	44.8	39.3	42.3
10	37.5	43.3	41.5	44.3	43.5	41.0	45.8	39.0	38.0

Table 4-8. Rebound number on the slab from Humbolt rebound hammer.

	Y distance (cm) from the origin (0,0)								
X distance (cm)	10	20	30	40	50	60	70	80	90
50	29	28	27	26	27	29	27	28	26
40	31	33	33	27	29	28	26	28	28
30	28	30	30	29	28	32	27	28	27
20	31	29	30	27	27	27	29	29	29
10	27	31	29	31	31	32	28	27	25

4.4.6. Finite Element

The results presented here are the outcomes of more than 100 trial and errors in ABAQUS in order to refine the mesh size, concrete properties, and Lamb wave properties. Selecting the mesh size is a trade-off between the accuracy of the model and time of analysis. The mesh size was fine-tuned to have a relatively high accuracy with a shorter time of analysis.

Considering the explanation in the previous sections, the dynamic explicit analysis was carried out. The explicit dynamic integration algorithm's maximum temporal discretization was set to 0.001 μs to ensure a consistent time increment for the FE analysis in this work. The consistent time increment allows wave frequencies to be discretized correctly, reducing waveform disturbances. The simulation lasts 200 micro seconds to guarantee that all essential wave reflections from the delamination and specimen bottom are captured. The largest element was 1/10 of the shortest wavelength. The focused images with one constant velocity (i.e., 3238 m/s) are shown in the following graphics (Figure 4.21) for the ultrasonic data of the FE simulation with delamination.

The screenshots of stress wave propagation in FE models are shown in the Figure 4.22. Wave propagation is complicated by reflection and refraction at the delamination interface. Even though much of the energy is found above delamination, some of it is transmitted into the concrete specimen beneath it, allowing imaging of the specimen.

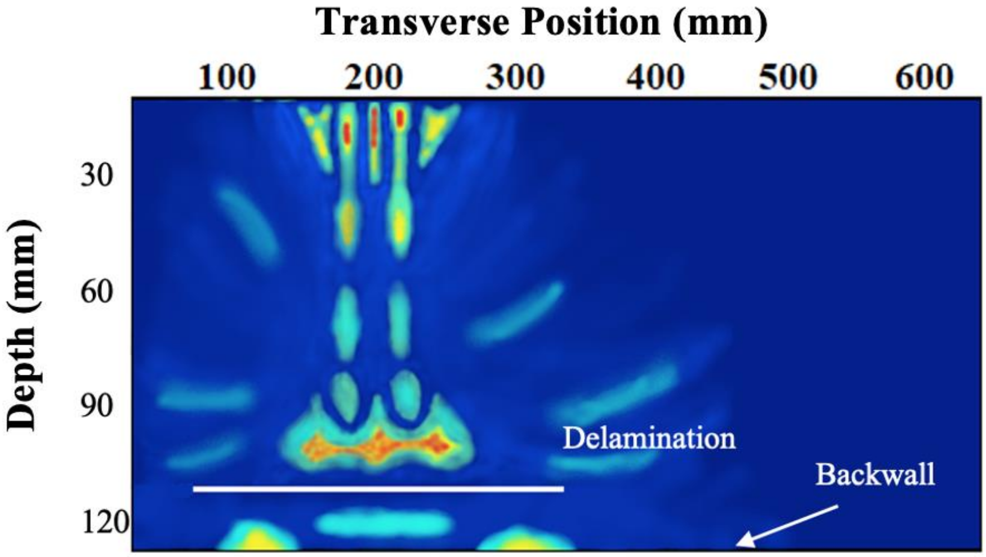

Figure 4.21. Wave propagation snapshots resulting from FEM simulation after excitation of the transducers at the location of the larger delamination Point 1.

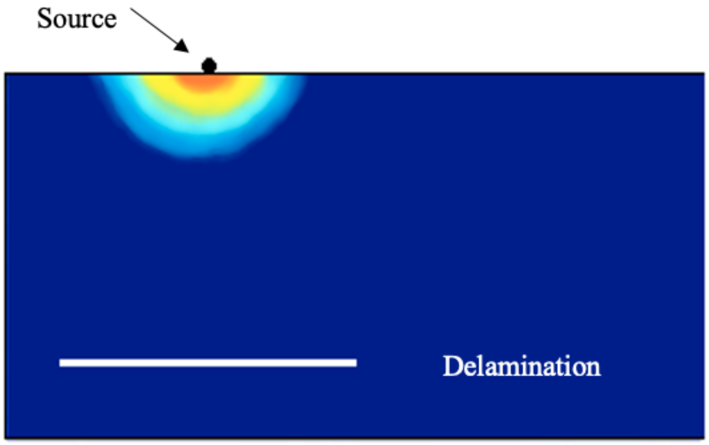

a) T=10 μs

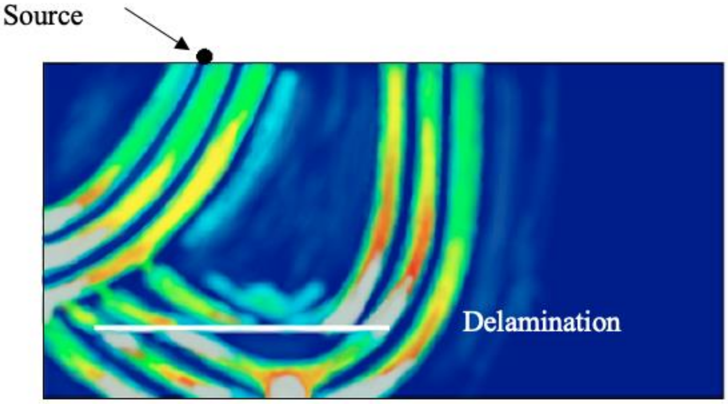

b) T=100 μs

Figure 4.22. Wave reflection and refraction around the delamination, after a) 10 μs, b) 100 μs.

The recorded displacement control wave was obtained using the received sensor. The comparison of experimental responses from repeated UPE measurements at a specific location showed agreement at the time of pulse conversion (i.e., depth of delamination and backwall), but showed randomness at other times. Figure 4.23 depicts an example of UPE repletion at a specific location (x=20 cm, y=40 cm). Therefore, in comparison of the experimental and finite element results the focus is on these critical points (delamination and backwall locations). The minor differences between the two pulses are justifiable since the actual properties of the concrete slab can be different from the tested samples and assumed values (i.e., Poisson's ratio). In addition, the plexiglass can be moved under the concrete weight.

Figure 4.24 shows the comparison between experimental wave and simulated wave by finite element at Point 1. This figure shows that the experimental and numerical results are in agreement at the location of the delamination and backwall in time of wave conversion and amplitude of the waves at those events. The minor differences between the two waves can be due to the assumptions/errors made in determining concrete compressive strength or plexiglass movements while pouring concrete.

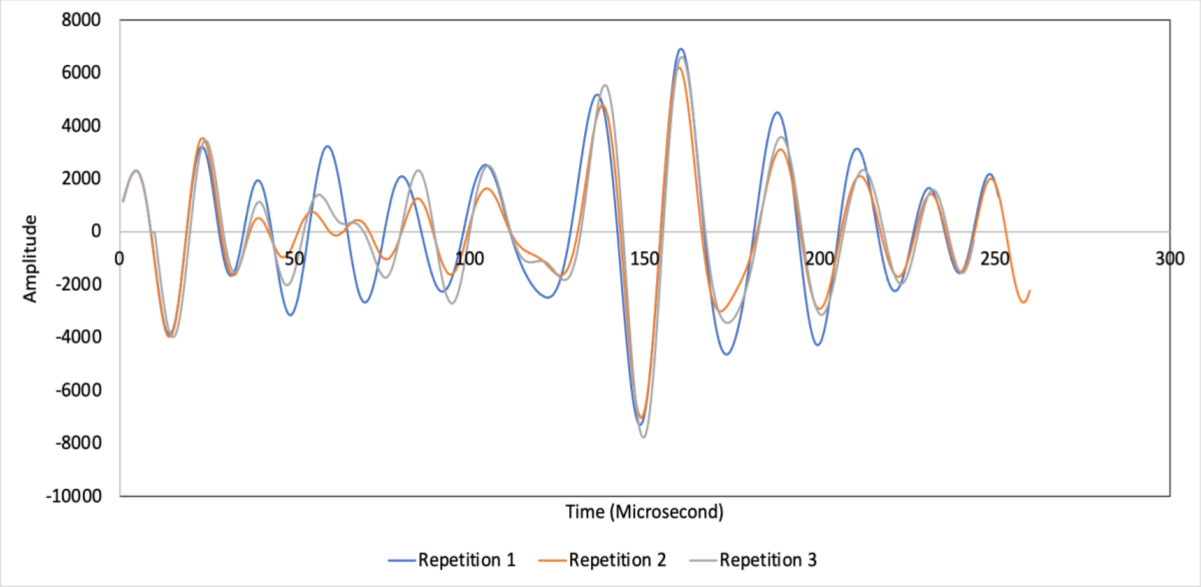

Figure 4.23. UPE repetition at a specific location (x=20 cm, y=40 cm).

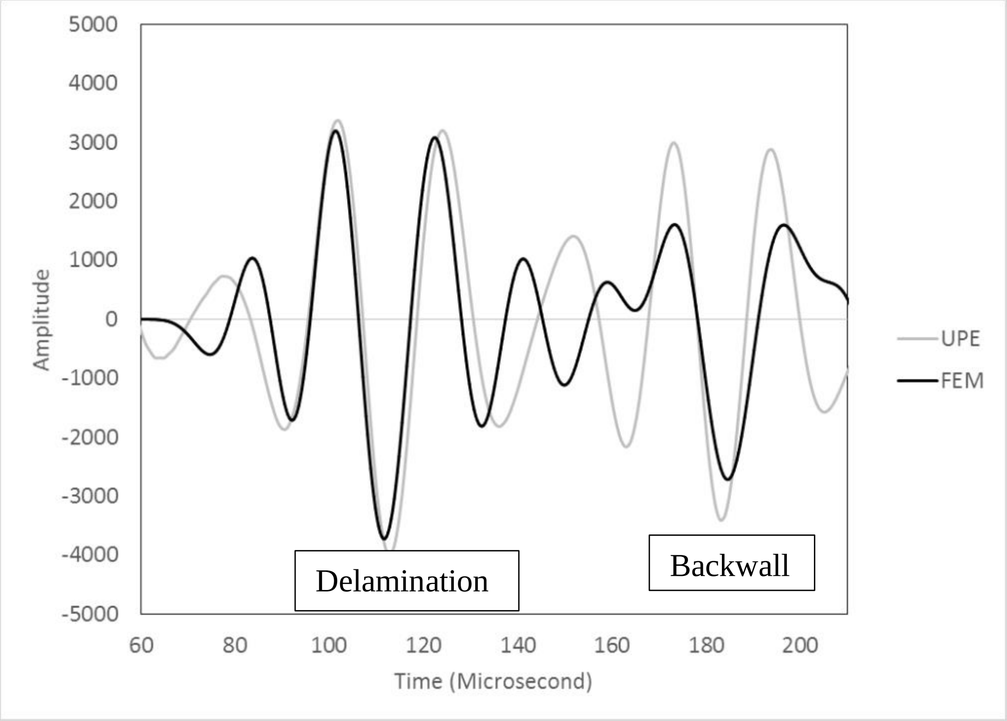

Figure 4.24. Comparison of signals at a delaminated location at Point 1 (x=28 cm, y=20 cm).

In addition, the wave propagation over the concrete slab surface and thickness are illustrated in Figure 4.25. In this figure and figures 4.26 to 4.28 the location of the transducer is at Point 1. Figure 4.26 demonstrates vertical wave propagation over the slab's thickness at different sections in x-direction. Figure 4.25 and Figure 4.26 show the wave propagation through the depth of the slab. Even though refraction and reflection of the energy happens at the location of the delamination, a fraction of the wave propagates through the delamination to the backwall. As a result, in Figure 4.24 there are two distinct wave peaks which are at the locations of the delamination and backwall.

Figure 4.27 shows radial wave propagation in X and Y directions. The radial wave propagations show the interaction between the concrete and the plexiglass and the reflection and refraction of the Lamb wave around the delamination. In addition, the wave reflections at the edges (Figure 4.27b) verify the uncertainties in results of methods work based on wave propagation (discussed in Figure 4.18 explanation).

Figure 4.28 shows the shear stress at contact surfaces of the plexiglass and the slab surface. It should be noted in a case where there is only one material (e.g., sound concrete) there is no fluctuation in the stress curve, and the relationship between the stress and time is a quadratic relationship.

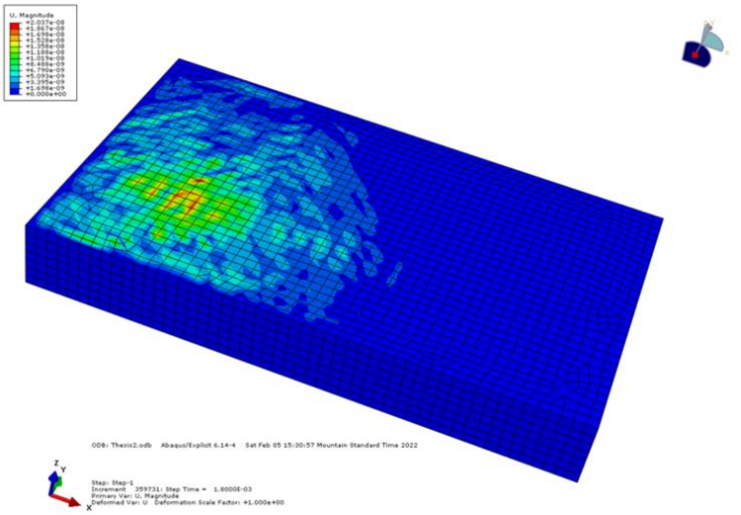
U, Magnitude
+2.037e-08
+1.867e-08
+1.698e-08
+1.528e-08
+1.358e-08
+1.188e-08
+1.019e-08
+8.488e-09
+6.790e-09
+5.093e-09
+3.395e-09
+1.698e-09
+0.000e+00
ODB: Thesis2.odb Abaqus/Explicit 6.14-4 Sat Feb 05 15:30:57 Mountain Standard Time 2022
Z
Y
X
Step: Step-1
Increment 359731: Step Time = 1.8000E-03
Primary Var: U, Magnitude
Deformed Var: U Deformation Scale Factor: +1.000e+00

(a)

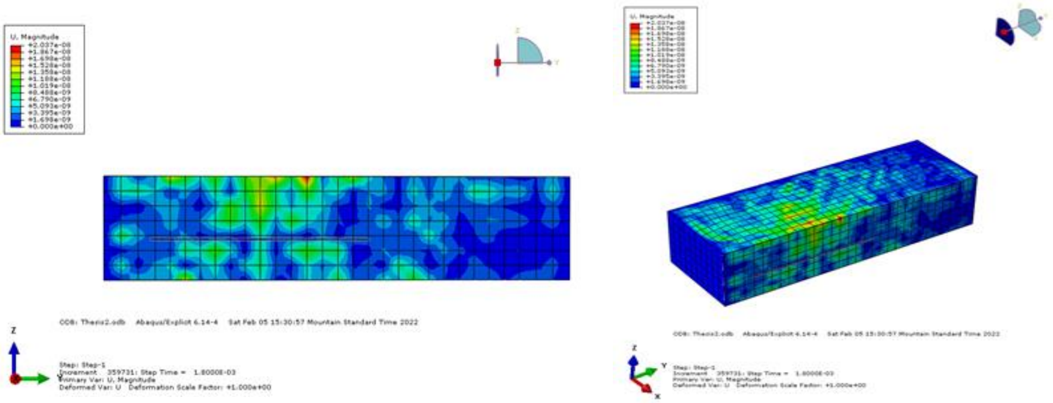

(b)

Figure 4.25. Wave propagation simulation by finite element, a) plan view of the slab, b) side view of the slab.

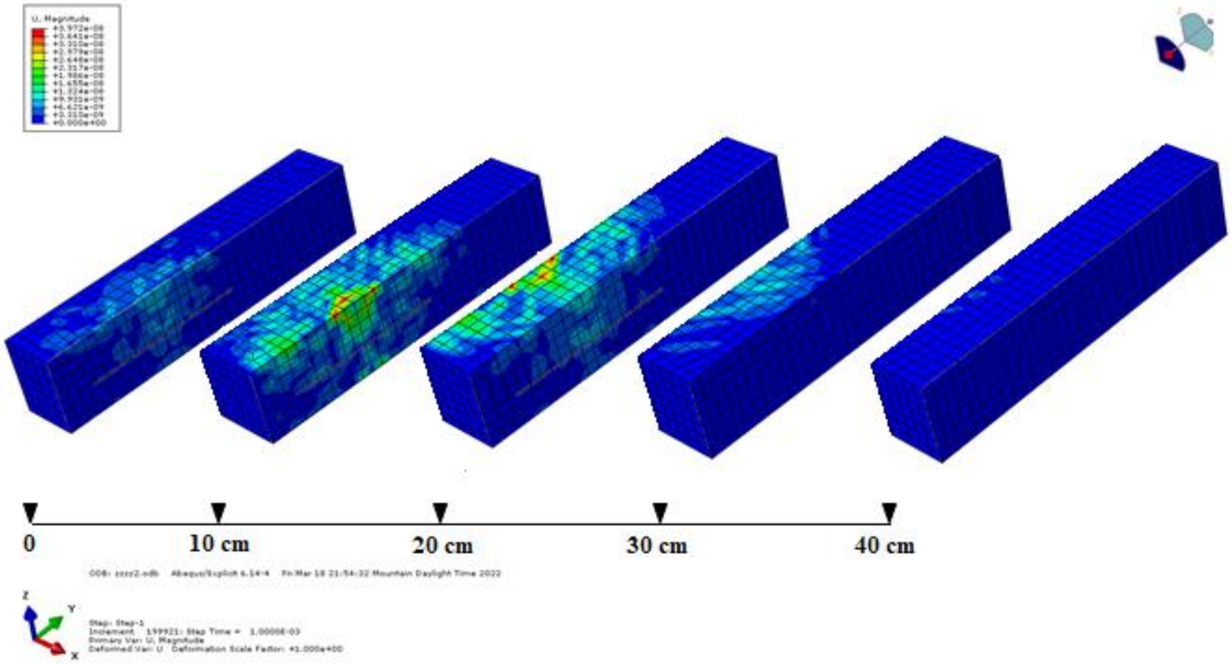

Figure 4.26. Vertical wave propagation over the slab's thickness at different sections in x-direction (along the length of the slab).

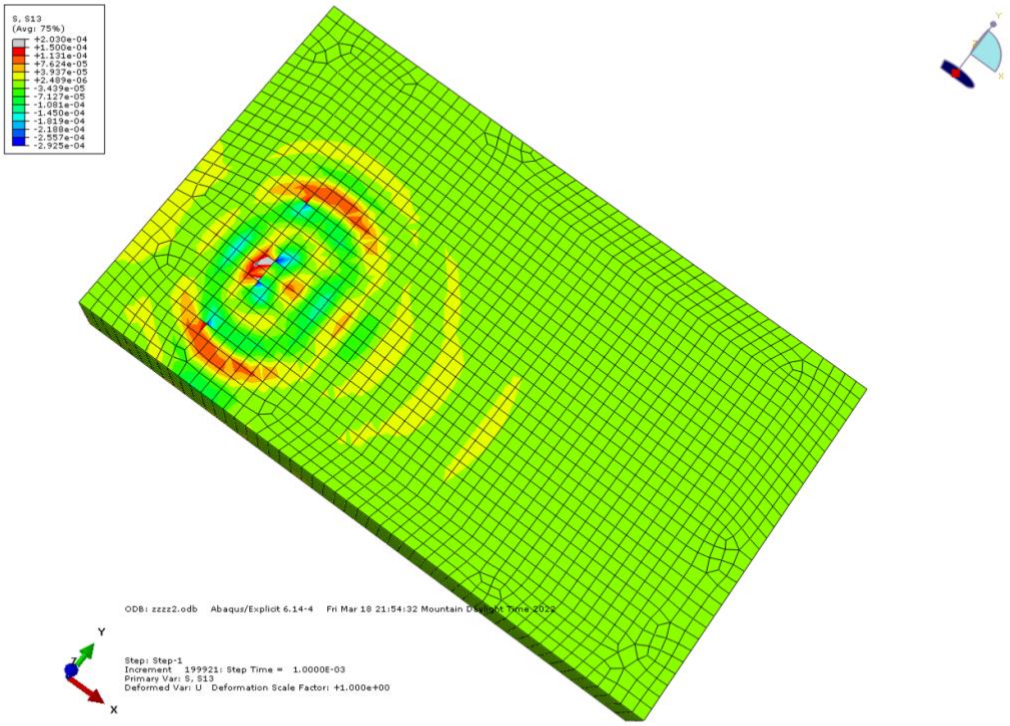
S, S13
(Avg: 75%)
+2.030e-04
+1.500e-04
+1.131e-04
+7.624e-05
+3.937e-05
+2.489e-06
-3.439e-05
-7.127e-05
-1.081e-04
-1.450e-04
-1.819e-04
-2.188e-04
-2.557e-04
-2.925e-04
ODB: zzzz2.odb Abaqus/Explicit 6.14-4 Fri Mar 18 21:54:32 Mountain Daylight Time 2022
Y
Z
X
Step: Step-1
Increment 199921: Step Time = 1.0000E-03
Primary Var: S, S13
Deformed Var: U Deformation Scale Factor: +1.000e+00

a) Radial wave propagation in y-direction

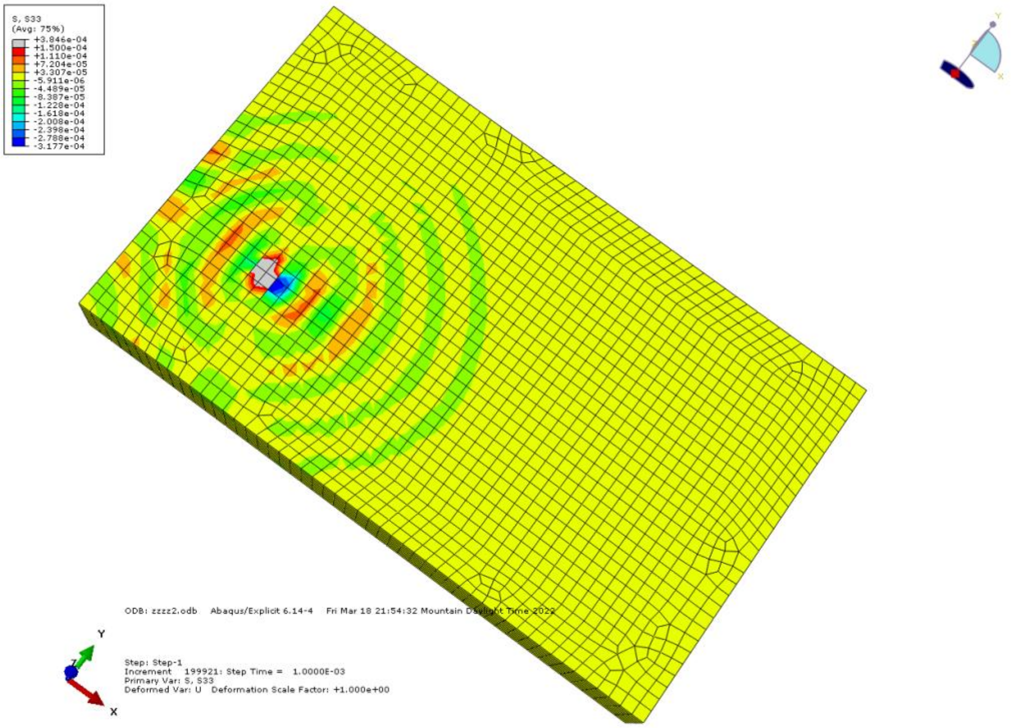
S, S33
(Avg: 75%)
+3.846e-04
+1.500e-04
+1.110e-04
+7.204e-05
+3.307e-05
-5.911e-06
-4.489e-05
-8.387e-05
-1.228e-04
-1.618e-04
-2.008e-04
-2.398e-04
-2.788e-04
-3.177e-04
ODB: zzzz2.odb Abaqus/Explicit 6.14-4 Fri Mar 18 21:54:32 Mountain Daylight Time 2022
Y
Z
X
Step: Step-1
Increment 199921: Step Time = 1.0000E-03
Primary Var: S, S33
Deformed Var: U Deformation Scale Factor: +1.000e+00

b) Radial wave propagation in x-direction

Figure 4.27. Radial wave propagation in y and x directions

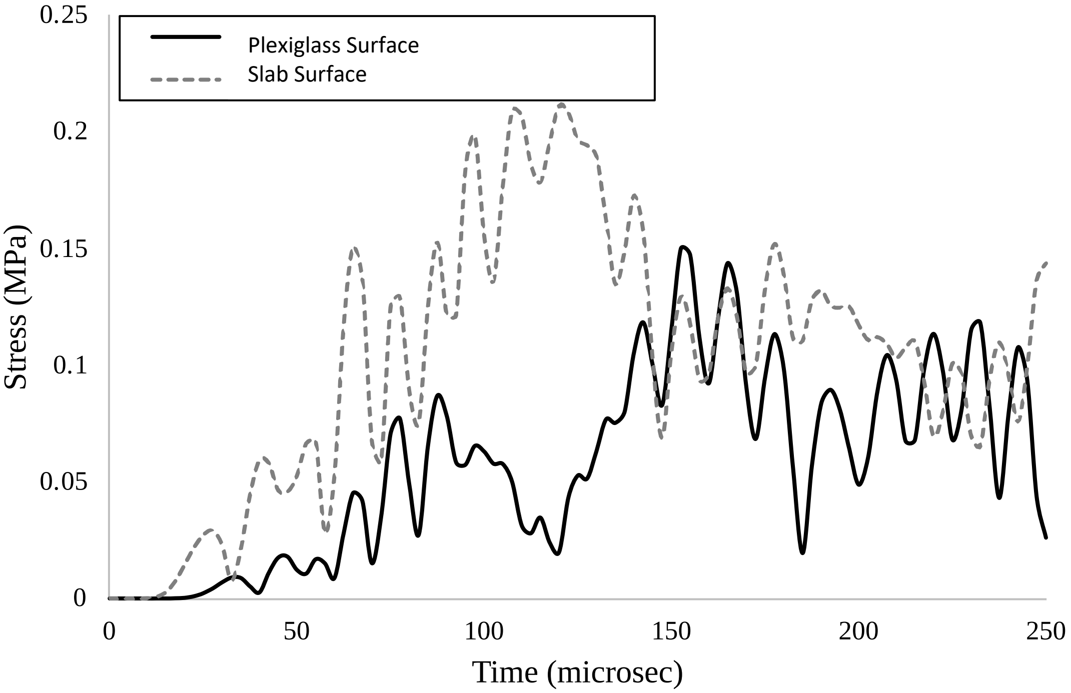

Figure 4.28. Stress change at the contact surface of the plexiglass and slab at Point 1.

The results and wave propagation at Point 2 (specified in Figure 4.7 and Figure 4.10) are also shown in Figure 4.29 and Figure 4.30. At this location, since there is no delamination, only the backwall is observed in wave reflections (i.e., one distinct peak in Figure 4.29). Figure 4.30 shows the wave propagation and dissipation in the slab in vertical and horizontal directions. However, this point is in the vicinity of the smaller delamination, so the edges of the smaller delamination can be seen in vertical and radial wave propagation simulation (red parts in Figure 30).

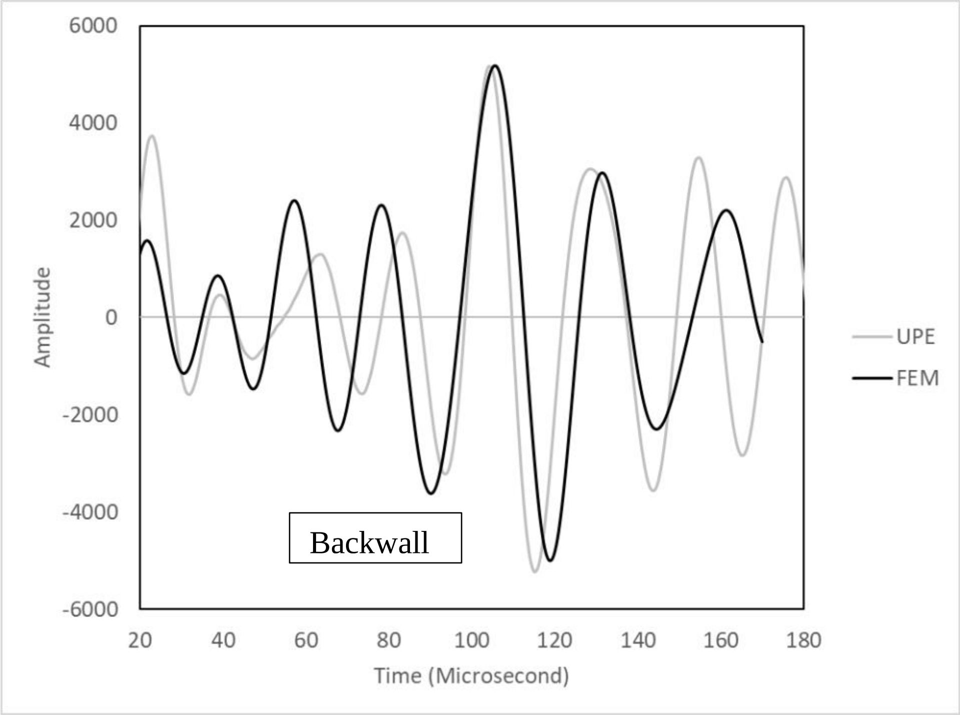

Figure 4.29. Comparison of signals at a sound concrete location (Point 2; x=72, and y=20 cm).

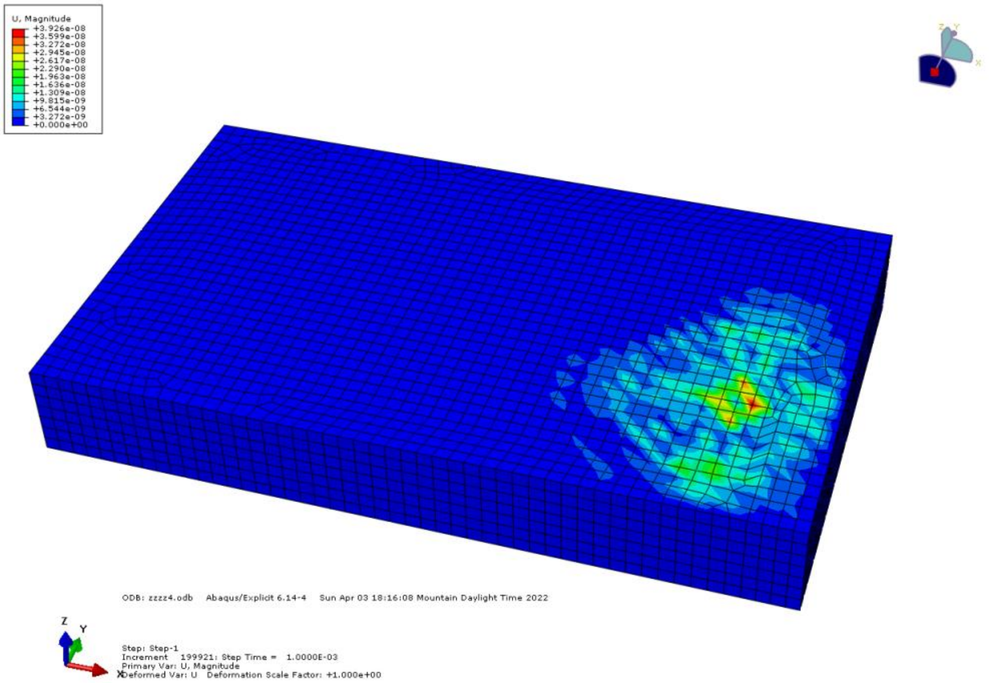
U, Magnitude
+3.926e-08
+3.599e-08
+3.272e-08
+2.945e-08
+2.617e-08
+2.290e-08
+1.963e-08
+1.636e-08
+1.309e-08
+9.815e-09
+6.544e-09
+3.272e-09
+0.000e+00
ODB: zzzz4.odb Abaqus/Explicit 6.14-4 Sun Apr 03 18:16:08 Mountain Daylight Time 2022
Z
Y
X
Step: Step-1
Increment 199921: Step Time = 1.0000E-03
Primary Var: U, Magnitude
Deformed Var: U Deformation Scale Factor: +1.000e+00

a) Vertical wave propagation

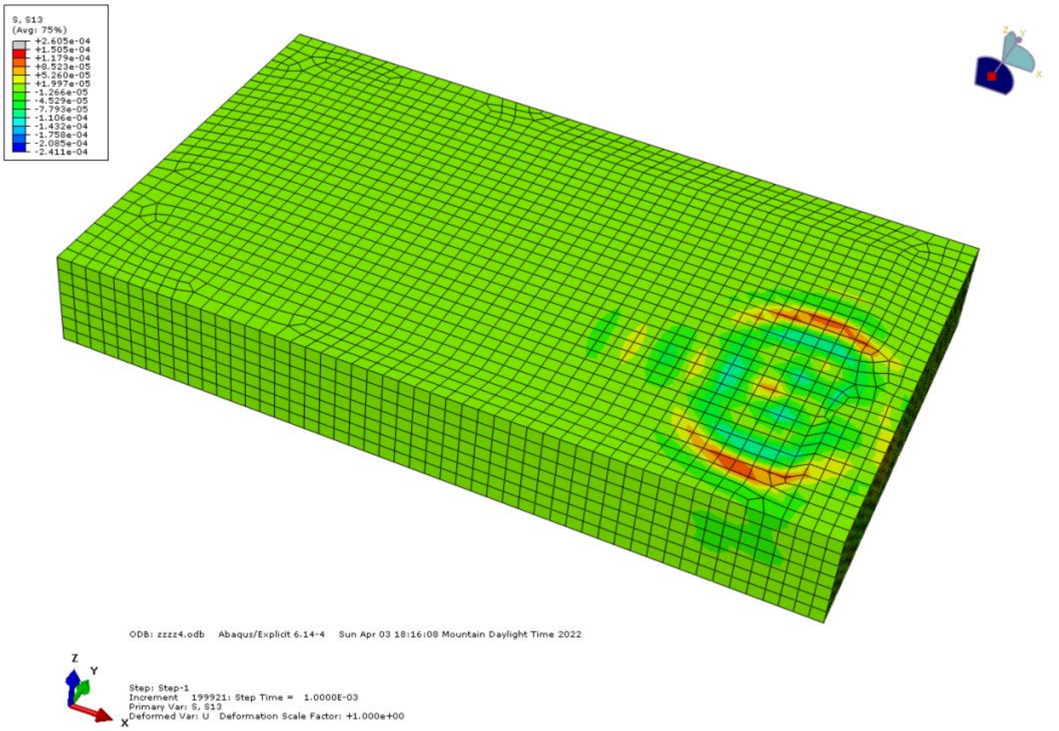
S, S13
(Avg: 75%)
+2.605e-04
+1.505e-04
+1.179e-04
+8.523e-05
+5.260e-05
+1.997e-05
-1.266e-05
-4.529e-05
-7.793e-05
-1.106e-04
-1.432e-04
-1.758e-04
-2.085e-04
-2.411e-04
ODB: zzzz4.odb Abaqus/Explicit 6.14-4 Sun Apr 03 18:16:08 Mountain Daylight Time 2022
Z
Y
X
Step: Step-1
Increment 199921: Step Time = 1.0000E-03
Primary Var: S, S13
Deformed Var: U Deformation Scale Factor: +1.000e+00

b) Radial wave propagation in y-direction

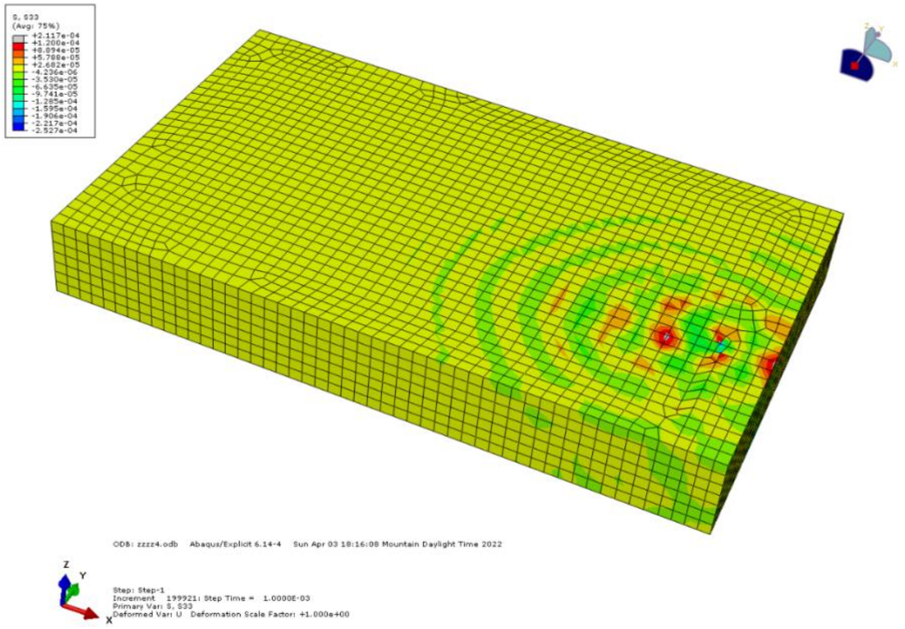
S, S33
(Avg: 75%)
+2.117e-04
+1.200e-04
+8.894e-05
+5.788e-05
+2.682e-05
-4.236e-06
-3.530e-05
-6.635e-05
-9.741e-05
-1.285e-04
-1.595e-04
-1.906e-04
-2.217e-04
-2.527e-04
ODB: zzzz4.odb Abaqus/Explicit 6.14-4 Sun Apr 03 18:16:08 Mountain Daylight Time 2022
Z
Y
X
Step: Step-1
Increment 199921: Step Time = 1.0000E-03
Primary Var: S, S33
Deformed Var: U Deformation Scale Factor: +1.000e+00

c) Radial wave propagation in x-direction

Figure 4.30. Vertical and radial wave propagation in the slab

4.5 Summary & Conclusions

In this study, a variety of non-destructive testing was employed to evaluate a concrete slab in terms of voids and delamination. To this end, a concrete slab with artificially embedded delamination was tested with UPV, UPE, GPR, and two rebound hammers. As the results of testing on a small beam in this study suggested, the UPV can be employed to find the location and extent of the delamination or void in a concrete element when both sides of the concrete element are accessible. Since in evaluating concrete slabs in bridge decks or rigid pavements this may not always be possible, another form of UPV, such as UPE can be used. The advantages of UPE over UPV include using smaller transducer size with the same frequency and dry versus lubricated contact. In this experiment UPV was used on the companion cylinder to monitor the strength gain and to estimate the compression wave velocity in concrete.

UPE and GPR were introduced in other studies as NDTs that can be used to detect delamination, however the accuracy of these methods in the field often lacks a proper assessment due to limited and constrained access within the concrete to be able to verify the “ground truth” conditions. While GPR has been used more extensively, UPE testing with such multisensory devices has been limited. Therefore, the main objective of this study was to evaluate the accuracy of GPR and UPE in controlled laboratory conditions. The results show that UPE can estimate the depth of delamination with a deviation of 0.1 to 2.4 cm, and the accuracy is highly dependent on the level of maturity of the concrete and whether it is moist or dry. On the other hand, when thin delamination occurs (i.e., representing early ages of this distress) and/or absence of reinforcement corrosion, GPR is not able to accurately detect such effects. Furthermore, the potential impact of the presence of moisture needs STFT and migration analysis, which is further discussed in the next chapter.

Another objective of this study was assessing whether a rebound hammer could be sensitive for detecting delamination. The corrosion in concrete and the hollowness due to delamination leads to a decrease in compressive strength. Therefore, a decrease in rebound number at delaminated areas is expected. However, in this study, since the concrete was relatively new and the delaminated area was not hollow (i.e., represented by plexiglass) the effects on rebound number were negligible.

In order to simulate the Lamb wave propagation in the concrete slab, a linear-elastic finite element model was built in ABAQUS. Two points on the slab, one above the delaminated area and another one on a sound concrete, were used to compare the responses of the UPE and finite elements. The finite element simulated the wave propagation in concrete and around delamination and the results of reflected pulses from the experiment and numerical models were compared. This comparison showed a very good agreement between the two methods. The minor discrepancies can be due to the possible movement of the plexiglass or the variability between the slab and the cylinder which were used in determining the concrete properties.

Chapter 5. Condition Assessment of Bridge Decks with Ground Penetrating Radar

5.1. Bridge Deck Inspection & GPR

Concrete bridge decks are inspected regularly for condition assessment. Pre-stressed bridge deck members are vital components of the concrete bridge superstructure. Their condition may affect the overall bridge performance as well as the safety and smooth operation of traffic. Condition assessment of bridge decks is examined and compared in time to the original design and construction quality. Often, the original design plans and construction records may not be available for older structures. Therefore, in addition to detecting the defects, inspectors need to collect information on rebar location, concrete cover depth, and thickness of overlays is needed (Cheilakou et al., 2012).

In terms of bridge deck condition, objectives of inspections include detection of defects, such as cracking, corrosion of the rebars, delamination, assessment of cover depth and thickness of any overlays (Cheilakou et al., 2012). Conventional testing methods, and in some cases destructive in nature, for bridge deck inspection include visual surveys, coring, chain drag, half-cell potential, chloride resistivity, and, sounding. The shortcomings of these methods are: (i) time consuming in nature, labor intensive, and costly, (ii) require extensive traffic control during inspection, and (iii) raise significant concerns on the safety of inspectors and the driving public while in-situ testing is taking place. Thus, agencies are now looking into adopting non-destructive testing, NDT, methods for condition assessment. Contrary to conventional and destructive tests, several of the NDT methods are fast and less expensive alternatives of inspection. Ground Penetrating Radar (GPR) is one of these NDTs identified as rapid and reliable (Gucunski et al., 2013).

GPR employs electromagnetic waves to detect layer thicknesses, material quality, presence of rebar and any abnormality beneath the surface. GPR emits electromagnetic waves towards the pavement materials and collects the reflections. Any variation in dielectric constant due to detection of new material or deterioration can be reflected in the response signal. Variation in dielectric properties of materials implies not only potential deterioration but also moisture concentration. (Goulias et al., 2015; Goulias, 2017a). Accuracy of GPR in detecting abnormalities and interfaces for bridge decks has been extensively studied and reported in numerous past studies (Gucunski et al., 2013; Martino et al., 2014; Gagarin et al., 2017, 2020). GPR can be used to accurately determine the quality and thickness of layers (e.g., asphalt, concrete cover or unbound aggregate), rebar location and conditions (sound or corroded), structural features (piers, bracing beams), defects (such as cracking, delamination, voids, honeycombing, segregation) and moisture concentration (Hugenschmidt et al., 2006; Simi et al., 2012; Goulias, 2017b; Gagarin et al., 2017). Maser (1991) used GPR on 32 asphalt overlaid decks in New England. Comparison of GPR data with "ground truth" conditions before rehabilitation and right after removing the asphalt overlay showed high consistency between variation of dielectric constant and deteriorated areas. Romero et al. (2000) used GPR to develop a contour map for concrete replacement, specifying which areas need to be replaced with new concrete. Alani et al. (2013) employed GPR for studying two bridge decks in the UK to evaluate the location and spacing of rebars, estimate cover depth of concrete, and identify sub-surface defects. They concluded that repeatability of GPR surveys was very consistent and accurate with ground truth conditions and assessed how the presence of moisture was influencing GPR response. Similarly, another study on bridge decks (Goulias et al., 2015) assessed the accuracy of GPR surveys in relation to ground truth conditions and examined the impact of the presence of moisture on signal reflection using Short Time Fourier Transfer (STFT) analysis.

In order to expand the laboratory testing of GPR in concrete elements with defects, the testing results of a pre-stressed bridge deck in the south-eastern portion of Sicily, Italy, were analyzed. Objective of that study undertaken in cooperation with the University of Catania, in Italy, was to survey with GPR the current conditions, such as thickness of the asphalt overlay, depth of the rebars and deterioration of the reinforcement. The GPR results were verified by boring holes on key locations and surveys on open joints in the proximity of the bridge pillars. The open joints are often the source of significant moisture infiltration in bridge deck layers and materials with potential consequences on concrete degradation and reinforcement corrosion. The GPR unit used in that study was equipped with two antennas of 600 and 2000 MHz frequencies. The higher the frequency the higher the resolution however lower the penetration depth is. Thus, the use of both frequencies provided both accuracy and depth of penetration. Depth of penetration depends on several factors, and among them, central frequency and resistivity of materials. Since bridge deck thickness is finite, the GPR with dual frequencies of 600 MHz and 2000 MHz was appropriate for the survey. Such GPR units are commonly available to highway agencies in Italy and around the world with minimal cost. The devices are simple to run and are supplied with user friendly software for data analysis, facilitating thus the interpretation of results.

With GPR surveys it is always necessary to have proper calibration following the manufacturer's guidelines. Furthermore, "ground truth" information from construction drawings or cores is desired in order to verify initially the GPR response. In this study for the forensic investigation of this older bridge, no drawings or as-built construction data were available. Thus, construction drawings from similar bridges constructed in that time period in the region with the same pre-stressed method and construction techniques were used as described later in the manuscript. In addition to these, the geometric characteristics of the bridge deck (such as top and bottom deck elevation, geometric dimensions of the bridge deck surface, longitudinal and transverse curvatures and slopes, surface defects and other features) were verified with remote sensing methods such as Terrestrial Laser Scanning (TLS) and reported elsewhere (Cafiso et al., 2018). To further complement the "ground truth" information, inspections on open joints and drilled boring holes at the bridge deck were used in order to verify in various locations overlay thickness, concrete cover, depth of the reinforcement, and potentially detect, when possible, any corrosion or delamination.

5.3. GPR Wave Propagation Principles

As mentioned earlier, the GPR transmitter antenna emits electromagnetic waves in the microwave band through materials and layers. The reflection signal is received by the same antenna in a monostatic system, or by a receiver antenna in a bi-static system. The change in the dielectric constant of materials during the propagation and reflection is a sign of either a variation in the homogeneity of the material (Lahouar et al., 2002), or materials with different dielectric properties (e.g., asphalt, concrete, rebars), and/or the presence of defects (e.g., voids, cracking, delamination in concrete). Most GPR systems are equipped with a receiving and transmitting system suitable for working with different frequencies simply by changing the type of antenna. The antennas are transducers that convert electrical current into electromagnetic waves that propagate in the medium, and vice versa convert the electromagnetic wave into electrical impulses. The principles of GPR for each specific detection purpose stated above are briefly explained next.

5.3.1. Overlay Thickness

Thickness of the asphalt layer (overlay) can be calculated by two methods: two-way travel time, Equation 1, (Goulias et al., 2016), or the common midpoint method (Lahouar et al., 2002) when multiple GPR channels are available.

$$D = c.\Delta t/2\sqrt{\varepsilon_r} \qquad (5\text{-}1)$$

where:

Δt = travel time

c = speed of light in air

ε_r = relative permittivity equal to $\varepsilon_r = \frac{\varepsilon}{\varepsilon_0}$

where ε is the permittivity of material and ε_0 is the permittivity of vacuum, $8.89 \times 10^{-12} F/m$

D = thickness of the layer

Since overlays are thin layers, it is often challenging to differentiate the reflection from the top and bottom of the layer. This problem mostly appears when the layer thickness is comparable to the wavelength of the received EM pulse. This represents the “thin layer problem” (Zhao et al., 2015). For lower resolutions, signal processing techniques, known as super-resolution techniques, need to be applied. Antennas with a center frequency of 2000 MHz can provide a sufficient resolution to measure a minimum layer thickness less than 2.5 cm (1 in.) with an accuracy of 0.25 cm (0.1 in.) (ASTM D4748). For the bridge deck in this study the overlay thickness is about 3 to 4 cm, so the 2000 MHz antenna is deemed to be capable of accurately detecting such overlay with sufficient resolution. Thus, the two-way travel time method was employed.

5.3.2. Concrete Cover & Rebar Location

The thickness of the concrete cover is an indication of the construction quality. Bridge deck areas with insufficient cover are often associated with higher levels of corrosion, potential presence of delamination, and higher concentrations of moisture. Concrete cover plays a significant role in protecting the rebars from corrosion. When GPR approaches above a rebar, Figure 5.1, the two-way travel time versus travel distance has a parabolic shape, Equation 2 (Al-Qadi et al., 2005).

$$t^2 = \frac{4}{v^2}x^2 - \frac{8x_0}{v^2}x + t_0^2 + \frac{4x_0^2}{v^2} \tag{5-2}$$

where *t* is two-way travel time, *x* is the travel distance, *v* is the EM wave speed in concrete, and $d_0 = vt_0/2$. When the reflected parabolic shape is fit to Equation 1, the distance from the apex to the surface is the cover depth.

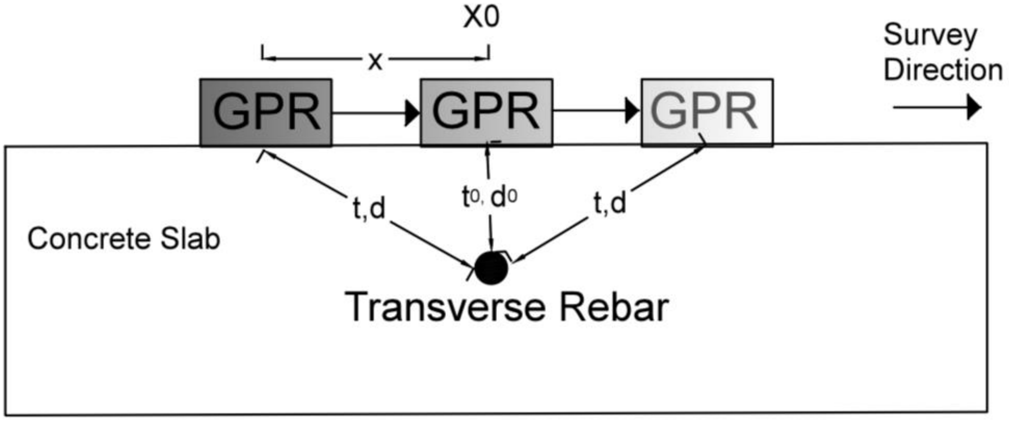

Figure 5.1. GPR travel time and distance for a rebar in concrete (Al-Qadi et al., 2005).

5.3.3. Corrosion of Rebar

The attenuation of the signal reflection amplitude from a rebar in relation to the remaining reflections indicates corrosion potential. GPR has been proven to be successful in detecting active corroded areas in many studies (Cady and Gannon, 1992; Barnes and Trottier, 2000; Barnes et al., 2008; Sultan and Washer, 2017). ASTM D6087 recommends two approaches for detecting deterioration at the top of reinforcing rebars; “the bottom deck reflection attenuation technique;” and, the “top reinforcing reflection attenuation technique”. Both approaches employ signal reflection amplitudes. In the “bottom deck reflection attenuation technique” deterioration is detected based on the relative reflection amplitudes from the surface and the bottom of the bridge deck. In the “top reinforcing reflection attenuation technique” the relative reflection amplitudes from the top layer of reinforcement are used to assess deterioration. Further details of both methods are provided in ASTM D6087. The attenuation of signals that can be observed in B-scans are due to the variation in amplitude of the reflected signals. ASTM D6087-15 suggests that reflections with 6 to 8 dB less than the maximum amplitude observed represent potentially corroded areas. Dinh et al. (2014) showed that the deriving correlation coefficient between time series data of GPR acquired at different time slots, can be one of the methods for detecting corrosion of the rebars. In that method, the GPR time series data at any age of a bridge deck should be compared with the reference time series data of the same bridge deck. The reference data can be acquired at early ages when the bridge deck and rebar are still sound and healthy. Generally, since the correlation coefficient varies from 0 to 1, when a correlation coefficient between a specific age and the reference data is closer to 1 indicates healthier rebars and bridge deck (Dinh et al., 2014). Martino et al. (2014) proposed a statistical model to evaluate the condition of the rebars. The model suggested that the amplitude histogram for a healthy bridge deck is quite symmetric and almost perfectly normal.

5.3.4. Effect of Moisture

The dielectric constant of pavement materials ranges from 4 to 10, whereas the dielectric constant of water is 81. Thus, the presence of moisture will locally alter the reflection and transmission pattern (Maser, 1996; Goulias et al., 2015; Goulias, 2017a). Presence of moisture leads to an increase in wave attenuation and a decrease in the velocity of the electromagnetic wave (Li et al., 2015). Goulias and Scott (2015), used Short Time Fourier Transform analysis, STFT, to identify the areas with moisture concentration. It indicated that the presence of moisture appears in the form of time delay in the time domain of GPR data, Figure 2, and reduces the frequency and energy of the signal. Figure 5.2 illustrates an analytical waveform of moist versus dry concrete in the time domain diagram. It also indicates that the back-surface reflection of the moist deck is delayed versus the dry bridge deck, and that moisture related dispersion reduces the bottom surface signal energy. With two dimensional STFT analysis (a frequency versus time representation of the amplitude versus time information), reduced high frequency content and reduced signal amplitudes are observed (both caused by moisture dispersion phenomena). Thus, a time delay associated with the presence of moisture is observed. By using these analyses, a relative moisture map for the examined bridge deck can be generated, differentiating high moisture content areas from lower ones.

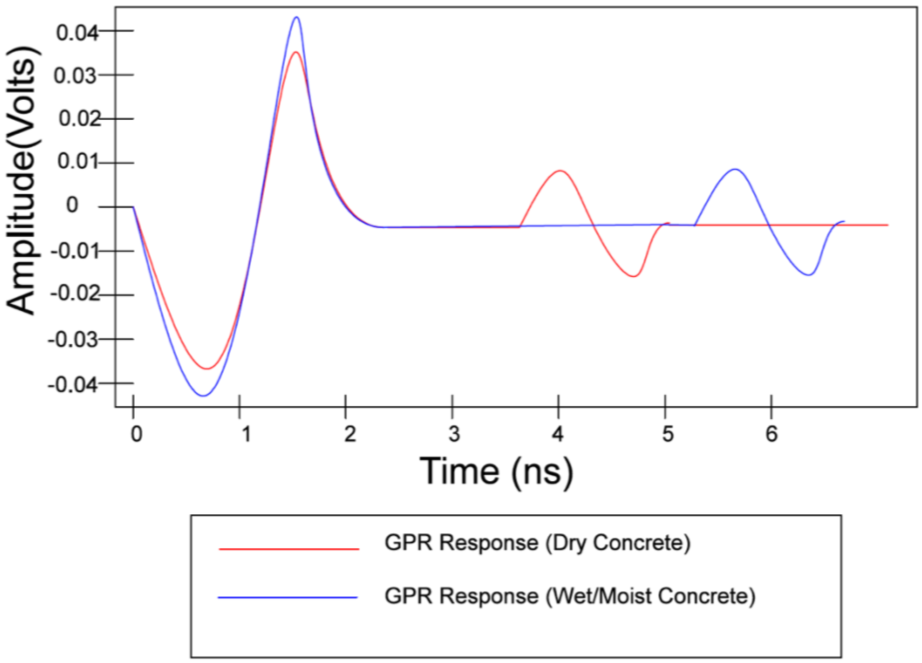

Figure 5.2. Schematic example of waveform of time domain bridge deck GPR, comparison of wet vs. dry. (Goulias and Scott, 2015)

5.4. Characteristic of Surveyed Bridge Deck & GPR Data Collection

The GPR data were collected on a bridge closed to traffic on the Siracusana state road 124 (SS 124). The state road SS 124 is an Italian highway that crosses the south-eastern portion of Sicily in the east-west direction. The bridge was constructed and opened to traffic in the early ‘90s. The bridge is supported by a series of pillars that are about 32 meters apart. In each section bound by two pillars, the deck consists of 5 cross and 4 longitudinal beams. Along the bridge deck examined are two open joints at 88 and 185 m from the starting point. The bridge consists of two lanes both of which are 3.75 meters wide. The width of the entire roadway is 9.45 meters where 7.50 meters is the width of the travel lanes while the shoulders have a width of about 1 meter. A section of the bridge with a length of approximately 320 meters was examined with GPR (i.e., georadar). In order to map the surface of the bridge deck (Figure 5.3b) a grid was created consisting of 5 longitudinal GPR surveys that covered the entire roadway, and 21 transversal surveys, Figure 5.3. The longitudinal alignment with path numbers 1, 3 and 5 were surveyed from the start point to the end point, as shown in Figure 5.3a, while paths 2 and 4 were surveyed in the opposite direction. The transverse survey paths have perpendicular direction and were investigated on the central portion of the bridge, covering the entire cross section between the longitudinal alignments 1 and 3. The first two transverse alignments were at the first visible joint, joint 1, while the subsequent alignments were three meters from the previous one. Assessing the GPR accuracy in thickness detection was achieved through site inspections on the two open joints by directly measuring layer thicknesses, and by drilling inspection holes 4 cm deep at a distance of 16 m from joint 1, Figure 5.4a and Figure 5.4b, respectively. Bridge design and construction drawings for these types of precast concrete bridges built in the region of Catania at the same time and using the same designs were also considered for complementing the "ground truth" conditions. The near ground-coupled georadar GPR system used in this study consisted of transmitting and receiving components, a wave reading and a graphic return system. The georadar belongs to the University of Catania Road Testing Laboratory, "TILAB". It is equipped with 2 antennas of 2000 and 600 MHz frequencies that can provide high resolution measurements. The georadar was capable of investigating depths of a few meters from the road surface.

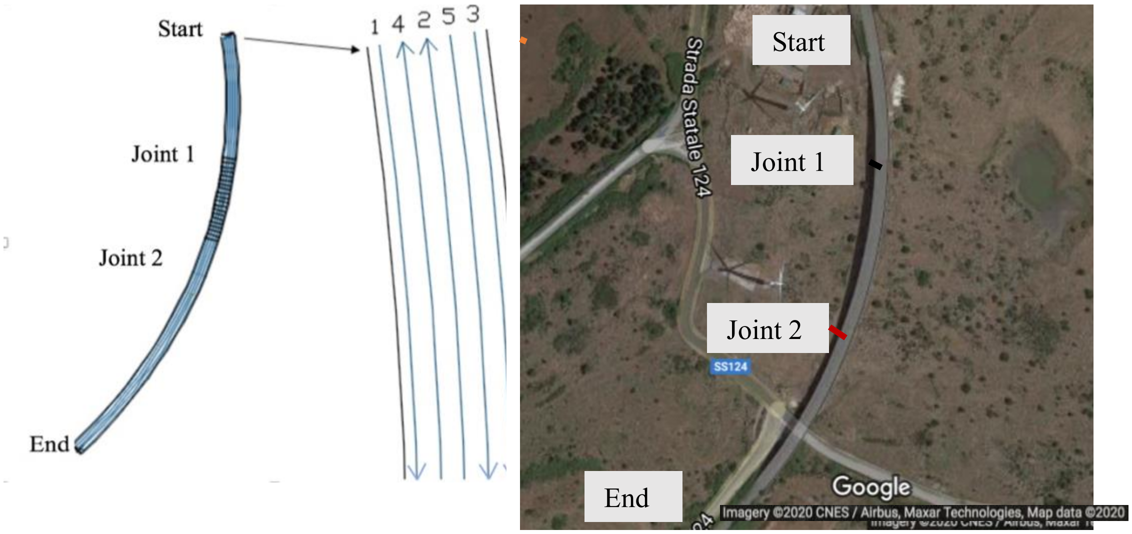
Start
Joint 1
Joint 2
End
1 4 2 5 3
Strada Statale 124
Start
Joint 1
Joint 2
SS124
End
Google
Imagery ©2020 CNES / Airbus, Maxar Technologies, Map data ©2020

(a) **(b)**

Figure 5.3. GPR Surveys and bridge deck joints, a) Survey alignments, b) Overall view of survey paths (image source: Google©2020).

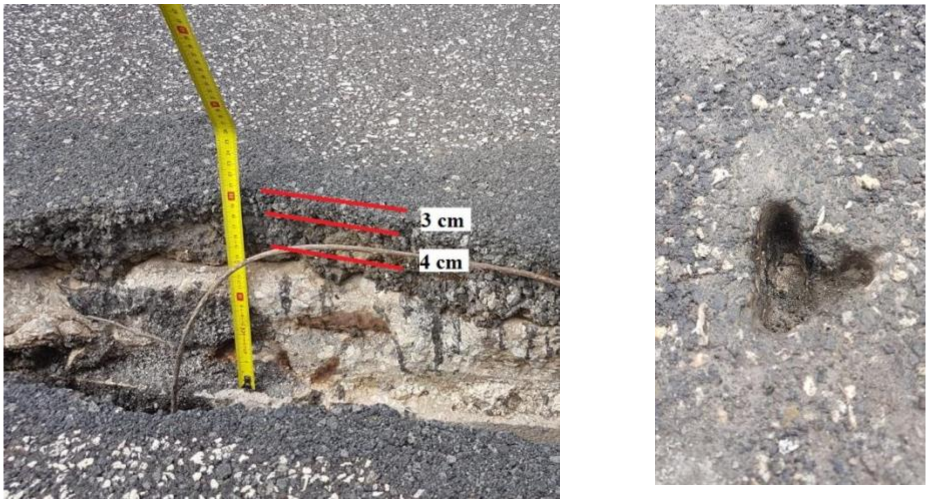

(a) **(b)**

Figure 5.4. Open joint measurements and drilled holes, a) Open joint 1, b) Drilled holes.

5.5. Signal Processing

Before any post processing analysis for detecting thickness, cover depth, rebar location, and other condition parameters, preliminary processing of the raw signals is needed in order to filter out possible noise. The signal processing included the following.

5.5.1. Time-zero Correction

For air-coupled and near ground-coupled GPR the gap of air between the antenna(s) and the surface of the pavement under investigation should be eliminated in order to compare the reflection time, and depth of inhomogeneity at different locations of the survey path. To this aim, a fixed and unique point as a time-zero reference for the GPR data should be selected. Since in this study a near ground-coupled GPR was employed, in contrast with an air-coupled which is usually mounted on a fast-moving vehicle, the fluctuations were negligible. Therefore, the distance between antenna and the ground surface has been measured and considered as a gap that should be removed to find the reference point. After the time-zero correction is applied, the distance to the surface of the inspected area (asphalt overlay in this case) is equal to zero.

5.5.2. Band-pass Filtering

Human-induced or antenna ringing noises should be removed by filtering in order to improve visual quality of the data. Filtering methods can be simple such as band-pass filters, or more complex involving domain and transfer filters. The higher complexity filter does not necessarily produce better results. In the frequency domain, low or high-pass filters are common. In a low-pass filter only low-frequency components of the data are considered. This approach is effective in producing noise reduction. On the contrary, in a high-pass filter only high-frequency components of the data are considered. This approach is suitable for removing signal drifts and low frequencies. A band-pass filter is a combination of low and high-pass filters. The range of frequency components considered are defined as the “pass region” (Jol, 2008). These filters remove noise for frequencies higher or lower than the GPR main frequency. The selected range should not be too narrow to avoid losing useful data. Cassidy and Jol (2009) suggested that the pass region should be set symmetrically around the peak signal frequency with a bandwidth equal to 1.5 times the peak value. Thus, for an antenna with a central frequency of 2000 MHz the band-pass would be at least 500 to 3500 MHz (bandwidth equal to 1.5 x 2,000=3,000 MHz, centered and symmetric around the central frequency of 2,000 MHz, thus providing a bandpass of 500 to 3500 MHz).

5.5.3. Background Removal

The “non-target” environment, such as rocks, sands and cavities, and electromagnetic devices like cell phones add noise to the reflected signal. Different filtering methods can be used for removing those background noises in order to increase signal-to-noise ratio (SNR) and produce a high-quality image. In most cases, the noisy components periodically appear in the horizontal axis. Thus, a Clear-X filtering algorithm is used to remove unwanted components along the x-axis (Hashim et al., 2011). This process is called background removal and the method used is subtracting the mean value of the amplitude (or median in some cases) from each A-scan as described in Equation 3 (Benedetto et al., 2017).

$$y'(n) = y(n) - \frac{1}{K}\sum_{k=1}^{K} y_k(n) \qquad (5\text{-}3)$$

with $y(n)$ and $y'(n)$ being the amplitude of the nth sample of the processed and raw trace respectively, and with n ranging from 1 to N. After applying the background removal by the average of the amplitude for each A-scan, the probability distribution of amplitude is obtained which would be symmetric along the A-scan.

5.6. Analysis & Results

5.6.1. Asphalt Overlay Thickness

To determine the thickness of the overlay and its uniformity the analysis was carried out at the vicinity of the joints. Figure 5.5 shows the thickness detection at the two open joints 1 and 2. Since a high frequency antenna gives a better resolution the signal from the 2000 MHz antenna was used. From the B-Scan of joint 1, Figure 5.5a, three different interfaces are detected at depths of 3, 6 and 10 cm for the location milepost 86 preceding joint 1, and at depths of 4, 8 and 11 cm after joint 1, at milepost 89. The A-scan at these locations, Figures 5.6a and 5.6b, provide the signal amplitude peaks at the aforementioned depths. The one to two cm difference between the depths of the various layers at the locations before and after joint 1, verified as well with the "ground truth" inspection surveys at the vicinity of the joint, can be associated with long term permanent damage or as-built construction quality. For example, long term deterioration in concrete, rebar corrosion and presence of delamination as well as cracking may very well affect a portion of the bridge deck producing such variability in measured thicknesses from one section to the next of the joint. In terms of construction quality and uniformity, joints represent a transition from one section to the next of the bridge deck. Thus, one to two cm deviation from the specified target design features may very well reflect "as-built" construction quality and/or specified tolerances. The layer thicknesses from the GPR scans have been validated by physically measuring such thicknesses at the open joints and the drilled holes, Figure 5.4.

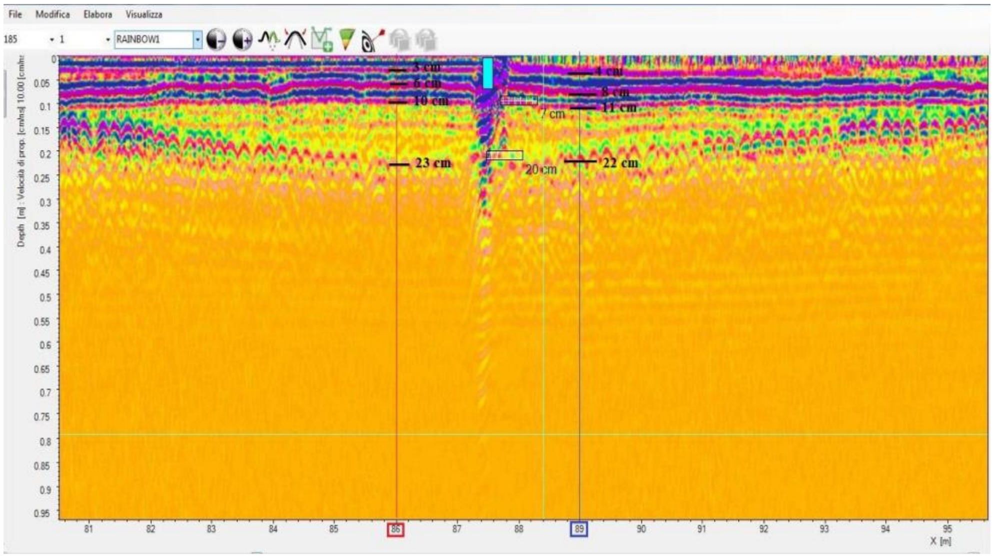
File
Modifica
Elabora
Visualizza
185
1
RAINBOW1
Depth [m] : Velocità di prop. [cm/ns] 10.00 [cm/ns]
0
0.05
0.1
0.15
0.2
0.25
0.3
0.35
0.4
0.45
0.5
0.55
0.6
0.65
0.7
0.75
0.8
0.85
0.9
0.95
3 cm
6 cm
10 cm
23 cm
7 cm
20 cm
4 cm
8 cm
11 cm
22 cm
81
82
83
84
85
86
87
88
89
90
91
92
93
94
95
X [m]

(a)

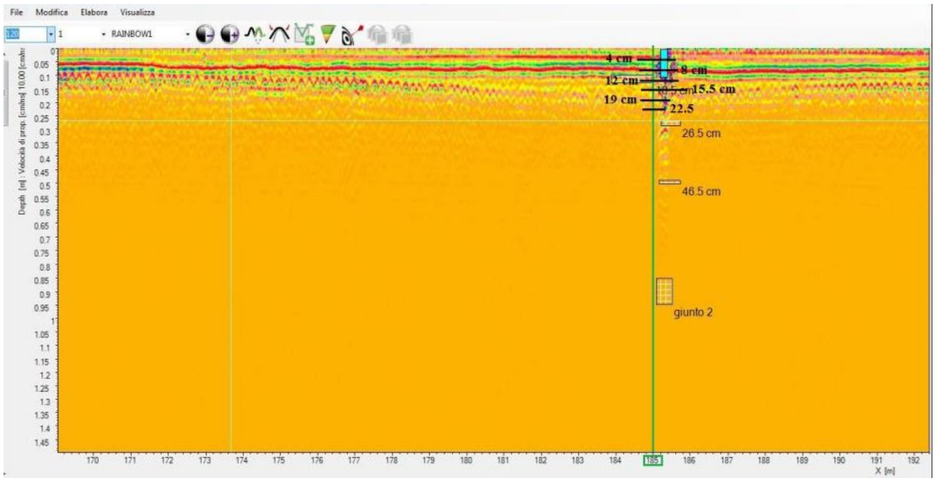
File
Modifica
Elabora
Visualizza
RAINBOW1
Depth [m] - Velocità di prop. [cm/ns] 10.00 [cm/ns]
4 cm
8 cm
12 cm
10.5 cm
15.5 cm
19 cm
22.5
26.5 cm
46.5 cm
giunto 2
X [m]

(b)

Figure 5.5. GPR B-Scan with depth of asphalt overlay at location close to a) joint 1, and b) joint 2.

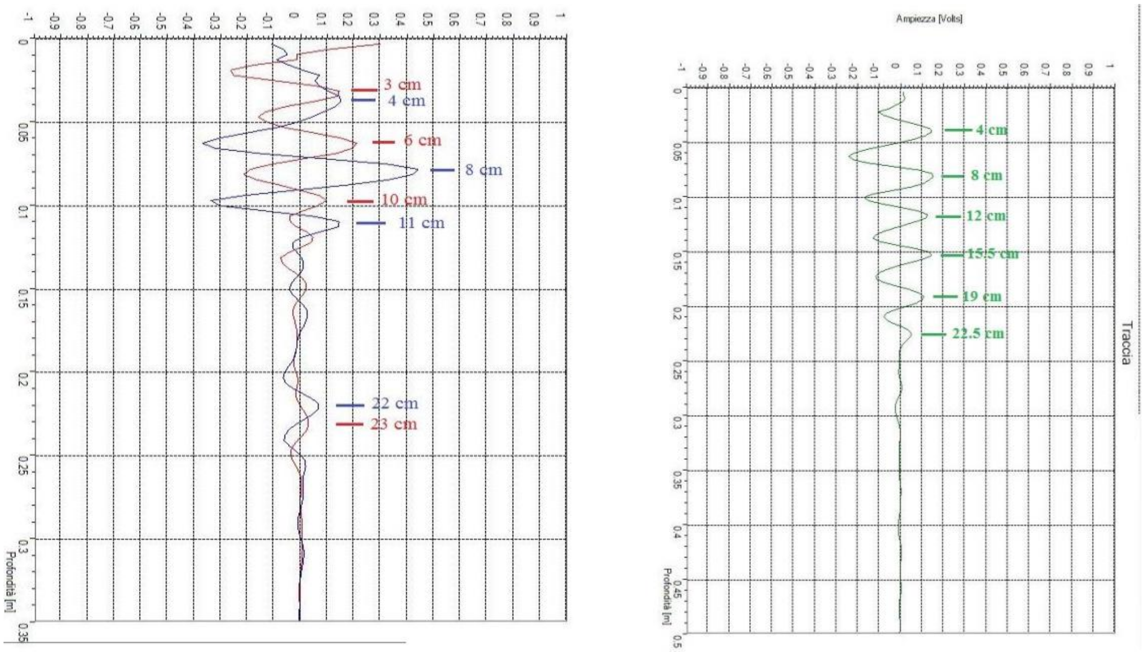

(a) (b)

Figure 5.6. A-scan of GPR for locations close to a) joint 1, and b) joint 2.

Note: red, blue, and green traces correspond to mileposts 86, 89 and 185, respectively.

5.6.2. Cover Depth and Reinforcement Condition

The bridge under investigation is supported by a series of pillars that are about 32 meters apart. The hyperbolas identified in the radargram indicate the location of the rebars that have a curved pattern with nadir at the pillars. An attenuation of the signal is observed at specific locations of the rebars reflecting the presence of moisture and deterioration/corrosion. To quantify the potential effects of the presence of open joints on signal attenuation (i.e., infiltration of moisture producing corrosion and concrete deterioration) the A-scans at different locations of the radargram were examined and compared. These were located near the pillars (joint 1) and in the center distance between two consecutive pillars. First the responses at two locations were compared: one 3 meters before joint 1, milepost 84; and the second one 3 meters after joint 1, milepost 91. The distance of 3 m was chosen so that any interference from the presence of the pillar is negligible. In Figure 5.7a the vertical lines represent the respective locations of the analyzed traces. The A-scans in Figure 5.7b reveal similar results for the two locations. However, the depth of reinforcement at milepost 84 is at 20 cm while for milepost 91 is at 21 cm. Below the reinforcement the signal starts to attenuate faster for milepost 91 relative to milepost 84.

Next the signals of two other locations were examined, one in close proximity to the pillar and the second one halfway between the pillars. This analysis was carried out considering the first open joint, joint 1, above the pillar. The objective was to assess whether the presence of pillars or open joints had an influence on signal response.

In Figure 5.8a the vertical lines represent the positions of the analyzed signal traces at mileposts 72 and 86. The green line is located at 86 meters from the starting point of the GPR surveys and corresponds to the first open joint. The red line is at 72 meters and represents the middle point between the pillars. The depths of the hyperbolas are respectively 24 cm and 14 cm, thus there is a difference of 10 cm. The same difference of 10 cm was detected on all the successive pillars of the longitudinal surveys.

Signal traces for these two locations are shown in Figure 5.8b. Consequently, the two signals are similar up to the depth of 10 cm in terms of amplitude and location of positive and negative peaks. After this depth the signal of the location close to the pillar (open joint 1) begins to attenuate faster than the signal of the farther away location from the pillar. Since milepost 86 is close to the open joint, the water infiltration produces corrosion and concrete deterioration in this location.

From the comparison of signal traces at locations away from the open joints and pillars it is concluded that the detected GPR signal is not influenced, and thus there is no signal interference affecting the curvilinear form of the hyperboles in the radargram. Thus, due to the curvature shape of the reinforcement present in these pre-stressed concrete slabs the concrete cover has the highest thickness at pillars, around 24 to 25 cm, and the lowest in the middle between two pillars, at about 14 cm.

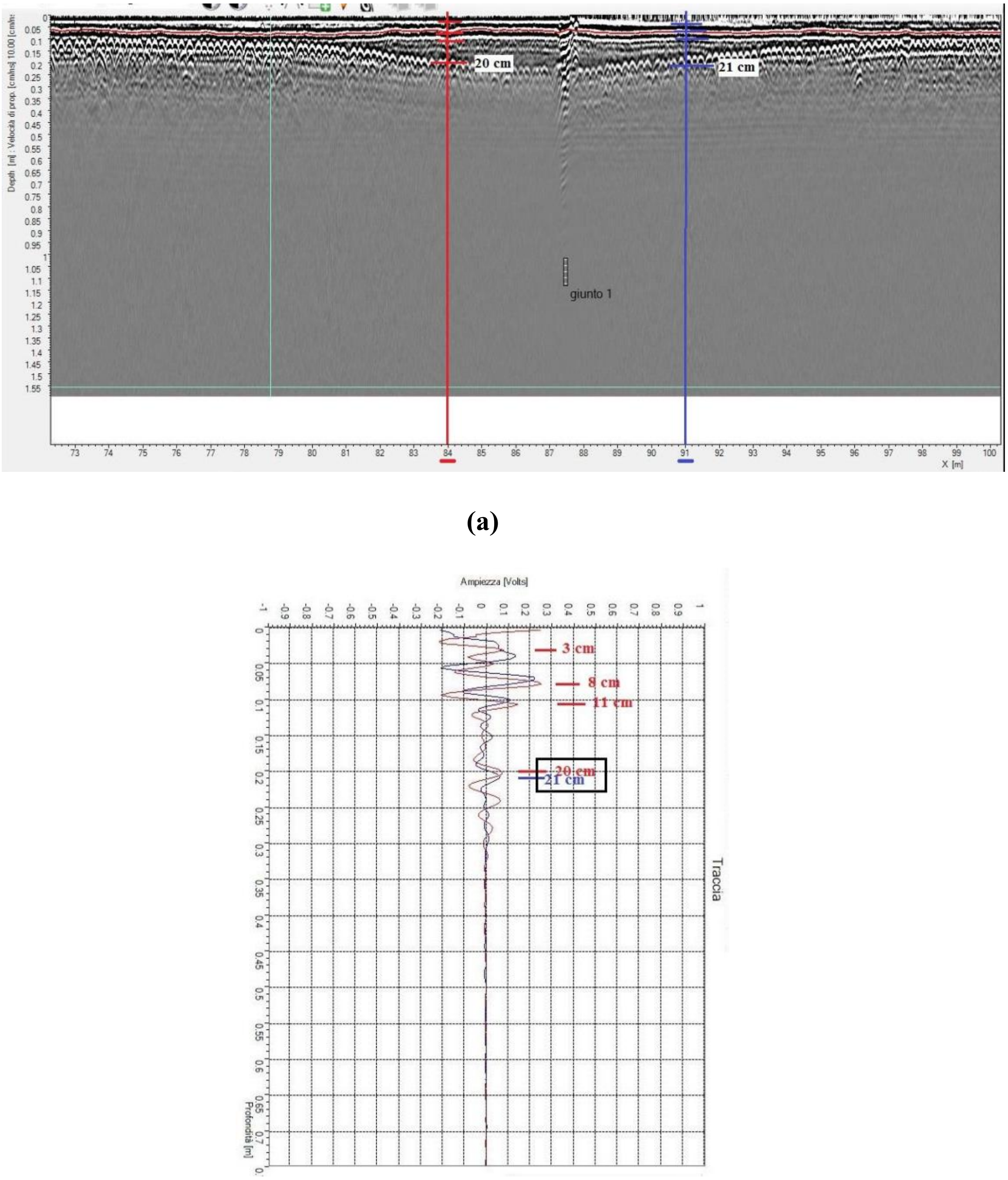

(a)

(b)

Figure 5.7. GPR signal at the proximity of joint 1. a) B-scan, b) A-scan.

Note: red and blue signal traces correspond to mileposts 84 and 91, respectively.

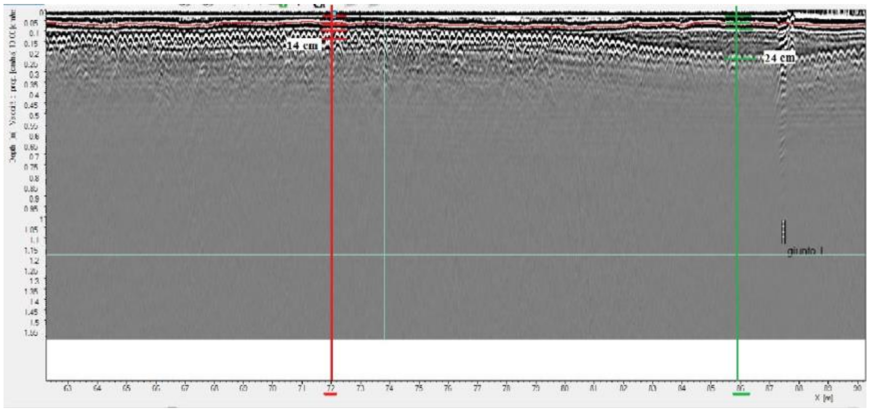

(a)

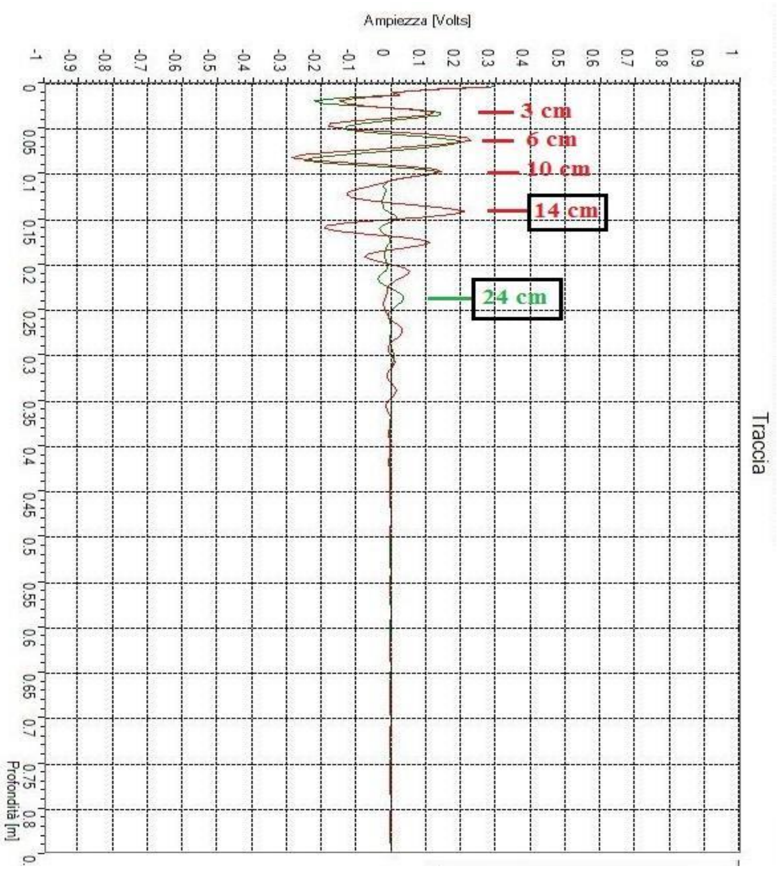

(b)

Figure 5.8. GPR signal at mileposts 72 (green) and 86 (red). a) B-scan, b) A-scan.

5.6.3. Rebar Conditions

It is expected that potential corrosion of the reinforcement will considerably decrease the amplitude of the reflected signal. Another factor influencing this amplitude is the depth of the examined object (rebar). In order to assess if the observed signal attenuation was caused by rebar corrosion, consecutive hyperboles at the same depths were compared.

Examining the B-scan of Figures 5.9a and 5.9b it can be observed that there are missing hyperbolas in some locations. Example locations of missing hyperbolas include at around 7 m from the pillar, Figure 5.9, at mileposts 28 m to 29 m from the starting location of the GPR survey. The A-scans of Figure 5.10 indicate that corrosion of the rebars is present in this same area. The signal amplitudes at a depth of 17 cm at mileposts 28.7 m and 29.2 m are 0.2 and 0.02 volts respectively. Therefore, such a difference in decibels (calculated from $A_{db} = 20 \times logA$, where A_{db} is the reflection amplitude in decibels, A is the reinforcement reflection amplitude) is more than 20 dB, which surpasses the threshold identified by ASTM C6087-15 (i.e., 6 to 8 dB). The time delay in signal propagation at milepost 28.7 from the starting location of the GPR survey and at depths of 21 cm and 24 cm indicates the presence of moisture. Presence of moisture and corrosion of rebars in the proximity of the pillars is expected since the joints are open and thus moisture can easily penetrate and reach the exposed rebars.

5.7. Summary & Conclusion

In this study, a bi-static GPR system was employed in order to inspect the bridge deck of an old precast concrete bridge in south Italy due to concerns of its condition. The pre-stressed bridge deck slabs placed on the pillars had exposed joints. Therefore, the layers' thicknesses detected by GPR could be directly measured at those locations. Furthermore, drilled inspection holes provided additional verification of layer thicknesses at other locations for ground truth evaluation. The analysis approach of the reflected signals proposed in this study provided significant conclusions on the condition of the bridge deck. At the open joint locations, material deterioration and reinforcement corrosion were detected from signal attenuation due to environmental exposure and moisture concentration. Overlay thickness and curvature of the reinforcement throughout the bridge spans was detected as well, along with the location of missing rebars.

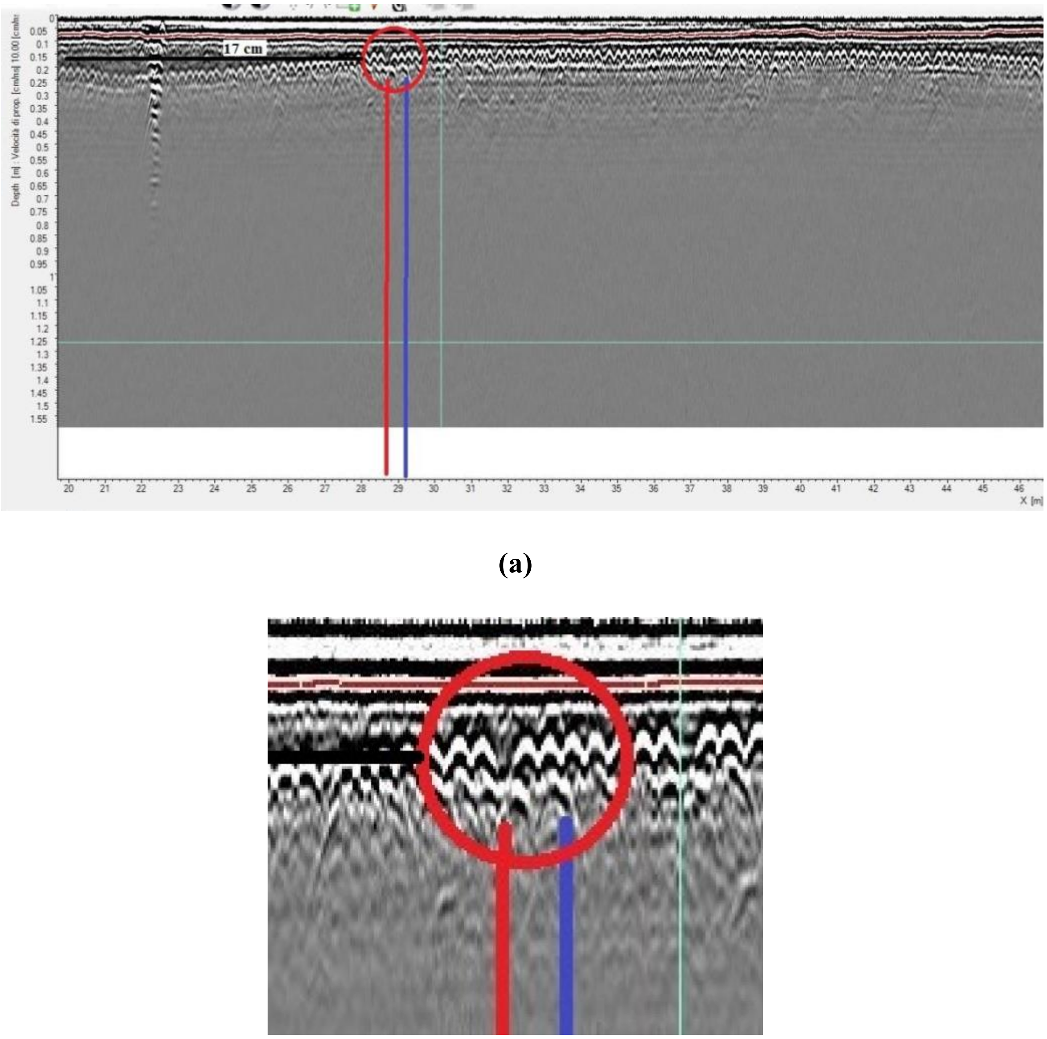

(a)

(b)

Figure 5.9. GPR signal at mileposts 28.7 and 29.2m, a) B-Scan, b) Enlarged B-scan.

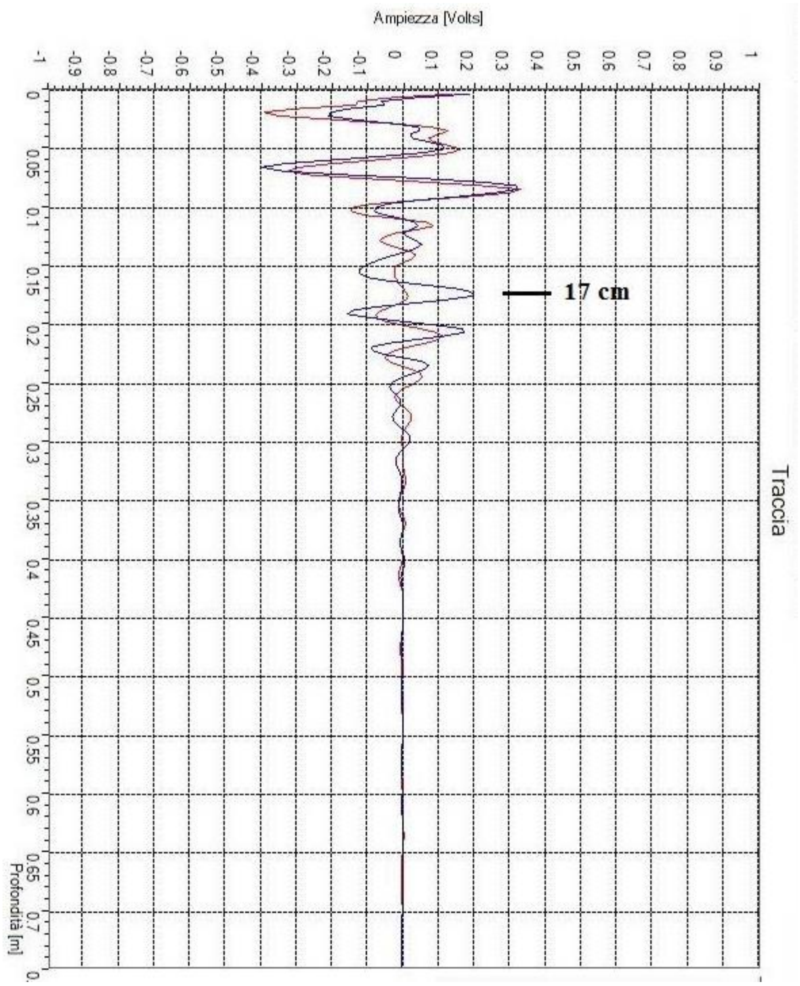

Figure 5.10. GPR signal at mileposts 28.7 m (red) and 29.2 m (blue), A-Scan.

Chapter 6. Development of Alternative Sequence Classification Networks for Predicting Condition Rating of Bridge Decks

6.1. Introduction

The deterioration and required maintenance of critical infrastructure components, such as highways and bridges, requires billions of dollars of federal funding for many years (Fiocco, 1998; ASCE 2021; FHWA, 2021). Bridge inspection and data collection are a crucial part of Bridge Management System (BMS) for effective maintenance and rehabilitation investments. Regularly scheduled bridge inspections are currently the norm in the US since they provide valuable information in current condition and input for life cycle assessment. Furthermore, the Federal Highway Administration (FHWA) requires the regular inspection of such critical infrastructure components. The condition survey data of US bridges are stored in the National Bridge Inventory (NBI) database since 1992. Such database can be used to build data-driven models to predict the condition of highway bridges. Accurate condition predictions of bridges will provide reliable input for effective management and rehabilitation strategies and optimal allocation of resources and increased safety.

Current efforts in predicting condition ratings of bridges include base models, survival models, and machine learning, ML, models. Base models are deterministic statistic-based models using historical data of bridge condition ratings from one set of bridges to forecast the condition of similar bridges. Survival models are probabilistic deterioration models based on a combination of survival analysis and Markov chain theory. In survival analysis, the remaining life of a bridge structure is calculated statistically. Thus, in the case of bridge deck condition the remaining life, in terms of deterioration to change into the following lower level of condition, is statistically determined. ML models are developed to forecast bridge conditions using deep learning algorithms. Under the Federal highway long-term bridge performance (LTBP) program an interactive web-based tool, InfoBridge, was developed that utilizes the three methods to predict the condition index of bridges (FHWA, 2021).

Contrary to the base and survival models, ML models (i) can predict the condition rating of bridge decks with different length of input data, and (ii) can capture highly complex relations between variables and features (i.e., parameters affecting bridge performance), that otherwise may be challenging when relying on just engineering judgment.

Machine learning methods have been used in civil engineering applications such as concrete strength prediction (Chou et al., 2014; Yu et al., 2018; Nguyen et al., 2019), structural damage recognition (Mangalathu & Jeon, 2019) and other areas. Gao & Elzarka (2021) utilized a Decision Tree algorithm for scheduling culvert inspection based on their condition. Khalef & El-adaway (2021) employed natural language processing (NLP) and machine learning classifiers, such as K-nearest neighbor (KNN), support vector machine (SVM), decision tree, XGBoost, and others, to identify significant changes in federal aviation administration (FAA) contracts.

Huang (2010) used artificial neural network (ANN) to predict the bridge deterioration by pattern classification with accuracy of 75.39%. Nguyen and Dinh (2019) employed ANN on NBI data, by using only 8 parameters as input features to predict the condition rate of the bridge decks with accuracy of 73.6%. A sensitivity analysis also showed that most important predicting features are the age of the structure and the design load. Liu and Zhang (2020) developed a model to forecast bridge deck conditions from 26 NBI features and 2 climate factors (i.e., annual number of freeze-thaw cycles and annual number of snowfalls). The study generated a convolutional neural network (CNN) which is useful when dealing with sequential data. However, to avoid inconsistency among condition ratings in the NBI database bridges with ascending condition rating were eliminated. Assaad & El-adaway (2020) employed artificial neural network (ANN) and K-nearest neighbor to predict the bridge deck condition. They showed that ANN can outperform the K-nearest neighbor model on Missouri NBI data by providing an accuracy of 91.44% versus 89.88%.

Objective of this study was to develop alternative ML algorithms that better capture the highly complex relations between variables and features (i.e., parameters affecting bridge performance), by using sequential classification models and deep learning. Both long short-term memory (LSTM) and convolutional neural network (CNN) were utilized to predict the condition rating of bridge decks. Data quality and processing, network architecture and performance assessment approaches are presented along with the models and study findings. In this study, a preliminary statistical analysis was performed on the NBI data to find the most relevant predictors. In addition, wider range of data (bridges of the states of Maryland and Massachusetts) were used in order to develop predicting model responsive to wider range of conditions. Selected models developed in this study outperformed those from previous studies. The results of sequence-to-sequence classification of a CNN on a subset of data (bridges with at least 10 records of condition index) showed the accuracy of more than 97% in estimating bridge condition.

6.2. National Bridge Inventory (NBI) database

The NBI database includes data from 617,084 bridges nationwide collected since 1992 (FHWA, 2020). From these, 5402 are located in Maryland. While several engineering features are measured and included in the database, the intervals of inspection are usually determined by the individual states and should be conducted at least every 24-months. The NBI features can be categorized in one of the following classes: bridge identification, age, geometric data, navigation data, bridge classification, load rating and posting, proposed improvements, inspection data and condition ratings. Condition ratings are used to describe the existing, in-place bridge as compared to the as-built condition. Condition ratings are evaluated for deck, superstructure, substructure, and culvert. In this study, bridge deck condition rating was the focus of the analysis. While the NBI contains 137 features, some of these are correlated (FHWA 1995). For example, age can be calculated based on the inspection year and year built, or year reconstructed and year built. Therefore, a subset of these features was considered in this study, Table 6-1.

6.3. Neural Network for Sequence Data

After reviewing the NBI data for the above features, the format of the data was formulated to sequence data points for each bridge. These sequences do not qualify for time series forecasting due to the limited number of data points in some cases. On the other hand, ML can be trained to find bridges with similar conditions and behavior and predict the future condition. To this end, long short-term memory (LSTM) modeling was used, which is a form of recurrent neural network (RNN) and convolutional neural network (CNN) for sequence-to-one classification, and sequence-to-sequence classification. Figure 6.1 presents the models used for bridge sequence classification.

Table 6-1. Description of NBI features selected for analysis.

Category	No.	Feature	Description	Item Number	Data Type
Identification	1	Structure Number	Unique code for each bridge	8	-
	2&3	Longitude and latitude		16 & 17	Num[(a)]
Classification	4	Toll	Toll statues	20	Cat[(b)]
	5	Maintenance	Agencies responsible for the maintenance	21	Cat
Inspection	6	Date of inspection	Date of inspection	90	Num
	7	Designated Inspection Frequency	Number of months between designated inspections.	91	Num
Age and Service	8	Traffic lanes on the structure	The number of lanes being carried by the structure	28A	Num
	9	Average daily traffic (ADT)	Average daily traffic for the route.	29	Num
	10	Year of average daily traffic	The year represented by the ADT.	30	Num
	11	Percent of Truck Traffic		109	Num
	12	Age	Calculated from the difference between the current year (2020) and inspection year.	--	Num
Load Rating and Posting	13	Design load	indicate the live load for which the structure was designed	31	Cat
Structure Type and Material	14	Structure kind	Type of structure for the main span(s)	43A	Cat
	15	Structure Type	The predominant type of design and/or type of construction	43B	Cat
	16	Deck Structure Type	The type of deck system on the bridge (only concrete; class 1 and 2)	107	Cat
	17	Surface Type, Membrane Type, Deck Protection	Wearing surface and protective system of the bridge.	108 (A, B, C)	Cat
Geometric	18	Structure Length	Represent the length of the structure.	49	Num
Condition	19	Condition Rating of Deck	Describes the overall condition rating of the deck.	58	Cat

[(a)] Numerical

[(b)] Categorical

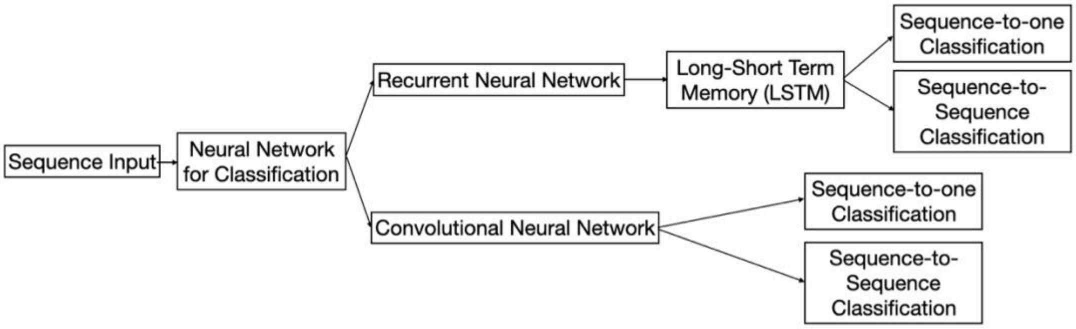
Sequence Input
Neural Network for Classification
Recurrent Neural Network
Convolutional Neural Network
Long-Short Term Memory (LSTM)
Sequence-to-one Classification
Sequence-to-Sequence Classification
Sequence-to-one Classification
Sequence-to-Sequence Classification

Figure 6.1. Summary of neural network models used for bridge sequence classification.

6.3.1. Long Short-Term Memory (LSTM)

This method classifies sequence data using a long short-term memory (LSTM) network. An LSTM network is a type of recurrent neural network (RNN) that learns long-term dependencies between time steps of sequence data. The structure of a LSTM cell is shown in Figure 6.2. The main difference between the RNN and LSTM is the presence of the gating system which controls the flow of information. The activation function of the gates is the sigmoid function with outputs of 0 and 1. The governing equations are (Wang et al., 2018):

$$i_t = \sigma(W_{xi}x_t + W_{hi}h_{t-1} + b_i) \quad (6\text{-}1)$$

$$f_t = \sigma(W_{xf}x_t + W_{hf}h_{t-1} + b_f) \quad (6\text{-}2)$$

$$o_t = \sigma(W_{xo}x_t + W_{ho}h_{t-1} + b_o) \quad (6\text{-}3)$$

$$c_t = f_t \odot c_{t-1} + i_t \odot tanh\,(W_{xc}x_t + W_{hc}h_{t-1} + b_c) \quad (6\text{-}4)$$

$$h_t = o_t \odot tanh\,(c_t) \quad (6\text{-}5)$$

Where: W is the weight and b is the bias; i, f, and o denote the input gate, forget gate, and output gate, respectively; c denotes memory cell and h denotes hidden vector sequence; σ is the activation function. Although the equations of the gates have the same form, the weight matrices are different in values and in their functions. Input gate controls information flowing into memory cell c_t. Forget gate controls information of the last memory cell c_{t-1} accumulated in the current memory cell c_t. The output gate influences information flowing into the hidden state h_t. With the system of gating units, the gradient is well controlled, thus preventing the gradients vanishing, or exploding problem, which is a major issue for RNNs.

The LSTM model inputs sequence data into a network and makes predictions based on the individual time steps of the sequence data. One of many advantages of LSTM is that the length of each sequence can be different, considering the difference in record length for each bridge or feature in the NBI data. Thus, such an ML approach is suitable for this modeling.

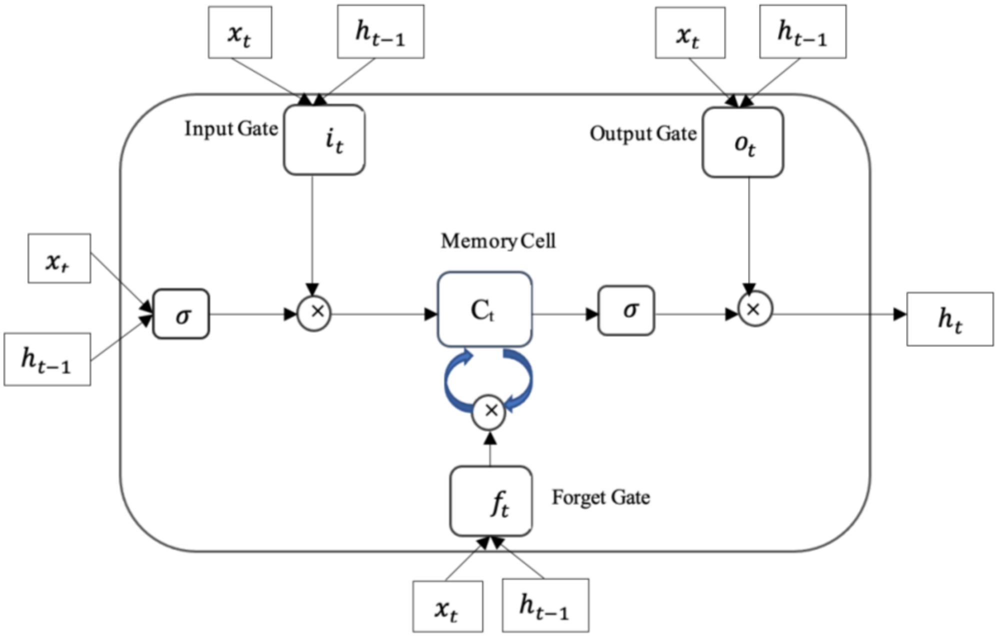
x_t
h_{t-1}
x_t
h_{t-1}
Input Gate
i_t
Output Gate
o_t
Memory Cell
x_t
h_{t-1}
σ
×
C_t
σ
×
h_t
×
f_t
Forget Gate
x_t
h_{t-1}

Figure 6.2. Long short_term memory cell (Wang et al., 2018).

6.3.1.1. Network Architecture

The long short-term memory (LSTM) network modeled in this study includes a sequence input layer, a BiLSTM layer, a fully connected layer, a softmax layer, and a classification layer. Each layer is briefly described next:

- ***Sequence Input Layer*:** A sequence input layer inputs sequence data to a network.
- ***BiLSTM Layer*:** As opposed to conventional RNN, which as a forward network can only exploit input data, in LSTM, a bidirectional layer can be employed. A bidirectional LSTM (BiLSTM) layer learns bidirectional long-term dependencies between time steps of time series or sequence data in both forward and backward directions. Figure 6.3 presents a BiLSTM layer.

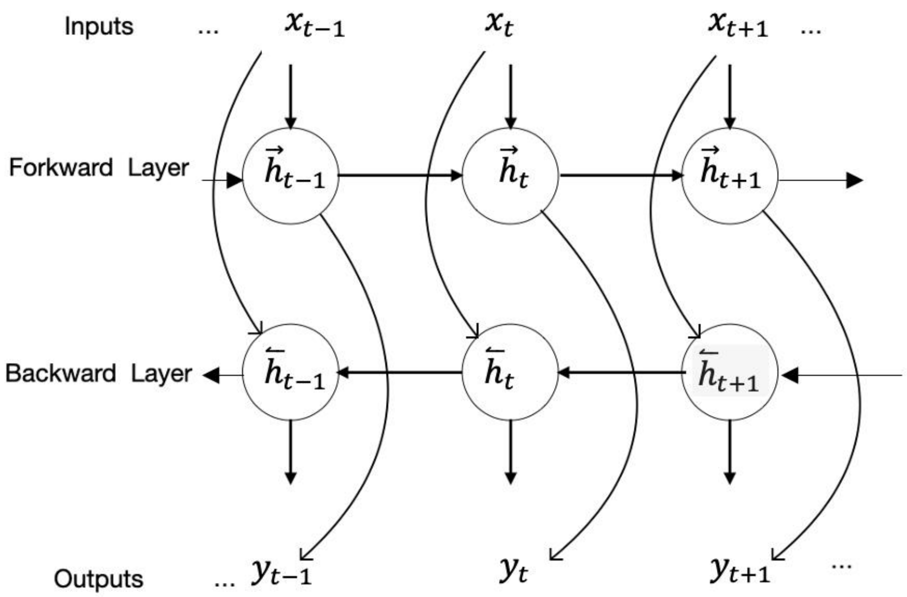

Figure 6.3. Bidirectional long short_term memory layer (Wang et al., 2018).

- ***Softmax Layer****:* A softmax layer applies a softmax function to the input. A Softmax layer is used when there are multiple classes as output. In the softmax layer, input, which is a vector x of k real numbers, is normalized into a probability distribution consisting of k probabilities proportional to the exponentials of the input numbers.
- ***Classification Layer:*** A classification layer computes the cross-entropy loss for multi-class classification problems with mutually exclusive classes. For typical classification networks, the classification layer must follow the softmax layer. In the classification layer, the train network takes the values from the softmax function and assigns each input to one of the K mutually exclusive classes, which refer to condition ratings in this study (0 to 9). The cross-entropy function is defined from (Bishop, 2006):

$$loss = -\sum_{i=1}^{N}\sum_{j=1}^{K} t_{ij} \ln y_{ij} \qquad (6\text{-}6)$$

where *N* is the number of samples, *K* is the number of classes, t_{ij} is the indicator that the ith sample (i.e., bridge) belongs to the jth class (i.e., condition rating), and y_{ij} is the output for sample *i* for class *j*, which in this case, is the value from the softmax function. That is the probability that the network associates the ith input with class *j*. Given a bridge (bridge *i*), y_{ij} vector includes the probabilities of that bridge belonging to each class (*j*). For example, y= (0.1, 0.1, 0, 0.1, 0, 0.2, 0, 0, 0, 0.5) means the probability that bridge *i* has a condition rating of 9 is 0.5, and that is the most probable class. Therefore, bridge *i* is classified as a bridge with a condition rating of 9.

6.3.1.2. Optimization Algorithm (Solver)

For improving the performance of the neural network, the loss should be minimized. A solution for this optimization problem is changing and updating the parameters in order to find the minimum for the loss function. A gradient-based model updates the parameters in the direction of the steepest descent. The amount of the update or size of each step is called the "learning rate". The learning rate can be constant for all epochs or can be reduced in uniform intervals. Stochastic gradient descent (SGD) performs a parameter (weights) update for each set of input and output that are present in the training set. The only problem is that its convergence behavior is usually unstable, especially for relatively larger learning rates and when the training datasets contain diverse examples. In a stochastic gradient descent approach with momentum, the convergence properties are improved. The momentum term has physical meanings. Momentum improves SGD to follow the dimensions in which gradients point in the same direction and avoid those dimensions in which gradients keep on changing directions (Ruder, 2016).

Another optimization method is adaptive moment estimation (ADAM), a method for efficient stochastic optimization that only requires first-order gradients with little memory requirement (Kingma and Ba, 2014). The method computes individual adaptive learning rates for different parameters from estimates of first and second moments of the gradients.

6.3.1.3. Sequence-to-one and Sequence-to-Sequence classification using LSTM

To train a deep neural network to classify the sequence data, a sequence-to-one or sequence-to-sequence LSTM network can be used. A sequence-to-sequence LSTM network can be employed to make different predictions for each individual time step of the sequence data. The architecture of sequence-to-sequence LSTM network used in this study is similar to sequence-to-one LSTM architecture, except a conventional LSTM layer is used instead of the BiLSTM layer. Contrary to sequence-to-one classification where the class of each sequence is the latest condition rating, in sequence-to-sequence classification input at each time step is labeled with the next inspection's condition rating. Architecture of both LSTM networks is shown in Figure 6.4.

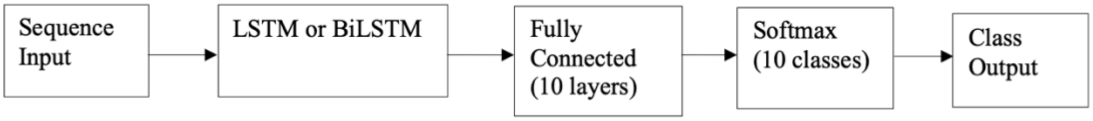

Figure 6.4. Architecture of LSTM networks.

6.3.2. Convolutional Neural Network (CNN)

There are three types of layers in a convolutional neural network: convolutional layers, pooling layers, and fully connected layers:

- ***Convolutional Layers (CONV):*** Convolutional neural network is a particular type of neural network developed for applying on two-dimensional image data. However, it can be employed for one-dimensional and three-dimensional data. Similar to a traditional neural network, a convolution is a linear operation which includes the multiplication of a set of weights with the input. Since this technique was designed for two-dimensional data, the multiplication is done for an array of input data and a two-dimensional array of weights, called a filter or a kernel. The filters are the "neurons" of the layer. They have input weights and output values. The input size is a fixed square called a patch or a receptive field. A convolution is the application of a filter to an input that results in an activation. Repeated application of the same filter to an input result in a map of activations called a feature map. A given filter scans across the entire previous layer and moves one time step at a time. Each position results in an activation of the neuron and the outputs are collected in the feature map. Every filter is a small window (with width and height, a.k.a. filter size), which extends through the full depth of the input volume. For example, a typical filter on the first layer of a CONV might have size 5x5x87 (i.e., 5 width and height, and 87 features). As the filter slides over the width and height of the input volume a 2-dimensional activation map is produced that gives the responses of that filter at every spatial position. A small filter size such as 1×1, 2×2, or 3×3 is simple and captures information from local data. Whereas a large filter size such a 5×5 filter is making the model more computationally expensive.

- ***Pooling Layers:*** After convolutional layer(s), pooling layers are used to generalize or compress the feature representations. Thus, by down-sampling the previous layers feature map, the overfitting of training data is reduced. There are two common techniques applied in a pooling layer, taking the average or the maximum of the input data to create its feature map.
- ***Fully Connected Layers (FC):*** Fully connected layers are the normal flat feed-forward neural network layer. Fully connected layers connect every neuron in one layer to every neuron in another layer.
- ***Dropout Layer:*** A relatively small and noisy training data set can lead to overfitting problems. In that case, the neural network learns from the noise in the data, which results in poor performance of the model when evaluated by a new data set (e.g., a testing data set). A dropout layer randomly drops data from input or sets input elements to zero. By doing so, the network architecture among iterations is changed and overfitting is avoided (Srivastava et al., 2014).

6.3.2.1. Sequence-to-Sequence Classification Using 1-D Convolutions (Temporal Convolutional Network, TCN)

Potential benefits of using temporal convolutional networks (TCN) can be: a) better computation parallelism (in contrast to RNN, where the predictions for later time steps must wait for their predecessors to complete); b) better control over the receptive field size (i.e., the receptive field size is more adjustable by stacking more dilated casual convolutional layer or increasing the filter size); c) better control of the network's memory footprint during training (contrary to LSTM, which take up a lot of memory to store partial results for its multiple cell gates. In a TCN the filters are shared across a layer; and d) more stable gradients (Bai et al., 2018).

A TCN architecture, shown in Figure 6.5, consists of multiple residual blocks, each containing two sets of dilated causal convolution layers with the same dilation factor, followed by normalization, ReLU activation, and spatial dropout layers. In a residual block, the value at the beginning of the block (x) is directly added to the end of the block ($x + F(x)$). A 1-by-1 convolution layer is included on the input for when input and output do not have the same dimension, and a final activation function is applied. While some of the layers were explained in the previous section, the remaining are described next.

- ***Dilated Casual Convolution:*** In order to enable very deep models (i.e., when there is more than one hidden layer) with a relatively reduced number of parameters, a suitable approach is to stack many convolution layers with small receptive fields. The main building block of a temporal convolutional network is a dilated causal convolution layer which operates over the time steps of each sequence. In this context, "causal" means that an output at time t is convolved only with data from time t and earlier in the previous layer, and no information is leaked from future to the past (Bai et al., 2018). To achieve large receptive field sizes the dilation factor of subsequent convolution layers is increased exponentially. Dilation is equivalent to bringing a fixed step between every two adjacent filter taps. For dilation factor (d) equal to 1, the dilated convolutional layer acts like a regular convolutional layer. When d increases, the convolutional layer captures a wider range of input from the previous layer (Bai et al., 2018).
- ***Instance Normalization:*** In order to give equal weight/importance to each feature, the continuous features should be normalized. The instance normalization function normalizes the input by first calculating the mean μ and the variance σ^2 for each observation over each input channel in each training example. Then it calculates the normalized activations as:

$$\hat{X} = \frac{X-\mu}{\sqrt{\sigma^2+\varepsilon}} \qquad (6\text{-}7)$$

where ε is a very small value to avoid zero in the denominator.

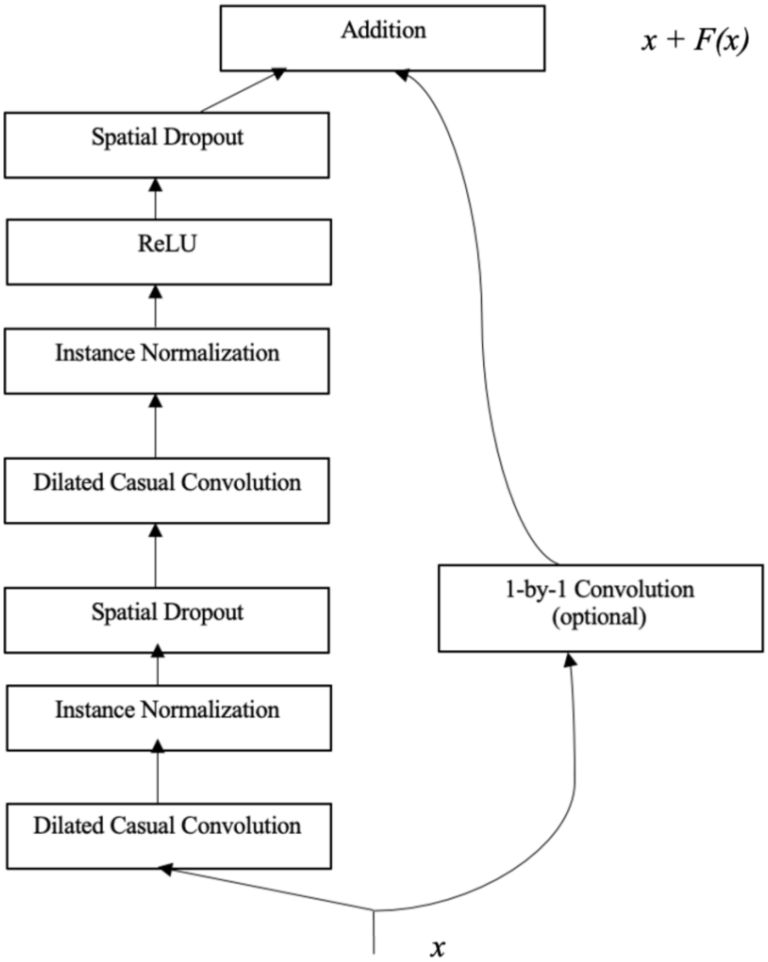
Addition
x + F(x)
Spatial Dropout
ReLU
Instance Normalization
Dilated Casual Convolution
Spatial Dropout
Instance Normalization
Dilated Casual Convolution
1-by-1 Convolution
(optional)
x

Figure 6.5. Architecture of temporal convolutional network (TCN).

- ***Rectifier Linear Unit (ReLU):*** In a neural network, the activation function is responsible for transforming the summed weighted input from the node into the activation of the node or output for that input. The rectified linear unit (ReLU) is a simple and quick activation function. The ReLU is a piecewise linear function that returns the input if the input is positive or returns zero, otherwise. Equation 6-8 describes the ReLU.

$$f_{ReLU}(x) = \begin{cases} x & x > 0 \\ 0 & x < 0 \end{cases} \tag{6-8}$$

The rectified linear activation function overcomes the vanishing gradient problem, allowing models to learn faster and perform better. The gradient of the loss function approaches zero, so-called vanished, when a lot of layers use specific activation functions such as the sigmoid function. The equation of the sigmoid function is as following:

$$S(x) = \frac{1}{1+e^{-x}} \quad (6\text{-}9)$$

As can be seen in Equation 6-9, the sigmoid function projects a large input space into a small output space between 0 and 1. Thus, even a large change in the input will appear only as a small change in the output.

- ***Spatial Dropout:*** As explained in the previous section, the role of dropout layer is avoiding overfitting. However, when adding the dropout layer before the 1×1 convolutional layer, generally increases the training time but does not prevent overfitting. Since the adjacent feature maps can be correlated, if only one of them is dropped, the outputs can still be correlated. On the other hand, in a spatial dropout layer, the adjacent cells in the dropped-out feature map are either all 0 (dropped-out) or all active. This method improves the performance of the model by keeping out the dependent cells (Tompson et al., 2015).

6.4. Data Pre-processing

As mentioned earlier, the performance of the alternative ML models was tested on Maryland bridges. In this study, concrete bridge decks with cast-in-place concrete and precast concrete were identified in the NBI deck structure type (item 107). The condition rating system is often qualitative and depends on the inspector's expertise and opinion. Din and Tang (2016) reported some of the challenges associated with the NBI data and employed spatial and temporal processing to identify outliers. The study concluded that one of the most important issues was reported increases in condition rating with no inputs in reconstruction or rehabilitation. In a machine learning approach, if these variations are not specified and identified, the model can be misleading or not accurate. Therefore, such instances require particular attention during the review of the dataset to be used in ML modeling. An example of such occurrence in increase of condition rating is shown in Figure 6.6. For example, for this bridge the condition rating increased from 5 to 6 and then again from 4 to 7. The first one can be due to either maintenance or difference in the inspector's judgment, but the second increase is believed to be due to maintenance. Thus, review of the dataset in ML modeling is an important step. In order to keep as much as possible of the useful information and a suitable size of the dataset for the analysis, the missing values can be inferred. Random forest is an approach that can be used to estimate missing data of continuous and/or categorical data. In this method, a random forest model is built for each variable. Then the model was used to predict missing values in the variable based on the observed values. The advantage of random forest method includes a) handling non-normally distributed data; and b) developing non-linear relationships among variables (Hong and Lynn, 2020). For example, the missing data of latitude, longitude, ADT, and year ADT were substituted by a combination of available records outside the NBI database and random forest estimates. For example, since there have been none, or more than one set of latitude and longitude for a specific bridge, latitude and longitude reported for bridges in a specific county were used. Random forest was employed to predict ADT and year ADT based on the bridge latitude, longitude, and available ADT data from historic traffic counts in the State.

Longitude and latitude of bridges were initially selected since the location of the bridge can be related to climate and weather conditions. Freeze and thaw cycles and thermal fatigue (related to changes in diurnal and night temperature) affect deck performance and condition. Total annual snowfall (SNOW, in millimeters) and number of days with snowfall greater than 1 inch (25 mm) (DSNW) were parameters selected from the National Centers for Environmental Information (NOAA) data base. Based on the longitude and latitude of each station in Maryland, the data of the closest station to each bridge was used to extract SNOW and DSNW for each year.

In the NBI database, bridges may have data with length of 1 to 27 records. Figure 6.7 provides the distribution of such records, while Figure 6.8, provides the distribution of bridges with different lengths of data sequence after removing bridges with irregular condition records.

In order to implement categorical data such as “Toll” or “Deck Structure Type”, one-hot encoding was employed. In the one-hot encoding method, the column including the categorical data is replaced by numerical columns, consisting of 0 and 1. Basically, each column is the response to the question of whether the case belongs to each category or not. For example, for feature “Deck Structure Type”, a column representing code 2 (concrete precast panel), includes 1 when the deck structure type is concrete precast panel, and 0 for other cases. This approach changes the number of columns/ features from 19 to 87. The continuous variables, except condition ratings, are normalized in order to assign equal weight/importance to each feature.

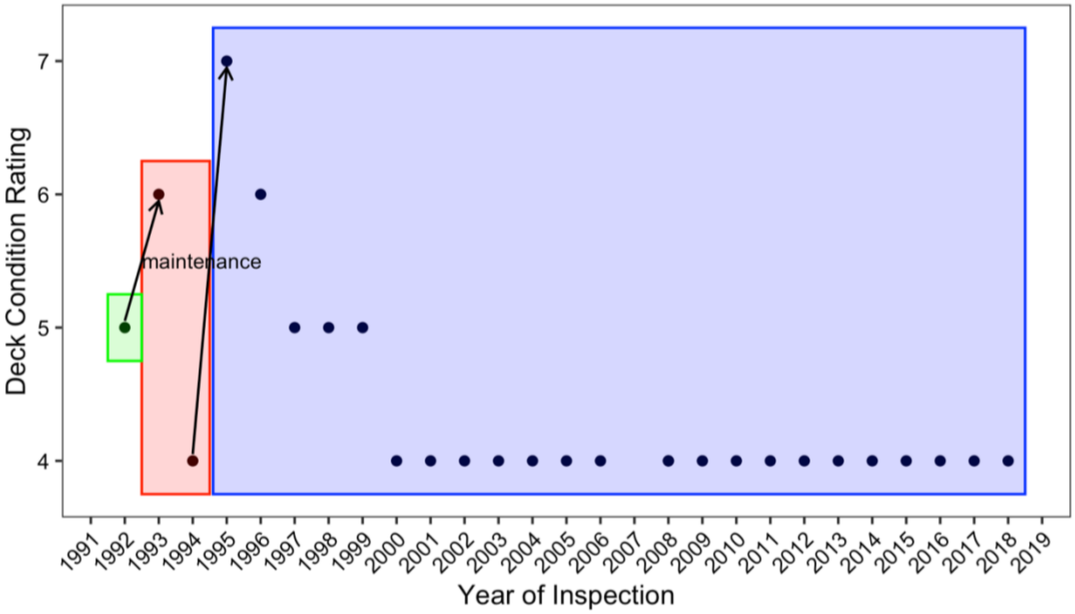

Figure 6.6. Variation in deck condition rating of a bridge for 27 years.

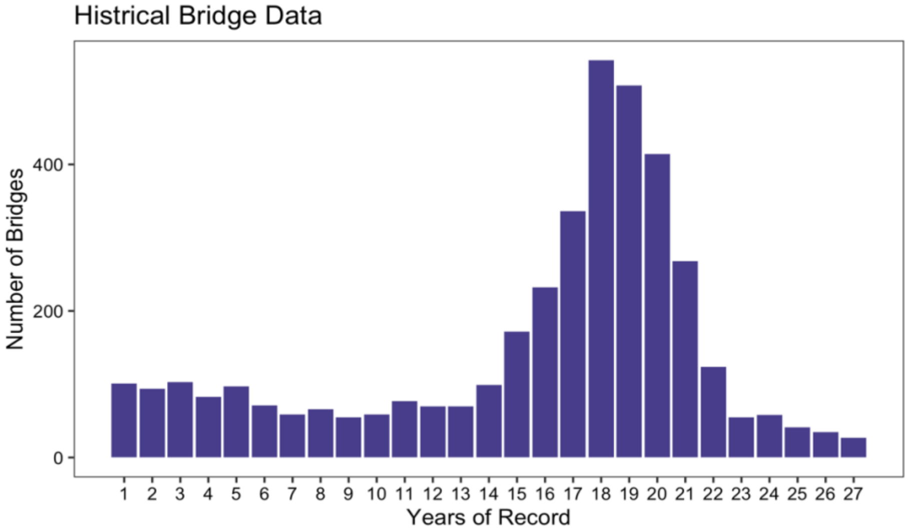

Figure 6.7. Distribution of sequence length of Maryland's bridges.

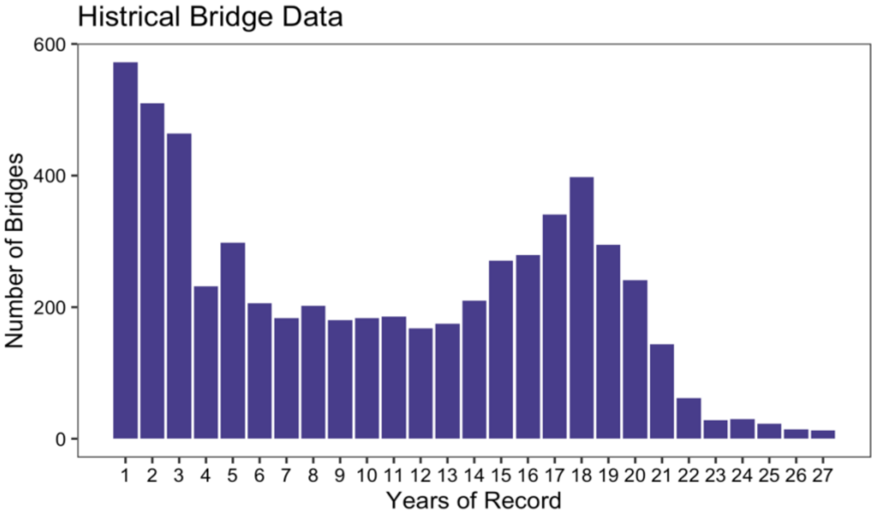

Figure 6.8. Distribution of sequence length of Maryland's bridges after data cleaning.

6.4.1. Dimensionality Reduction

Curse of dimensionality (Taylor, 1993) is a phenomenon when the number of features is relatively high in relation to the observations. The high dimensionality may lead to increase in time or memory requirement for analysis processing, or overfitting problems and decrease in testing accuracy. In order to reduce the number of features, feature selection method is employed using scores or statistical methods. The features are divided into categorical data and numerical data since for each type of data the method is different. The data type for each feature was presented in Table 1. For categorical data two statistical approaches were employed to select the most related features to the output: the Pearson's chi-squared hypothesis test; and the mutual information approach. Pearson's chi-squared statistical hypothesis is an example of a test for independence between categorical variables. The chi-square test of independence compares the observed frequencies of a categorical data with the expected frequencies of the categorical data. The null hypothesis in this case is that the input and output are independent. If the p-value of the test result is less than or equal to a significance level, the null hypothesis is rejected, and the variables are dependent. The mutual information approach is a measure of the dependencies between variables while decreasing the entropy or surprise from the dataset transformation. The results of Pearson's chi-squared test and mutual information are shown in Figure 6.9. The bars represent the score of the features under assessment. From the Pearson's chi-squared the most relevant features include load, maintenance, deck protection, structure type, and membrane. From the mutual information method, the most relevant features include deck protection, load, structure kind, structure type, and surface type. Thus, the common features selected by both methods (i.e., load, deck protection, and structure type) can be selected, or build two models with features selected from each method and then compare the results.

For selecting the most relevant numerical features, analysis of variance (ANOVA) was employed. ANOVA uses the F-test to compare between-group variability to within-group variability. Equal variance between groups means that feature has no significant impact on the response and can be removed from model training. The p-values for each feature are shown in Table 6-2. The selected features from this method are those with low p-values, which include age, inspection frequency, inspection year, year ADT, and ADT.

Based on the selected features from such approaches three data sets, see Table 6-3, were prepared to train the models. The model with the highest accuracy will identify which features are the most relevant.

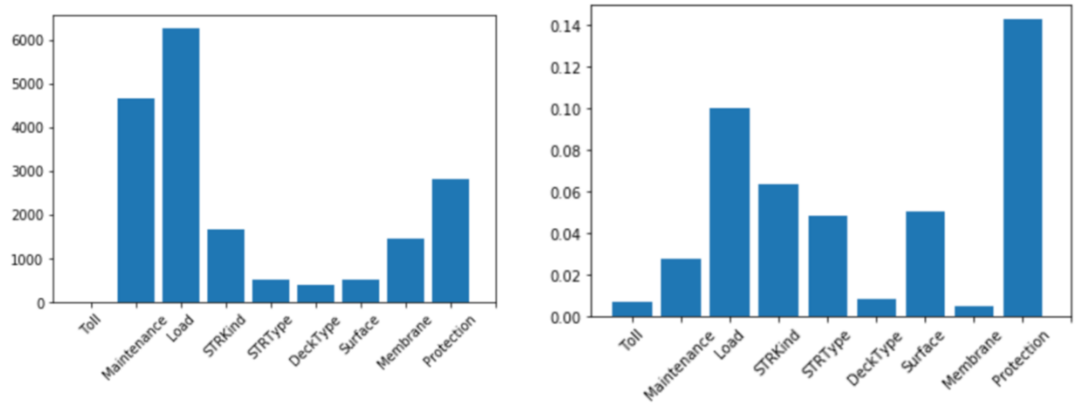

(a) Pearson's chi-squared **(b) Mutual information**

Figure 6.9. Score of categorical features, with (a) Pearson's chi-squared & (b) Mutual information.

Table 6-2. P-values of numerical features.

LAT	LONG	Lanes	ADT	Year ADT	Truck	Age	Year of Inspection	Length	Inspection Frequency
2.34e-20	2.29e-18	4.85e-33	5.50e-42	3.55e-43	2.51e-27	0.0	4.07e-61	1.12e-26	0.00e+00

Table 6-3. Datasets from the data reduction analysis.

Dataset	Features	
Maryland NBI_1	Selected numerical features + selected categorical features (from chi-squared method)	Age, Inspection Frequency, Inspection Year, Year ADT, ADT, Length, Load, Maintenance, Protection, Structure Kind, and Membrane.
Maryland NBI_2	Selected numerical features + selected categorical features (from mutual information method)	Age, Inspection Frequency, Inspection Year, ADT, Year ADT, Length, Protection, Load, Structure Kind, Structure Type, and Surface Type.
Maryland NBI_3	Selected numerical features + selected categorical features (common between two methods)	Age, Inspection Frequency, Inspection Year, Year ADT, ADT, Length, Load, Protection, and Structure Kind.

6.5. Results of ML Modeling

The results of the alternative ML models explored in this study are presented next.

6.5.1. Long-Short Term Memory (LSTM): Sequence-to-one Classification

The input data for this model includes the sequences for each bridge and the latest condition rating for each bridge is the class of that sequence. Therefore, there are 10 classes corresponding to condition ratings of 0 to 9. The bridges selected for learning should have data reported for at least two years, in which the length of input is 1. The shape of the data is shown in Figure 6.10. In this example, the length of the sequences of the first and second bridge are 4 and 6, respectively. Some features like structure length are expected to stay constant through the years and others like ADT are expected to change through time.

During training, the training data are split into mini batches, during data cleaning, cases with only one data point are eliminated resulting in a dataset with about 3600 bridges. The size of the training data, validation data, and testing data was 70%, 10%, and 20%, respectively. The architecture of the network was shown in Fig. 4. To tune the parameters and find the best approach to classify NBI data, different case scenarios were tried. The best result was obtained when ADAM was used as a solver with a base learning rate of 0.001. To find the dataset with the highest performance, the three datasets introduced in Table 3 were trained by Sequence-to-one LSTM. The accuracy of testing on Maryland NBI_1, Maryland NBI_2, and Maryland NBI_3 was 84.4%, 84.94%, and 82.23%, respectively. Therefore, Maryland NBI_2 was selected to train the other models as well.

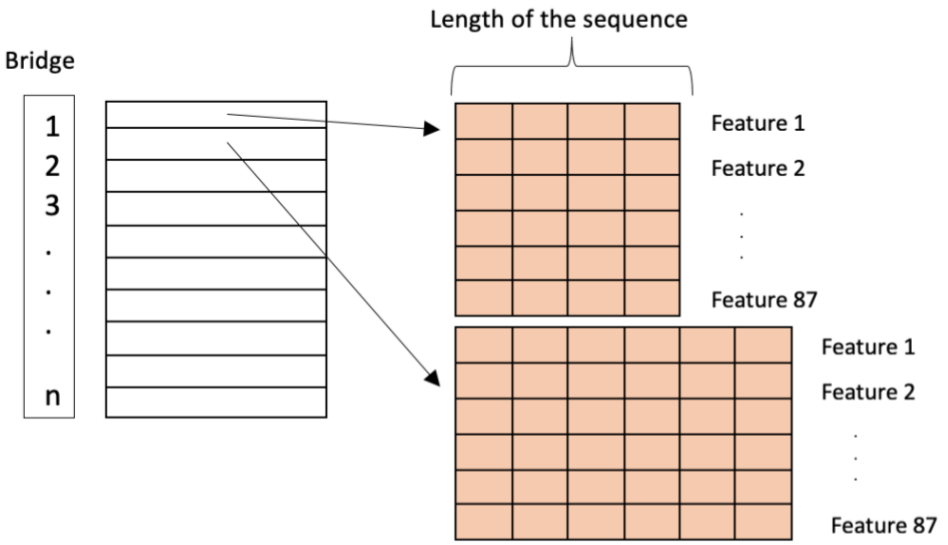
Length of the sequence
Bridge
1
2
3
.
.
.
n
Feature 1
Feature 2
Feature 87
Feature 1
Feature 2
Feature 87

Figure 6.10. Input data for LSTM for a bridge with length of sequence of 4 and 6.

The confusion matrix for sequence-to-one LSTM on Maryland NBI_2 with variable sequence lengths is shown in Figure 6.11. This confusion matrix shows for cases with condition rating greater than 3, the predicted class is within the range of actual class ±1. Therefore, even when the total accuracy of the model is at 82.5%, the incorrect predicted values (i.e., false positive or false negative) do not significantly impact the bridge management decisions. As Liu and Zhang (2020) suggested, the bridges with condition ratings less than 3 can be combined as one class or removed.

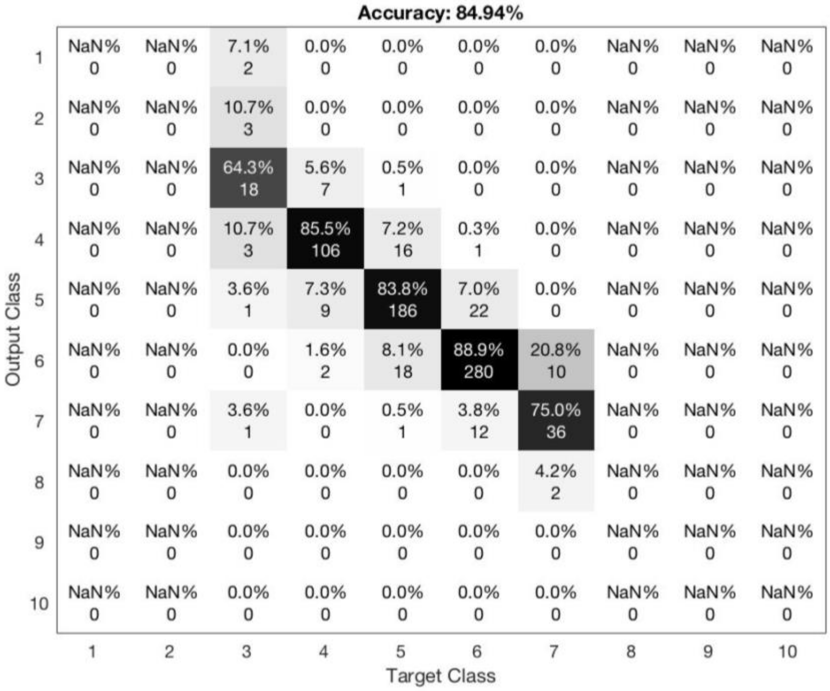

Figure 6.11. Confusion matrix for sequence-to-one LSTM for Maryland NBI_2 with variable sequence lengths.

6.5.2. Long-Short Term Memory (LSTM): Sequence-to-Sequence Classification

In this model the same data set was used as in the LSTM sequence-to-one classification. Figure 6.12 indicates how the data are labeled in a sequence-to-sequence classification. In this example, the bridge condition rating sequence has a length of 10 since the data have been collected biennially for 20 years. Each condition rating in the sequence (input) is labeled with the condition rating of the next inspection, (i.e., the class of each inspection rating is next year's condition rating). Table 6.4 summarizes the results of ML modeling with sequence-to-sequence LSTM. The results of training with sequence-to-sequence LSTM showed that SGDM is a better solver for optimization in this case, Table 6-4.

Figure 6.13 shows an example of surveyed and predicted condition rating for a bridge with length of 26 time-steps. Except the condition rating of the first year, all remaining predictions were equal to those reported in the dataset.

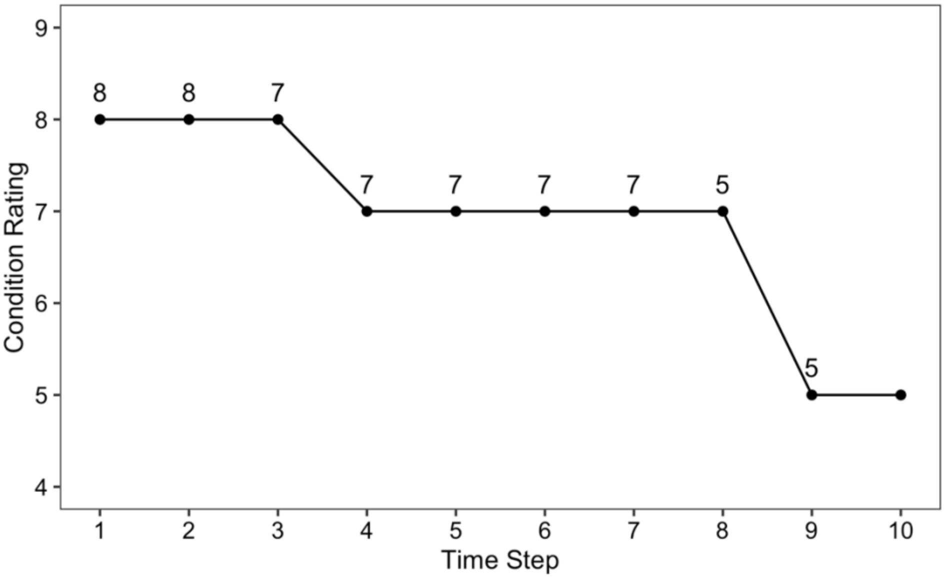

Figure 6.12. Labeling the sequence of condition rating sequence-to-sequence classification.

Table 6-4. Trial of sequence-to-sequence LSTM with different parameters

Trial No.	Solver	Mini-batch Size	Epochs	Base Learning Rate	Testing Accuracy
1	SGDM	32	50	0.01	85.10%

2	ADAM	32	50	0.001	78.0%

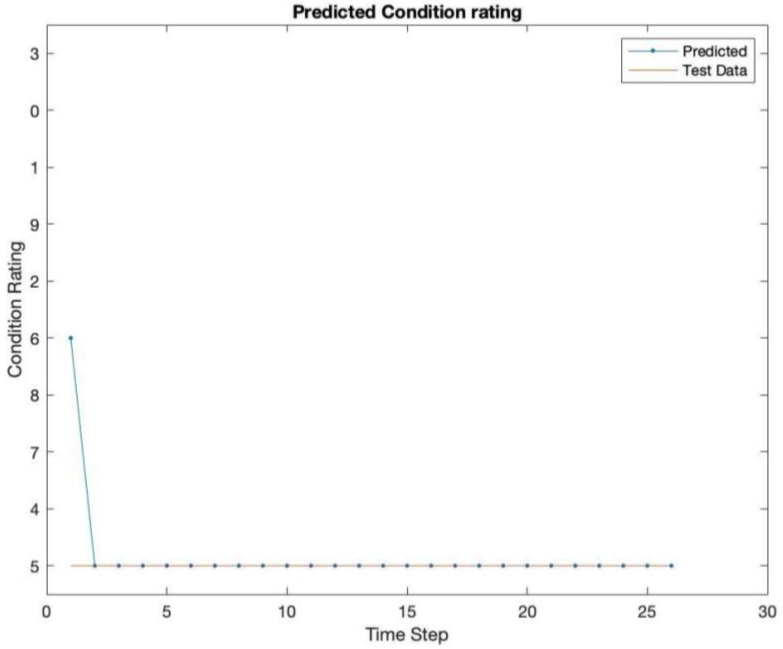

Figure 6.13. Comparison of predicted and actual condition rating of a bridge deck by sequence-to-sequence LSTM.

6.5.3. Convolutional Neural Network: Sequence-to-One Classification

The drawback of CNN sequence-to-one classification relative to LSTM is that the sequences should have similar length. Therefore, only bridges with sequence length of 10 or more with inspection intervals of 24 months were selected, resulting in about 3000 bridges. The first 10 data points of each sequence are selected to prepare a three-dimensional input (bridges, time steps, features). Figure 6.14 shows a schematic of the input data. The frequency of sampling is 0.5 year^{-1}, so that the total period is 18 years, and the condition rating for the 20th year is the class of the sequence. The layers include two CNN followed by a dropout layer for regularization, then a pooling layer. After the CNN and pooling, the learned features are flattened to one long vector and pass through a fully connected layer before the output layer is used to make a prediction. The fully connected layer is for providing a buffer between the learned features and the output to understand the learned features before making a prediction. For this model, first a standard configuration of 64 parallel feature maps (number of filters) followed by 128 and 256 feature maps, and a kernel size (filter size) of 3 was used. The feature maps are the number of times the input is processed or interpreted, whereas the kernel size (number of filters) is the number of input time steps considered, as the input sequence is read or processed onto the feature maps. The efficient ADAM version of stochastic gradient descent is then used to optimize the network, and the categorical cross entropy loss function is used, given that learning a multi-class classification problem is underway. A fully connected layer (dense layer) with 100 neurons and ReLU activation was added before the softmax layer.

The accuracy of testing for this model was 69.37%, Table 6-5, Trial No.1. Different parameters were tried to find the optimum architecture. Table 6-5 includes the summary of the various trials. To mention that trial No.4 is similar to the model proposed by Liu and Zhang (2020) providing similar performance. The filter size controls the number of time steps considered in each "read" of the input sequence, that is then projected onto the feature map (via the convolutional process). A large kernel size means a less rigorous reading of the data, which may result in a more generalized snapshot of the input. Figure 6.15 shows the architecture of Trial 6 with the highest accuracy.

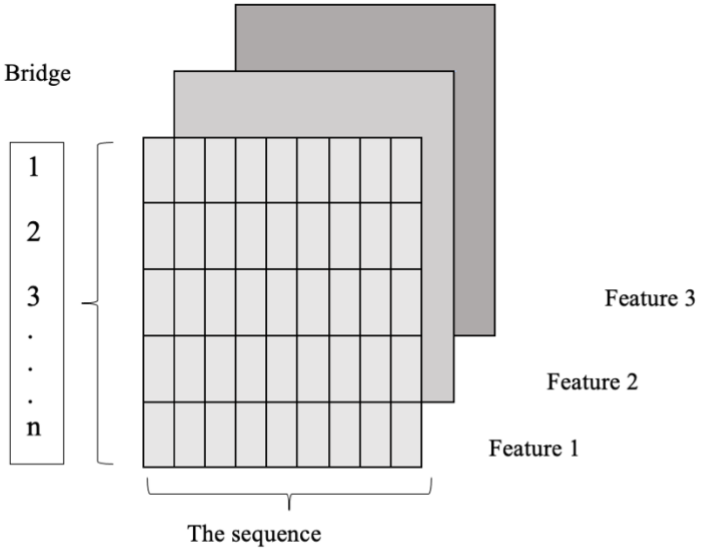

Figure 6.14. Input data preparation for sequence-to-one CNN (Liu and Zhang, 2020).

Table 6-5. Summary of the trials and results of the CNN sequence-to-one classification.

Trial No.	Number of filters			Size of filters			No. of FCs (Neurons)	Max Pooling	Testing Accuracy
	CONV1	CONV2	CONV3	CONV1	CONV2	CONV3			
1	64	128	256	3	3	3	1 (100)	Yes	69.37%
2	64	128	256	3	3	3	3 (100)	Yes	69.71%
3	64	128	256	3	3	3	3 (500)	Yes	70.65%
4	64	128	256	3	3	3	3 (500)	No	81.35%
5	128	128	-	5	5	-	3 (500)	No	81.41%
6	32	128	-	5	5	-	3 (500)	No	82.83%

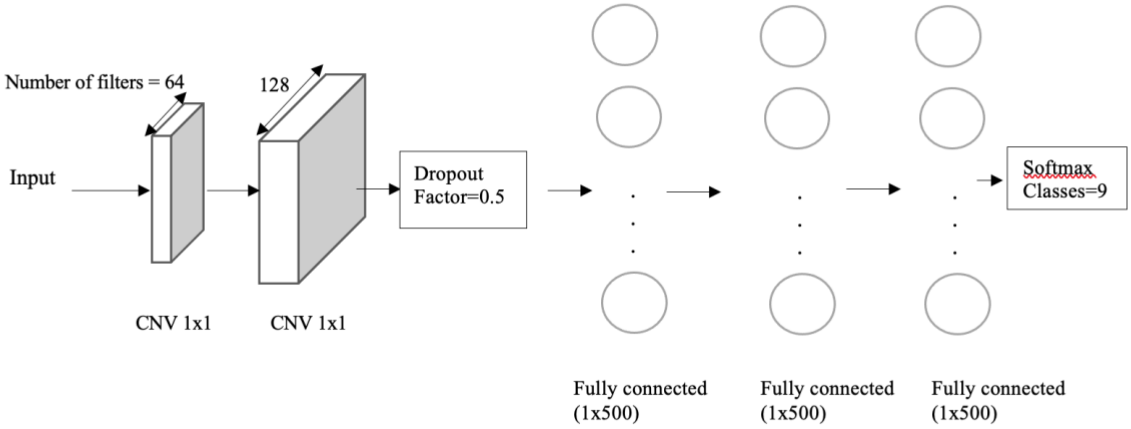

Figure 6.15. Architecture of sequence-to-one classification built in Trial 6.

6.5.4. Temporal Convolutional Network (Sequence-to-Sequence CNN)

Even though TCN can perform on data with different lengths, for sake of simplicity the lengths were kept uniform. Thus, the same data used in the sequence-to-one CNN were also used in the sequence-to-sequence CNN. However, the labeling was similar to the sequence-to-sequence LSTM classification (Figure 6.12). The TCN model was formed of 4 blocks, and input channels equal to the number of features. The mini-batch size was 100 and the dropout factor was 0.05. In contrast to other methods, the learning rate was not constant. The initial learning rate was 0.001 and after every 12 epochs it dropped by a 0.1 factor. Three different filters were tried with size of 3. The number of filters shows a significant impact on accuracy of testing. By changing the number of filters from 100 to 150 and then to 300, the accuracy increases from 94.04% to 95.22% and 95.99%. This is because a larger number of filters provides the ML algorithm the opportunity to consider the data through a greater window and learn from similar cases. The ML algorithm was also tested when condition rating was considered as the only input as well. The accuracy of testing of this model (with 300 filters) was 95.95%. This implies that the ML algorithm learns from condition rating per-se more than any other variable.

To compare the performance of the different models, the Maryland NBI_2 data was split manually (as opposed to randomly) and the alternative networks were trained and tested. The results are shown in Table 6-6. The first portion of the Table presents the results of models where training sequences with different length is possible, while the second portion is related to the results of models with sequence length of 10. The network architectures are comparable with the best-case scenarios of each model tested in the previous sections. Even though different optimization methods (solver) were tried for each model, Table 6-6 presents those with the highest testing accuracy. The results indicate that in addition to the network considered, performance depends on whether constant sequence length or variable sequence length is used. Furthermore, for the sequence-to-one LSTM model on input sequences with variable lengths, ADAM outperforms SGDM with a difference of 5.5%. On the other hand, in the case of constant length sequences, SGDM method outperforms ADAM solver by 3.3%. The results showed that even though sequence-to-sequence CNN should be able to train dataset with different sequence length, a low accuracy was observed and thus the model was not considered. Sequence-to-sequence LSTM provided better performance than sequence-to-one LSTM, and sequence-to-sequence CNN performed better than sequence-to-one CNN. Overall, sequence-to-sequence CNN provided better accuracy.

Table 6-6. Alternative Model Performance

Model	Data	Accuracy of Testing
LSTM (Sequence-to-One)	Variable Length (>1)	83.18%
LSTM (Sequence-to-Sequence)	Variable Length (>1)	88.93%
Model	Data	Accuracy of Testing
LSTM (Sequence-to-One)	Constant Length=10	88.87%
LSTM (Sequence-to-Sequence)	Constant Length=10	89.16%
CNN (Sequence-to-One)	Constant Length=10	86.41%
CNN (Sequence-to-Sequence)	Constant Length=10	95.22%

6.6. Assessing ML Models Response with Additional Data

In order to evaluate the proposed models with data from other states, the bridge data of the state of Massachusetts (MA) were added to the database. In order to randomize the results, in the first step, the location data and state codes are eliminated as the previous case. The number of bridges included in this section from Maryland (MD) and Massachusetts (MA) data after data cleaning is 16,052 with different length of data, and 2,461 with length of at least 10 records. In order to find the most relevant data to this dataset, ANOVA, Pearson's chi-square, and mutual information was performed on the data and the same features showed high relevance and score. However, primary analysis with sequence-to-one LSTM showed that instead of the second group (Table 6-3) the first group of the features provided better accuracy for the testing dataset. The accuracies of testing on this database with previous ML models are summarized in Table 6-7 for comparison purposes. One of the reasons for the decrease in LSTM modeling can be the length of the Massachusetts data. Majority of MA data have a short length (i.e., more than 7700 bridges have only 4 or less records of evaluation). Figure 6.16 shows the confusion matrix for sequence-to-one LSTM on sequences with lengths higher than 10 (first scenario in Table 6-7). Similar to the previous modeling with the Maryland NBI_2 dataset (Figure 6.11), the confusion matrix shows for cases with condition rating greater than 3, the predicted class is within the range of actual class ±1. To investigate the effect of the location and weather, longitude and latitude of the bridges were added to the training and testing data. However, no further improvement was observed.

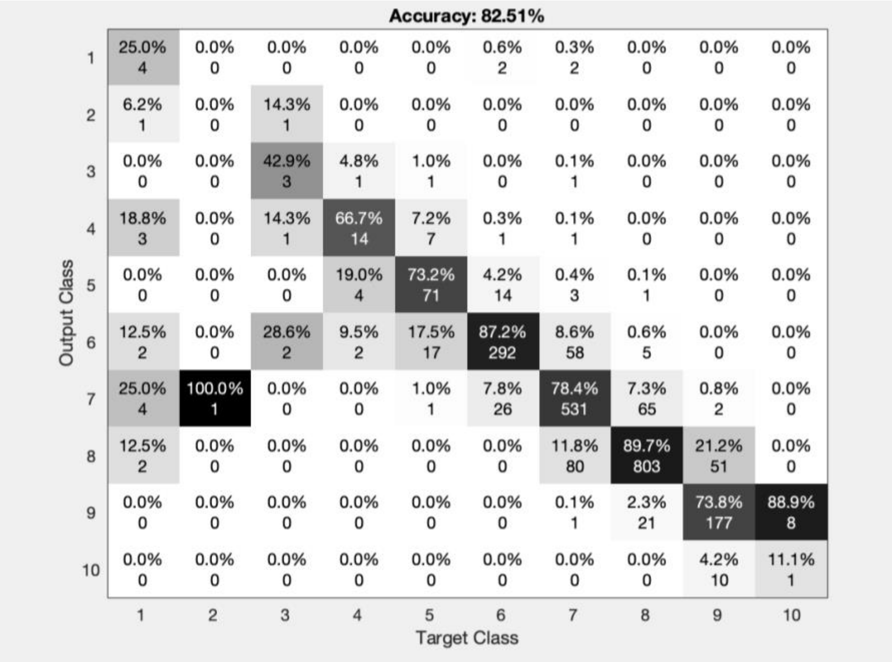

	1	2	3	4	5	6	7	8	9	10
1	25.0% 4	0.0% 0	0.0% 0	0.0% 0	0.0% 0	0.6% 2	0.3% 2	0.0% 0	0.0% 0	0.0% 0
2	6.2% 1	0.0% 0	14.3% 1	0.0% 0	0.0% 0	0.0% 0	0.0% 0	0.0% 0	0.0% 0	0.0% 0
3	0.0% 0	0.0% 0	42.9% 3	4.8% 1	1.0% 1	0.0% 0	0.1% 1	0.0% 0	0.0% 0	0.0% 0
4	18.8% 3	0.0% 0	14.3% 1	66.7% 14	7.2% 7	0.3% 1	0.1% 1	0.0% 0	0.0% 0	0.0% 0
5	0.0% 0	0.0% 0	0.0% 0	19.0% 4	73.2% 71	4.2% 14	0.4% 3	0.1% 1	0.0% 0	0.0% 0
6	12.5% 2	0.0% 0	28.6% 2	9.5% 2	17.5% 17	87.2% 292	8.6% 58	0.6% 5	0.0% 0	0.0% 0
7	25.0% 4	100.0% 1	0.0% 0	0.0% 0	1.0% 1	7.8% 26	78.4% 531	7.3% 65	0.8% 2	0.0% 0
8	12.5% 2	0.0% 0	0.0% 0	0.0% 0	0.0% 0	0.0% 0	11.8% 80	89.7% 803	21.2% 51	0.0% 0
9	0.0% 0	0.0% 0	0.0% 0	0.0% 0	0.0% 0	0.0% 0	0.1% 1	2.3% 21	73.8% 177	88.9% 8
10	0.0% 0	0.0% 0	0.0% 0	0.0% 0	0.0% 0	0.0% 0	0.0% 0	0.0% 0	4.2% 10	11.1% 1

Figure 6.16. Confusion matrix of sequence-to-one LSTM for MD and MA bridges (variable lengths)

Table 6-7. Alternative Model Performance with MD and MA data.

Model	Data	Accuracy of Testing
LSTM (Sequence-to-One)	Variable Length (>1)	82.51%
LSTM (Sequence-to-Sequence)	Variable Length (>1)	84.90%
Model	Data	Accuracy of Testing
LSTM (Sequence-to-One)	Constant Length=10	80.51%
LSTM (Sequence-to-Sequence)	Constant Length=10	85.60%
CNN (Sequence-to-One)	Constant Length=10	92.18%
CNN (Sequence-to-Sequence)	Constant Length=10	97.23%

6.7. Summary & Conclusions

In this study alternative ML models were explored using the NBI database. These included long short-term memory (LSTM) and convolutional neural network (CNN) with sequence-to-one and sequence-to-sequence classification to predict the condition rating of bridge decks. The objective was predicting bridge deck condition rating based on a sequence of condition ratings and variables in NBI that affect performance. In sequence-to-one classification, the condition rating of the last bridge deck assessment was the class of the whole sequence, whereas in sequence-to-sequence classification the class of each condition rating was its condition rating at the next assessment. Sequence-to-sequence classification models outperformed the sequence-to-one classification that past studies have focused on. Thus, the proposed models outperformed those developed in previous studies in terms of accuracy in prediction. While bridges from the state of Maryland were initially used in this study the State of Massachusetts bridge deck data were added from NBI to assess the validity of these models to a wider set of bridges and region. As expected, expanding the data with bridge decks from other regions affected model response, yet provided acceptable level of accuracy. Such effects are attributed to the impact of wider set of climatic effects on materials and structures' performance; wider range of materials and mixtures used; alternative construction and quality control practices and specifications; variations in design standards for the same type of bridge deck and structures; and other material and construction practices. Further ML modeling can address transferability to other regions and bridge deck types, and assessing the effect of introducing new data from sources other than NBI.

Chapter 7. Conclusions and Recommendations

In this study, alternative non-destructive testing (NDT) methods were examined for potential adoption in the QA of concrete. The objective of the research was to assess the accuracy and precision of these methods in detecting concrete quality and flaws or features within concrete members. The integration of these NDTs in QA will overcome some shortcomings of conventional destructive methods since the NDTs are quick, inexpensive, impose less disruption to traffic and structure since they do not require cores, and can be repeated with minimal impact on cost and testing time.

Other specific objectives included: a) developing relationships between maturity index and those concrete properties that are obtained from NDT, which can decrease or possibly eliminate the number of concrete samples tested in compressive strength and other destructive tests; b) assessing non-uniformity in conventional concrete by employing different NDTs, and eventually using chloride permeability tests; c) assessing NDTs in detecting and locating defects in a concrete slab; d) expanding the laboratory study with field results in assessing GPR response in evaluating a deteriorated bridge deck; and e) predicting the condition of infrastructures such as bridges with high accuracy to decrease the frequency of testing and thus the associated cost and effort.

a) Relationships between maturity index and concrete properties from NDT

Chapter 2 presented the results of extensive experiments, which were a combination of destructive and non-destructive tests on 11 concrete mixtures, were presented. The tests included compressive strength, infrared thermography (IRT), ultrasonic pulse velocity (UPV), fundamental resonance frequency, and rebound hammer. The results showed strong relationships between UPV and resonance frequency with maturity index. Also, the same was concluded when IRT was used instead of embedded sensors. The strong relationships of UPV and resonance frequency with maturity index led to developing a generalized model, or "master curve" concept, to predict concrete properties at different ages based on maturity index and defining transfer functions using the most relevant parameters (such as compressive strength, unit weight, and other). The NDT data and maturity index of these mixtures was also used to develop a model for predicting compressive strength with high R^2 (i.e., 0.93). It should be noted that even though the NDTs, such as UPV, IRT, and resonant frequency, have high accuracy and precision in predicting compressive strength, rebound hammer results did not provide the same repeatability level for the laboratory samples.

b) Assessing non-uniformity in concrete with NDTs

In Chapter 3 experiments on a series of concrete samples were designed to evaluate the accuracy and precision of NDTs, such as UPV, IRT, and resonance frequency, in assessing concrete uniformity. Various concrete samples with different mixtures and production procedures were prepared to represent honeycombing and segregation in concrete. UPV was the most accurate NDT in identifying honeycombing and segregation within concrete. Since the voids in honeycombed and segregated samples are localized, resonant frequency was not able to identify the defected samples and/or the defect extent as accurately as UPV. The limitation in sample size and dimension ratio makes the method more disadvantageous for this detection purpose. For the segregated concrete samples rapid chloride permeability (RCP) and rebound hammer testing were also performed. The rapid chloride permeability was performed to relate density and permeability to the degree of segregation and NDT response. The difference in chloride permeability was in total agreement with UPV difference at the top and bottom of the segregated samples and to some degree with the rebound number results. Rebound hammer showed good relationship with the results of UPV and RCP. This could be the result of the high sensitivity of the rebound hammer to the presence of coarse aggregate at the vicinity of the concrete surface.

c) Detecting delamination in concrete with NDTs

The results of the experimentation in evaluating ultrasonic pulse echo (UPE) and ground penetrating radar (GPR) response in detecting delamination in concrete slab was presented in Chapter 4. Alternative NDTs, such as IRT and UPV, were only used to estimate the shear wave velocity in concrete from similarly cured concrete samples. The measurements with UPE were repeated from day 1 to day 60. Testing was repeated two or three times a day to evaluate the repeatability of each method. The accuracy of UPE in detecting delamination depth and extent was improved as the concrete surface dried. UPE was able to estimate the depth of delamination with a deviation of 0.1 to 2.4 cm. GPR only showed minor evidence of presence of delamination. This was due to the dielectric properties of the selected material representing delamination (i.e., plexiglas), limited thickness of both the delamination layer and dimensions of the slab. The presence of rebar also contributed to such limitation. Rebound hammer was also performed on the concrete slab since a decrease in rebound number at delaminated areas (due to hollowness) was expected. However, in this study, since the concrete was relatively fresh and the delaminated area was not hollow (i.e., represented by plexiglass) the effects on rebound number were negligible. To simulate the Lamb wave propagation in the concrete slab, a linear-elastic finite element model (FEM) was built in ABAQUS. The results of the finite element simulation were compared with the experimental results. FEM not only provides a quantitative means of assessing the NDT performance, but also provides the means of modeling complex field conditions and reducing the need for costly experimental testing. The depth of the delamination identified by FEM was comparable to the experimental results and the minor discrepancies that can be due to the possible movement of the plexiglass or the discrepancies between the concrete actual properties and assumed values in FEM.

d) Evaluating bridge deck health with GPR

In order to evaluate GPR response in bridge deck condition assessment, two GPR antennas with frequencies of 600 MHz and 2000 MHz were used on an older bridge.

The experimental results of this study were used to identify the thickness of the asphalt overlay on the concrete deck, and the location and condition of the reinforcement. The results were validated with ground truth data obtained from drilled holes and open bridge deck joint surveys. This study indicated that the location and the extent of the asphalt overlay thickness and corroded reinforcement can be determined with accuracy of 1 to 2 cm. In addition, the condition of the reinforcement was assessed and the location of the corroded or missing rebars were identified through a series of B-scans. The use of GPR in health monitoring and assessing the condition of bridge superstructure and substructure is recommended to avoid a potential disastrous collapse of the bridge, with substantial cost and safety consequences.

e) Predicting bridge deck condition with Machine Learning

Transition from lab to field conditions where more complex conditions may be encountered between causes and effects needs extensive testing and analysis. As it was shown in this study, field validation of NDT testing requires the use of "ground truth" data in order to compare and assess the accuracy. The demanding cost and effort, and the many other factors involved in field investigations and discussed in this study, are the impulses for the need to predict the condition of infrastructure in conjunction with routine field assessment. To better capture the complex relationships and sequence nature of the features affecting bridge deck condition, and thus provide improved predictions from past ML studies using such databases, this study employed sequential long short-term memory (LSTM) and convolutional neural networks (CNN) modeling. The advantage of this approach is that the input length (i.e., number of condition observations from previous years) is not fixed. Thus, it can consider all the NBI data recorded every year, and/or a flexible set of sequence, while traditional ML classification models explored in past studied were based on sequential observations with a fixed length of data. The accuracy of the developed models for predicting bridge deck conditions was high, ranging from more than 80% all the way to 97% depending on the model and the various hyperparameters used in each case.

In terms of future work, the findings of this study need to be validated and expanded by performing sensitivity analysis on sample dimension, concrete mixture proportion, and types. Also, other NDTs that can be incorporated in QA, for both field and laboratory conditions (i.e., impact echo), should be considered in future studies. Thus, the important findings presented in chapters 2 and 3 can be further expanded to develop universally accepted models for maturity modeling and acceptance of concrete uniformity for QA. With respect to GPR for detecting very thin layers of delamination, alternative materials with variable dielectric properties should be used in laboratory samples. Degree of reinforcement corrosion should be also considered. To overcome sample size limitation and improve GPR detection for such thin layer samples, stepped frequency GPR (SF-GPR) can be employed. In terms of field condition assessment, further testing on deteriorated bridge decks, including some core testing, should be considered. With respect to enhancing ML modeling for predicting bridge deck condition, data from a variety of diverse geographical regions should be selected. Similarly, alternative bridge deck type structures may be considered. Every year new data is added to the NBI database, so the proposed ML algorithms should be updated with the new data for further fine tuning and enhancing the proposed models' prediction accuracy. Finally, other machine learning algorithms, such as time series forecasting and model ensemble techniques, can be developed to further improve condition rating predictions for a longer period of time.

Bibliography

1. Al-Qadi, I., and Lahouar, S. (2005). "Part 4: Portland cement concrete pavement: measuring rebar cover depth in rigid pavements with ground-penetrating radar." Transportation Research Record: Journal of the Transportation Research Board, (1907), 80-85.
2. Alani, A. M., Aboutalebi, M., and Kilic, G. (2013). "Applications of ground penetrating radar (GPR) in bridge deck monitoring and assessment." Journal of Applied Geophysics, 97, 45-54.
3. Alipour, M., Harris, D. K., & Barnes, L. E. (2017). Pattern recognition in the national bridge inventory for automated screening and the assessment of infrastructure. In Structures Congress 2017 (pp. 279-291).
4. Amini, K., Cetin, K., Ceylan, H., & Taylor, P. (2019). Development of prediction models for mechanical properties and durability of concrete using combined nondestructive tests. Journal of Materials in Civil Engineering, 31(2), 04018378.
5. Anugonda, Phanidhar, Joshua S. Wiehn, and Joseph A. Turner. (2001). "Diffusion of ultrasound in concrete." Ultrasonics 39(6), 429-435.
6. Arras, B., Wolf, E., Rodriguez, D. D., & Nazarian, S. New Methodology for Evaluating Incompatibility of Concrete Mixes in Laboratory: A Feasibility Study (No. CAIT-UTC-NC37), 2019.
7. ASCE. (2021). 2021 report card for America's infrastructure. https://www.infrastructurereportcard.org/wp-content/uploads/2020/12/2021-IRC-Executive-Summary.pdf. Last accessed: 01/30/2021.
8. Assaad, R., & El-adaway, I. H. (2020). Bridge infrastructure asset management system: Comparative computational machine learning approach for evaluating and predicting deck deterioration conditions. Journal of Infrastructure Systems, 26(3), 04020032.
9. ASTM D4748 (2015). "Standard test method for determining the thickness of bound pavement layers using short-pulse radar." ASTM International, West Conshohocken, PA. doi: https://doi.org/10.1520/D4748-10R15
10. ASTM D6087 (2015)e1. "Standard test method for evaluating asphalt-covered concrete bridge decks using ground penetrating radar." West Conshohocken, PA. ASTM International, doi: https://doi.org/10.1520/D6087-08R15E01
11. ASTM International. ASTM C215-14. (2014). Standard Test Method for Fundamental Transverse, Longitudinal, and Torsional Resonant Frequencies of Concrete Specimens. West Conshohocken, PA. doi: https://doi.org/10.1520/C0215-14
12. ASTM International. ASTM C805-18. (2018). Standard Test Method for Rebound Number of Hardened Concrete. West Conshohocken, PA.
13. Azari, H., Nazarian, S., and Yuan, D. "Assessing sensitivity of impact echo and ultrasonic surface waves methods for nondestructive evaluation of concrete structures." Construction and Building Materials 71 (2014): 384-391.

14. Azenha, M., Faria, R., and Figueiras, H. Thermography as a Technique for Monitoring Early Age Temperatures of Hardening Concrete. Construction and Building Materials, 2011, 25(11), 4232-4240.
15. Bai, S., Kolter, J. Z., & Koltun, V. (2018). An empirical evaluation of generic convolutional and recurrent networks for sequence modeling. arXiv preprint arXiv:1803.01271.
16. Barnes, C. L., & Trottier, J. F. (2002). Phenomena and conditions in bridge decks that confound ground-penetrating radar data analysis. Transportation research record, 1795(1), 57-61.
17. Barnes, C. L., and Trottier. J. F. (2000) “Ground-penetrating radar for network-level concrete deck repair management”, ASCE Journal of Transportation Engineering, Vol 126, No 3, pp. 257- 262.
18. Barnes, C. L., Trottier, J. F., and Forgeron, D. (2008). “Improved concrete bridge deck evaluation using GPR by accounting for signal depth–amplitude effects.” NDT & E International, 41(6), 427-433.
19. Benedetto, A., Tosti, F., Ciampoli, L. B., and D’amico, F. (2017). “An overview of ground-penetrating radar signal processing techniques for road inspections.” Signal processing, 132, 201-209.
20. Bishop, C. M. Pattern Recognition and Machine Learning. (2006). Springer, New York, NY.
21. Bogas, J. Alexandre, M. Glória Gomes, and Augusto Gomes. 2013. "Compressive strength evaluation of structural lightweight concrete by non-destructive ultrasonic pulse velocity method." Ultrasonics 53, no. 5, 962-972.
22. Breul, Pierre, Jean-Marie Geoffray, and Younés Haddani. "On-site concrete segregation estimation using image analysis." Journal of Advanced Concrete Technology 6, no. 1 (2008): 171-180.
23. Breysse, D. (2012). “Nondestructive evaluation of concrete strength: An historical review and a new perspective by combining NDT methods. Construction and Building Materials.”, 33, pp.139-163.
24. Bryant, J. (2014). “Durability Testing - Rapid Chloride Permeability.” SMART COCRETE, doi: https://info.kryton.com/blog/2014/11/durability-testing-rapid-chloride-permeability-test. Website last accessed: 29 July 2021.
25. Cady, P. D., and Gannon, E. J. (1992). “Condition evaluation of concrete bridges relative to reinforcement corrosion.” Volume 8: Procedure Manual (No. SHRP-S-330).
26. Carper, K.L. (1987). “Structural Failures During Construction.” Journal of performance of constructed facilities, 1(3), 132-144.
27. Cassidy, N. J., and Jol, H. M. (2009). “Ground penetrating radar data processing, modelling and analysis.” Ground penetrating radar: theory and applications, 141-176.
28. Chang, T.P., Lin, H. C., Chang, W.T., Hsiao, J.F. (2006). "Engineering properties of lightweight aggregate concrete assessed by stress wave propagation methods." Cement and Concrete Composites 28(1), 57-68.
29. Cheilakou, E., Theodorakeas, P., Koui, M., Moustakidis, S., and Zeris, C. (2012). “Application of ground penetrating radar (GPR) as a diagnostic

technique in concrete bridges inspection." 42nd International Conference and NDT Exhibition: NDE for Safety 2012, Czech Republic.

30. Chen, J., Bharata, R., Yin, T., Wang, Q., Wang, H., Zhang, T. (2017). "Assessment of sulfate attack and freeze-thaw cycle damage of cement-based materials by a nonlinear acoustic technique." Materials and Structures 50(2), 105.
31. Chou, J. S., Tsai, C. F., Pham, A. D., & Lu, Y. H. (2014). Machine learning in concrete strength simulations: Multi-nation data analytics. Construction and Building Materials, 73, 771-780.
32. Clemena, G.G., and McKeel, W.T. (1978). "Detection of Delamination in Bridge Decks with Infrared Thermography" Proc. Commission on sociotechnical systems national research council, Transportation Research Board, Washington D.C.
33. Datta, D., & Kishore, N. N. (1996). "Features of ultrasonic wave propagation to identify defects in composite materials modelled by finite element method." NDT & E International, 29(4), 213-223.
34. Davis, A. G., F. Ansari, R. D. Gaynor, K. M. Lozen, T. J. Rowe, H. Caratin, F. D. Heidbrink et al. (1998). "Nondestructive test methods for evaluation of concrete in structures." American Concrete Institute, ACI 228.
35. Demirdag, S., Yavuz, H., & Altindag, R. (2009). The Effect of Sample Size on Schmidt Rebound Hardness Value of Rocks. *International Journal of Rock Mechanics and Mining Sciences*, 46(4), 725-730.
36. Din, Z. U., & Tang, P. (2016). Automatic logical inconsistency detection in the National Bridge Inventory. Procedia Engineering, 145, 729-737.
37. Dinh, K., Zayed, T., Romero F., Tarussov, A. (2014). "Method for analyzing time-series GPR data of concrete bridge decks." Journal of Bridge Engineering 20 (6) 04014086, http://dx.doi.org/10.1061/(ASCE)BE.1943-5592.0000679.
38. Ede, A. J. (1967). An Introduction to Heat Transfer Principles and Calculations. Pergamon, Tarrytown, N.Y.
39. El-Newihy, A. (2017). Application of impact resonance method for evaluation of the dynamic elastic properties of polypropylene fiber reinforced concrete (Doctoral dissertation).
40. Emily Pollock. "Italy's Morandi Bridge Collapse—What Do We Know?" Engineering.com (2018). Date of visit: 2019. < https://www.engineering.com/BIM/ArticleID/17517/Italys-Morandi-Bridge-CollapseWhat-Do-We-Know.aspx>
41. Faraway, J. J. (2004). Linear models with R. Chapman and Hall/CRC.
42. FHWA, U. (1995). Recording and coding guide for the structure inventory and appraisal of the nation's bridges. Recording and coding guide for the structure inventory and appraisal of the nation's bridges. US Department of Transportation, Bridge Management Branch, FHWA, Washington, DC.
43. FHWA. (2020). Datasets between 1983 and 2019, National Bridge Inventory, Washington, DC. Accessed March 30, 2021. https://www.fhwa.dot.gov/bridge/nbi/ascii.cfm

44. FHWA. (2021). Bipartisan infrastructure law. https://www.fhwa.dot.gov/bipartisan-infrastructure-law/. Last accessed 01/30/2022.
45. Fiocco, M. (1998). US Freight Economy in Motion. Federal Highway Administration, Washington, D.C.
46. Gagarin N., Mekemson J., Goulias, D. (2017). "Second-generation analysis approach for condition assessment of transportation infrastructure using step-frequency (SF) ground-penetrating-radar (GPR) array system." 10th International Conference on the Bearing Capacity of Roads, Railways and Airfields." BCCRA 2017, Athens, Greece.
47. Gagarin, N., Goulias, D., Mekemson, J., Cutts, R. and Andrews, J. (2020). Development of Novel Methodology for Assessing Bridge Deck Conditions Using Step Frequency Antenna Array Ground Penetrating Radar. Journal of Performance of Constructed Facilities, 34(1), p.04019113.
48. Gao, C., & Elzarka, H. (2021). The use of decision tree based predictive models for improving the culvert inspection process. Advanced Engineering Informatics, 47, 101203.
49. Gao, X., Zhang, J., & Su, Y. (2019). Influence of vibration-induced segregation on mechanical property and chloride ion permeability of concrete with variable rheological performance. Construction and Building Materials, 194, 32-41.
50. Ghods, P., Alizadeh, R., Salehi, M., and De Carufel, S. (2017). Embedded Wireless Monitoring Sensors. U.S. Patent Application 15/474, 175, filed October 5.
51. Goulias, D. (2016) "Manual using Non-destructive Testing and Case Studies on Non-Structural Precast Concrete Products in Highway Construction." NDE/NDT for Highway and Bridges: Structural Materials Technology (SMT) Conference, Portland.
52. Goulias, D. (2017a) "A novel segmentation approach for identifying homogeneous pavement sections using GPR data." International Journal of Pavements, 16(1).
53. Goulias, D. (2017b). "Effective implementation of GPR for condition assessment and monitoring – phase 2." Final Research Report, SP509B4K, Maryland State Highway Administration, MSHA, Hanover, MD.
54. Goulias, D. (2017c). "Improving the Core Products of Highway Quality Assurance Programs." Federal Highway Administration (FHWA) DTFH61-14-D-00009.
55. Goulias, D. (2019) "FHWA Manual Incorporating NDT into the QA of Nonstructural Concrete Products for Highway Construction" 98th Transportation Research Board Annual Meeting. Presentation at the AFH20 Management of Quality Assurance Committee.
56. Goulias, D. (2019). "FHWA Manual Incorporating NDT into the QA of Nonstructural Concrete Products for Highway Construction" 98th Transportation Research Board Annual Meeting. Presentation at the AFH20 Management of Quality Assurance Committee.
57. Goulias, D. G., Cafiso, S., Di Graziano, A., Saremi, S. G., & Currao, V. (2020). "Condition assessment of bridge decks through ground-penetrating radar in

bridge management systems." Journal of Performance of Constructed Facilities, 34(5), 04020100.

58. Goulias, D., Ali, A. (1998). "Evaluation of Rubber Filled Concrete and Correlation Between Destructive and Non-Destructive Testing Results." ASTM Cement, Concrete and Aggregates Journal, 20(1), 140-144.
59. Goulias, D., and Scott, M. (2015). "Effective implementation of ground penetrating radar (GPR) for condition assessment & monitoring of critical infrastructure components of bridges and highways" (No. MD-15-SHA-UM-3-11).
60. Graveen, C., Weiss, J., O., Jan, and Nantung, T. (2003). Implications of Maturity and Ultrasonic Wave Speed Measurements in QC/QA for Concrete. *Brittle Matrix Composites*, 7, 379-388. Woodhead Publishing.
61. Gucunski, N., Imani, A., Romero, F., Nazarian, S., Yuan, D., Wiggenhauser, H., Shokouhi, S., Taffe, A., and Kutrubes, D. (2013). "SHRP 2 Report S2-R06A-RR-1: Nondestructive testing to identify concrete bridge deck deterioration". Transportation Research Board of the National Academies, Washington, DC.
62. Hansen, W. (1986). Static and dynamic modulus of concrete as affected by mix composition and compressive strength, ACI Spec. Publ. SP 95, American Concrete Institute, 115.
63. Hansen, W., and Surlaker, S. (2006). Embedded Wireless Temperature Monitoring Systems for Concrete Quality Control, Whitepaper.
64. Hansen, W., Static and dynamic modulus of concrete as affected by mix composition and compressive strength, ACI Spec. Publ. SP 95, American Concrete Institute 1986, 115.
65. Hashim, M., Jaw, S. W., and Marghany, M. (2011). "Ground penetrating radar data processing for retrieval of utility material types and radius estimation. In 2011 IEEE International RF & Microwave Conference (pp. 191-196). IEEE.
66. Hassan, A.M.T. and Jones, S.W. (2012). Non-destructive testing of ultra-high-performance fiber reinforced concrete (UHPFRC): A feasibility study for using ultrasonic and resonant frequency testing techniques. Construction and Building Materials, 35, 361-367.
67. Hobbs, B. (1991). Development of a construction quality control procedure using ultrasonic testing. Brick and Block Masonry, 1, 636-644.
68. Hong, S., Lynn, H.S. (2020). Accuracy of random-forest-based imputation of missing data in the presence of non-normality, non-linearity, and interaction. BMC Med Res Methodol 20, 199. https://doi.org/10.1186/s12874-020-01080-1
69. Huang, Y. H. (2010). Artificial neural network model of bridge deterioration. Journal of Performance of Constructed Facilities, 24(6), 597-602.
70. Hugenschmidt, J., and Mastrangelo, R. (2006). "GPR inspection of concrete bridges." Cement and Concrete Composites, 28(4), 384-392.
71. Janků, M., Cikrle, P., Grošek, J., Anton, O., & Stryk, J. (2019). Comparison of infrared thermography, ground-penetrating radar and ultrasonic pulse echo for detecting delaminations in concrete bridges. Construction and Building Materials, 225, 1098-1111.

72. Johnson, D., Johnson, G., & Robertson, I. N. (2010). Quantifying Segregation in Self-Consolidating Concrete through Image Analysis (Doctoral dissertation, Master’s Thesis Report, Department of Civil and Environmental Engineering, University of Hawaii, Honolulu, HI).
73. Jol, H. M. (Ed.). (2008). “Ground penetrating radar theory and applications”. Elsevier.
74. Kesler, C.E. and Higuchi, Y., Determination of compressive strength of concrete by using its sonic properties, Proc. ASTM, 53, 1044, 1953.
75. Khalef, R., & El-adaway, I. H. (2021). Automated Identification of Substantial Changes in Construction Projects of Airport Improvement Program: Machine Learning and Natural Language Processing Comparative Analysis. Journal of Management in Engineering, 37(6), 04021062.
76. Kingma, D. P., & Ba, J. (2014). Adam: A method for stochastic optimization. arXiv preprint arXiv:1412.6980.
77. Komlos, K., Popovics, S., Nürnbergerová, T., Babal, B. and Popovics, J.S. Ultrasonic pulse velocity test of concrete properties as specified in various standards. Cement and Concrete Composites, 1996, 18(5), 357-364.
78. Kozlov, V. N., Samokrutov, A. A., & Shevaldykin, V. G. (1997). Thickness measurements and flaw detection in concrete using ultrasonic echo method. Nondestructive Testing and Evaluation, 13(2), 73-84.
79. Lahouar, S., Al-Qadi, I., Loulizi, A., Clark, T., and Lee, D. (2002). “Approach to determining in situ dielectric constant of pavements: development and implementation at interstate 81 in Virginia.” Transportation Research Record: Journal of the Transportation Research Board, (1806), 81-87.
80. Leśnicki, Krzysztof J., Jin-Yeon Kim, Kimberly E. Kurtis, and Laurence J. Jacobs. (2011). "Characterization of ASR damage in concrete using nonlinear impact resonance acoustic spectroscopy technique." NDT & E International 44(8), 721-727.
81. Li, J., Walubita, L. F., Simate, G. S., Alvarez, A. E., and Liu, W. (2015). “Use of ground-penetrating radar for construction monitoring and evaluation of perpetual pavements.” Natural Hazards, 75(1), 141-161.
82. Lin, S., Shams, S., Choi, H., & Azari, H. (2018). “Ultrasonic imaging of multi-layer concrete structures.” NDT & E International, 98, 101-109.
83. Lin, Y., Sansalone, M., & Carino, N. J. (1990). Finite element studies of the impact-echo response of plates containing thin layers and voids. Journal of Nondestructive Evaluation, 9(1), 27-47.
84. Liu, H., & Zhang, Y. (2020). Bridge condition rating data modeling using deep learning algorithm. Structure and Infrastructure Engineering, 1-14.
85. MacLeod, G. (1971). An assessment of two non-destructive techniques as a means of examining the quality and variability of concrete in structures. No. Tech Rpt. 42.454 R&D Rpt.
86. Mahmoudipour, M. (2009). Statistical Case Study on Schmidt Hammer, Ultrasonic and Core Compression Strength Tests’ Results Performed on Cores Obtained from Behbahan Cement Factory in Iran. In 5th International Workshop of NDT Experts.

87. Maierhofer, C., Zacher, G., Kohl, C., & Wöstmann, J. (2008). Evaluation of radar and complementary echo methods for NDT of concrete elements. Journal of Nondestructive Evaluation, 27(1), 47-57.
88. Maierhofer, Ch., Arndt, R., Rollig, M., Rieck, C., Walther A., Scheel H., Hillemeier B. (2006). “Application of impulse-thermography for non-destructive assessment of concrete structures” Cement & Concrete Composites, 28, 393–401.
89. Malhotra, V. M., and Carino, N. J. (2003). Handbook on Nondestructive Testing of Concrete, CRC press.
90. Mangalathu, S., & Jeon, J. S. (2019). Machine learning–based failure mode recognition of circular reinforced concrete bridge columns: Comparative study. Journal of Structural Engineering, 145(10), 04019104.
91. Marković, N., Stojić, D., Cvetković, R., Radojičić, V., & Conić, S. (2018). Numerical modeling of ultrasonic wave propagation–by using of explicit FEM in ABAQUS. Facta Universitatis, Series: Architecture and Civil Engineering, 16(1), 135-147.
92. Martino N., Birken, R., Maser, K., and Wang M. (2014). “Developing a deterioration threshold model for assessment of concrete bridge decks using ground penetrating radar.” The 93rd Annual Meeting of the Transportation Research Board, Washington, D.C, No. 14–3861, (Accession Number: 01519232).
93. Martino, N., Maser, K., & Birken, R. (2015). “Adapting a Ground Coupled GPR Threshold Model for Use with Air Coupled GPR Systems.” Proc. NDT-CE.
94. Maryland State Highway Administration, (2018). “Standards Specifications.” Hanover, MD.
95. Maser, K. (1991). “Bridge deck condition surveys using radar: Case studies of 28 new England decks.” Transportation Research Record 1304.
96. Maser, K. R. (1996). Condition Assessment of Transportation Infrastructure Using Ground-Penetrating Radar. ASCE Journal of Infrastructure Systems, 2(2), 94–101.
97. Mele V. (2018). “Bridge management system in Italy” DICAT Symposium, on “Prove ad alto rendimento per controlli e manutenzione di infrastrutture stradali [High performance tests for road infrastructure checks and maintenance].” 18 July. Catania, IT (in Italian).
98. Misak, L., Corbett, D., & Grantham, M. (2019). Comparison of 2D and 3D ultrasonic pulse echo imaging techniques for structural assessment. In MATEC Web of Conferences 289, 06003. EDP Sciences.
99. Nan, W., HAN. A.M. (2008)."Experiment and application of the combined method of pulse velocity and rebound hardness in tunnel engineering.” Journal of Nanjing University of Technology (Natural Science Edition) 4.
100. National Center for Environmental Information, Data Tools. Accessed August 8, 2020. https://www.ncdc.noaa.gov/cdo-web/datatools/selectlocation
101. Nguyen, T. T., & Dinh, K. (2019). Prediction of bridge deck condition rating based on artificial neural networks. Journal of Science and Technology in Civil Engineering (STCE)-NUCE, 13(3), 15-25.

102. Nguyen, T., Kashani, A., Ngo, T., & Bordas, S. (2019). Deep neural network with high-order neuron for the prediction of foamed concrete strength. Computer-Aided Civil and Infrastructure Engineering, 34(4), 316-332.

103. Omar, T., Nehdi, M.L., and Zayed, T. (2017). “Integrated Condition Rating Model for Reinforced Concrete Bridge Decks.” Journal of Performance of Constructed Facilities, 31(5). https://doi.org/10.1061/(ASCE)CF.1943-5509.0001084

104. Petro Jr, J.T. and Kim, J. (2012). “Detection of delamination in concrete using ultrasonic pulse velocity test.” Construction and Building Materials, 26(1), 574-582.

105. Pollock, E. (2018). “Italy’s Morandi Bridge Collapse—What Do We Know?” Engineering.com Date of visit: 2019. < https://www.engineering.com/BIM/ArticleID/17517/Italys-Morandi-Bridge-CollapseWhat-Do-We-Know.aspx>

106. Proceq Manual (2017). for Silver Schmidt Operating Instructions. Silver Schmidt & Hammerlink, doi: https://www.proceq.com/uploads/tx_proceqproductcms/import_data/files/SilverSchmidt_Operating%20Instructions_English_high.pdf

107. Qasrawi, Hisham Y. (2000). "Concrete strength by combined nondestructive methods simply and reliably predicted." Cement and concrete research 30.5 739-746.

108. Rao, S.K., Sravana, P. and Rao, T.C. (2016). Relationship between Ultrasonic Pulse Velocity and Compressive Strength for Roller Compacted Concrete Containing GGBS. Int. J. Appl. Eng., 11(3), 2077-2084.

109. Romero, F. A., Roberts, G. E., and Roberts, R. L. (2000). “Evaluation of GPR bridge deck survey results used for delineation of removal/maintenance quantity boundaries on asphalt-overlaid, reinforced concrete deck.” In Structural Materials Technology IV-An NDT Conference, Atlantic City, NJ.

110. Ruder, S. An overview of gradient descent optimization algorithms. Accessed April 14, 2021. https://ruder.io/optimizing-gradient-descent/index.html#momentum,

111. Safawi, M. I., Iwaki, I., & Miura, T. (2004). “The segregation tendency in the vibration of high fluidity concrete.” Cement and concrete research, 34(2), 219-226.

112. Sajid S., Chouinard L. (2017) “Reliability of Resonant Frequency test for Strength Estimation in 566 Concrete Using Probabilistic Methods. “Proceedings Structural Health Monitoring.

113. Sansalone, M., and N. J. Carino. (1989). Detecting Delaminations in Concrete Slabs with and without Overlays Using the Impact-Echo Method. ACI Materials Journal, 86(2), 175–184.

114. Santhanam, M., and Sanish, K.B. (2012). Characterization of Strength Development of Concrete Using Ultrasonic. 18th World Conference on Non-destructive Testing, Durban, South Africa, K.B.

115. Saremi S.G., Goulias D. (2020). “Concrete Strength Gain Monitoring with Non-Destructive Methods for Potential Adoption in Quality Assurance.” Journal of Construction and Building Materials, 260.

116. Saremi, S.G., Goulias, D. (2021). “Non-destructive Testing for Strength Gain Monitoring of Concrete in Quality Assurance.” Presented at 100th Annual Meeting of the Transportation Research Board, Washington, D.C.
117. Saremi, S.G., Goulias, D. Zhao, Y. (2022). “Development of Alternative Sequence Classification Networks for Predicting Condition Rating of Bridge Decks.” Journal of Performance of Constructed Facilities. In Revision.
118. Saremi, S.G., Goulias, D., Akhter A.A. (2020). “Non-destructive Testing Methods in Quality Assurance and Quality Control of Concrete for Monitoring Strength Gain During Production.” Presented at 99th Annual Meeting of the Transportation Research Board, Washington, D.C.
119. Saremi, S.G., Goulias, D., Akhter A.A. (2022a). “NDT in Quality Assurance of Concrete for Assessing Production Uniformity.” Presented at 101st Annual Meeting of the Transportation Research Board, Washington, D.C.
120. Saremi, S.G., Goulias, D.G., Akhter, A.A. (2022b). “Non-Destructive Testing in Quality Assurance of Concrete for Assessing Production Uniformity.” Transportation Research Record, 03611981221103871.
121. Sharma, M.R. and Gupta, B.L., (1960). Sonic modulus as related to strength and static modulus of high strength concrete, Indian Concr. J. (Bombay), 34(4), 139.
122. Simi, A., Manacorda, G., and Benedetto, A., (2012) “Bridge deck survey with high resolution ground penetrating radar.” 14th International Conference on Ground Penetrating Radar (GPR), Shanghai, 489-495. doi: 10.1109/ICGPR.2012.6254915
123. Solla, M., Lagüela, S., González-Jorge, H. and Arias, P. (2014). “Approach to Identify Cracking in Asphalt Pavement Using GPR and Infrared Thermographic Methods: Preliminary Findings.” NDT & E International, 62, 55-65.
124. Spagnolini, U. (1997) "Permittivity measurements of multilayered media with monostatic pulse radar." IEEE Transactions on Geoscience and Remote sensing 35(2), 454-463.
125. Srivastava, N., G. Hinton, A. Krizhevsky, I. Sutskever, R. Salakhutdinov. (2014). "Dropout: A simple way to prevent neural networks from overfitting." Journal of Machine Learning Research. 15, 1929-1958.
126. Su, Z., & Ye, L. (2009). Identification of damage using Lamb waves: from fundamentals to applications, 48. Springer Science & Business Media.
127. Sultan, A. A., and Washer, G. A. (2017). “Reliability analysis of ground-penetrating radar for the detection of subsurface delamination.” Journal of Bridge Engineering, 23(2), 04017131.
128. Tanyidizi, H., and Coskun, A. (2008). Determination of the Principal Parameter of Ultrasonic Pulse Velocity and Compressive Strength of Lightweight Concrete by Using Variance Method. Russian Journal of Nondestructive Testing, 44(9), 639–646. © Pleiades Publishing, Ltd.
129. Taylor, C. R. (1993). Dynamic programming and the curses of dimensionality. Applications of Dynamic Programming to Agricultural Decision Problems., 1-10.

130. Tharmaratnam, K., & Tan, B. S. (1990). Attenuation of ultrasonic pulse in cement mortar. Cement and Concrete research, 20(3), 335-345.

131. Tompson, J., Goroshin, R., Jain, A., LeCun, Y., & Bregler, C. (2015). Efficient object localization using convolutional networks. In Proceedings of the IEEE conference on computer vision and pattern recognition, 648-656.

132. Tsubokawa, T., Mizukami, J., Esaki, T., Hayano, K. (2007). "Study on infrared thermographic inspection of de-bonded layer of airport flexible pavement" 2007 FAA Worldwide Airport Technology Transfer Conference, Atlantic City, New Jersey, USA

133. Turgut, P. Research into the Correlation between Concrete Strength and UPV Values. www.NDT.Net, 2004, 12(12).

134. Uddin, M. A., Jameel, M., Sobuz, H. R., Islam, M. S., & Hasan, N. M. S. (2013). "Experimental study on strength gaining characteristics of concrete using Portland Composite Cement." KSCE Journal of Civil Engineering, 17(4), 789-796.

135. Upadhyaya, S., Goulias, D. and Obla, K. (2014). "Maturity-Based Field Strength Predictions of Sustainable Concrete Using High-Volume Fly Ash as Supplementary Cementitious Material." Journal of Materials in Civil Engineering, 27(5), 04014165.

136. Uysal, M., & Yilmaz, K. (2011). "Effect of mineral admixtures on properties of self-compacting concrete." Cement and Concrete Composites, 33(7), 771-776.

137. Van der Wielen, A., Courard, L., & Nguyen, F. (2012). Static detection of thin layers into concrete with ground penetrating radar. Restoration of Buildings and Monuments, 18(3/4), 247-254.

138. Wang, J., Wen, G., Yang, S. and Liu, Y. (2018). "Remaining useful life estimation in prognostics using deep bidirectional LSTM Neural Network." Prognostics and System Health Management Conference (PHM-Chongqing), Chongqing, China, pp. 1037-1042, doi: 10.1109/PHM-Chongqing.2018.00184.

139. Wu, S. R., & Gu, L. (2012). Introduction to the explicit finite element method for nonlinear transient dynamics. John Wiley & Sons.

140. Yang, C., Gupta, R. (2018). "Prediction of the Compressive Strength from Resonant Frequency for Low-Calcium Fly Ash-Based Geopolymer Concrete." ASCE Journal of Materials in Civil Engineering. 30(4).

141. Yim, H. J., Bae, Y. H., & Kim, J. H. (2020). Method for evaluating segregation in self-consolidating concrete using electrical resistivity measurements. Construction and Building Materials, 232, 117283.

142. Yu, Y., Li, W., Li, J., & Nguyen, T. N. (2018). A novel optimized self-learning method for compressive strength prediction of high-performance concrete. Construction and Building Materials, 184, 229-247.

143. Zhao, S., Shangguan, P., and Al-Qadi, I. L. (2015). "Application of regularized deconvolution technique for predicting pavement thin layer thicknesses from ground penetrating radar data." NDT & E International, 73, 1-7.

144. Zhu, J., Kee, S.H., Han, D. and Tsai, Y.T. (2011). “Effects of air voids on ultrasonic wave propagation in early age cement pastes.” Cement and Concrete Research, 41(8), 872-881.